PROCEEDINGS OF THE IAEA TECHNICAL COMMITTEE MEETING ON RF LAUNCHERS FOR PLASMA HEATING AND CURRENT DRIVE

November 10-12, 1993, Naka, Japan

August 1994

(Ed.) Takumi YAMAMOTO, Haruyuki KIMURA and Tsuyoshi IMAI

Proceedings of the IAEA Technical Committee Meeting on
RF Launchers for Plasma Heating and Current Drive
November 10-12, 1993, Naka, Japan

(Ed.) Takumi YAMAMOTO, Haruyuki KIMURA and Tsuyoshi IMAI

Naka Fusion Research Establishment
Japan Atomic Energy Research Institute
Naka-machi, Naka-gun, Ibaraki-ken

This is the proceedings of the IAEA Technical Committee Meeting on Radio-Frequency Launcher for Plasma Heating and Current Drive held on November 10-12, 1993 at Naka Fusion Research Establishment of Japan Atomic Energy Research Institute (JAERI). 23 papers including 9 invited papers were presented. In the topics related with ion cyclotron range of frequencies, ten papers were presented and critical issues of the launcher for plasma heating in large device were discussed. In particular, it was pointed out that radiation spectrum and structure of the launcher and materials of Farady shield play a key role to suppress impurity contamination into a plasma. New launchers installed for JET and D Ⅲ-D are expected to drive the plasma current efficiently. In the lower hybrid range of frequencies, there were eight papers, which discussed structure, conditioning methods, coupling to the plasma and heat load of a launcher. New advanced launchers, taking account of the heat load, were proposed for a next generation device. Five papers were presented in the electron cyclotron range of frequencies and characterized versatility and simple launcher of the system compared with others.

COMMITTEE MEMBERS

Scientific Programme Committee

J. Jacquinot   : JET Joint Undertaking, Culham,UK
T. Nagashima   : ITER Garching Co-Center, Germany
R. Prater   : General Atomics, San Diego,USA
Y. Terumichi   : Kyoto University, Kyoto, Japan
G. Tonon   : Association Euratom-CEA, Cadarache,France
J.R. Wilson   : Princeton Plasma Physics Laboratory Princeton, USA
T. Yamamoto   : Japan Atomic Energy Research Institute, Naka Japan

Local Organizing Committee

T. Yamamoto   : Chairman
H.Kimura   :
T.Imai   :
M.Hashimoto   : Secretary

プラズマ加熱及び電流駆動における高周波ランチャーに関する
ＩＡＥＡ主催の技術検討会のプロシーディング
1993年11月10－12日、那珂町

日本原子力研究所那珂研究所核融合装置試験部

（編）山本　　巧・木村　晴行・今井　　剛

　　本プロシーディングは、那珂研において平成5年11月10－12日に開催されたプラズマ加熱及び電流駆動における高周波ランチャーに関する技術検討会のものである。発表件数は23件であった。イオンサイクロトロン周波数帯では、10件の発表があり、主に大型装置における加熱用アンテナの問題点が検討された。特に、放射スペクトルとファラディーシールドの構造及び材料が不純物発生の抑制に対して重要であることが指摘された。ＪＥＴとDⅢ－Dでは、電流駆動用のランチャーが取付けられ、今後の実験が期待される。低域混成波周波数帯では、8件の発表があり、ランチャーの構造、コンディショニング、プラズマとの結合及びランチャー先端部の熱負荷についての検討結果が示された。次世代用に先端部の熱負荷を考慮した、簡素化されたランチャーが提案された。電子サイクロトロン周波数帯では、5件の発表があり、応用の多様性と簡単なランチャー構造が特徴付けられた。

Contents

目　　　次

PREFACE

A 3-day Technical Committee Meeting on Radiofrequency Launchers for Plasma Heating and Current Drive was hosted by Japan Atomic Energy Research Institute (JAERI), Japan under the auspices of the International Atomic Energy Agency (IAEA). It was held on November 11-12, 1993 at the Naka-site of JAERI. The IAEA was represented by V.V. Demchenko. The meeting was attended by about 40 participants from seven countries. Participation to the meeting was based on the nomination of specialist by the IAEA Member States.

The objective of the meeting was to review the present status of the plasma and RF launcher interaction for the plasma heating and current drive in various frequency ranges (Ion cyclotron to electron cyclotron) and to discuss the possible technical solution of the RF launchers to be installed on large fusion machine. The technical aspects of the current RF launching system were discussed also.

The programme consisted of 9 presentation sessions chaired by H.Kimura, D.Moreau (Association Euratom-CEA, Cadarache, France), G.Tonon, V.Erckmann (IPP Garching, Germany), R.Wilson, S.Santini (ENEA, Frascati, Italy), V.Bhatnagar(JET Joint Undertaking, Culham, UK), R.Prater, W. Baity (ORNL, USA), and a summary session by T.Imai in which summary talks on ECRF, LHRF and ICRF were conducted by R.Prater, G.Tonon and H.Kimura , respectively. 23 papers were presented and nine of them were invited papers. We wish to thank all the authors for the large amount of work they have produced in order to make the meeting fruitful and successful, and also the session chairmen and particularly R.Prater, and G.Tonon for summarizing the papers.

The authors wish to express their sincere gratitude to the IAEA, particularly Dr. V.V. Demchenko and Prof. T. Sekiguchi, member of IAEA-IFRC, for their help in organizing the meeting. Assistance from members of administration office of Naka Fusion Research Establishment during the meeting was greatly appreciated.

T.Yamamoto, H.Kimura, T.Imai
Naka Fusion Research Establishment
Japan Atomic Energy Research Institute
Naka-machi, Naka-gun Ibaraki-ken
311-01, Japan

1. Ion Cyclotron Range of Frequencies

1. 1 Launching Fast Waves in Large Devices

J Jacquinot, V P Bhatnagar, A Kaye, T Brown

JET Joint Undertaking, Abingdon, Oxon (UK)

ABSTRACT

Design features of JET A2-antennae including that of remote location of ceramic are outlined. These antennae are being installed in preparation for the new divertor phase of JET that will commence in 1994. The experience of antenna design gained at JET is carried forward to present an outline in blanket/shield design of an antenna for launching fast waves in ITER for heating and current drive. Further, a new wide band antenna the so called "violin antenna" is presented that features high plasma coupling resistance in selected bands in the 20 - 85 MHz frequency range.

1. INTRODUCTION

Ion cyclotron resonance heating antennae that are used to launch fast waves in tokamak plasmas consist of sections of short-circuited strip lines covered by a Faraday screen made of arrays of metal rods. Such antennae have been used for nearly the last two decades with success in plasma heating but the contamination of plasma with additional RF-specific impurity release had been a major concern until 1987. Since then the understanding of the mechanism of impurity release, namely the sputtering caused by the ions accelerated in the field created by rectification in RF sheaths has lead to the following three golden rules to eliminate ICRF specific impurities: (i) use low-Z screen material such as Be (B or C) which has self-sputtering coefficient less than unity, (ii) align the screen rods with the total magnetic field and (iii) use $(0, \pi)$-phasing between the two straps of an antenna. In a less restricted operation of the system, one or more of above rules may be violated, although Be-screen may still rescue the situation especially in the current drive phasing for which $\Delta\phi \neq 0$ or π.

A significant contribution has been made by JET in resolving this impurity production problem. The early designs of JET A_{01} and A_{02} antennae (1985 - 86) and the knowledge gained from their operation culminated in the design of A1-antennae having a tilted beryllium screen with two current straps in each antenna so that they can be phased. In conjunction with automated phasing and matching techniques using multiple feedback controls, including that on the antenna-plasma coupling resistance, the ICRH system at JET has become a versatile tool routinely requested by JET operators in a variety of plasma conditions. This has led to new regimes that were not accessible before and allowed to maintain high power after transition to advanced confinement regimes. A power of 22 MW for more than 2.5 s to an L-mode plasma and about 3 MW (limited only by in-vessel components) for as long as 1 minute has been

coupled to JET plasmas. ICRH produced H-modes, pellet enhanced plasmas (PEP) with H-modes, improved background ion heating in high-minority scenarios, sawteeth control by minority current drive, synergy with the lower hybrid current drive (LHCD) and the high bootstrap current regimes are some of the most notable examples in JET ICRF experiments.

This paper is organised as follows. In Section 2, we present the design features of JET A2-antennae that are being installed in JET for the new divertor phase of JET in 1994. An outline design of fast wave antennae for the next step tokamaks is given in Section 3. In Section 4, we present a new concept of the traditional short-circuited strip line antenna that can operate over a wide frequency band (20 - 85 MHz) which is likely to be required to take full advantage of the fast wave heating and current drive scenarios available for the next step. Discussion and conclusions of this paper are given in Section 5.

2. THE JET A2-ANTENNA

2.1 Background to the A2-Antennae

The so-called A1-antennae have been operating in JET since 1987, originally with water-cooled nickel screens but since 1989 with radiation cooled beryllium screens. These latter screens have demonstrated ICRF operation with negligible impurity production leading to the production of long elm-free H-modes with ICRH alone. A new set of four ICRF antennae structures with four straps each have now been constructed for the pumped divertor phase of JET, in order to maintain good coupling with the much increased distance from the separatrix to the torus wall. These so-called A2-Antennae [1] have several novel features, a number of which are relevant to next step antennae.

2.2 Main Design Features

The A2-antennae have been developed to give good coupling to the new JET divertor plasma for which the separatrix is typically 0.5 m from the low field side vacuum wall. This has enabled the design of a large antenna having a depth to the backwall of typically 0.35 m, which enables efficient coupling with a plasma/screen distance of typically 7 cm. The septa and sidewalls are slotted to a depth of 80 mm in order to minimise the degradation of the spectrum by the image currents, whilst maintaining good isolation between adjacent conductors (measured to be typically 20 dB). A section through this antenna is shown in Fig 1. A typical spectrum of the A2-antenna radiated power in the plasma is shown in Fig 2 for phasing between the straps $\Delta\phi = 0, \pi/2$ and π.

The large projection of the antenna into the torus has the adverse effect that the antenna is very exposed to violent flux changes during disruptions. Design values of 150, 120 and 15 Tesla per second have been used for the vertical, radial, and toroidal fields respectively. At the same time, the maximum load to be supported by the torus was limited to 5 tonnes per

antenna side. As a result, the antenna has been fabricated from thin inconel sheet, in the range 0.8 to 3 mm, with a convoluted design which accommodates the consequentially large thermal expansion. Many links to the torus support the antenna against deformation during disruptions. Also, it has been necessary to incorporate resistors in the mounting arms for the screen elements to further reduce disruption forces. These resistors (typically 100 milli-ohm) are formed by nickel plating beryllium oxide substrates. The JET duty cycle 1/60 can be achieved with radiation cooling alone, and no active cooling is provided. These aspects of the design are likely to be peculiar to the particular requirements of the JET pumped divertor. It is to be anticipated that next step devices will have antennae incorporated into, and supported from, the blanket/first wall.

The screen elements themselves are solid beryllium rods 24 mm in diameter, tilted to be parallel to the magnetic field to avoid the formation of RF sheaths and reducing the impurity production. The antennae are protected to the sides by poloidal limiters with graphite or beryllium tiles projecting 17 mm in front of the screen, and to the top and bottom by dedicated carbon fibre tiles projecting 3 mm in front of the screens.

As originally conceived, the current straps were supported from the housing by ceramic tubes. Following extensive high power RF testing, and subsequent mechanical tests, the antennae are being installed in JET without these supports. This gives an assembly which closely simulates a potential ITER design (see Fig 3) of current strap and vacuum transmission line, where ceramics are precluded by the high neutron flux.

The antennae are mounted in pairs in each quadrant of the torus. The design is such that the four conductors are nearly equispaced in the slim plasma configuration. In the first instance, the antennae will be installed to match the fat plasma, and in this case the spacing between the central two straps is some 50 mm larger. Combined with the slotted sidewalls, this array of straps gives these antennae a good potential fast wave current drive capability [2].

The residual coupling between current straps in such an array complicates the matching of the antennae and reduces the maximum coupled power when operating at other than 0 or 180 degree phase shift between straps. A so-called conjugate matching network is being installed at JET to compensate for this coupling. This may also be an essential aspect of next step designs.

2.3 Current Status of the A2-Antennae

The A2-antennae are presently being prepared for installation in the torus (see Fig 4), which should be complete before the end of 1993. The prototype antenna has been extensively tested [3] in the JET RF test bed up to full voltage (42 kV peak) and duty cycle (60 :1). In addition, critical components

such as the resistors and vacuum transmission lines have been individually RF tested. Operation of these antennae should start early in 1994.

3. ANTENNAE FOR NEXT STEP TOKAMAKS

3.1 General Requirements

The design of ICRF antennae for next step tokamaks will have important additional requirements when compared to present generation systems. In particular, the intense neutron flux both restricts the materials which can be used in the antenna and vacuum transmission lines, and imposes critical requirements on the reliability and low maintenance of the system. The antennae must achieve the same low levels of maintenance as required of the blanket. Experience with present systems shows that this can only be achieved by simplification of the designs, in particular in the vacuum transmission lines. Incorporation of the antenna into the blanket, with no independent remote maintenance requirement, with mechanical support/magnetic shielding from the blanket structure and with near line-of-sight access for the transmission lines offers the best potential for achieving this critical requirement.

The antennae are likely to be located near the mid plane for efficient fast wave current drive and must therefore be protected from the local intense alpha particle flux. In addition, there may be substantial erosion of the plasma facing surface due to the intense heat flux during a disruption although experience at JET indicates a net deposition of material on the outer wall. Such erosion would necessitate a remote refurbishing capability. Power dissipation in the antenna becomes dominated by the neutron flux, and efficient active cooling is essential.

The reliability required of the antenna also demands a fail-safe arc detection system. Melting of stainless steel at an arc may result from a few hundreds of joules energy deposition in a system delivering four megawatts to the plasma. This will require further development of back-up protection systems, possibly optically based.

3.2 Outline Designs Based on JET Experience

A conceptual antenna for a next step tokamak based on JET experience has been produced for NET [4]. The basic structure is a helical pipe forming the screen and cooling the housing, in conjunction with a large section current strap of sufficient stiffness to not require insulating supports inside the vacuum window.

An extension of this design has been proposed also for ITER [5] as illustrated in Fig 5. This uses the same basic helical coil structure, but has been increased substantially in length. This enables the use of a so-called 'violin' current strap (see below), with the feeder line connection close to one end. Such a design fits into the proposed blanket with direct line of sight access

for the transmission line and no ceramics inside the vacuum vessel. The conductor size is sufficient to water cool the six megawatt dissipation in the lower blanket and may be used for this purpose, with the return via the adjacent antenna.

This antenna design is in a number of respects simulated by the JET A2-antenna. Also shown in Fig 3 is a representation of the A2-antenna with the current straps straightened, drawn to the same scale.

The power dissipations in this antenna have been estimated as in Table 1. The power is dominated by the neutron dissipation, which requires a low residence time of the cooling water in the high flux region. A number of parallel screen cooling loops are therefore required. Stainless steel is anticipated for the current strap and housing, with no surface coating. The increased RF losses are modest ($\simeq$ 2% of generator power) and do not justify the technical risk of surface coatings.

The critical area of this outline design is the stress in the screen tubes during a disruption. This determines the depth of slotting of the sidewalls and probably requires the use of high strength alloys such as Inconel 718. A low Z material coating (preferably Beryllium) of the plasma facing surface is required and must be repairable in-situ.

4. VIOLIN ANTENNA CONCEPT

A new concept of the traditional short-circuited strip-line antenna [5], the so-called "violin antenna", see Fig 6, is used in which a long strap is connected in parallel with a very short section. The latter acts as a matching element located within the antenna and improves the power coupling capability especially at low frequencies where the plasma coupling is generally poor. The short section also supports the feed-line central conductor. This design is based on a long length (2.6 m) of the shielded strip line antenna (which is possible to accommodate in the next step devices) such that its electric length is quarter-wave long at a low frequency (~ 10 MHz) and becomes multiples of $\lambda/4$ in the frequency range of interest (20 - 85 MHz). The effect of the plasma on the strip line is included by a radiation resistance R_r (Ω/m) which increases with frequency for the fast wave. Plasma effects reduce the inductance of the antenna but this reduction is practically independent of frequency. For ITER-EDA parameters, R_r can be expressed as $R_r(\Omega/m) = R_{ro}(\Omega/m) \cdot \exp(\alpha_f \cdot f(MHz))$ where $R_{ro} = 2.5\ \Omega/m$ and $\alpha_f = 0.02$.

The antenna coupling resistance R_c is defined as Z_0 where Z_0 is the characteristic impedance of the feeding line and s is the voltage standing wave ratio in the line. For a long stripline, R_c exhibits multiple resonances when the real part of the antenna input admittance is close to the characteristic admittance of the line ($Y_0 = 1/Z_0$). The magnitude of R_c at these peaks increases with frequency since R_r increases with frequency. R_c is smaller at lower frequencies.

The addition of a short (0.4 m) strip line section in parallel with the long one (2.6 m) has the effect of cancelling the reactive part of the input admittance of the long section. This reduces the value of s in the line and increases R_c particularly at certain lower frequencies which can be chosen by selecting the relative lengths of the two sections. The cancellation of the reactive part at higher frequencies becomes weaker and the improvement in R_c is small. This is acceptable as R_c at higher frequency is already significantly high. For an input power of 2 MW, the maximum voltages on the feeder and the antenna straps are shown in Fig 7 in which parameter 'a', the distance of the last closed flux surface of the ITER plasma, is about 0.2 m from the central conductor front surface. It is noted that at the desired frequencies for heating and current drive of ITER: 22 MHz (e-TTMP current drive), 43 MHz (heating at $f = f_{CD}$), 60 MHz (heating and $f = 2 f_{CT}$) and 75 MHz (minority ion current drive), the maximum voltage in the feeder line $\left| V_{L\,max} \right| \leq 20$ kV and that in the antenna $\left| V_{A\,max} \right| \leq 35$ kV. The latter would reduce if the plasma is brought closer to the antenna.

At higher frequencies, when the antenna becomes longer than $\lambda/4$, the current flowing on the antenna reverses its sign depending on the number of times the current node appears on the antenna. A study of the radiated power as a functional of the poloidal mode number ($n_y = k_y\, r_A$ where r_A is the minor radius of the antenna location) shows that the radiated power decreases by a factor of about 0.85 in a case when electric length becomes $> \lambda/4$ (22 MHz) as compared to that when the length is $< \lambda/4$ (10 MHz).

5.   DISCUSSION AND CONCLUSIONS

As mentioned in the last section, the poloidal length of the violin antenna for ITER is about 3 m. We have neglected the effect of finite length of the antenna which can also affect the reactive part of the antenna impedance. This must also be taken into account in the final design. Modules of 6-strap (see Fig 8) at six locations around the torus that do not block any main horizontal access ports can be used. However, the directivity of such an array for TTMP current drive at 22 MHz suffers, particularly at the low toroidal mode numbers (70 % at $n_\phi = 10$) which are required for efficient current drive. Alternatively, 36 antenna straps can be placed in a row covering a quadrant of the torus. In such a case, the directivity is improved to 90 % at $n_\phi = 10$ and it is 98 % at $n_\phi = 20$. The power per strap can be used in the range of 2.5 - 4 MW for maximum voltages in the line of 30 kV. It is preferable to locate the antennae centred on the mid plane as otherwise the current drive efficiency decreases due to $k_{||}$-upshift due to poloidal field effects. When the toroidal field and the plasma currents are co-directional, the antenna located about 1.8 m below the mid plane suffers a degradation in current drive efficiency by a factor of 0.65 as compared to that at the mid plane.

The implementation of ICRF antenna on next step tokamaks is well based on present technology. Nonetheless, technical developments are required in a number of areas, most notably beryllium coating technology, arc protection, and alpha particle limiters. If materials other than water cooled nickel alloys are imposed to minimise active waste, much further understanding of alternative

materials is required, but this would parallel similar first wall and blanket studies. Much detailed design needs to be undertaken on the basis of existing technology with regard to stresses in the screen structure, cooling, selection of materials, optimisation of the spectrum and location in the torus, and realisation of 4 MW windows. The technology of ICRF antennae is nonetheless in good state to enable the implementation of such equipment in next step devices.

In conclusion, a viable outline proposal of fast wave antenna for ITER has been discussed. The violin antenna concept allows operation at a number of frequencies in a wide band (20 - 85 MHz) and dispenses with the need of a ceramic in the immediate vicinity of the antenna that will be subjected to a harsh neutron environment in a reactor. The use of continuous tubular helices that surround the central conductor forming the water cooled screen (without any welding joints facing the plasma) and the cooled housing represents a feasible technical design of the antenna. The water cooling channels through the central conductor itself reduce the number of pipes near the antenna. The neutron shielding properties of water in the cooling system of the antenna screen and that of the central conductor can be optimised and used to advantage for recovering some of the loss of shielding due to the antenna placement.

ACKNOWLEDGEMENT

REFERENCES

[1] Kaye, A. et al, Report JET-P(92)46, JET Joint Undertaking, Abingdon, Oxon, UK.
[2] Bhatnagar, V. P. et al, Proc. IAEA TCM on Fast Wave Current Drive in Reactor Scale Tokamaks, Arles, France (1991) 110.
[3] Brown, T., et al, SOFE Conf. (1993), Hyannis Port (USA).
[4] Brown, T., "Design Study of NET ICRF Antennae", Report NET contract NET/90-806.
[5] Jacquinot, J. et al, Presentation at ITER Tech. Meeting on RF Heating and Current Drive, Garching, October 1993.
[6] Bhatnagar, V. P., Jacquinot, J., Report JET-P(93)76, JET Joint Undertaking.

TABLE 1

	M W
RF Losses	0.09
Plasma Radiation	0.42
Neutron Dissipation	0.60
Total Power Losses	1.1
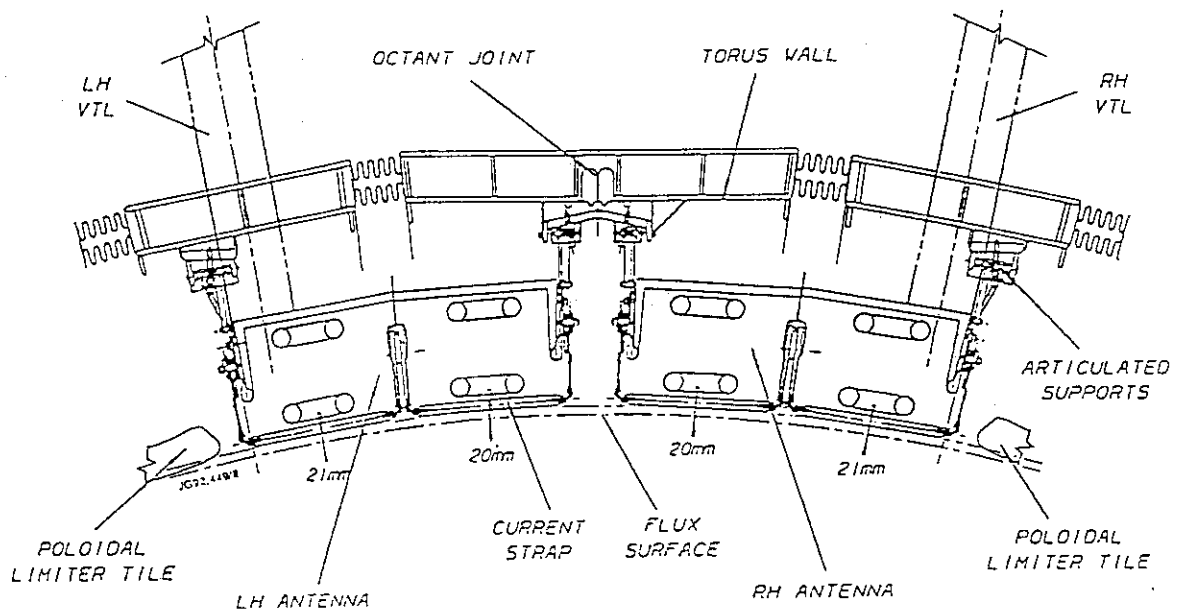
Fig 1. A horizontal section through a pair of the JET A2-antenna as installed in the torus.
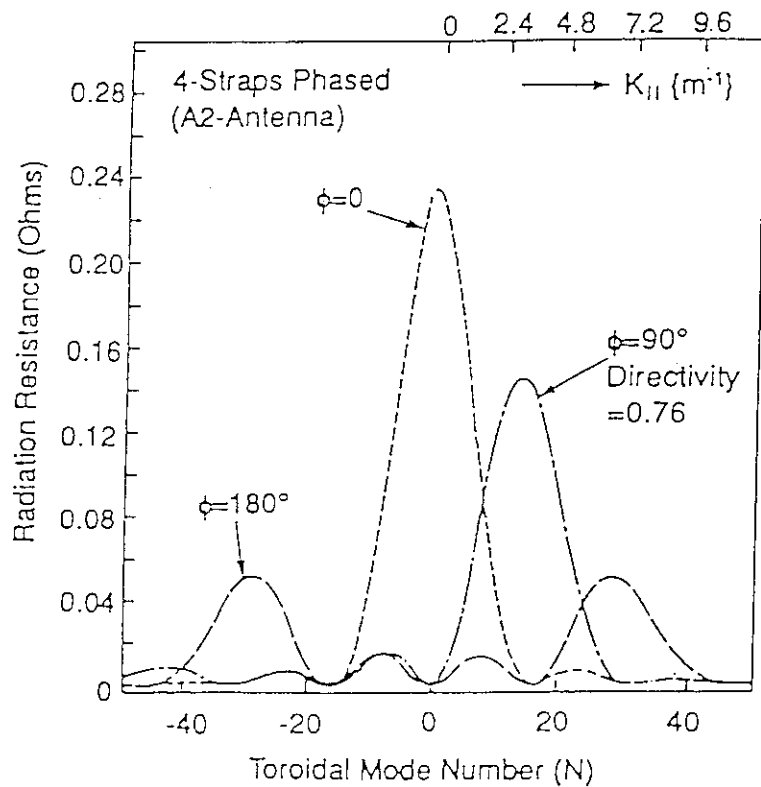
Fig 2. Typical computed radiated power spectrum in the plasma for 4-strap A2-antenna with a phase shift $\Delta\phi = 0, 90°$ and $180°$.

COOLING IN / OUT
VARIABLE STUB
CERAMIC SUPPORT
FROM GENERATOR
PUMP
DOUBLE WINDOWS
COOLING TO THE BLANKET
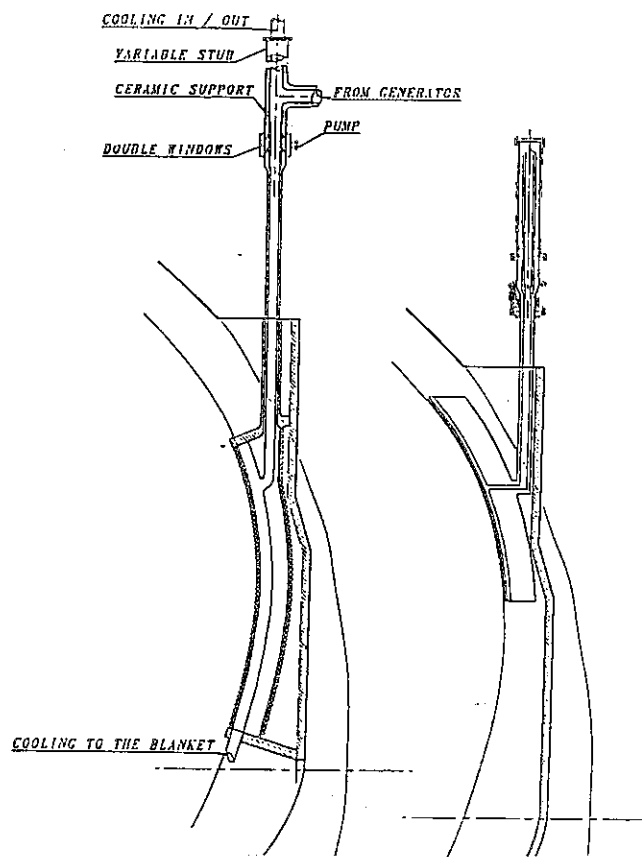
Fig 3. A poloidal view of a proposed "violin antenna" for ITER, together with a stylised view (distorted to allow a dimensional comparison) of the JET A2-antenna to the same scale.
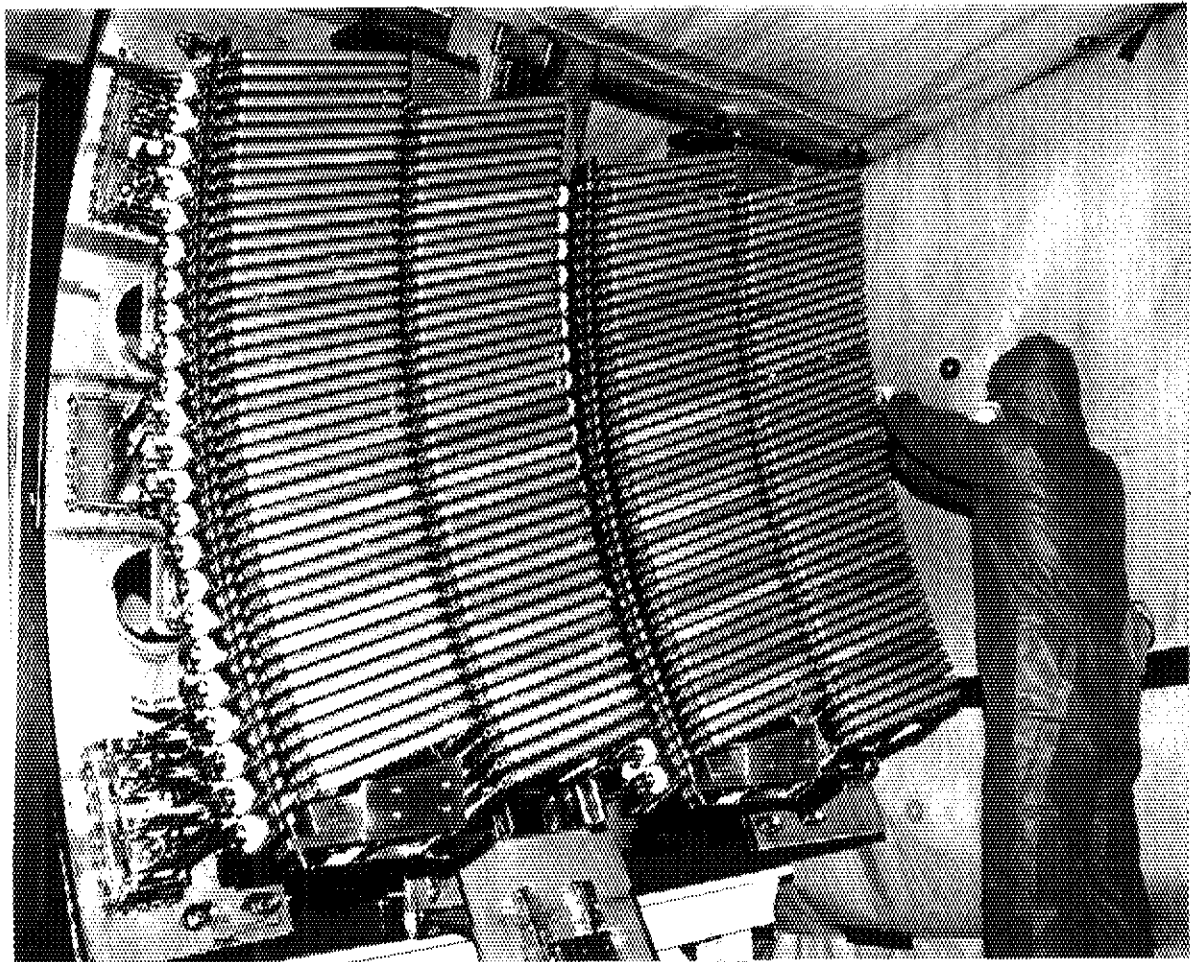
Fig 4. A photograph of a JET 4-strap A2-antenna with Be screen prepared for installation in the torus.
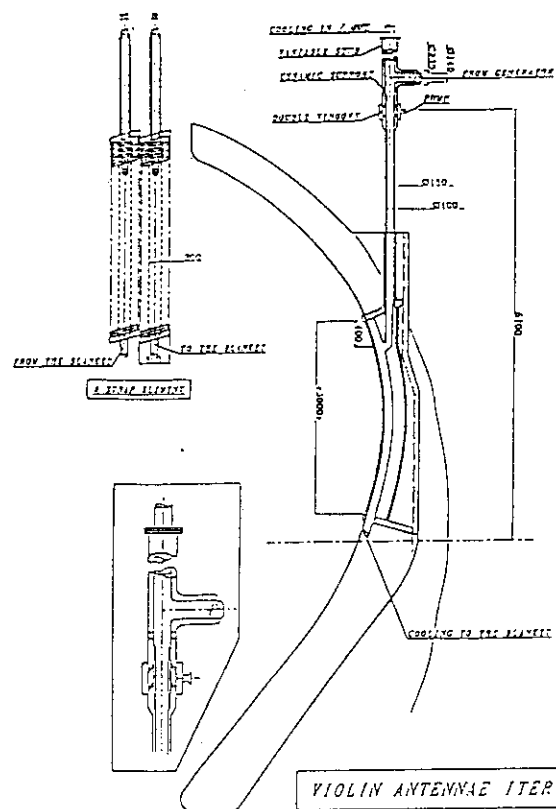
Fig 5: A poloidal section of the "violin antenna" integrated into the low field side ITER first wall/shield blanket. Inset shows a stub through which water cooling is introduced via the central conductor.

Short circuits

2.6m

Coax feed
$Z_O = 30\Omega$

JG93.578/4

0.4m

Nuts

Bridge
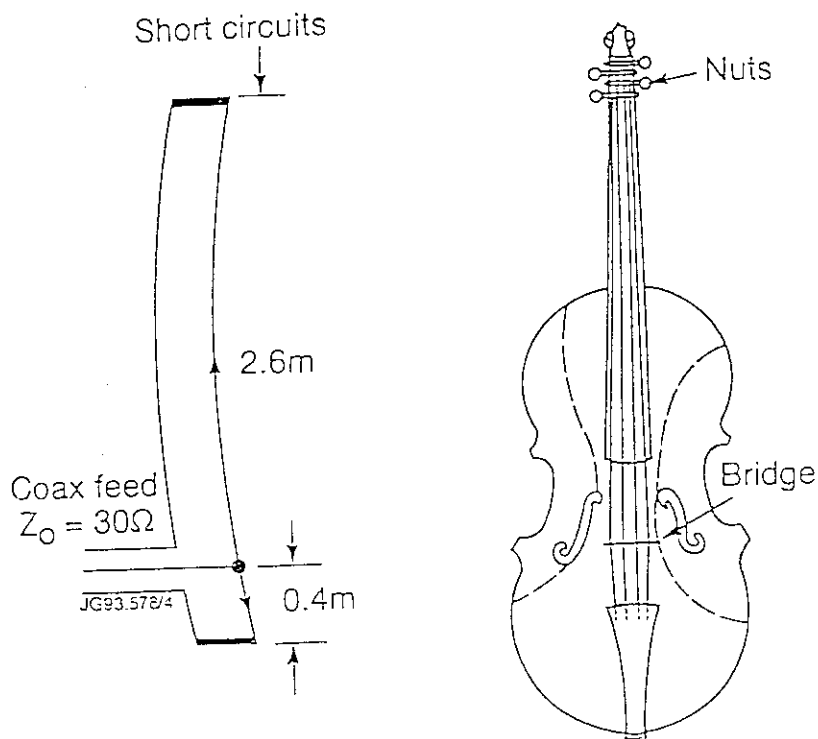
Fig 6: A schematic of the asymmetrically excited multiple resonance wide band antenna, the so-called "violin antenna".
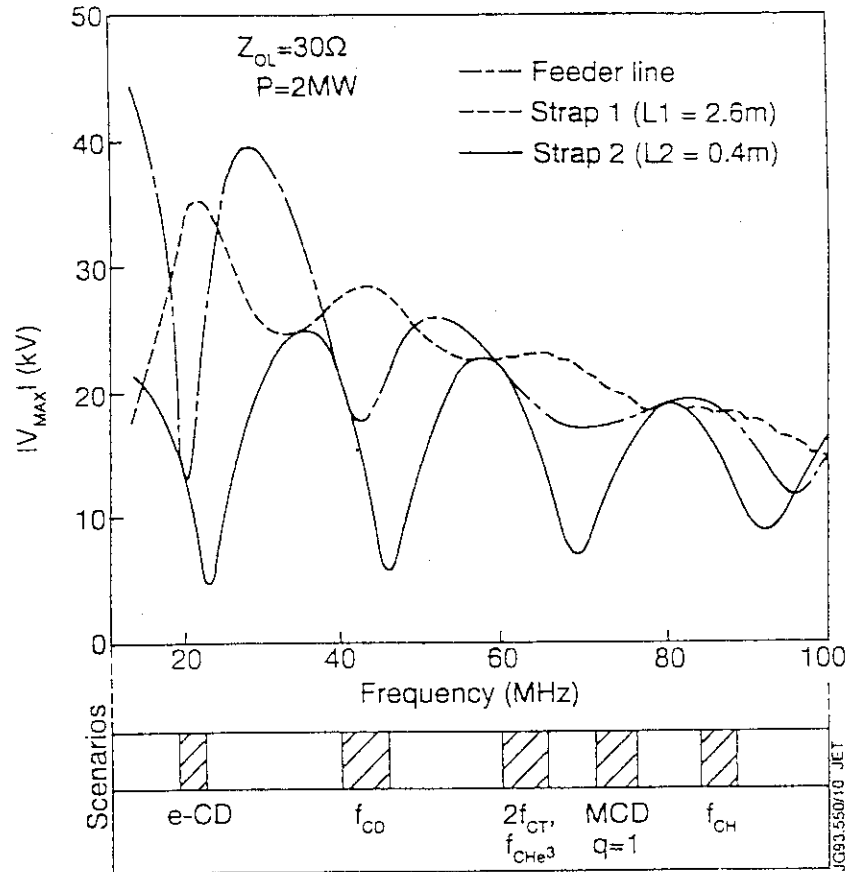
Fig.7: Magnitude of the maximum voltage in the feeder line and the two sections of the trip line "violin antenna" is plotted as a function of frequency. The shaded areas show the frequency bands of the fast wave scenarios of ITER-EDA.
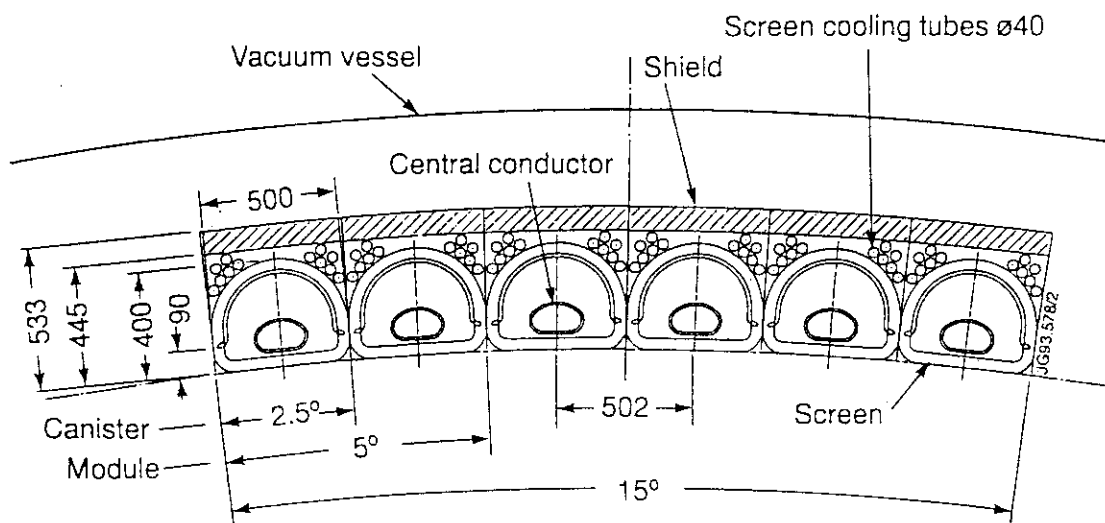
Fig.8 A plan view of a 6-strap version of the fast wave antenna for ITER-EDA

1.2 Technology Development for LHD ICRF Heating

T. Watari, R. Kumazawa, T. Mutoh, T. Seki, F. Shimpo, S. Masuda
National Institute for Fusion Science, Nagoya 464-01, Japan

Abstract

ICRF heating system for steady state operation of Large Helical Device (LHD) was developed and tested. The R&D test set which consists of a transmitter, transmission lines, a matching stub tuner, a vacuum feedthrough, a vacuum chamber, and a test antenna, have been constructed. To remove the resistive heat load generated RF current, all the components are cooled with water which circulates inside them. The structure of water inlet/outlet of the coaxial transmission lines were newly designed and tested. The coaxial line has a large diameter of 240mm in order to ensure high RF stand off voltage . The steady state operation test was carried out at 30kW (which is equivalent to 500kW in the heating experiment) for 30 minutes. Temperature increment of the test antenna and the outer conductors of the transmission line were measured and it was confirmed that they stay within the acceptable level. The 30 minutes test run shows that the newly designed integral components have high enough cooling capability and stand off voltage for the steady state heating experiment in the LHD

1. Introduction

 ICRF heating is considered as one of the high power heating scheme in the Large Helical Device Project and, simultaneously, it is expected as a heating power source for the steady state operation of LHD together with ECH.
 The design of the ICRF heating system for the LHD are reported in several papers [1-3]. On the antenna design, an analytical research have been done to minimize the energy loss by the direct particle loss [1]. And, experimental optimization have been done at CHS and Heliotron E by several authors[4,5].
 Recently, ICRF heating equipments are well developed and are being successfully operated in large tokamaks. However, in most of the experiments, the heating durations are less than several seconds and there is few experiences for the steady state high power ICRF heating. We need to acquire it for LHD project.
 In Ref.[3], we developed a feedback impedance matching system to follow the change of the plasma loading during the operation.
 In this paper, we report the first trial of the water cooled RF system. Water circulates inside the inner conductors of the transmission lines, the stubs, the vacuum feedthrough and the antenna current strap. Steady state operation test was carried out at power level of 30 kW without any additional load, which is equivalent to 500 kW in coming plasma heating experiment with 5 ohm of loading resistance.

2. ICRF Heating System in Large Helical Device

A high power RF source(3MW/ 30minutes) has been constructed for the ICRF heating of the Large Helical Device (LHD) prior to the 12 MW which will be prepared for the high power RF experiments. The RF frequency range is variable from 25 to 100 MHz in order to cover various heating regimes including minority heating regime with proton (and He3) minority ions, higher harmonic heating, and ion Bernstein wave heating. First priority of the heating mode is fast wave excitation by using the loop antennas which are installed inside the vacuum chamber. Besides the fast wave antenna, a folded wave guide[6] coupler is being designed. It is used to excite ion Bernstein wave and is also capable of producing plasma in wide range of magnetic field strength.

The schematic view of the fast wave antenna for LHD is shown in Fig.1. The antenna is located at the outward side of the torus. With this location of the antenna, a fast wave is incident from the high field side due to the characteristics of the heliotron/torsatron magnetic configuration. Ion cyclotron damping is the main heating mechanism. However, due to the torus effect, we can also choose low field side incidence of the wave with a specific choice of the RF frequency. Mode conversion of the wave takes place at the two ion hybrid resonance layer and electron landau damping dominates the heating mechanism.

The antenna loading resistance was calculated by using the wave analysis code for various position of the return conductor with fixed antenna loop position. The change of the return conductor position causes the change of the inductance of the antenna which also changes the voltage standing wave ratio (VSWR). Figure 2 shows the calculated maximum possible launched power from the antenna to the LHD plasma with an assumed standoff voltage limit on the transmission line. The calculation shows that relatively small distance between the antenna loop and the return current maximizes the injection power. The clearance between the plasma surface and the chamber wall is almost 30 cm, which may be large enough to facilitate a movable antenna.

3. Steady State ICRF Test Set

A steady state ICRF test set was constructed to develop the technology of the steady state and high power ICRF system. The schematic view of the ICRF test set is shown in Fig.3. RF transmitters are connected at the left end of the transmission line. The RF power of the transmitter is designed to be 3 MW with 30 minutes duration. The frequency can be tuned between 25 and 100 MHz continuously.

The coaxial transmission line has characteristic impedance of 50 ohm and large diameter of 240 mm. The outer conductor is made of aluminum and the inner conductor is made of copper. To improve stand off voltage, the coaxial line is filled with SF6 gas of 3 atoms. DC-cut section is necessary to disconnect the LHD device from the ground. RF leakage from it is anticipated to cause even more serious nuisance in a steady state operation than in pulse operations. We newly designed the low RF leak

DC-cut for this test set. The gap of the outer conductor is covered by multi layer low pass filters to suppress the leak of the RF voltage to outside. The leaked RF power is reduced to less than -80 dB of the main line.

The inner conductors of the test set are cooled by water which is supplied from the outside chiller unit. The inlet and the outlet of the water is at the T or L-junction of the coaxial line. The structure of the inlet/outlet of the cooling water is shown in Fig. 4. Through these ports, all inner conductors including the vacuum feed through and the antenna loop are cooled by water from the inside efficiently. O-ring seal is used to ensure the water seal at every junction and contact fingers are used to make sure the electrical contact. The water seal is tested up to 7 atom. and the working pressure is about 5 atoms.

A test ICRF antenna is designed and constructed to establish the technology of the reliable cooling and high stand off voltage equipment in the vacuum. The structure of the test ICRF antenna and the cooling water channels are shown in Fig. 5. The length of the loop antenna is 60 cm and the width of the antenna including the carbon plates is 38 cm. The cooling water circulates through the T-junction, the feedthrough, the coaxial line in the vacuum, the antenna current strap and the return conductor, and flows back through the piping structures shown in the Fig. 5. The shape of the test antenna is flat, though the real ICRF antenna in Fig. 1 has three dimensional helical structure in order to fit to the shape of the LHD plasma surface. The test antenna has single layer Faraday screen pipes and carbon plates. The heat deposition due to the induced RF current is estimated to be the largest on the latter.

4. Steady State Operation Test

Steady state operation test was carried out at the frequency of 50 MHz and the RF power of 30 kW. There was no additional antenna load in the circuit. The peak standing wave voltage on the transmission line was about 20kV (0-peak). This power level is equivalent to 500kW heating experiment with 5 ohm of expected plasma loading resistance. Cooling water is lead to all inner conductors and screen pipes to remove the loss RF power. The surface temperatures of the test antenna were measured with the IR camera through the BaF vacuum window. The time evolution of the temperatures are plotted in Fig. 6. Following the switching on of the RF power, the temperatures of the carbon side plates and the edge of the Faraday shields were increased rapidly. They saturated after 10 to 15 minutes exceeding 100 degree. The temperatures of the antenna current strap and central part of the Faraday screen pipes are saturated a little more earlier. During this long shot, the output RF power gradually drifted between 25 and 34 kW. The gas pressure of the vacuum chamber was increased as the temperature of the carbon plates increased. The increase of the gas pressure sometimes caused the RF breakdown inside the vacuum chamber. Therefore, the experimental run of Fig. 6 was obtained after the several conditioning runs.

The IR radiation signals from the edge of Faraday screen may be contaminated by the ray emitted from the carbon protector and reflected by the edge of the Faraday screen. This may be the reason of the difference of the time evolution of temperatures between center and edge of the Faraday screen. Except for the carbon plates and the edge of the screen pipes, temperatures saturated within 10 minutes and its increment was less than 50 degree.

On the transmission line, outer conductor is not cooled artificially. The temperatures of the upside of the coaxial line were measured by thermometers at several positions. The temperature increments after 30 minutes operation are shown in Fig. 7. The calculated standing wave voltage is also plotted in a same frame. The maximum temperature increment was observed at the minimum point of the standing wave voltage and it coincides with the current maximum point. There is a pre-matching stub close to the feed through section in the test set. In the experiment, the stub length was a quarter wave length. By using the pre-matching stub, the peak RF current on the transmission line between matching stubs and pre-matching stub can be suppressed to about 1/3 from the original value. So, the temperature increase on the transmission line will not be a serious problem for higher power experiment.

5. Summary

The steady state ICRF heating system for the Large Helical Device has been developed. The ICRF test set was constructed and a developmental research has been started. All the components including the antenna current strap, impedance matching tuners, and transmission lines was cooled by circulating water. The operation run of 30 minutes at 30 kW was carried out without any additional load. The peak standing wave voltage was 20 kV and it was equivalent to the 500 kW plasma heating experiment. The temperatures of the antenna structure stayed below 50 degree and saturated within 10 minutes. The temperature increase of the transmission line was less than 20 degree. The goal of this developmental experiment is to successfully demonstrate 180kW run for 30 minutes. This corresponds to 3MW injection in the coming LHD experiments. The present result indicates that this target is within the operational range of this system and will be reached in the near future. An improvement of heat removal from the carbon plates by use of back copper plates may be required in the further experiment.

References

[1] T. Mutoh, A. Fukuyama, T. Watari, et.al, ICRF Heating Program of the Large Helical Device, First International Toki Conference on Plasma Physics and Controlled Nuclear Fusion, Toki,1989NIFS-Proc report ISSN 0915-6348 (1990) 175

[2]   T. Mutoh, R. Kumazawa, T. Watari,et.al, ICRF Antenna Design in Large Helical Device (in Proceedings of 14th IEEE Symposium on Fusion Engineering, San Diego,USA 1991) Vol.1 1991 ,pp103

[3]   R.Kumazawa, T.Watari, T.Mutoh, et.al, Feedback Control Matching System for Temporal Change of Plasma Loading Resistance in High Power/Steady State ICRF Heating on the Large Helical Device, (in Proceedings of the 17th Symposium on Fusion Technology, Rome, 1992), Vol.1 p554

[4]   K.Nishimura, R.Kumazawa, T.Mutoh,et.al,   High Power ICRF Heating in CHS, (in proc. of 5-th Toki Conference, Toki, 1993),16p16

[5]   H. Okada, H.Zushi, K.Kondo, et.al, ICRF Heating with Hydrogen and Helium Minority in Heliotron-E, (proc. of 5-th Toki Conference, Toki, 1993),16p15

[6]   R. Kumazawa, T.Mutoh, T. Seki,et.al,Development of Folded Wave guide Antenna for LHD ICRF Heating in Large Helical Device,(in proc. of 5-th Toki Conference, Toki, 1993), 16p21

To Cooling System

To Oscillator

Feedthrough

Cryostat chamber

Vacuum chamber

Helical coil

Plasma

Poloidal coil

1m
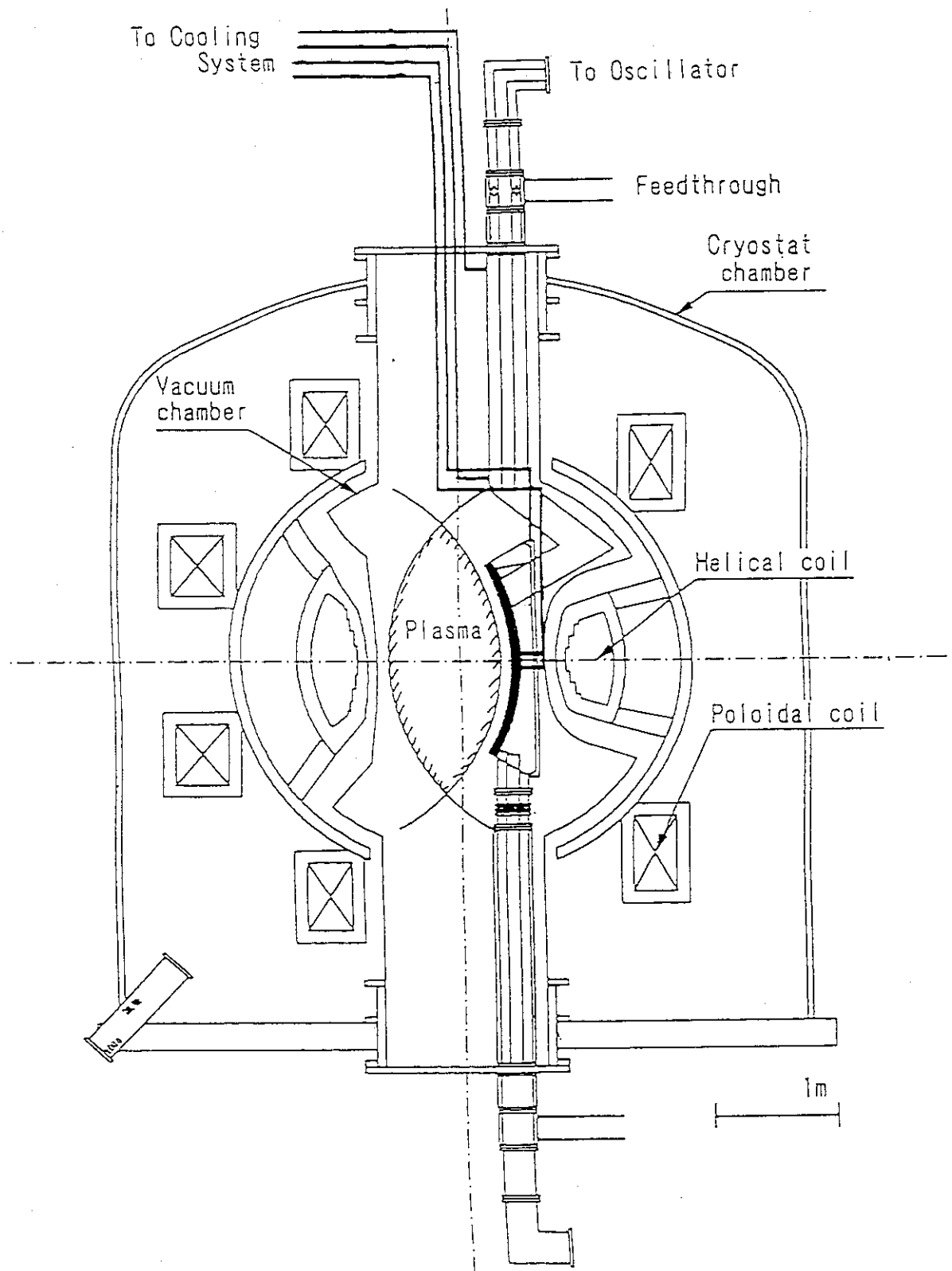
Fig.1 Schematic view of the Large Helical Device and ICRF antenna on the cross section of the toroid. Left hand side is the center of the major radius. Length from the top to the feedthrough section is 3.8m.
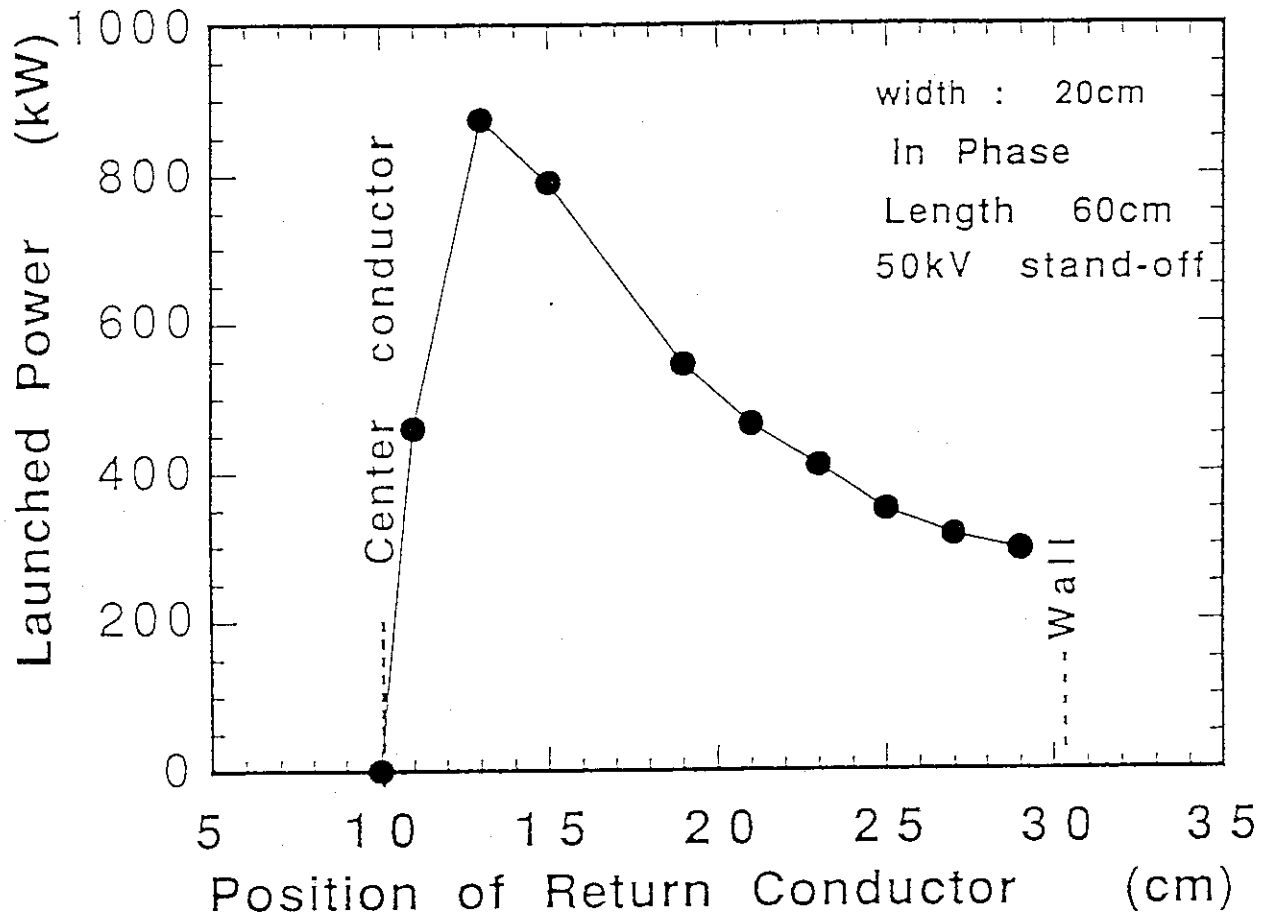
Fig.2 Calculation of the launched power from the one loop
antenna with given RF standoff voltage on the transmission
line. Positions of the center conductor and the plasma
surface are fixed and the position of the return conductor
is changed.
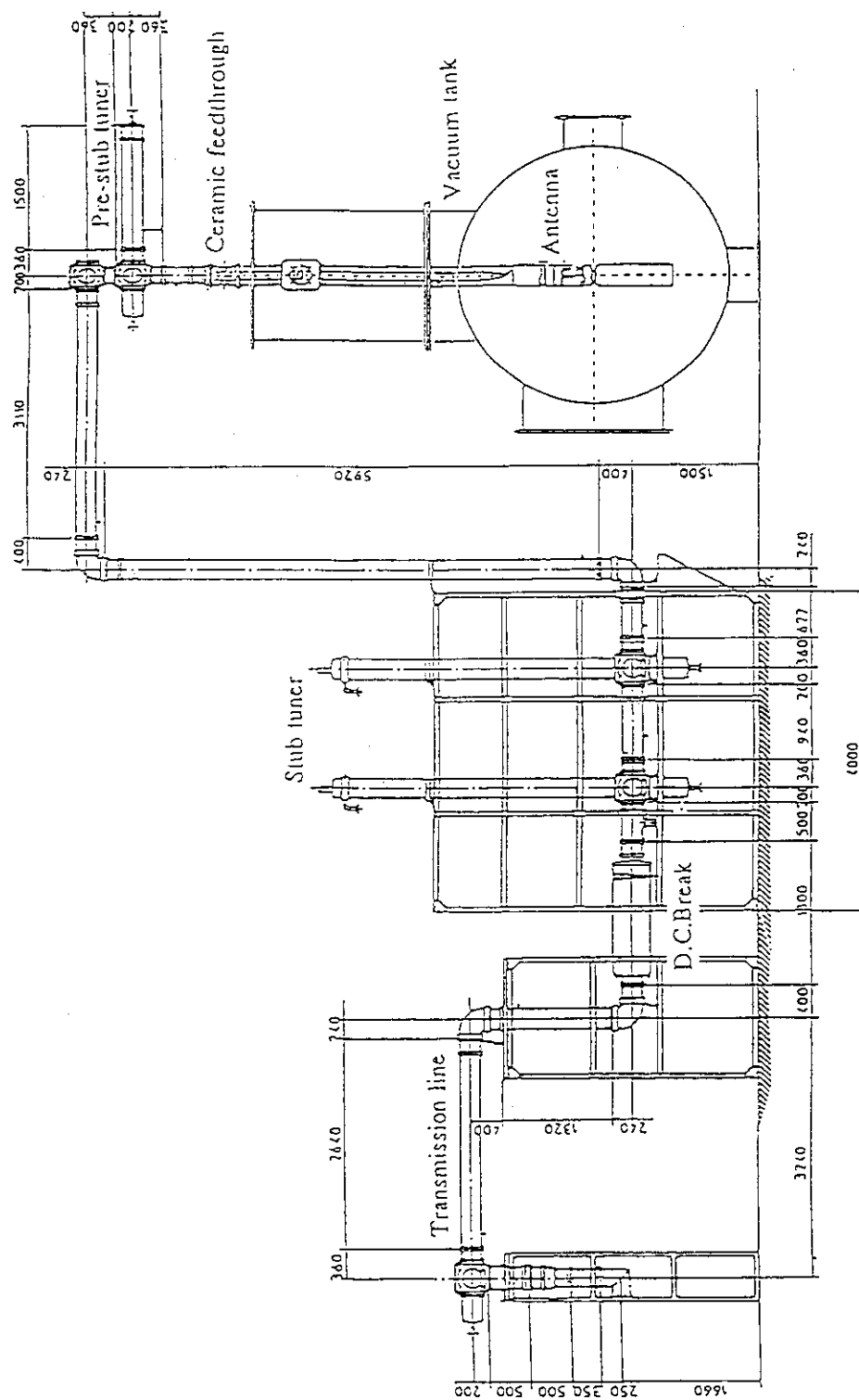
Fig.3 View of the transmission line and the test vacuum chamber of the steady state ICRF test set. Transmitter is connected at the left end of the coaxial line.
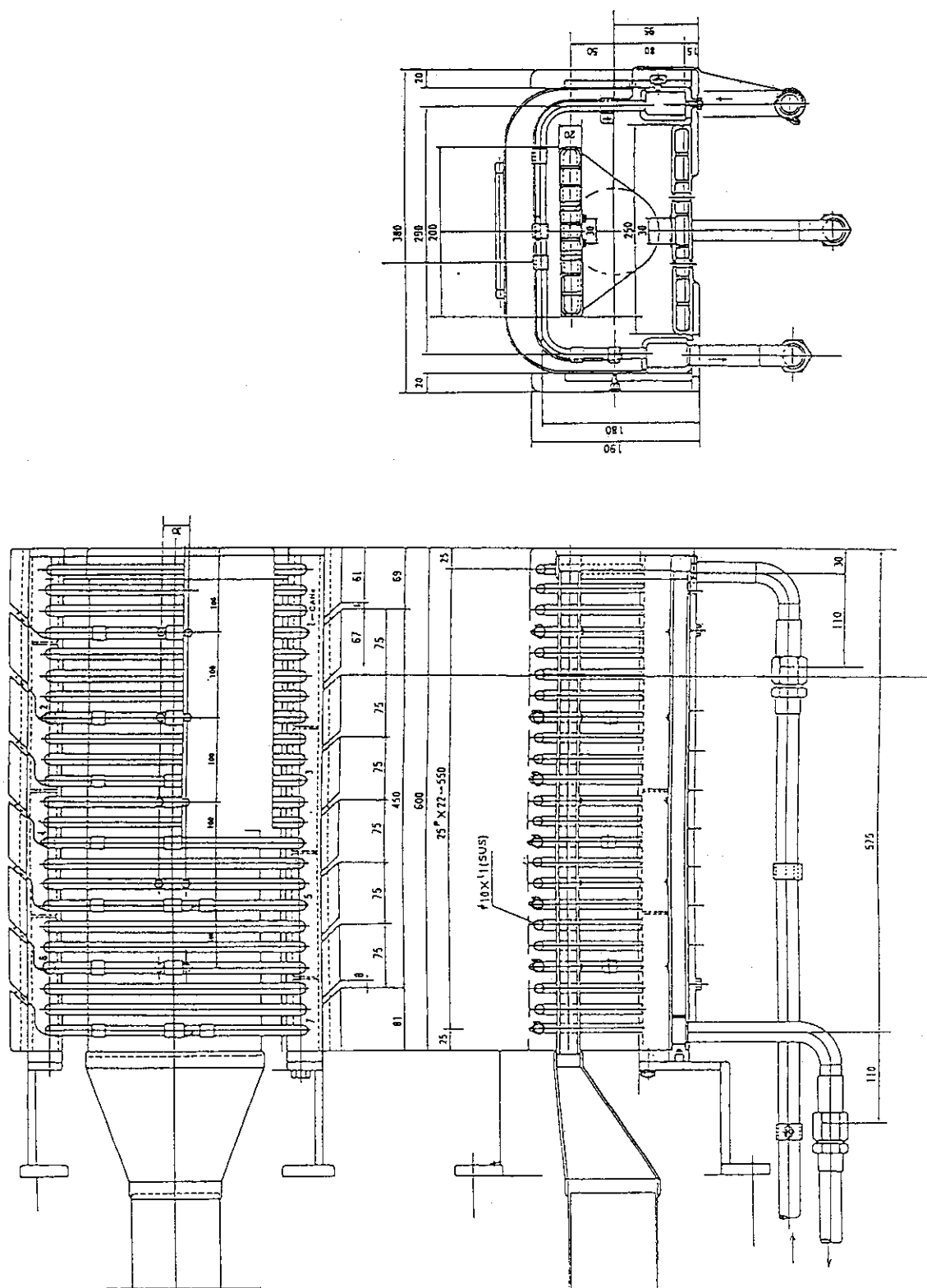
Fig. 4 Cross section of the T-junction of coaxial line. There are two water flow paths inside of the inner conductor. Up side is connected to stub and bottom side connected to the water pipe of outside.
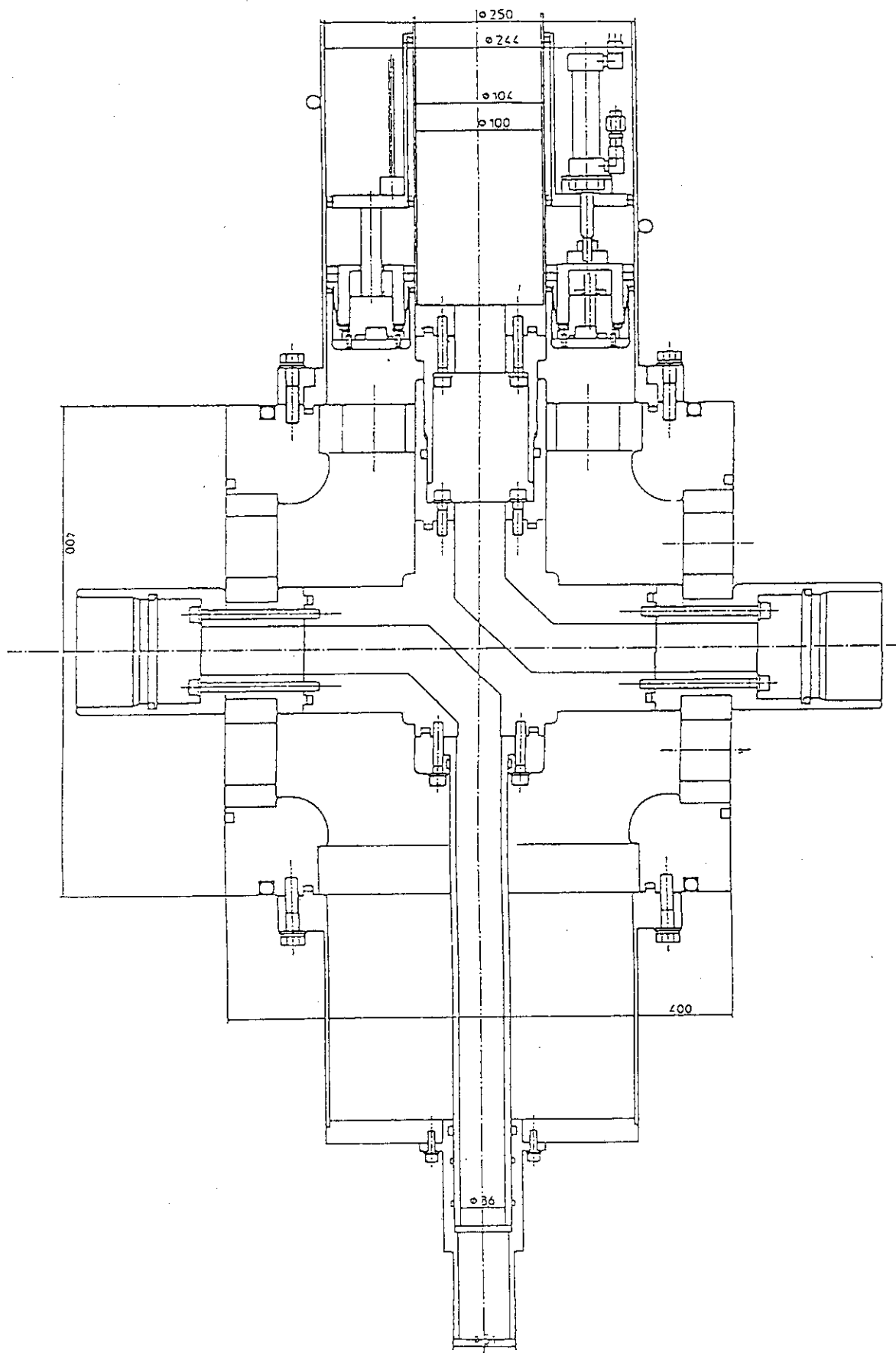
Fig.5 Drawings of the test ICRF antenna for the steady state
operation test.
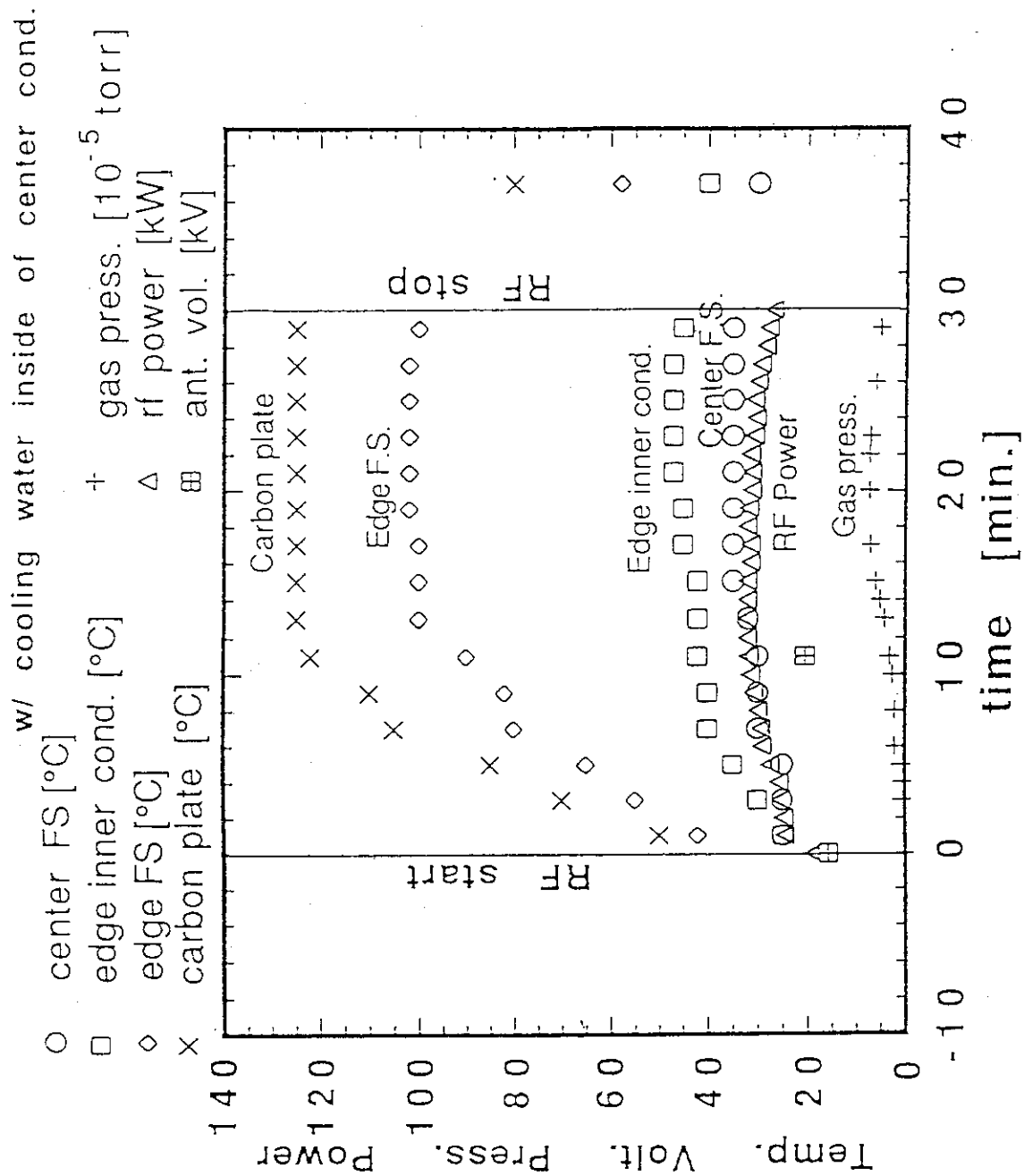
Fig.6 Time evolution of temperatures of the test ICRF antenna in a 30 minutes operation. RF power and gas pressure are also shown. RF power is about 30 kW during the test run.
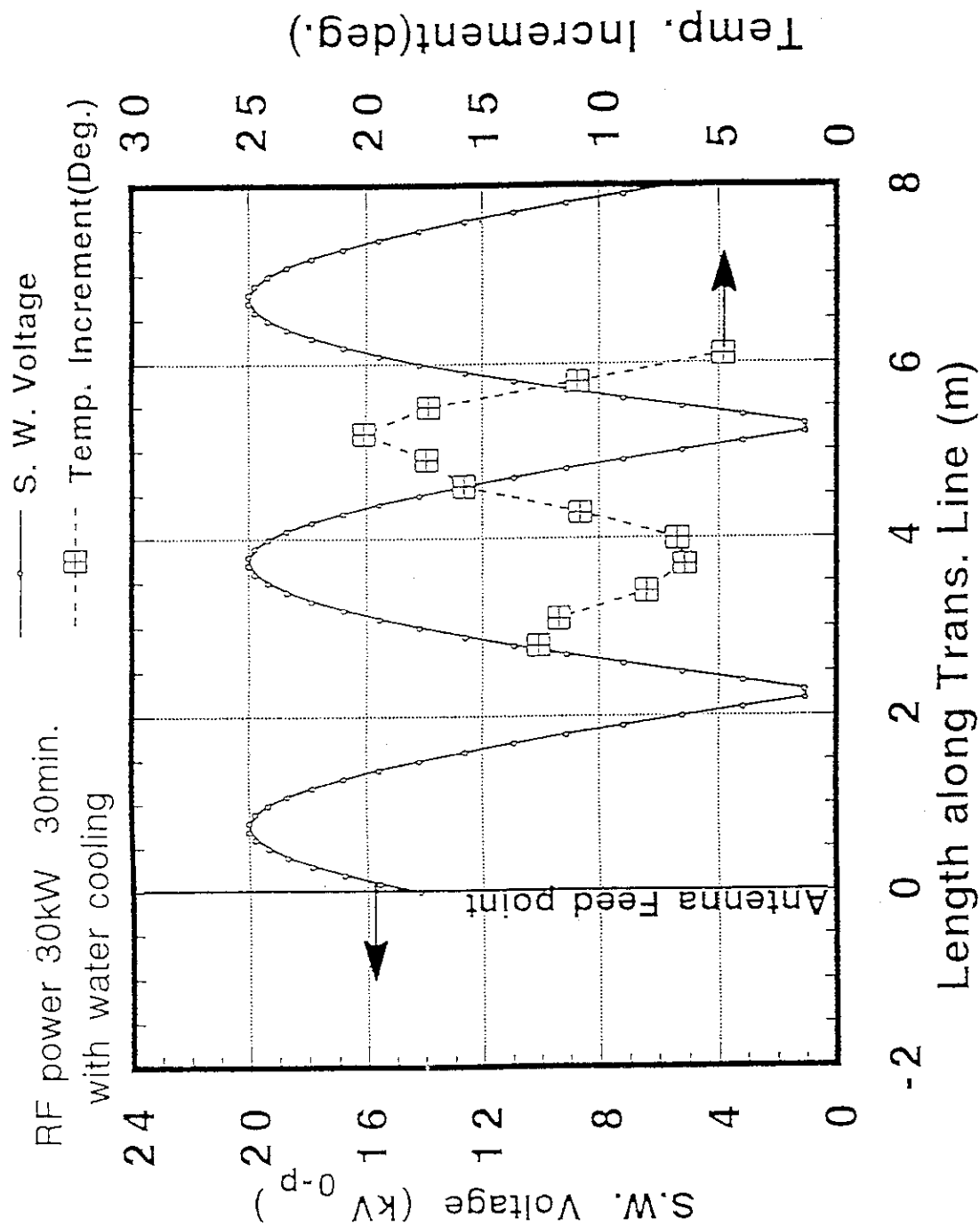
Fig.7 The time evolutions of temperatures at various outer conductor positions on the transmission line during the 30 minutes test run. Calculated standing wave voltage is also plotted. The temperature increment is maximum at the RF current peak point.

1.3 Fast Wave Current Drive Technology Development at ORNL

F. W. BAITY, D. B. BATCHELOR, R. H. GOULDING, D. J. HOFFMAN,
E. F. JAEGER, P. M. RYAN

Oak Ridge National Laboratory, Oak Ridge, Tennessee, USA

J. S. DEGRASSIE, C. C. PETTY, R. I. PINSKER, R. PRATER

General Atomics, San Diego, California, USA

ABSTRACT

The technology required for fast wave current drive (FWCD) systems is discussed. Experiments are underway on DIII-D, JET, and elsewhere. Antennas for FWCD draw heavily upon the experience gained in the design of ICRF heating systems with the additional requirement of launching a directional wave spectrum. Through collaborations with DIII-D, JET, and Tore Supra rapid progress is being made in the demonstration of the physics and technology of FWCD needed for TPX and ITER.

INTRODUCTION

Steady-state current driven by fast waves in the ion cyclotron range of frequencies (ICRF) is predicted to have comparable efficiency to other possible current drive methods for break-even plasmas. The requirement of driving current places the additional demand of asymmetric phasing on ICRF systems. Maximizing the current drive involves a tradeoff between maximizing the current drive efficiency of the antenna and maximizing the power handling. Reduction of impurities with asymmetric phasing is also a concern.

Given the interaction between the antenna and the plasma edge, it is important to have realistic models of the fields produced by the antenna, including 3-D effects, and of the wave behavior in the plasma including details of the edge region. A number of tools have been developed to optimize the design and performance of FWCD antennas. These include modeling the effects of slots in the antenna sidewalls, modeling the current drive efficiency in plasma with realistic antenna geometry, and modeling the coupled transmission line systems with decouplers. In addition, bench testing of FWCD antennas has been conducted to verify the models and to develop practical tuning and matching algorithms.

Experiments have been underway since 1990 with a single four-element FWCD array on DIII-D operating at 60 MHz. During this time a number of modifications have been made both to the antenna and to the external matching circuit in order to optimize performance. In collaboration with JET, modeling and design of power compensators for the JET A_2 antennas has been undertaken. Some form of power compensation is required in order to operate at full source power whenever the phasing between elements is other than 0° or 180°. A prototype system has been tested on DIII-D. Two new 4-element FWCD antennas under construction for DIII-D are designed to have pulse lengths of 10 s

and to operate at up twice the power of the existing FWCD antenna in the frequency range of 30 to 120 MHz.

PROOF-OF-PRINCIPLE ANTENNA FOR DIII-D

The first embodiment [1,2] of the present four-strap antenna array on DIII-D, shown in fig. 1, was designed in 1989. The array occupies a 1.0-m × 0.5-m recess in the vacuum vessel wall with coaxial feeders extending out through two separate ports. The array consists of two enclosures, each housing two straps, mounted side by side. Each enclosure was covered by a two-tier Faraday shield of copper-plated Inconel 625 rods coated with 10 μm of Ti(C,N). Between each pair of straps was a slotted septum giving coupling coefficients of 4% (between straps 2 and 3) and 7% (between straps 1 and 2 and between straps 3 and 4). These values of mutual coupling were chosen based on the anticipated plasma loading and to be able to maintain arbitrary phasing between adjacent straps.
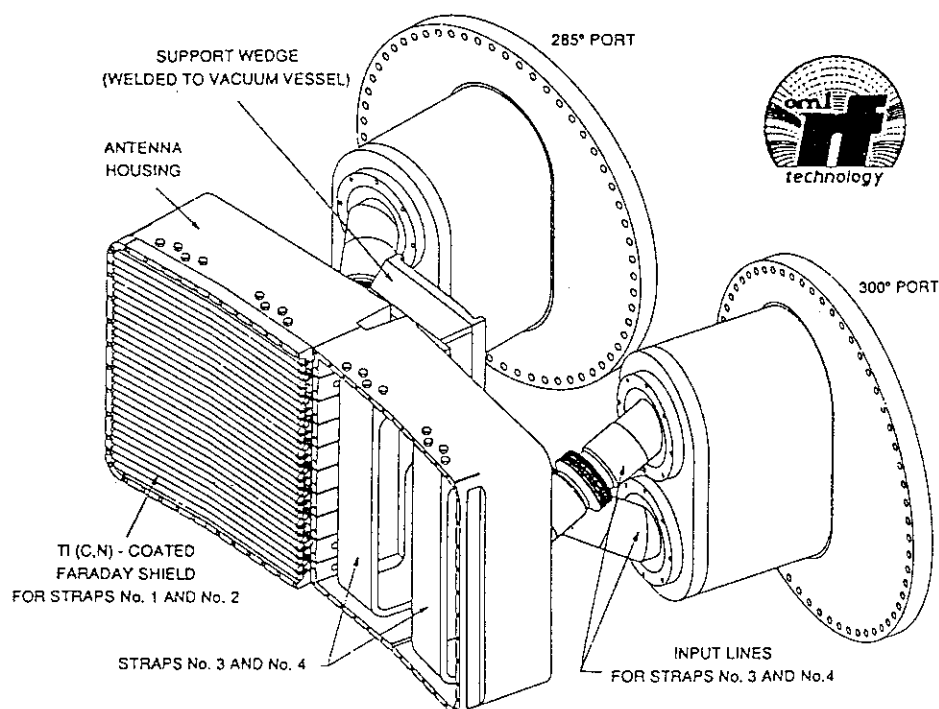
Fig. 1. Fast wave current drive antenna for DIII-D (30-60 MHz, 2 MW, 2 s, four strap)

The antenna is powered from a single RF transmitter having a nominal output of 2 MW from 30 to 60 MHz. A full-scale mockup of the array was used for measurements of antenna parameters and for developing phasing and impedance matching algorithms. Two phasing circuits were proposed: one, employing eleven tuning elements, provided the capability of arbitrary phasing between adjacent straps, and the other, employing five tuning elements, provided the capability of phasing at only 0°, ±90° or 180° between straps [3,4]. The latter circuit was implemented on DIII-D, both to save cost and to reduce the complexity of phasing and matching as much as possible for initial experiments. Figure 2 is a schematic drawing of the circuit used on DIII-D.

Experiments from plasma operation on DIII-D [5-7] led to the conclusion that antenna performance could be improved by increasing the mutual coupling between adjacent straps. Accordingly, the antenna was modified by removing the slotted septum separating the two straps in each enclosure and by deepening the slots between the two enclosures. This increased the coupling coefficients to 7% and 9%.
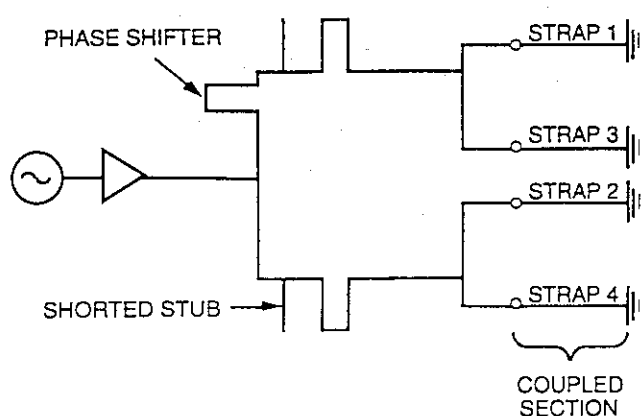
Fig. 2. The phasing and impedance matching circuit used in the initial FWCD experiments on DIII-D.

In addition it was found that the impurity generation from the Faraday shield at 90° phasing, as evidenced by Ti radiation, was almost the same as 0°, whereas impurity generation is minimized at 180° phasing. In order to reduce impurity production as much as possible, it was decided to take advantage of two new developments: boronization of the vacuum vessel and coating the Faraday shield with B_4C. The early boronization system on DIII-D consisted of two diborane feeds, one through the antenna port and the other on the opposite side of the tokamak. Meanwhile, plasma spraying of B_4C had been under development at Cadarache, France and was used on new Faraday shields installed on Tore Supra. High heat flux testing of this B_4C coating was conducted at ORNL with excellent results, exceeding the capabilities of Ti(C,N).

Therefore, a new Faraday shield was installed, having a single-tier of copper-plated Inconel rods angled at 12° to the horizontal in order to align the elements with the static magnetic field at the antenna location under normal plasma operating conditions. The new shield, following recent ICRF practice, has an optical transparency of 45%, and was coated with 100 μm of B_4C at SNMI (Avignon, France). Figure 3 is a photograph of the new Faraday shield. The combination of the new Faraday shield coating and boronization of the entire vacuum vessel has reduced impurities to negligible levels.

With the new configuration the antenna has been operated at 1.6 MW and up to 90% of the design joule limit. The power limit appears related to interactions between the edge plasma and the B_4C coating, often with the release of macroscopic flakes into the plasma. The flaking is primarily restricted to one of the two Faraday shields. This shield has a B_4C coating which is thicker than the specified 100 μm, and the additional thickness may be responsible for the poorer bonding.

Between the time of the removal of the original Faraday shield and the installation of the single-tier shield, the antenna was operated in plasma without a Faraday shield for a brief period. Experimental time during the shieldless operation was insufficient to draw firm conclusions, but two observations of note were that: (1) the power limit of the antenna was lower than it was with a Faraday shield, although the limiting mechanism was not identified, and (2) impurities (primarily copper) did not increase.

ANTENNA ANALYSIS

A number of codes have been written or adapted to aid in the design of FWCD antennas [8]. The goal is to determine the basic parameters of the antenna in the presence of plasma, such as the self and mutual inductance, capacitance, and loading per unit length of the current strap. These parameters are used as inputs for transmission line analysis of the remainder of the system. This provides the ability to determine the net power delivered to the plasma and the electrical load that the antenna will present to the power distribution system, in order to predict currents, voltages, and heat loads throughout the system.
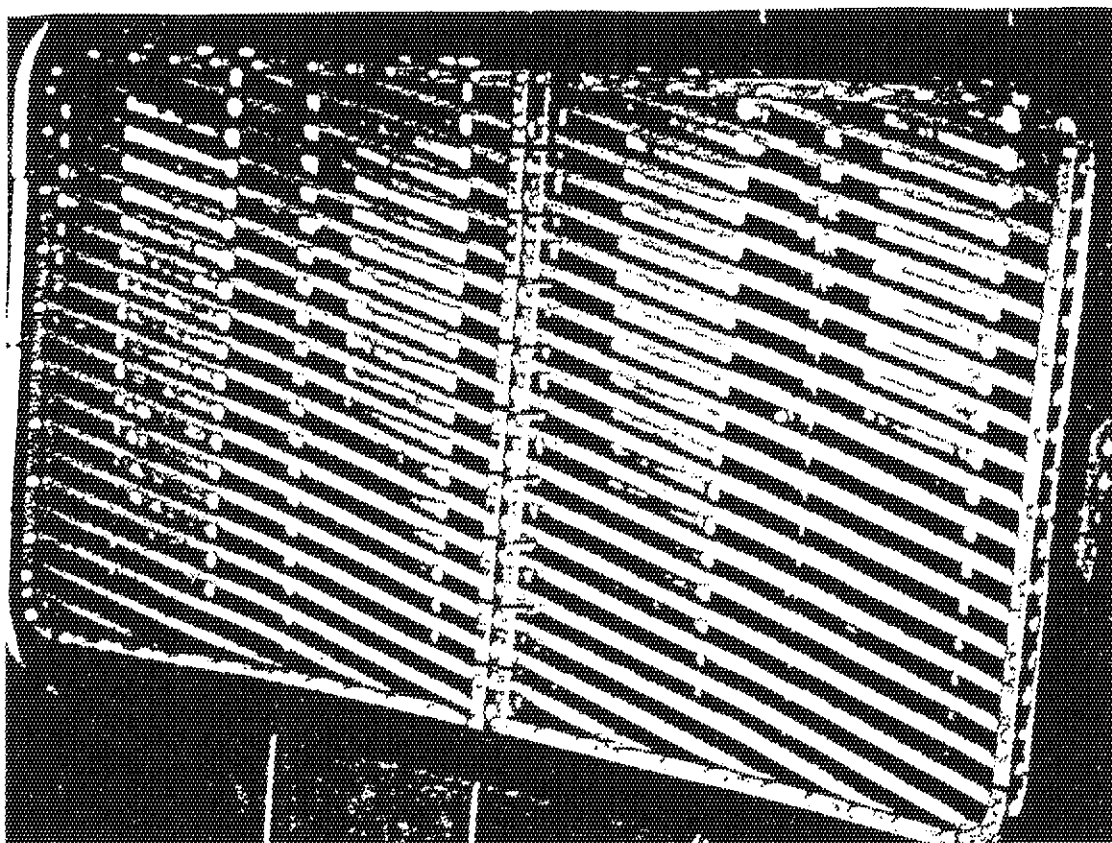
Fig. 3. New B$_4$C-coated Faraday shield for DIII-D. The shield is tilted at 12° to align with the magnetic field lines at the antenna location. Visible at the right side are the horns of a microwave reflectometer for measurements of the edge density.

The effects of the enclosure surrounding the current strap, the finite poloidal extent of the strap, and the influence of the Faraday shield have been modeled with two-dimensional and three-dimensional magnetostatic codes. The influence of the ends of the antenna enclosure and the current strap configuration are shown in fig. 4 for the case of the long-pulse FWCD antennas for DIII-D. This calculation assumes constant current in the poloidal direction (low-frequency limit) so that the shape of the curves is due solely to geometric effects. The factor α is the length attenuation due to a given geometry. Finite wavelength effects cause additional reduction in the effective length of the current strap. The Faraday shield effect on phase velocity must be known in order to calculate this factor. Figure 5 shows the effects of finite wavelength at 120 MHz for the same geometry as in fig. 4.

Heating of the Faraday shield from a combination of plasma bombardment and RF dissipation is often the limiting factor in antenna operation. The heating from RF-induced currents can be of concern for FWCD antennas due to the advantages for directionality of operating with larger antenna-to-plasma gaps.

Modeling the influence of sidewall currents is crucial in determining the directionality of the wave spectrum generated by a FWCD array. Return currents in the antenna sidewalls generate waves with high $k_\parallel$ traveling in the opposite direction to the main peak launched by the antenna, as shown in fig. 6. While the undesired peak at high reverse $k_\parallel$ evanesces more rapidly than the low $k_\parallel$ peak, these currents lead to higher voltages in the antenna structure and therefore to lower power limits.

Finally, the wave spectrum determined by the three-dimensional antenna modeling becomes the source term for PICES [9], a three-dimensional full-wave plasma code, to calculate power deposition profiles and current drive efficiency.
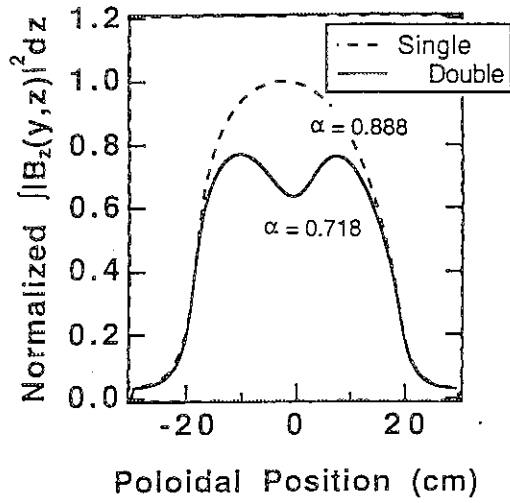
Fig. 4. The effect on the toroidal magnetic flux 2.5 cm in front of the current strap of finite poloidal extent of the strap for single and double strap configurations with the dimensions of the long-pulse FWCD for DIII-D. This calculation was made in the low frequency limit (uniform current in the strap). α is the attenuation factor resulting from purely geometrical effects.
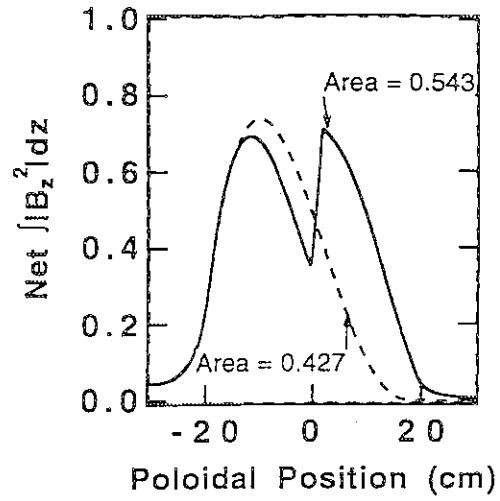
Fig. 5. The combined effects of finite wavelength at 120 MHz and finite poloidal extent on the toroidal magnetic flux 2.5 cm in front of the current strap for the same geometry as in fig. 4. The double strap configuration produces 25% more loading than the single strap configuration at this frequency.
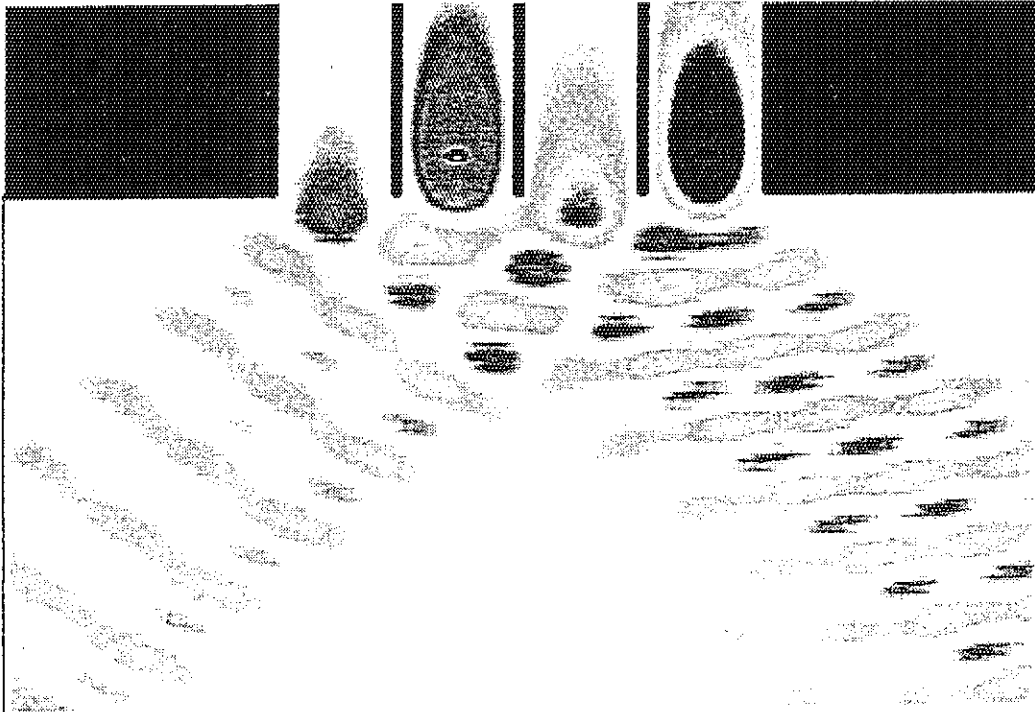
Fig. 6. Electric fields in the plasma generated by a four-strap array phased at 90° for DIII-D conditions as calculated by the two-dimensional cold plasma recessed antenna code, RANT. Low-$k_\parallel$ waves in the forward direction result from the currents on the straps. The smaller-amplitude, high-$k_\parallel$ waves in the reverse direction result from the return currents in the sidewalls.

DECOUPLER DESIGN

The phasing and matching circuit used for the first experiments on DIII-D is shown in Fig. 2. The resonant loops combining straps 1 and 3 and straps 2 and 4 reduce the system to a two-port network. The power in the two feed lines is unbalanced when operated with equal strap currents at a phase other than 0° or 180° due to the mutual coupling between straps. This uneven power split necessitates the use of an unmatched tee at the transmitter end. The ratio of the powers in the two lines for equal antenna currents at 90° is given by

$$\frac{P_A}{P_B} = \frac{1 - kQ}{1 + kQ},$$

where k ($\equiv$M/L) is the effective coupling coefficient between the two lines and Q is the quality factor. The condition kQ = 1, where all the power appears in line B, corresponds to a series resonant load resistance of approximately 1.5 Ω for the present DIII-D configuration. The term series resonant load resistance refers to the value of the impedance measured one-quarter wavelength ahead of the resonant loop tees. For kQ > 1 the circuit is unstable and difficult to control. The loading resistance under typical FWCD operating conditions on DIII-D is of this order, so the powers are typically substantially unbalanced.

A decoupler which effectively cancels the effects of the mutual coupling between straps can be added to provide an equal power split between the two feed lines. A decoupler is advantageous whether in a system like DIII-D, where an antenna array is fed from a single RF source or like JET, where separate sources are used for each array element. In the case of separate power sources per element a decoupler is required in order to operate at full power. ORNL and JET are collaborating on modeling and design of a decoupler arrangement for use with the JET A$_2$ antenna arrays [10-13].

A prototype decoupler has been tested on the DIII-D system [11,14]. The decoupler, consisting of an 80-mm-diameter, 50-Ω, 3-dB hybrid junction with two ports terminated with tunable stubs, was connected at the resonant loop tees, which are at a voltage maximum, as shown in fig. 7. When the decoupler is exactly tuned, the power transferred from one resonant loop to the other circulates through the decoupler, resulting in an equal powers in the two feed lines for all phase angles. This was demonstrated during plasma operation, as shown in fig. 8, when the phase between the resonant loop tees was varied through 360° without readjustment of any tuning elements on a sequence of fourteen plasma shots where the antenna loading resistance was maintained at 1.5 Ω. The RF power was 0.1 MW on all shots.
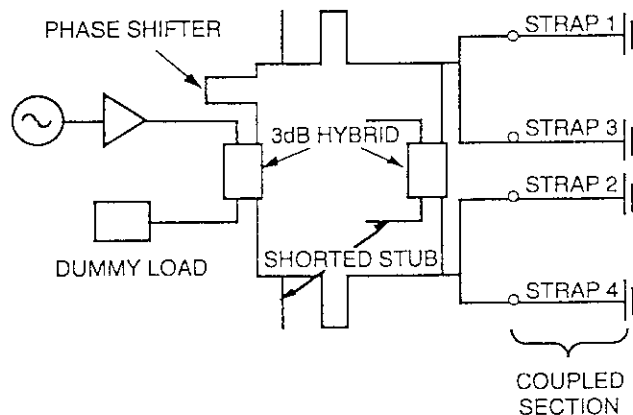
Fig. 7. The phasing and impedance matching circuit used for the prototype decoupler tests on DIII-D.
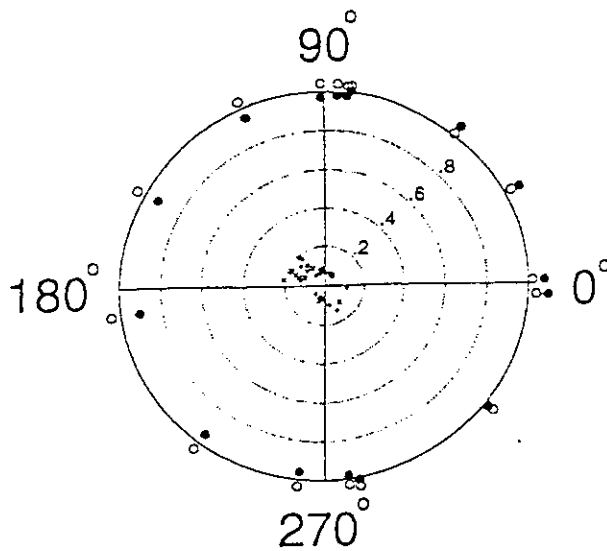
Fig. 8. 14-shot phase scan with the decoupler tuned. The solid circles are the ratio of the voltages at the two resonant loop tees, the open circles are measured on the generator side of the matching network. The ×'s and ◊'s are the reflection coefficients on the generator side of the two feed lines. No adjustments of the matching network were made during the scan.

LONG-PULSE FWCD ANTENNAS FOR DIII-D

Two long-pulse FWCD antennas for DIII-D have been designed [15] and will be installed in early 1994. These antennas will increase the available FWCD power from 2 MW to 6 MW for pulse lengths of up to 2 s, and to 4 MW for up to 10 s. When operated at 90° phasing into a low-density plasma ($\sim 4 \times 10^{19}$ m^{-3}) with hot electrons (~ 10 keV), the two new antennas are predicted to drive approximately 1 MA of plasma current. Specifications for these antennas are given in Table 1.

The antennas incorporate extensive water cooling. The Faraday shield, however, is uncooled, and is the primary factor limiting the pulse length. The new antennas are designed to mount at the 0° and 180° toroidal locations in ports originally housing movable limiters. These ports restrict the width of the arrays to 75 cm. All four coax feeds pass through a single port. The antennas are modular, with separate water feeds for each array element, simplifying installation and maintenance. All internal surfaces are nickel plated.

Table 1. DIII-D Long-Pulse FWCD Antenna Specifications

Maximum power	2 MW (4 MW with second RF source)
Maximum pulse length	10 s
Number of array elements	4
Frequency range	30-120 MHz
Phasing (between adjacent elements)	0°, ±90°, 180°
Dimensions	75 cm × 46 cm

The Faraday shield consists of a single layer of 13-mm-diameter nickel-plated molybdenum rods with a 100-μm-thick plasma sprayed coating of boron carbide on the plasma-facing side. The rods are inclined at a 12° angle to match the pitch of the local magnetic field at the shield location. The rods are mounted to the antenna housing individually by thin Inconel strips to allow for differential thermal expansion of the Faraday shield relative to the antenna housing. The length of the Inconel strips was chosen to provide the desired magnetic coupling between adjacent antenna elements.

Figure 9 is a front view of the antenna array, showing the four elements with the feed lines extending to the vacuum feedthroughs at the port cover flange.

At the upper frequency of operation of 120 MHz, the electrical length of a single current strap with a phase velocity of 0.6c (due to the Faraday shield) is longer than a

quarter wavelength. Since there is not room for two coaxial feeds per element, the current strap is divided into two poloidal segments. Three-dimensional modeling of the RF magnetic field amplitudes was used to compare the double strap configuration to a single strap at 60 and 120 MHz. The poloidal distributions of the integrated toroidal magnetic flux are shown in Fig. 10. The double strap produces more total flux at the plasma boundary at 120 MHz, whereas the single strap is superior at 60 MHz. However, the double strap configuration results in a lower voltage between the antenna and Faraday shield than a single strap, so the double strap is practically equivalent to the single strap even at 60 MHz. Below 60 MHz the double strap exacts a penalty, but the antenna design was optimized for higher frequency operation.
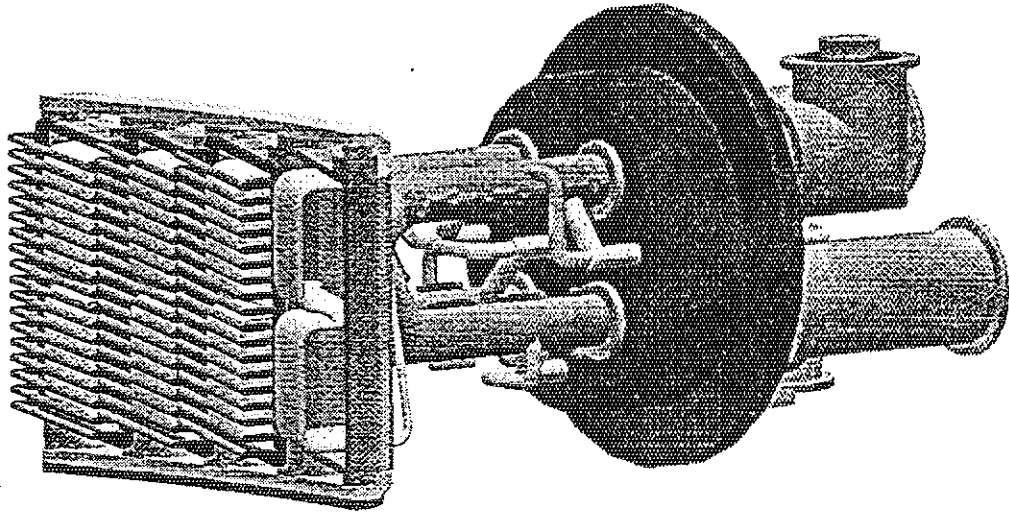
Fig. 9. Long-pulse FWCD antenna for DIII-D.

The maximum power capability of the antenna with a peak voltage of 30 kV appearing anywhere in the antenna structure is shown in Fig. 11 as a function of antenna loading resistance for 60, 90, and 120 MHz. The value plotted is the total power for the array with the 30–kV peak voltage occurring on any element of the array at 90° phasing.
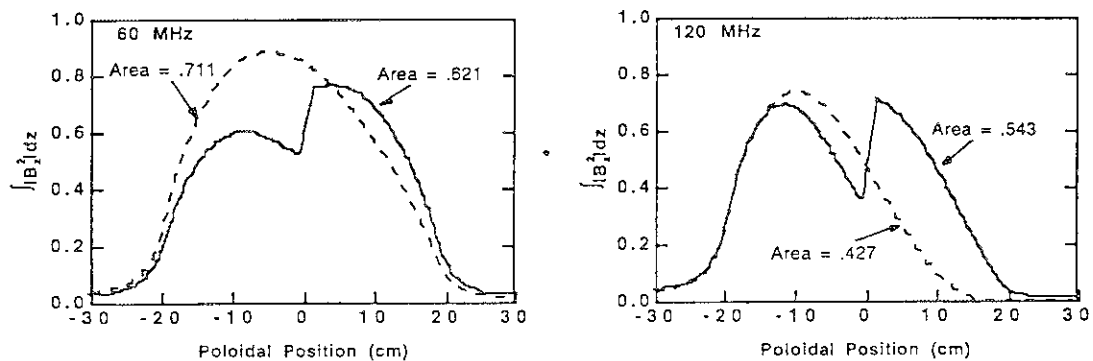
Fig. 10. Net $\int |B_z|^2 |dz$ distribution 2.5 cm in front of the current strap for single and double strap configurations at 60 and 120 MHz.

The wide frequency range of operation causes voltage and current maxima to occur throughout the transmission line. In particular, the vacuum feedthrough is near a voltage minimum at 120 MHz, but near a voltage maximum at 60 MHz. Thus, all components must be designed to handle high voltages. Based on superior voltage standoff in feedthrough tests conducted at ORNL [16] comparing copper, nickel, silver, and gold electrodes, nickel plating was selected for all components in vacuum.
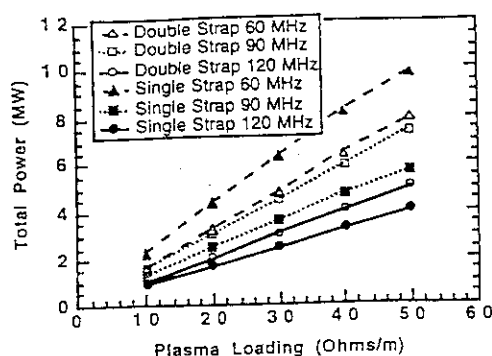
Fig. 11. Maximum power per array as a function of plasma loading with a 30 kV peak voltage limit for 60, 90, and 120 MHz.

The external transmission line system will be of the same basic design as that used successfully on the existing FWCD antenna on DIII-D with some refinements [17]. The circuit is shown schematically in Fig. 12. The loops connecting modules 1 and 3 and modules 2 and 4 are adjusted to produce phasing of either 0° or 180° between alternate modules. The decoupler stub balances the power on the two feed lines and the susceptance null stubs result in a purely real impedance at the output of the quarter-wave transformers.
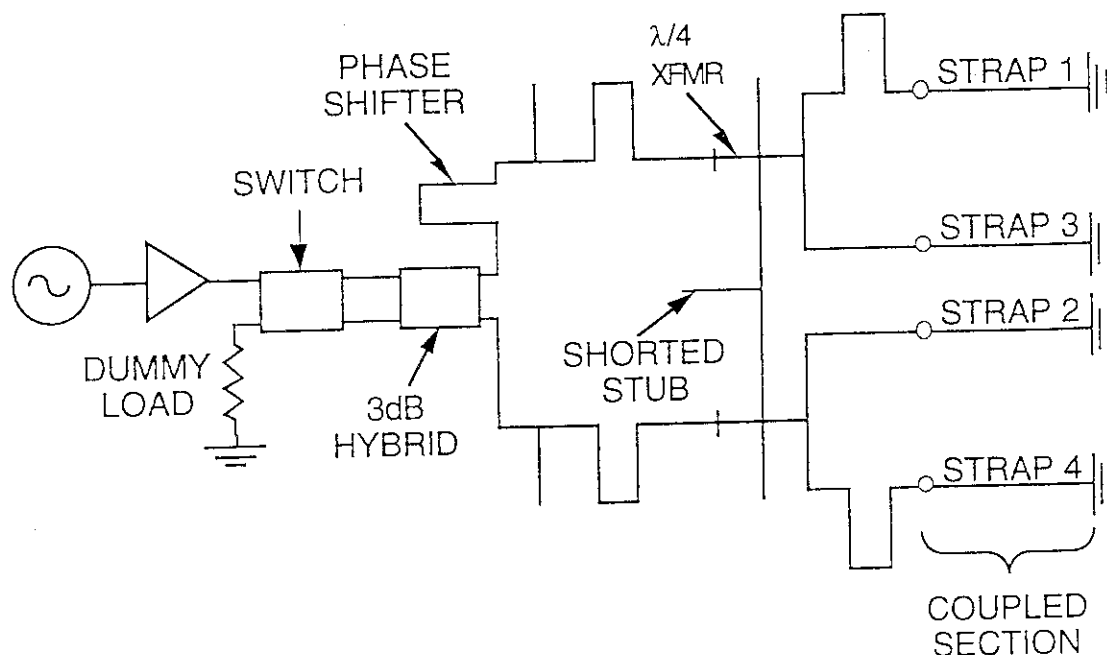
Fig. 12. The tuning and matching circuit, incorporating a single-stub decoupler and quarter-wave transformers, to be used with the long-pulse FWCD antennas.

SUMMARY

The technology of FWCD systems is being advanced rapidly through the development of new tools to analyze complex antenna structures in three dimensions and through the design and manufacture of antenna arrays and phase control systems. The interaction of the plasma with the antenna requires accurate modeling of the entire FWCD system and of the plasma response. Experiments on DIII-D and elsewhere have demonstrated key aspects of FWCD, although at fairly modest levels to date. With new high-power FWCD antennas due to become operational on both DIII-D and JET in 1994, the experimental validation of FWCD needed for implementation on future tokamaks can be expected in the near future.

ACKNOWLEDGEMENTS

REFERENCES

[1] F. W. Baity et al., in Fusion Technology 1990, (North Holland, Amsterdam, 1990), vol. 2, p. 1035.

[2] R. H. Goulding et al., in Proc. 17th Europ. Conf. on Controlled Fusion and Plasma Physics, Amsterdam, 1990 (European Physical Society, Petit-Lancy, 1990) vol. 14B, part III, p. 1311.

[3] R. H. Goulding et al., "Phased operation of the DIII-D FWCD antenna array with a single power source," to be published in Fusion Engineering and Design.

[4] R. I. Pinsker et al., in Proc. 14th IEEE/NPSS Symp. on Fusion Engineering, San Diego, 1991 (IEEE 91CH3035-3, Piscataway, NJ, 1992) vol. I, p. 115.

[5] C. C. Petty et al., Phys. Rev. Let. 69 (1992) p. 289.

[6] R. I. Pinsker et al., in Plasma Phys. and Contr. Fusion Research 1992, (IAEA, Vienna, 1993) Vol. I, p. 683.

[7] R. Prater et al., in Proc. IAEA Tech. Comm. Meeting on Fast Wave Current Drive in Reactor Scale Tokamaks, Arles, 1991 (Association EURATOM-CEA, Centre d'Etudes Nucléaires de Cadarache, 1991) p. 308.

[8] P. M. Ryan et al., "Methods of calculating selected geometrical effects in the design of ICRH antennas," to be published in Fusion Engineering and Design.

[9] E. F. Jaeger et al., Nucl. Fusion 33 (1993) p. 179.

[10] R. H. Goulding et al., in Fusion Technology 1992, (North Holland, Amsterdam, 1993) p. 515.

[11] R. H. Goulding et al., "Power compensators for phased operation of antenna arrays on JET and DIII-D," in Radiofrequency Power in Plasmas: Proc. 10th Topical Conf., Boston, 1993, to appear.

[12] R. H. Goulding et al., "Design and control of phased ICRF antenna systems," in Proc. 15th IEEE/NPSS Symp. on Fusion Engineering, Cape Cod, October 11-15, 1993, to appear.

[13] A. G. H. Sibley et al., "Power optimisation in the rf systems in JET and future systems," in Proc. 15th IEEE/NPSS Symp. on Fusion Engineering, Cape Cod, October 11-15, 1993, to appear.

[14] R. I. Pinsker et al., "Experimental test of a two-port decoupler in the DIII-D fast wave current drive system," in Proc. 15th IEEE/NPSS Symp. on Fusion Engineering, Cape Cod, October 11-15, 1993, to appear.

[15] F. W. Baity et al., "Design of long-pulse fast wave current drive antennas for DIII-D," in Radiofrequency Power in Plasmas: Proc. 10th Topical Conf., Boston, 1993, to appear.

[16] F. W. Baity et al., in Proc. 13th European Physical Society Conference on Controlled Fusion and Plasma Heating, Schliersee, 1986 (European Physical Society, 1986) vol. 10C, part II, p. 157.

[17] J. S. deGrassie et al., "4 MW upgrade to the DIII-D fast wave current drive system," in Proc. 15th IEEE/NPSS Symp. on Fusion Engineering, Cape Cod, October 11-15, 1993, to appear.

1. 4   ICRF Heating Antennas for ALCATOR C-Mod

Y. Takase, S. N. Golovato, M. Porkolab, Alcator Group

Plasma Fusion Center
Massachusetts Institute of Technology
Cambridge, MA 02139 U.S.A.

Abstract. Initial ICRF coupling studies were performed successfully on the Alcator C-Mod tokamak with all-metallic first wall, using a radially movable single current strap (monopole) antenna. The plasma loading is 10–30 times the vacuum loading, which is sufficient to inject 2 MW of RF power through one two-strap (dipole) antenna. The observed loading is consistent with predictions of full-wave calculations. Up to 1 MW of RF power (antenna power density of $\gtrsim 10\,\text{MW/m}^2$) has been injected into the C-Mod plasma with no increase in the fractional radiated power P_{rad}/P_{in}. Definite signs of both ion and electron heating were observed at power levels of 0.4 MW and higher ($P_{RF}/P_{OH} \gtrsim 0.3$) in the D(H) minority heating regime. High power heating experiments with 4 MW of source power and two dipole antennas will begin in early 1994.

1. Introduction

The Alcator C-MOD tokamak ($R = 0.67\,\text{m}$, $a = 0.21\,\text{m}$, $\kappa \leq 1.8$, $B \leq 9\,\text{T}$, $I \leq 3\,\text{MA}$) is a versatile compact tokamak which is capable of running over wide ranges of magnetic field, current, density, and plasma shape including limiter and both closed and open divertor configurations. The Alcator C-Mod ICRF experiments can characterize antenna-plasma coupling, antenna power handling, and heating in high density diverted plasmas, and impurity generation at high power densities in an all-metallic first wall environment. Initial ICRF coupling studies began in August 1993 using a radially movable single-strap (monopole) antenna [1] in conjunction with a radially movable outboard limiter. Up to 1 MW of ICRF power at 80 MHz has been injected and definite indications of both ion and electron heating have been observed. High power heating experiments will begin in early 1994 using two fixed position two-strap (dipole) antennas [2] and an RF source power of up to 4 MW.

2. Single-strap antenna

Initial ICRF coupling experiments were carried out using the movable single-strap antenna. This antenna is made of silver-plated Inconel components. The Faraday shield consists of two layers of triangular cross section Inconel rods which are copper plated and then titanium carbide coated. The width of the current strap is 10 cm and the antenna box sidewalls are slotted. The RF power is fed through two 6″ vacuum feedthroughs from both ends of the current strap, and the strap is grounded at the center. The antenna box is protected by protection tiles made of titanium carbide coated TZM molybdenum alloy. The antenna has 15 cm of radial movement capability, and can be partially retracted into the vacuum vessel port.

2.1. Antenna loading measurements

Antenna-plasma coupling studies were performed making use of the radial movability of the monopole antenna. The aim of the coupling measurements was to determine the optimum antenna and limiter positions for the dipole antennas consistent with optimal plasma configuration for proper divertor operation. The edge density profile was measured with Langmuir probes embedded in outboard limiter tiles and in antenna protection tiles. Figure 1 is a plot of the experimentally measured antenna coupling resistance (defined as the equivalent load resistance at the end of a $50\,\Omega$ transmission line, minus the vacuum loading resistance) as a function of the antenna radial position. Also shown is the coupling resistance calculated from the radiation resistance predicted by the full-wave code FELICE [3]. A transmission line model of the antenna was used to relate these two different measurements of the plasma loading of the antenna. The data were obtained in single-null diverted plasmas with the separatrix at $R = 91$ cm and the outboard limiter at $R = 93$ cm. In obtaining the calculated coupling resistance, the experimentally measured density profile was used up to the outboard limiter radius. In these plasmas, the density at the outboard limiter was $1 \times 10^{19}\,\mathrm{m}^{-3}$. The density in the shadow of the outboard limiter decays exponentially with a characteristic scrape-off length of approximately 1 cm. At present, the best agreement is obtained if the region outside the outboard limiter is represented by vacuum. These values are to be compared with the vacuum loading of $0.5\,\Omega$. The coupling resistance increases with increasing edge density, but not necessarily with the central density. Coupling resistances of over $15\,\Omega$ have also been measured when the antenna was positioned closer to the separatrix.

2.2. Antenna power handling

The transmitter has been operated at output power levels of up to 2 MW at 80 MHz into a dummy load. On the RF vacuum test stand, the antenna and the transmission line
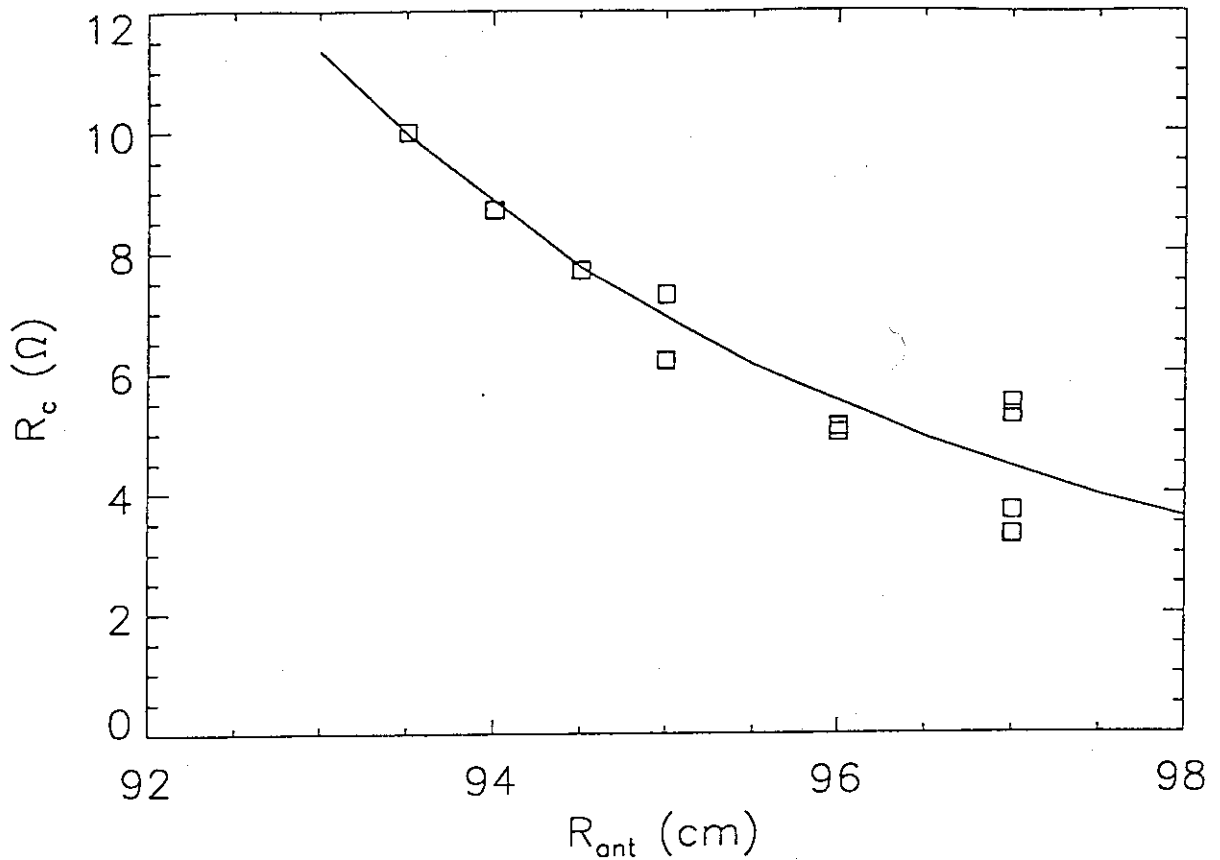
Fig. 1. Experimentally measured antenna coupling resistance (squares) and predictions of FELICE full-wave calculation (solid line) as functions of the antenna radial position. Measured density profile was used up to the outboard limiter ($R = 93$ cm) and a vacuum gap is assumed from this radius to the antenna position. The separatrix was located at $R = 91$ cm.

components were conditioned up to a peak RF voltage of 70 kV prior to installation on Alcator C-Mod. During vacuum conditioning on Alcator C-Mod, power (voltage) levels of 0.25 MW (50 kV) for short pulses (6 ms) and 0.20 MW (45 kV) for longer pulses (160 ms) were achieved. Maximum rf power of 1.0 MW (22 kV) for short pulses (10 ms) and 0.8 MW (20 kV) for longer pulses (80 ms), corresponding to a power density of $\gtrsim 10\,\mathrm{MW/m^2}$, have been injected successfully into the plasma with no increase in the fractional radiated power, P_{rad}/P_{in}. RF powers of 0.5 MW for 400 msec have been injected reliably into the C-Mod plasma. These results do not represent the antenna power handling limit, only what has been achieved over the short experimental time thus far devoted to RF experiments.

2.3. Heating effects and impurity generation

The primary heating scenario during this period was hydrogen minority heating in deuterium majority plasmas at $B_T = 5.3\,T$ and $I_p = 0.85\,MA$ ($P_{OH} \simeq 1.3\,MW$). A major objective during this campaign was to characterize both heating effectiveness and impurity generation. A hydrogen minority tail was observed up to at least 20 keV (limit of the present neutral particle analyzer). A small deuterium tail and a substantial deuterium bulk heating, were also observed on the charge exchange neutral particle energy spectrum. Because of the low minority concentration used in these experiments (of order 1%, with large uncertainties), second harmonic absorption by deuterium ions was probably possible. The neutron flux increase indicates deuterium majority heating of as much as 500 eV with 0.5 MW of RF power at the lowest density studied ($\bar{n}_e = 0.9 \times 10^{20}\,m^{-3}$). The electron temperature increase is most pronounced inside the $q = 1$ radius. While there is only a small change in the ohmic electron temperature profile throughout the sawtooth cycle, a substantial central peaking of the electron temperature profile is observed with ICRF heating, indicating central electron heating. The central electron temperature increase was 200 eV at the top of sawteeth and 100 eV averaged over sawteeth with 0.75 MW of RF power at $\bar{n}_e = 2.5 \times 10^{20}\,m^{-3}$. The sawtooth period doubles, from the ohmic value of 5 msec to 10 msec. The stored energy increase inferred from magnetics (EFIT equilibrium reconstruction and diamagnetic measurement) is of order 5 kJ, with large uncertainties. This corresponds to roughly 10% increase in the total stored energy.

The radiated power from the main plasma increases, but the molybdenum line radiation does not increase uncontrollably and the ratio of the radiated power to the total input power P_{rad}/P_{in} does not increase from the ohmic phase. No increase in light emission is observed directly on the antenna surface. Initial data indicate that 2 cm of clearance is needed both on the inboard side (separatrix to inner wall) and the outboard side (separatrix to outboard limiter) to maintain an effective divertor configuration. Sufficient coupling resistance and high power density RF power injection without deleterious impurity generation can be achieved with the antenna Faraday shield positioned 1 cm behind the outboard limiter. These distances will be maintained for the new fixed position limiters and antennas.

3. Two-strap antennas

The rf power capability will be upgraded to 4 MW at the source (80 MHz fixed frequency) and high power heating experiments using two fixed-position dipole antennas will begin in early 1994. The two-strap antennas are made of copper-plated Inconel, and have

two current straps which can be phased either in phase or out of phase. The current strap design is the same as that for the single-strap antenna. The RF power is fed through four 4″ vacuum feedthroughs. One antenna has a titanium carbide coated Faraday shield and the other a boron carbide coated shield, but the two antennas are otherwise identical and are installed in adjacent ports such that the four current straps are approximately equally spaced toroidally. Each antenna is designed to deliver up to 2 MW (RF power density of 10 MW/m^2) and can be operated for up to 10 sec without active cooling. Such long pulses are planned for lower hybrid current driven plasmas at a reduced field of 4–5 T.

The minimum coupling resistance observed with the single-strap antenna was 5 Ω with the antenna positioned 3–4 cm behind the outboard limiter, and the peak RF voltage was 22 kV at 0.5 MW for this loading. A coupling resistance of 10 Ω is more typical with the antenna positioned 1 cm behind the limiter, but a coupling resistance for the dipole antenna is predicted to be a factor of 2 lower than the single-strap antenna. For a coupling resistance of 5 Ω, 2 MW of available RF power from one transmitter can be injected through one dipole antenna at a peak RF voltage of 45 kV. This will provide a total of 4 MW from two transmitters through two antennas for high power heating experiments which are scheduled to begin in early 1994.

4. Future plans

Future plans include testing of a folded waveguide antenna in collaboration with the Oak Ridge National Laboratory. Additional collaboration with the Princeton Plasma Physics Laboratory will include upgrading of the ICRF power capability by adding two tunable (40–80 MHz) FMIT transmitters and adding a new antenna aimed at electron heating and fast wave current drive. Longer range plan includes studies of advanced tokamak scenarios by adding up to 4 MW of lower hybrid power at 4.6 GHz for combined LHCD and ICRF heating and/or FWCD. Of particular importance in such a program is Alcator C-Mod's capability to run long pulses at lower fields (7 sec flattop at 5 T), which is up to an order of magnitude longer than the skin time at temperatures of $T_e \lesssim 5$ keV.

5. Conclusion

The monopole antenna has performed well in the all-metallic (mostly molybdenum) environment of Alcator C-Mod. Injected RF power levels of up to 1 MW have been achieved with no increase in the fractional radiated power P_{rad}/P_{in}. The location of the fixed position outboard limiters and dipole antennas have been finalized. The observed antenna loading is consistent with predictions of full-wave calculations, and is adequate to inject the full RF power through two dipole antennas. Definite signs of both ion and electron heating

were observed at power levels of 0.4 MW and higher. High power heating experiments with 4 MW of source power and two dipole antennas will begin in early 1994.

Acknowledgment

References

[1] Y. Takase, et al., Alcator C-Mod ICRF antenna design and analysis, in Proc. IEEE 13th Symp. Fusion Engineering, 1989, Vol. 1 (IEEE, New York, 1990) pp. 211–214.

[2] Y. Takase, et al., Engineering design and analysis of the Alcator C-Mod two-strap ICRF antenna, in Proc. 14th IEEE/NPSS Symp. Fusion Engineering, 1991, Vol. 1 (IEEE, Piscataway, NJ, 1992) pp. 118–121.

[3] M. Brambilla, Theory of Bernstein wave coupling with loop antennas, Nucl. Fusion 28 (1988) 549–563.

1.5 Recent Results of JT-60U ICRF Antenna Operation

T. Fujii, M. Saigusa, H. Kimura, S. Moriyama, H. Kubo, T. Sugie, N. Hosogane,

K. Yokokura, M. Terakado, K. Igarashi

Japan Atomic Energy Research Institute, Naka, Naka, Ibaraki 311-01, Japan

1. Introduction

Ion cyclotron range of frequencies (ICRF) heating is one of attractive plasma heating methods for a reactor grade tokamak because it is quite effective in wide ranges of the plasma density and temperature. An antenna, which should inject high power into plasmas, has been developed intensively because heating efficiency and coupling properties depend on its design. The antenna was operated at small antenna-plasma gaps of 0.02 - 0.05 m in JT-60 for out-of-phase mode ((π,0) phasing) which shows high heating efficiency to obtain high loading resistance [1] and similarly in other tokamaks [2, 3, 4]. However, in order to reduce heat load to the antenna from the plasma, wide gaps are required in the reactor grade tokamak, such as ITER where the gap is designed to be 0.15 m in CDA [5]. Two new antennas were fabricated for JT-60U, which are designed to obtain high loading resistance at wide gaps for (π,0) phasing.

2. ICRF Heating System

Figure 1 shows a schematic block diagram of the JT-60U ICRF heating system [6]. Total generator output is originally 6 MW for 10 sec and is increased to 8 MW for 3 sec by rising the screen grid voltage. An impedance matching circuit for each transmission line is composed of a stub tuner and a phase shifter. Phasing of the currents between toroidally adjacent straps and between poloidally adjacent straps is carried out by phase shifters in low power levels. There
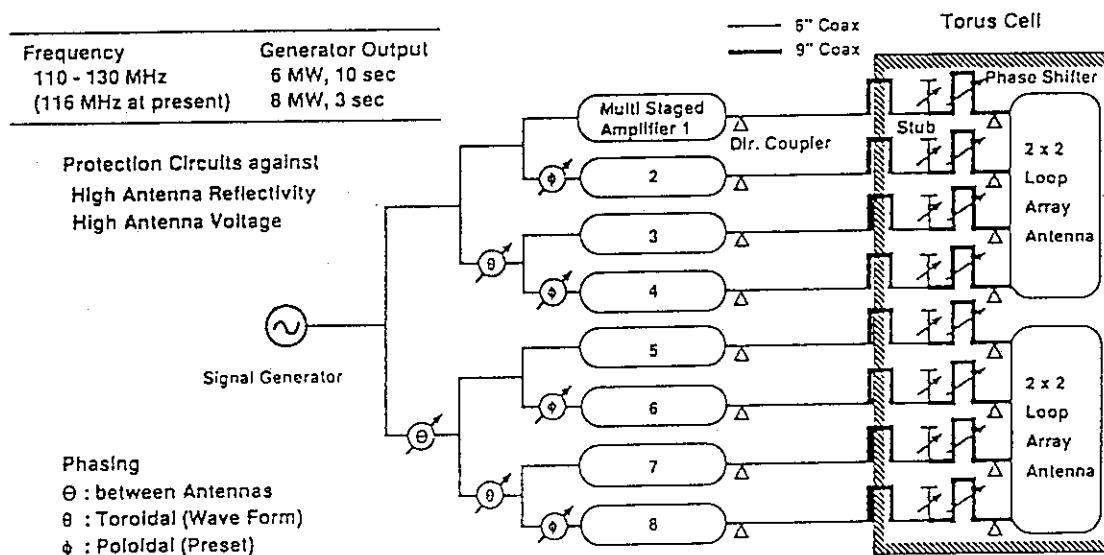
Fig. 1 Schematic block diagram of the JT-60U ICRF heating system.

are several protection circuits against high antenna reflectivity, high antenna voltage, large reflected power to the amplifier and so on. In particular, the circuit against high antenna reflectivity due to the antenna breakdown is quite useful for antenna conditioning. It has a notching function by which RF power is cut off within 200 μs if the reflectivity exceeds the preset value, and is turned on after the preset cut-off time, normally 2 ms for vacuum conditioning and 10 ms for plasma conditioning.

3. JT-60U Antenna

The front view of the JT-60U antenna is illustrated in Fig. 2. The antenna consists of 4 current straps (trombone shaped loops) short-circuited at the middle plane in the poloidal direction, which is basically similar to the JT-60 antenna. Each strap is 0.19 m in width and 0.32 m in height. The toroidal separation between the current straps is chosen to be 0.44 m to have the n// spectrum with n//peak ≈ 3 and Δn// ≈ 2.5 for (π,0) phasing at 116 MHz, which is calculated by the coupling code where the image current on the solid poloidal septum is considered [7]. The open type

Fig. 2 Illustration of the JT-60U ICRF antenna.

Faraday shield made of copper plated inconel pipes (15 mm in diameter) is provided to reduce RF dissipation. The poloidal septum leads easy impedance matching by suppressing the toroidal mutual coupling between the straps. Its position is the same in the major radius direction as that of the straps so that the arched Faraday shield, the septum and the recessed side antenna casing may have good transparency for RF magnetic field parallel to the toroidal magnetic field same as a slotted septum. The antennas are installed into the equatorial ports, P11 and P12 without bumper limiters, as shown in Fig. 3, but they are set behind the carbon tiles used as the first wall by 0.03 m.

Fig. 3 Front view of the JT-60U ICRF antennas installed.

4. Power Injection Capability

Antenna conditioning has been conducted well in the initial operation period. The phasing

mode is set at $(\pi,0)$ phasing which is expected to be higher heating efficiency than $(0,0)$ phasing. First we conditioned the antennas in vacuum loading up to the antenna maximum voltage $V_{max} = 42$ kV, where V_{max} is defined as the maximum standing voltage in the coaxial line connected to the current strap. ICRF power of 3.6 MW was coupled to plasmas after only about 70 conditioning shots where V_{max} reaches about 28 kV, as shown in Fig. 4. The coupled

Fig. 4 History of antenna conditioning in the initial operation period.

power was increased smoothly after the antenna conditioning. The maximum coupled power reaches 6.4 MW corresponding to the power density of about 6.1 MW/m^2 and V_{max} is 34 kV with $R_c \approx 3.9$ Ω. Here, the loading resistance is defined as the following expression

$$P_{net} = \frac{1}{2} R_c \left(\frac{V_{max}}{Z_0} \right)^2, \qquad (1)$$

where P_{net} is the transmitted power to the current strap and Z_0 is the characteristic impedance of the coaxial line, 50 Ω.

Anomalous antenna breakdown is observed during combined neutral beam injection (NBI) and ICRF heating for the particular magnetic field $B_t = 3.0$ T. Figures 5 (a) and (b) show time evolution of the forward and reflected powers of each current strap at $P_{IC} = 4$ MW for two successive shots of $B_t = 3.0$ T and $B_t = 2.83$ T, respectively. The notching for antenna protection works for $B_t = 3.0$ T but does not for slightly changing magnetic field $B_t = 2.83$ T. Moreover, sparks on the Faraday shield are found only for $B_t = 3.0$ T by monitoring the antenna front with a visible TV camera. Hot

Fig. 5 Time evolution of the forward and reflected powers of each current strap at $P_{IC} = 4$ MW for (a) $B_t = 3.0$ T and (b) $B_t = 2.83$ T.

spots are also seen in both antennas and are localized on the upper side of the Faraday shield blades in the lower part and near the toroidal center of the antenna. An ion cyclotron resonance layer of 7 ω_{cD} is located near the antenna for $B_t = 3.0$ T. Here, the resonance position is estimated carefully by considering the effect of the toroidal field ripple as well as the effect of the poloidal field because the ripple is fairly large values of about 2 % near the outer wall in the JT-60U. Thus, we infer that the sparks and the hot spots are caused by the energetic ions which are originally injected perpendicularly by NBI, diffuse to the resonance layer and then are accelerated by 7 ω_{cD} ICRF heating.

5. Coupling and Radiation Loss Properties

Figure 6 indicates the averaged loading resistance R_c over all the current straps as a function of the distance δ_{SF} between the separatrix and the Faraday shield. Open symbols indicate the data for $(\pi,0)$ phasing and closed symbols for $(0,0)$ phasing. The dotted line is a calculated result for $(\pi,0)$ phasing by the coupling code. The solid lines are simple fitting to the data. Fairly large antenna loading resistance is obtained, i.e. 4 Ω for $(\pi, 0)$ phasing at $\delta_{SF} = 0.13$ m, and 5 Ω for $(0, 0)$ phasing at very large

Fig. 6 Averaged loading resistance R_c as a function of the distance δ_{SF} between the separatrix and the Faraday shield.

distance of $\delta_{SF} = 0.33$ m although it decreases with δ_{SF}. The $(\pi,0)$ phasing data agree with the calculation, but the $(0,0)$ phasing data is much larger than the calculation.

Since the length of the evanescent layer for fast waves with $n_{//} > 1$ is almost same as δ_{SF} for the JT-60U plasmas, the loading resistance is roughly proportional to the expression [8]

$$R_c \propto \exp\left\{ -2 k_0 \delta_{SF} \left(n_{//}^2 + n_y^2 - 1 \right)^{0.5} \right\}, \tag{2}$$

where k_0 is the wave number in free space and n_y is the poloidal refractive index. The main parallel refractive index of the coupled power is estimated as $n_{//} \sim 2.8$ for $(\pi, 0)$ mode and as $n_{//} \sim 1.8$ for $(0,0)$ phasing from the slopes of the loading resistance shown in Fig. 6, where $n_y = 0$ is assumed. Then calculated $n_{//peak}$ for $(\pi,0)$ phasing is consistent with the estimated $n_{//}$ from the slope. Therefore, as for $(\pi,0)$ phasing it is inferred that the $n_{//}$ spectrum of the coupled power is close to the calculated one. On the other hand, the calculated $n_{//peak}$ is about 5 for $(0,0)$

phasing, much different from the estimated value from the slope. This discrepancy between the experiment and the calculation for (0,0) phasing seems to come from inexact modeling of the poloidal septum in the code because the image current on the septum may affect the $n_{//}$ spectrum much more strongly for (0,0) phasing than (π,0) phasing. Thus, we must treat the septum geometry exactly to calculate the loading resistance for (0,0) phasing.

The radiation loss properties during ICRF heating are investigated for (π, 0) phasing though there are not a number of data for (0,0) phasing at high power levels. Figure 7 shows the ratio of the incremental radiation loss to ICRF power $\Delta P_{rad}/P_{IC}$ from the main plasma as a function of ICRF power in deuterium and helium discharges for second harmonic minority heating of proton at $B_t = 4$ T. The data also include the results after boronization. The ratio of the incremental radiation loss decreases with ICRF power and is saturated at small values less than 10 % at power levels more than 4 MW. Possible explanation for this
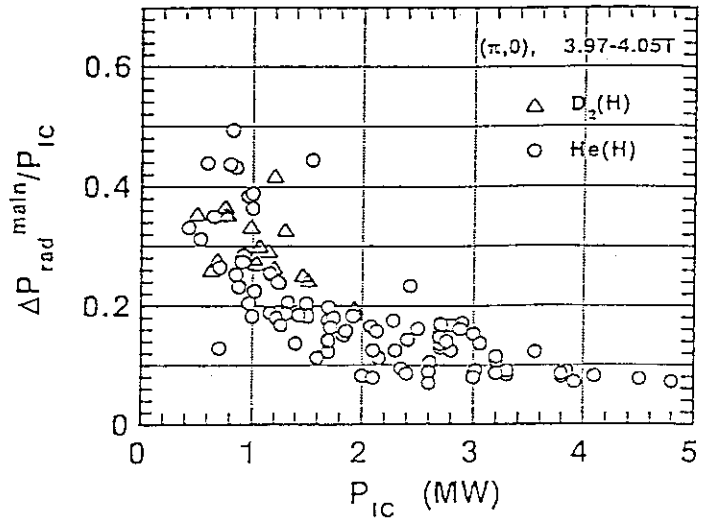
Fig. 7   Ratio of the incremental radiation loss to ICRF power $\Delta P_{rad}/P_{IC}$ from the main plasma as a function of ICRF power for (π,0) phasing.

power dependence of the radiation loss is the improvement of the power absorption, because the power absorption also increases with ICRF power and is saturated at about 100 % more than 2 MW. The effective ionic charge Z_{eff} is about 3 for helium ohmic discharges and it increases slightly by about 10 % during ICRF pulses of 4 MW level. The increase in the line emission intensity of light impurities such as carbon and boron shows a similar ICRF power dependence to that of the incremental radiation loss. Conversely, the metallic impurity nickel, which seems to come from the Faraday shield, has no correlation with the incremental radiation loss during ICRF heating. So that the increase in the radiation loss seems to be mainly caused by the light impurities from the first wall.

6. Conclusions

The JT-60U ICRF antennas are conditioned quickly with about 70 shots. The maximum coupled power is 6.4 MW for (π,0) phasing, corresponding to the power density 6.1 MW/m^2. Fairly large antenna loading resistance is obtained, i.e. 4 Ω for (π, 0) phasing at $\delta_{SF} = 0.13$ m, and 5 Ω for (0, 0) phasing at very large distance of $\delta_{SF} = 0.33$ m. This is desirable to an ICRF antenna operation in a reactor grade tokamak, such as ITER.

Anomalous antenna breakdown is observed during combined NBI and ICRF heating for $B_t = 3.0$ T. It is inferred to be caused by the energetic ions which are originally injected by NBI and then heated at $7 \, \omega_{cD}$ ICRF resonance near the antennas.

References

[1] T. Fujii, H. Kimura, M.Saigusa, et al., Nucl. Fusion **31** (1991) 137 - 154.

[2] M.J. Mayberry, S.C. Chu, R.I. Pinsker, R. Prater, Nucl. Fusion **30** (1990) 579 - 597.

[3] V.P. Bhatnagar et al., Plasma Phys. Controll. Fusion **33** (1991) 99 - 121.

[4] J. Hosea et al., Radio Frequency Power in Plasmas (AIP Conf. Proc. No. 244), Charleston (1991) 125 - 128.

[5] V.V. Parail et al., ITER Documentation Series No 32 (1991) 169 - 209.

[6] T. Fujii et al., Proc. 16th Symp. on Fusion Technology, London (1991) 1171 - 1175.

[7] M. Saigusa, T. Yamamoto, C.C. Petty et al., Nucl. Fusion **33** (1993) 421 - 434.

[8] V.L. Vdovin, Nucl. Fusion **23** (1983) 1435 - 1446.

1. 6 New Conceptual Antenna with Spiral Structure and Back Faraday Shield for FWCD

M.Saigusa, S.Moriyama, T.Fujii and H.Kimura

Naka Fusion Research Establishment,

Japan Atomic Energy Research Institute,

Naka-machi, Naka-gun, Ibaraki-ken, 311-01, Japan

Abstract

A new conceptual antenna, which we call as a spiral antenna, is proposed as a traveling wave antenna for fast wave current drive in tokamaks. The features of the spiral antenna are a sharp N_Z spectrum, easy impedance matching, N_Z controllable and good coupling. A back faraday shield is proposed for improving the cooling design of Faraday shield and better antenna-plasma coupling. A helical support which is a compact and wide band support is proposed as a kind of quarter wave length stub supports. The RF properties of the spiral antenna and the back Faraday shield have been investigated by using mock-up antennas. The VSWR of spiral antenna is low at the wide frequency band from 15 MHz to 201 MHz. The back Faraday shield is effective for suppressing the RF toroidal electric field between adjacent currents straps.

1. Introduction

Non-inductive current drive is necessary for continuous operation of a tokamak-type fusion reactor. The fast wave current drive (FWCD) is the most promising method for driving current in the central region of a high density and high temperature plasma.

The loop antenna has been adopted for exciting fast wave in the heating experiments. At the first phase of the FWCD experiments, the four loop antenna array was adopted in JFT-2M [1]. It was difficult to match the four loading impedances at the accurate phases and the same antenna currents, simultaneously, because of the strong mutual coupling among the antennas. The solid septum is effective for decreasing mutual coupling of antenna array, however, the image current on the solid septum make a counter directional N_Z spectrum [2]. The effect of image current on the slotted septum was still harmful for making a high directivity of Nz spectrum.

A new concept of a traveling wave antenna (TWA) was proposed by C. Moeller [3]. This concept is that the excitation of traveling wave in the tokamak plasma should be used the traveling wave antenna, that is a kind of slot antenna, with a ring resonator, as shown in Fig.1. The benefits of TWA are a easy impedance matching and a sharp N_Z spectrum. The comb line antenna proposed by C. Moeller is all metal and tight structure. The slow wave circuit of

the comb line antenna is made by adding the capacitance of the comb-like elements to the transmission lines.

The spiral antenna proposed by JAERI is one of the traveling wave antennas whose slow wave structure is made by the helical current strap wound around the central metal box.

2. Spiral Antenna

The conceptual view of the spiral antenna is shown in Fig. 2. The spiral current strap, which is wound around the central metal box, is supported by the quarter wave length stub, where the central metal box is supported by the side wall. The spiral antenna is the traveling wave antenna in both of the toroidal and poloidal directions. The main different point from the comb line antenna is a poloidal current profile due to the poloidal traveling wave antenna. Figures 3(a) and 3(b) show the poloidal current profiles of the spiral antenna and the comb line antenna. The voltage and current profiles of the spiral antenna are constant along the current strap in the poloidal and toroidal directions. On the other hand, the antenna current is minimum and the antenna voltage is maximum at the tip of the comb-like element in the comb line antenna. Therefore, the RF magnetic flux (made by antenna current) of the spiral antenna is larger than that of the comb line antenna. Then, the coupling of spiral antenna is probably better than that of the comb line antenna.

The double spiral phased (DSP) antenna array is a N_z controllable spiral antenna as shown in Fig.4. That is, the selection of co-current drive, counter-current drive and out-of-phase heating is possible by changing the phase difference between the two feeders: No.1 and No.2. The table 1 indicates the examples of phased operations of DSP antenna arrays. Of cause, the construction of the triple or quadruple spiral antenna arrays are available for the excitation of N_z spectrum with a high directivity. However, the operation of the multiple spiral antennas is as difficult as that of the conventional antenna array.

Table 1. Phase operation of DSP antenna array.

Phase Difference between No.1 & 2	Ant.1 & 5	Ant.2 & 6	Ant.3 & 7	Ant.4 & 8	Experiments
90°	0°	90°	180°	270°	Co-Current Drive
-90°	0°	-90°	-180°	-270°	Counter-Current Drive
0°	0°	0°	180°	180°	Heating in Out-of-Phase

3. Helical support

The neutron damage may degrade RF properties of ceramic insulators used in a fast wave antenna, so that the all metal antenna is suitable for a fusion reactor. A quarter wave length stub support is one of the components of all metal antenna. The principle of the quarter wave length stub support is the application of a high impedance RF circuit instead of

an insulator. The equivalent circuit is shown in Fig. 5(a). The input impedance of the shorted RF transmission line is given by $Z_S = j \cdot Z_0 \tan \beta L$, where Z_0 is the characteristic impedance, β is phase constant and L is the length from the short point. Z_S is very high impedance at the L of nearby the odd times of the quarter wave length, so that the current into this parallel circuit is very small.

The compact and wide band support demands the short wave length and the high Z_0 of the stub support. Therefore, the helical support is suitable for the all metal antenna, because that the wave length is shorted by helical structure and the Z_0 can be designed to be high.

The two types of helical support: the inner and outer helical supports are shown in Figs. 5(b) and 5(c), respectively. Figure of merit of shortening effect of the helical support is $\sqrt{1 + (\alpha \cdot r)^2}$, where "r" is winding radius and $\alpha \equiv \dfrac{d\theta}{dz}$. The shortening effect of the outer helical support is more effective than that of inner helical support, because of large r. The mechanical structure of the outer helical support is more tight than that of the inner helical one. On the other hand, the inner helical support has a simple structure, so that it can be made easier than the outer helical support.

4. Back Faraday shield

Faraday shield is one of the key issues on designing the antenna. ICRH experiments with and without the Faraday shield have been performed for checking the function of Faraday shield in TEXTOR [4]. The experimental results with and without Faraday shield are not so different except the impurity generation. However, the toroidal phasing of phased antenna array may excite the strong toroidal electric field along the magnetic field line, and the one of the functions of Faraday shield for adjusting the characteristic impedance of the strap is lost in the antenna without the Faraday shield. Then, the back Faraday shield (BFS) was proposed by JAERI. Figure 6 shows the conceptual view of the back Faraday shield, which is located behind the current strap. The functions of the back Faraday shield are to reduce the toroidal electric field and to decrease the characteristic impedance of the current strap. The low power test in a mock-up antenna proved that the BFS is effective for reducing the RF toroidal electric field.

5. Development of the spiral antenna for JFT-2M

The fast wave current drive system has the RF generator power of 800 kW at a frequency of 200 MHz in JFT-2M. The antenna design has been performed on the assumption of the poloidal 2 stage spiral antenna. Each spiral antenna will be fed by each ring resonator. The optimum N_Z spectrum for the fast wave current drive is calculated to be about 5 at a central electron temperature of 3 keV.

The mock-up antenna, which is upper half model with insulator antenna supports, was constructed for investigating the basic RF properties of the spiral antenna. The mock up

antenna consists of the eight turns spiral antenna and the central metal box with the back Faraday shield, as shown in Fig.7. Figure 8 shows the return loss from the one port of the mock-up spiral antenna with the other port terminated. The measured data indicates that the reflected points are mainly at the connecting points between the antenna feeder and the current strap. Because, the length calculated by the frequency interval of low reflection points agrees with the total antenna length (~4.5m). The VSWR at each connecting point is lower than 1.35 at the frequency range from 15 to 201 MHz. The reflected power is below 0.05% at the used frequency of 200 MHz, which is sufficient for the traveling wave resonance in the ring resonator.

6. Summary

The spiral antenna is proposed as the traveling wave antenna for the fast wave current drive. The benefits of the spiral antenna are the sharp N_z spectrum, the easy impedance matching, the N_z controllability and the good coupling. The back Faraday shield is proposed for suppressing the RF toroidal electric field and adjusting the characteristic impedance of the current strap for the conventional antenna array and the spiral antenna array. The helical support is proposed as a compact and wide band all metal support. In particular, the outer helical support is attractive, because of compact and tight structure. The tests of the mock-up antennas for the back Faraday shield and the spiral antenna in low power have been performed. The back Faraday shield reduces RF toroidal electric field between the adjacent antenna array. The RF properties of the mock up of spiral antenna are confirmed to be good at a wide frequency band from 15 to 201 MHz.

REFERENCES
[1] UESUGI, Y., YAMAMOTO, T., KAWASHIMA, H., HOSHINO, K., AIKAWA, H., et al., Nucl. Fusion 30 (1990) 831.
[2] SAIGUSA,M., FUJII,T., KIMURA,H., MORIYAMA,S., ANNOH,K., "ELECTRICAL DESIGN AND TEST OF ICRF ANTENNA FOR JT-60U", to be published on Fusion Engineering and Design, Feb. (1994).
[3] C.P.Moeller, et al., Proc. of EPS Topical Conf. on Radio Frequency Heating and Current Drive of Fusion Devices, Brussels, July, (1992) 53.
[4] van Nieuwenhove, R. et al., Nucl. Fusion, 31, No.9 (1991),1770.
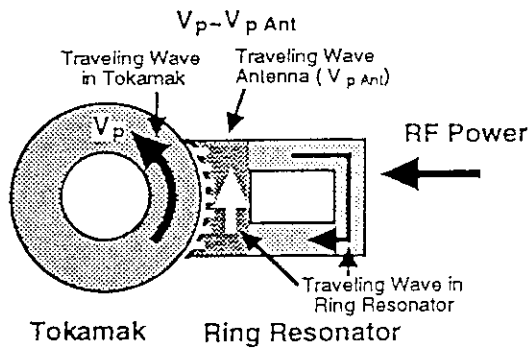
Fig.1 Principle of a traveling wave antenna with a ring resonator.
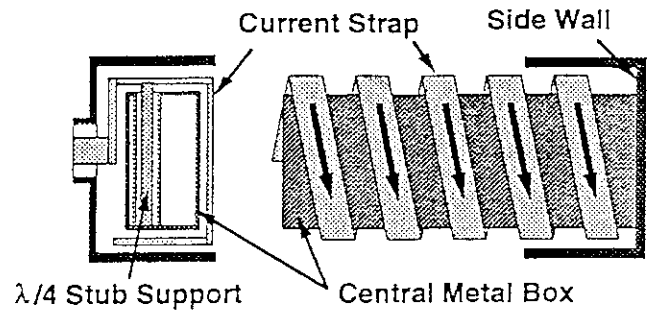
Fig.2 Conceptual view of Spiral Antenna

(a) Spiral Antenna
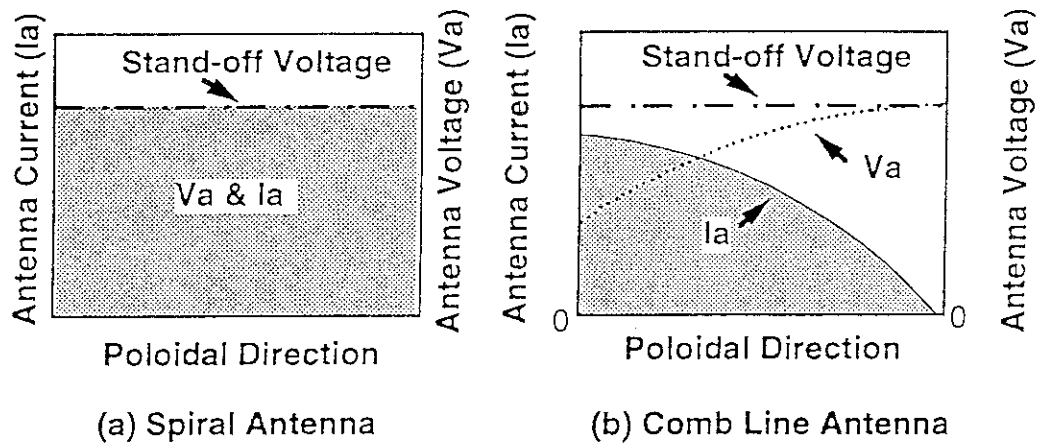
(b) Comb Line Antenna

Fig.3 Poloidal Current Profiles
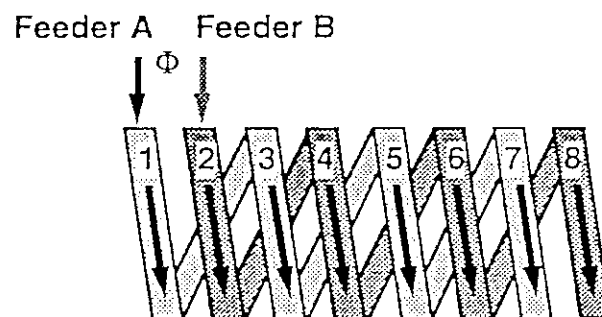
Fig. 4 Double Spiral Phased Antenna Array

$I_{total} \sim I_a$

I_s

| Zs (Support) | Za(Antenna) |

(a) Equivalent circuit of $\lambda/4$ stub support

Center
Conductor

Outer
Conductor

θ z r

(b) Inner helical

θ z r

(c) Outer helical

Fig.5 Helical Support

Faraday
Shield

Back
Faraday
Shield

Plasma

Current Strap
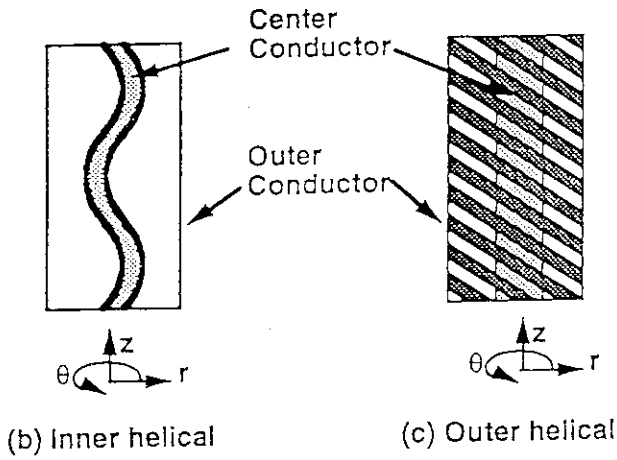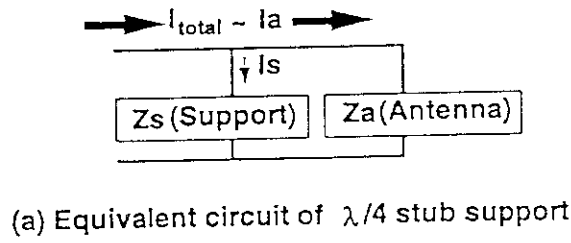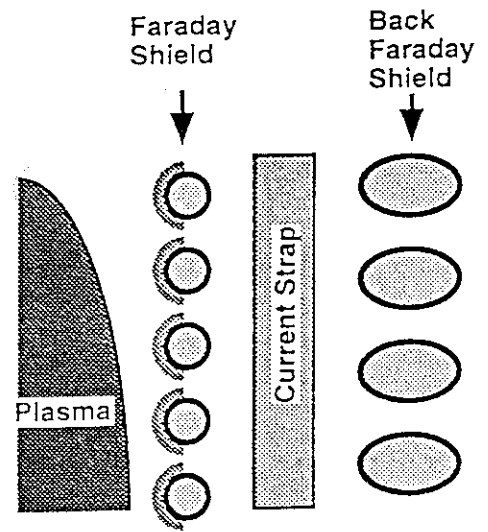
Fig. 6 Conceptual view of
back Faraday shield

BFS

20

172

200

Current
strap

17
11
39

360

Fig.7 Mock-up Spiral Antenna with BFS

S_{11} log MAG 5 dB/ REF 0 dB 1: -33.903 dB

200.000 001 MHz

0

-10

-20

-30

-40

-50

Returned Loss [dB]

1   101   201

Frequency [MHz]
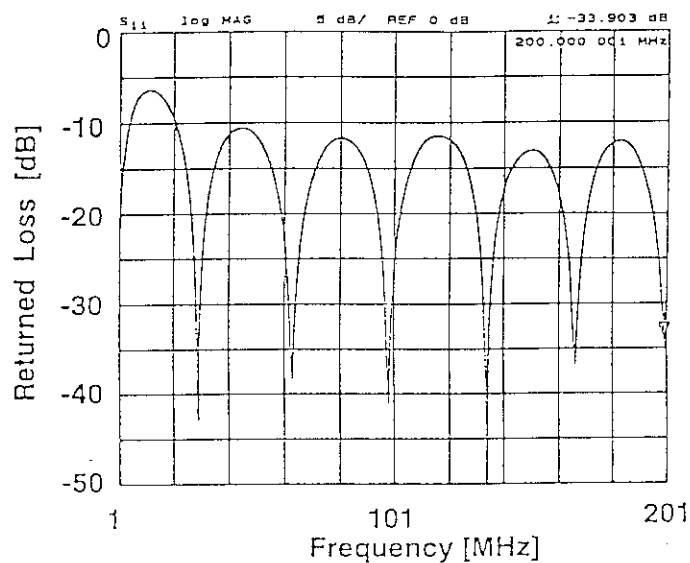
Fig.8 Returned loss of the mock-up spiral antenna

1.7   Combline Antennas for Launching Traveling Fast Waves

C.P. MOELLER, R.W. GOULD,* D.A. PHELPS, and R.I. PINSKER
General Atomics, San Diego, CA 92186-9784

ABSTRACT

The combline structure shows promise for launching traveling fast magnetosonic waves with adjustable $n_{\parallel}$ ($3 \leqslant n_{\parallel} \leqslant 6$) for current drive.[1] In this paper, the dispersion and damping properties of the combline antenna with and without a Faraday shield are given. The addition of a Faraday shield which eliminates the electrostatic coupling between current straps as well as between the straps and plasma offers the advantage of eliminating the need for the lumped capacitors which are otherwise required with this structure. The results of vacuum dispersion and damping measurements on a low power model antenna are also given.

INTRODUCTION

For current drive, it is necessary to launch a unidirectional wave, and desirable to vary the launched $n_{\parallel}$ in the range 3 to 6 during a discharge while presenting a matched load to the generator, even as the plasma position and edge density vary. These additional requirements are much more easily achieved by a radiating slow wave structure, fed at one end, than by the array of individually fed current straps presently used for launching fast waves. Such a structure is inherently a traveling wave device, in which the mutual coupling between radiating elements is part of the wave propagation, in contrast to individually fed radiating elements, for which the mutual coupling leads to unequal loading of the elements. A single point feed also eliminates the need for most of the external matching networks the individually fed current straps require. The input will appear matched to the external transmission line if the structure is long enough to radiate all of the incident power, if the output is terminated in a matched load, or if the structure is made part of a resonant ring. With a matched input, for the same total power, the voltage at the vacuum feedthrough may be lower than that at the feedthroughs of the individually fed straps with their high VSWRs.

A slow wave structure which has elements closely resembling the current straps of present fast wave antennas is the combline,[2] which is shown schematically in Fig. 1 configured as an antenna. Except for being open at the front, this structure is identical to commercially available bandpass combline filters. As with any bandpass filter, as the frequency varies within the passband, the phase shift from element to element ranges from 0 radians at the lower cutoff to π radians at the upper cutoff, although as will be seen, the range from $\pi/4$ to $\pi/2$ is the most desirable with regard to ohmic loss and radiated wavenumber spectral purity. The two disadvantages of the combline antenna as shown in Fig. 1 are the lack of a Faraday shield, and the lumped capacitance which is required at the end of each current strap. Although the required capacitance is small, the required area is inconveniently large. Both these drawbacks can be overcome by configuring a Faraday shield as shown in Fig. 2, so as to eliminate capacitive coupling between current straps, as will be discussed in the next section.
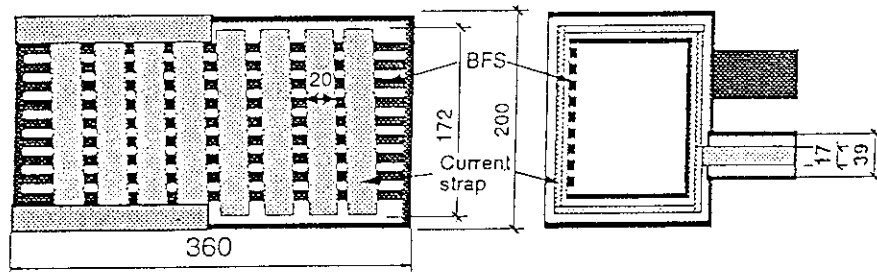
---

*Permanent Address: California Institute of Technology, Pasadena, CA 91125.

Moeller et al.
COMBLINE ANTENNAS FOR LAUNCHING TRAVELING FAST WAVES

VACUUM DISPERSION PROPERTIES

The vacuum properties will be analyzed with the plasma replaced by a conducting wall, with the surface impedance of the plasma treated as a perturbation on the vacuum solution, in a extension of an approach used by Golant.[3] We can regard the array of current straps and the conducting walls as a section of multi-conductor transmission line, which is governed by the equations:

and

$$\frac{\partial V_r}{\partial y} = - i\omega \sum_s L_{rs} I_s \quad , \tag{1}$$

$$\frac{\partial I_r}{\partial y} = - i\omega \sum_s C_{rs} V_s \quad , \tag{2a}$$

where y is the coordinate along a conductor, $V_r(y)$ and $I_r(y)$ are the voltage and current on the rth conductor at y, and L_{rs} and C_{rs} are the mutual inductance and capacitance per unit length, respectively, between the rth and s^{th} conductors. With an ideal Faraday shield, which does not affect inductances but completely shields each bar electrostatically, Eq. (2a) is replaced by

$$\frac{\partial I_r}{\partial y} = - i\omega C_0 V_r \quad , \tag{2b}$$

where C_0 is the capacitance per unit length of each bar to its shield. With all the conductors grounded at $y = 0$, and assuming an infinite array of identical elements, we can let $V_r = V^0 \sin(\beta y) \exp(-ir\theta)$ and $I_r = I^0 \cos(\beta y) \exp(-ir\theta)$, where θ is the phase shift from element to element to be determined and β is the propagation constant along y. From (1) and (2a), respectively, we then obtain $V^0/I^0 = - i(\omega/\beta) \sum_s L_{0s} \exp(-is\theta)$ $\equiv - i(\omega/\beta)L(\theta)$ and $I^0/V^0 = i(\omega/\beta) \sum_s C_{0s} \exp(-is\theta) \equiv i(\omega/\beta)C(\theta)$ where the $r = 0$ element is typical in the infinite array. With a shield the second equation is replaced by $I^0/V^0 = i(\omega/\beta)C_0$. Without the shield, $\beta/\omega = [L(\theta)C(\theta)]^{1/2} = 1/c$ for a TEM wave. With the shield, $\beta/\omega = [L(\theta)C_0]^{1/2}$. The dispersion relations are determined by the boundary conditions at $y = \ell$: $I_r/V_r = i\omega C_e$, C_e the lumped capacitance, without a shield and $I_r = 0$ and $\beta\ell = \pi/2$ with a shield. The corresponding dispersion relations are respectively

$$L(\theta)C_e = 1/[c\omega \tan(\omega\ell/c)] \quad , \tag{3a}$$

and

$$L(\theta)C_0 = 1/(2\,\ell\omega/\pi)^2 \quad . \tag{3b}$$

It is apparent that if $C_e = 0$ in (3a), the only solution is $\omega\ell/c = \pi/2$, giving zero pass band width and zero group velocity. With an electrostatic shield, corresponding to (3b), the lumped capacitance is unnecessary.

The total electromagnetic field energy in a unit cell without a shield is $W_{\text{cell}} = (1/4)V_p^2\{\ell/[c^2 L(\theta)\sin^2(k_0\ell)] + C_e\}$, while with the shield it is $W_{\text{cell}} = (1/8)V_p^2\ell\{C_0 + (\pi/2)^2/[\omega^2\ell^2 L(\theta)]\}$, where V_p is the peak voltage at the end of the strap. The power flow along the structure is then just $P_0 = W_{\text{cell}} d\omega/d\theta$.

We have solved for $C(\theta)$ using a variational technique for the geometry shown in Fig. 1. $L(\theta)$ is then obtained from $L(\theta) = 1/[C(\theta)c^2]$. With an ideal Faraday shield, $L(\theta)$ is presumed not to change, while we can calculate C_0 approximately using the same variational technique. An example of the dispersion properties is shown in Fig. 3, where, referring to Fig. 1, $w = 5$ cm, $t = 2.5$ cm, $s = 5.4$ cm, $\ell = 31.25$ cm, and $d_2 = 15$ cm to a conducting front wall. For case A, $d_1 = 5$ cm, $\ell = 31.25$ cm, and

and $C_e = 16$ pF; for case B, $d_1 = 2.5$ cm and $C_e = 20$ pF; case C is similar to A except $C_e = 0$, $l = 40$ cm, and there is a Faraday shield for which $C_0 = 96$ pF/m. Corresponding values of $V_p/(P_0)^{1/2}$ at the passband center, P_0 the input power, are $28\,V/W^{1/2}$ for case A, $32\,V/W^{1/2}$ for case B, and $25\,V/W^{1/2}$ for case C.

Regarding the spatial spectrum, the k_z values of the fields in the structure must satisfy $k_z = (\theta/p) + (2\pi N/p)$, where p is the period and N is an integer. The most troublesome harmonic has $N = -1$. By making p small, $k_{z(-1)}/k_{z(0)}$ can be made so large that the evanescent region can filter out the harmonic. In our example, $3 \leqslant |k_{z(-1)}/k_{z(0)}| \leqslant 7$.

PLASMA DAMPING

We have evaluated the plasma damping by determining $\mathrm{Im}\,n_z$. n_z can be written in a Taylor series as

$$n_z\left(\rho_p\right) = n_{z0} + \frac{dn_z}{d\rho}\bigg|_{\substack{\rho=\rho_r \\ u=u_r}} \left(\rho_p - \rho_r\right) + \cdots \quad , \tag{4}$$

where n_{z0} is the vacuum n_z evaluated above with a conducting wall at u_0, ρ_r is the surface impedance at u_r with this wall present, while ρ_p is the surface impedance at u_r with a plasma replacing this wall (see Fig. 4). The ρ's are normalized to 377 ohm, and $u = k_0 x$.

The derivative in (4), $dn_z/d\rho$, can be evaluated from dn_{z0}/du_0, the change in n_{z0} due to the movement of the front conducting wall, which we evaluated numerically. The position u_0 of the wall can be chosen so that $\mathrm{Re}\,\rho_p \approx \rho_r$, minimizing the importance of higher terms of the series. Assuming a 5 cm vacuum region($u_r/k_0 = 5$ cm), which is large in view of the radiated k_z, the distance along the structure for power to be reduced by $1/e$ is shown in Fig. 5 for two idealized DIII–D plasma profiles as a function of n_z. For purpose of comparison, the effective series resistance at the bottom of the strap necessary to reduce the power in the structure by $1/e$ in a meter is ≈ 0.57 ohm for case A and ≈ 0.24 ohm for case B. Even with this small loading resistance, the incident power is efficiently radiated, demonstrating the advantages of a slow wave structure. The predicted vacuum ohmic damping is in comparison only $\approx 1\%/\mathrm{m}$ for case A and $2\%/\mathrm{m}$ for case B.

Preliminary damping measurements using resistive films on a low power model have given the result that the measured damping is somewhat stronger than that calculated by the above model, so the curves of Fig. 5 are probably rather conservative.

CONCLUSIONS

We have described a periodic structure for efficiently launching traveling fast waves of high n_z. The n_z can be varied over a wide range with a moderate frequency change. The shielded version of this structure requires no loading capacitors and has lower peak voltages than the corresponding unshielded structure.

REFERENCES

1. Nathaniel J. Fisch and Charles F.F. Karney, Phys. Fluids 24, 27 (1981).
2. C.P. Moeller, S.C. Chiu, and D.A. Phelps, in *Proc. Europhys. Top. Conf. on RF Heating and Current Drive of Fusion Devices 1992*, Brussels, Vol. 16E, p. 53.
3. V.E. Golant, Sov. Phys. Tech. Phys. 16, 1980 (1972).
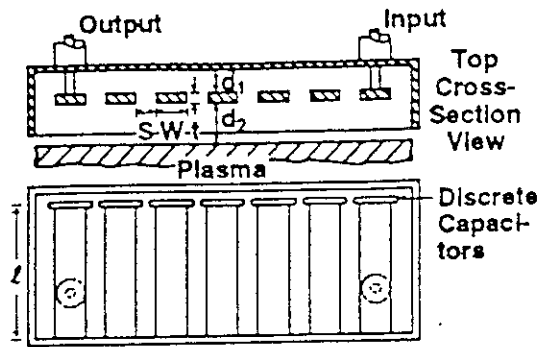
FIG. 1. Schematic of unshielded comb-line antenna.
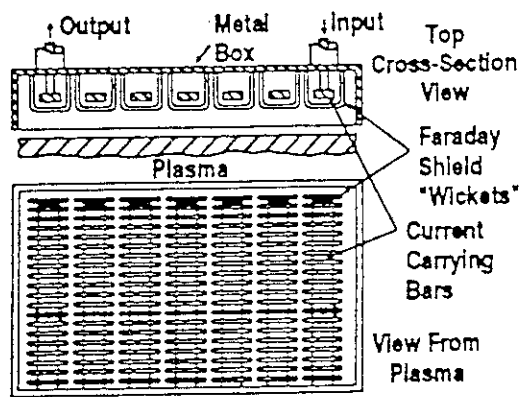
FIG. 2. Schematic of shielded comb-line antenna.
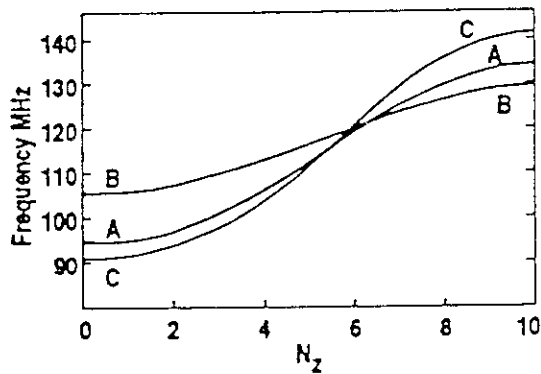
FIG. 3. Vacuum dispersion of the un-shielded (cases A and B) and shielded (case C) combline antennas. A has 5 cm backplane spacing, compared to 2.5 cm for B. C is similar to A except for the shield. Other dimensions are given in the text.

FIG. 4. Geometry of the loading calculation.

FIG. 5. Damping length for two ideal-ized DIII-D plasma profiles for cases A and B.

1.8   Concept of Ceramics-free Coaxial Waveguide

Hiroyuki ARAI

Division of Electrical and Computer Engineering, Faculty of Engineering
Yokohama National University, Yokohama-shi, Kanagawa 240, Japan

Abstract

A critical key point of the ITER IC antenna is ceramics support of an internal conductor of a coaxial antenna feeder close to the plasma, because dielectric loss tangent of ceramics enhanced due to neutron irradiation limits significantly the antenna injection power. This paper presents a ceramics-free waveguide to overcome this problem by a T-shaped ridged waveguide with arms for the mechanical support. This ridged waveguide has a low cutoff frequency for its small cross section, which has been proposed for the conceptual design study of Fusion Experimental Reactor (FER) IC system and the high frequency supplementary IC system for ITER.

This paper presents the concept of ceramics-free coaxial waveguide consisting of the coaxial-line and the ridged waveguide. This paper also presents the cutoff frequency and the electric field distribution of the ridged waveguide calculated by a finite element method and an approximate method. The power handling capability more than 3MW is evaluated by using the transmission-line theory and the optimized antenna impedance considering the ITER plasma parameters. We verify this transmission-line model by one-tenth scale models experimentally.

1. Ceramics-free coaxial waveguide

A mechanical support of an inner conductor of a coaxial-line is quarter wavelength stub shown in Fig. 1. A reflection coefficient by this junction is calculated by the equivalent circuit shown in Fig. 1 as,

$$\Gamma = \frac{Y_o - Y_s}{Y_o + Y_s} = -\frac{1}{1 + 2j\tan(\beta l)} \qquad (1)$$

where Y_s is the stub admittance , $\beta = 2\pi/\lambda$, and the stub length is l. The reflection coefficient at junction is shown in Table 1. A frequency band width is $\pm 40\%$ for power reflection less than 10%, which is not wide enough for an application of the ITER system[1]. Other disadvantages of the stub support are that its structure is not suitable for modular design and the mechanical support is not so strong. Therefore waveguide concept is required for mechanical support for coaxial-line.
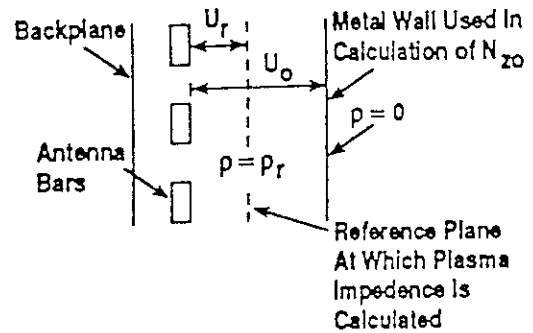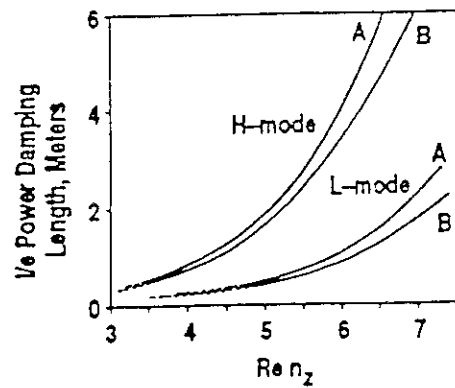
Figure 2 shows ceramics-free coaxial waveguide consists of coaxial-line and ceramics-free waveguide for mechanical support. For wide frequency band operation, the junction by the ridged waveguide is used below a cutoff. The reflection below the cutoff from the ridged waveguide is calculated by the cutoff waveguide theory.

$$\Gamma = exp\{-\sqrt{k_c^2 - k^2}\,l\} \qquad (2)$$

where k is wavenumber in free space and k_c is cutoff wavenumber of ridged waveguide. Figure 3 shows calculated reflection power S_{11} from the junction. The S_{11} is less than 10% above 10MHz for the cutoff frequency of the ridged waveguide being less than 40MHz. This frequency band width is suitable for the ITER application. Therefore a key design parameter is the cutoff frequency of the ridged waveguide.

2. T-shaped ridged waveguide with arms

In this paper, a T-shaped ridged waveguide with arms[2] is used to lower its cutoff frequency without using small gap. Figure 4 shows a T-shaped ridged waveguide with two arms on its both sides. The waveguide is a hollow conducting cylindrical tube with a cross section in the xy plane and is uniform along the z axis of the propagating direction. The waveguide is empty with the electrical parameters ε, μ. The waveguide walls ·are assumed to have infinite conductivity. According to these assumptions, electric and magnetic fields are expressed by the potential ϕ, and the functional $\Gamma(\phi)$ for FEM is given as follows.

$$\bar{E} = -j\omega\mu\bar{\nabla} \times \phi\bar{z} \qquad (3)$$

$$\bar{H} = \bar{\nabla} \times \bar{\nabla} \times \phi\bar{z} \qquad (4)$$

$$\Gamma(\phi) = \frac{1}{4}\mu k^2 \int\int (k^2\phi^2 - \phi_x^2 - \phi_y^2)dxdy \qquad (5)$$

where the subscripts x and y denote the partial derivative of ϕ by x and by y. Figure 5 shows the magnitude of the electric field distribution along the ridge surface at cutoff frequency. The electric field is almost uniform from the waveguide center to the corner C_3, and decay abruptly beyond a corner C_4. The electric field profile is concentrated between the waveguide center and the corner C_4, which indicates that this waveguide is a folded T-shaped ridged waveguide. The cutoff frequency f_c is approximated by the following equation[3][4],

$$f_c = \frac{c}{\pi}\sqrt{\frac{P_1}{(W - 2P_2 + 2P_3)WH}} \tag{6}$$

where c is the velocity of light. The errors of the approximation shown in Table 2 increase for long arms, however, an idea of the folded T-shaped ridge is useful to understand the waveguide cutoff frequency.

The waveguide impedance Z_r is a parameter for the transmission-line theory discussed in the next section. Since most of the energy is concentrated between the waveguide center and the corner C_4, the waveguide impedance $Z_{r\infty}$ at $k = \infty$ is given by the parallel-plate model whose width and gap spacing between plates are $W - 2P_2 + 2P_3$ and P_1.

$$Z_{r\infty} = 120\pi\frac{P_1}{W - 2P_2 + 2P_3} \tag{7}$$

Table 1 shows $Z_{r\infty}$ calculated by the FEM and by the parallel-plate model, in which we obtain fine agreement between them. Therefore, the waveguide impedance of the T-shaped ridged waveguide with arms is approximated by the following equation.

$$Z_r = 120\pi\frac{k}{\sqrt{k_{cr}^2 - k^2}}\frac{P_1}{W - 2P_2 + 2P_3} \tag{8}$$

The FEM analysis gives the waveguide characteristics and electric field distribution in detail, however, the cutoff frequency and the waveguide impedance is obtained by the simple model discussed in the above.

3. Analysis of ceramics-free coaxial waveguide

This section presents the analysis of ceramics-free coaxial waveguide shown in Fig. 6. Its inner conductor is a concave shape to obtain good impedance matching at the posts. The cross section at the post can be seen as a T-shaped ridged waveguide with arms. Since propagating energy is concentrated in a region between the concave conductor and the waveguide inner wall, the post under the concave conductor does not disturb the fields in this waveguide.

Two sections of the waveguide, the TEM (Transverse Electromagnetic) waveguide and the ridged waveguide, are characterized by the waveguide impedance and the propagation wavenumber as the transmission-line theory. Figure 7 shows the transmission-line model of the ceramics-free waveguide. The inner conductor is supported by three posts and the waveguide is terminated at 0-0' to the antenna of its input impedance Z_A. We assume an optimized antenna parameter for the ITER plasma in the calculation of Z_A[5][6]. The notation i-i' (i<7) denotes the junction between the TEM and the ridged waveguide. The waveguide length for the ITER is around 10m, which enables the stub tuning at the waveguide feed point 7-7' outside the cryostat. Therefore, the feed point is assumed to be matched to the waveguide in the following analysis model. The wave impedance of the TEM section Z_t is equivalent to $Z_{r\infty}$, because identical concave conductor is used for the TEM section in the ceramics-free waveguide. The impedance at i-i' in Fig. 7 is calculated by following equations by transmission line theory[7].

$$Z_{2m-1(2m-1)'} = Z_t\frac{Z_{2m-2(2m-2)'} + jZ_t\tan(kL_{2m-1})}{Z_t + jZ_{2m-2(2m-2)'}\tan(kL_{2m-1})} \tag{9}$$

$$Z_{2m2m'} = Z_r\frac{Z_{2m-1(2m-1)'} + jZ_t\tanh(\gamma_r L_{2m})}{Z_r + jZ_{2m-1(2m-1)'}\tanh(\gamma_r L_{2m})} \tag{10}$$

To estimate the maximum radiated power from the antenna, we define a power handling capability P_h as the radiated power P_o normalized by square the maximum voltage V_{mox} in the waveguide.

$$P_h = \frac{P_o}{V_{mox}^2} = \frac{Reall \times \frac{1}{Z_{77'}}}{V_{max}^2} \tag{11}$$

If we know the maximum voltage V_b not to cause the breakdown in the waveguide, we obtain the maximum power handing capability by multiplying P_h by V_b^2. Figure 8 shows the power handling capability for the cutoff

frequency of the ridged waveguide 50, 60, 70, and 80MHz, where a 10m long inner conductor is supported by two 50cm ridged waveguide sections. When the maximum voltage in the waveguide is 50kV (the magnitude of the electric field strength 20kv/cm for the minimum gap spacing 2.5cm), 3MW power handling capability is obtained for $P_A=0.0012$ in Fig. 8. The P_A is less than 0.0012 below 17MHz and for 45~55MHz when the cutoff frequency is higher than 70MHz. The cutoff frequency should be lower than 50MHz to obtain $P_A \geq 0.001$ within the frequency range of ITER IC system 15~80MHz.

4. Experiments

This section will verify the transmission-line theory by several one-tenth scale models. To measure resonant frequencies, we terminated a short or an open circuit to the model waveguide instead of an antenna. Though electrical short is given by attaching a conducting plate at the waveguide end, an ideal open circuit can not be obtained. We terminated no load to the waveguide, because the model waveguide impedance is 5~20Ω which is much smaller than the wave impedance in free space and gives an open condition approximately. The input impedance at the feed point for these loads become zero or infinite for at the resonance, and we obtain calculated resonant frequencies.

Three one-tenth scale models were used in the experiments. They are made by aluminum, and its parameters are shown in Table 1. A model 1 is a TEM waveguide with no ridged waveguide support, and an inner conductor is supported by dielectric posts. Models 2 and 3 are the ceramics-free waveguides with two/three ridged waveguide supports. The cutoff frequencies of the ridged waveguide section are 503.90MHz for model 2 and 447.95MHz for model 3 calculated by the FEM. Table 3 shows measured and calculated resonant frequencies. Measured results agree with calculated ones within 10% errors, which indicates the validity of the transmission-line theory. It is important to verify our theory terminating the scale model with an impedance which simulates a plasma load. However it is not easy to obtain the load which simulates the same frequency characteristics with a plasma. It will be left for the future problem.

5. Conclusion

We have proposed the ceramics-free coaxial waveguide for ITER IC (15~80MHz) system in which the TEM waveguide is supported mechanically by T-shaped ridged waveguide. The concept of this waveguide is applied to the mechanical support of the inner conductor of the coaxial-line. The power handling capability more than 3MW is evaluated by using the transmission-line theory and the optimized antenna impedance considering the ITER plasma parameters. We verified the theory experimentally by one-tenth scale models. The power handling capability of the ceramics-free waveguide depends on the impedance matching between the waveguide and the antenna input impedance, when the ridged waveguide section is much shorter than the wavelength and has low cutoff frequency. In addition, the cutoff frequency should avoid the vicinity of the frequency for the heating and the current drive. These conditions give various combination of TEM waveguide and the mechanical support section other than the example of this paper.

References

1. V.Parail et al., ITER Documentation Series, No. 32, IAEA, Vienna, 1991.
2. H.Kimura et al., Japan Atomic Energy Research Institute Report JAERI-M 91-094, 1991.
3. F.W.Perkins, Bull. Amer. Phys. Soc., vol. 26, p. 929, Sept. 1981.
4. H.Arai and N.Goto, IEEE Trans. Plasma Sci., vol. ps-13, no. 6, pp. 582-686, Dec. 1985.
5. H.Kimura et al., Proc. 4th Int. Symp. Rome, 1984 ,vol. 2, pp.1128-1135.
6. D.E.Post et al., ITER Documentation Series, No. 21, IAEA, Vienna, 1991.
7. R.E.Collin, "Field theory of guided waves," IEEE Press, New York, 1991.
9. H.Arai et al., IEEE Trans. Plasma Sci., vol. 21, no.3. pp.265-270, Jun. 1993

Talbe 1 Reflection coefficient at junction
fc is center frequency for stub

f/fc	Γ	Γ²
0.5(1.5)	0.447	0.2
0.6(1.4)	0.341	0.116
0.7(1.3)	0.246	0.060
0.8(1.2)	0.160	0.025
0.9(1.1)	0.078	0.006
1.0	0.0	0.0

Talbe 2 Cutoff frequency and waveguide impedance
FEM is Finite Element Method, FTR is Folded T-shaped Ridge model,
PPW is Parallel Plate Waveguide model,
$W=300$, $H=700$, $T_1=T_2=T_3=35$, $P_1=P_2=25$ (mm), $k_1=K_2=0$

P_3(mm)	f_c(MHz)		$Z_{r\infty}$(Ω)	
	FEM	FTR	FEM	PPW
100	49.21	49.12	17.12	20.94
300	40.94	35.73	10.65	11.10
500	36.39	29.40	7.55	7.54

Talbe 3 Resonant frequency (MHz) of one-tenth model waveguide
$W=35$, $H=75$, $T_1=12$, $T_2=T_3=2.4$(mm), $k_1=k_2=0$.
Model 1 is TEM waveguide without ridged waveguides,
Parameters of Model 2 are $L_1=L_5=158.7$, $L_3=158.6$, $L_2=L_4=12.0$,
$P_1=6$, $P_2=2.5$, $P_3=27.6$(mm),
Parameters of Model 3 are $L_1=L_3=L_5=L_7=116.0$, $L_2=L_4=L_6=12.0$,
$P_1=4.2$, $P_2=2.5$, $P_3=27.6$(mm).

model 1		model 2		model 3	
theory	measured	theory	measured	theory	measured
150.0	139.9	185.0	201.4	187.4	195.8
300.0	294.7	328.2	312.2	334.2	339.7
450.0	413.5	463.2	446.5	456.0	416.7
600.0	593.0	615.1	599.0	596.8	610.1
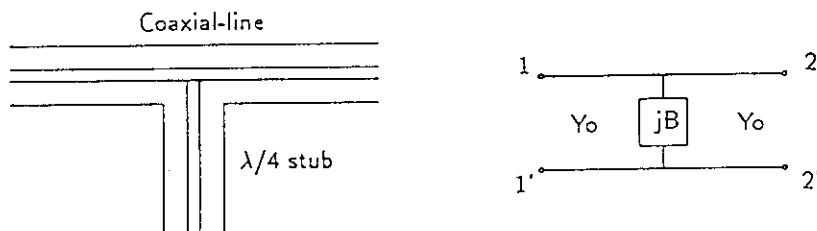
Figure 1: Equivalent circuit for junction
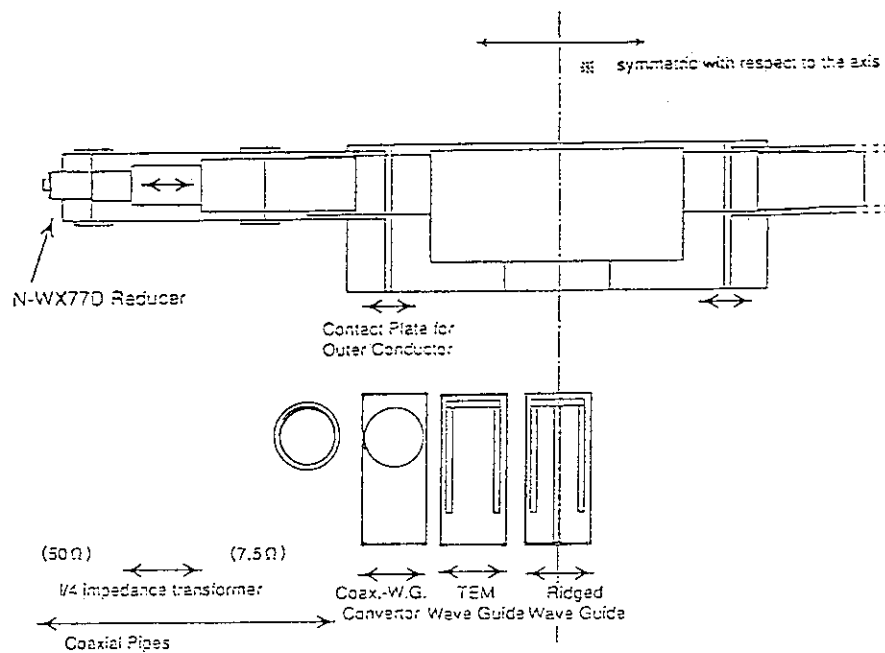
Figure 2: Ceramics-free coaxial waveguide
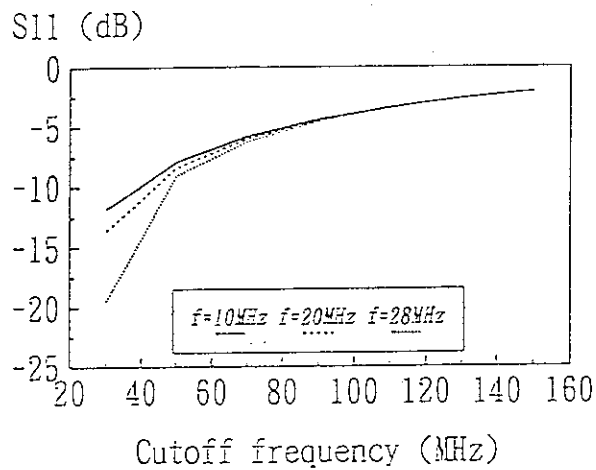
Figure 3: Reflection from ridged waveguide of l=50cm
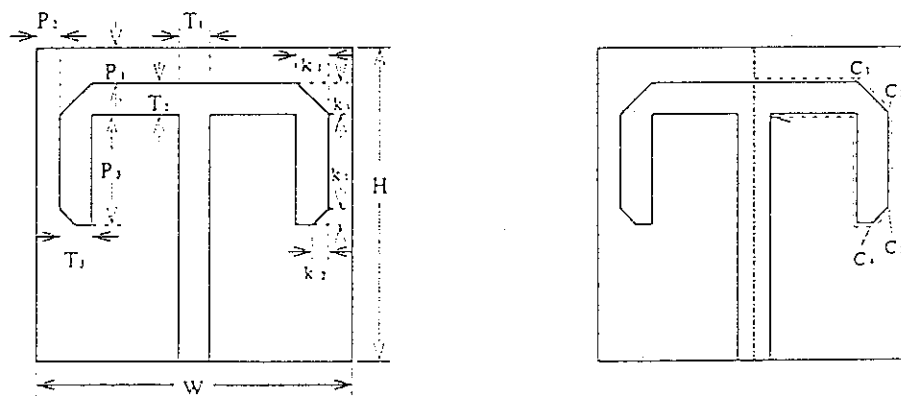
Figure 4: Cross section of T-shaped ridged waveguide with arms
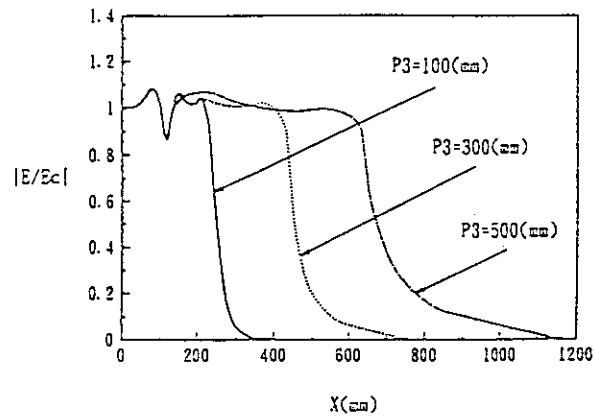
Figure 5: Electric field distribution along ridge
$T_1=T_2=T_3=30$, $P_1=P_2=25$, $k_1=25$, $k_2=12.5$, $w=300$, $H=700$(mm).
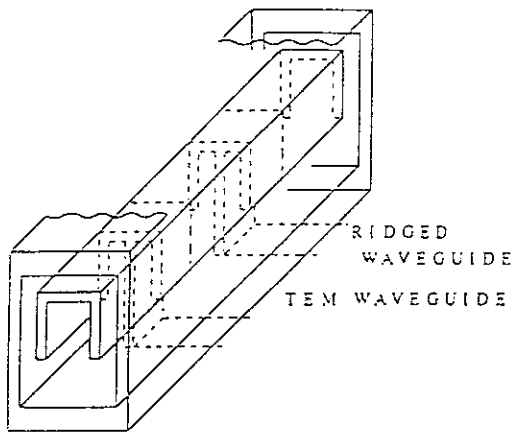
Figure 6: Ceramics-free coaxial waveguide
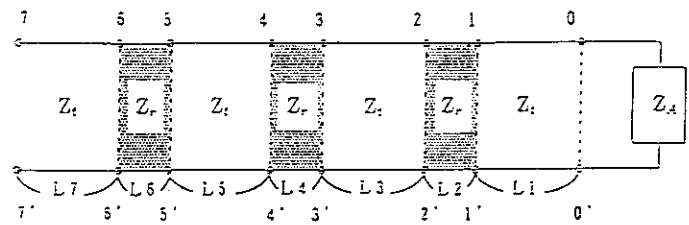
Figure 7: Transmission line model of ceramics-free
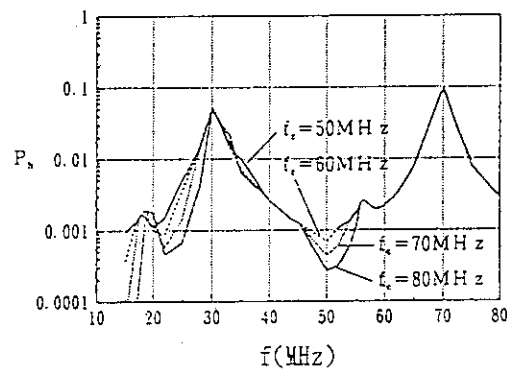
Figure 8: Normalized radiation power as a function of frequency
$Z_t=7.5\Omega$, $L_2=L_4=50$cm

1. 9 Development of Ceramic-free Antenna Feeder

S. Moriyama, H. Kimura, T. Fujii, M. Saigusa
Japan Atomic Energy Research Institute

H. Arai
Yokohama National University

Introduction

One of the major critical points of the IC antenna for next-generation tokamaks is a ceramic support of an internal conductor of a coaxial antenna feeder close to the plasma. Enhancement of dielectric loss tangent of ceramics due to neutron irradiation may limit antenna power injection capability significantly. We propose a ceramics-free antenna feeder line employing a ridged waveguide as a local support inside the cryostat which is applicable to a wide frequency range, e.g., 15-80 MHz (for ITER CDA parameters) and within constraints of ITER ports.

Figure 1 shows the schematic view of the antenna designed for ITER employing ceramics-free antenna feeder lines. Inner conductor of the coaxial line connected to the current strap of the antenna is mechanically supported by the all metal ridged waveguide section. This structure enables ceramic vacuum windows to place far from the plasma where neutron flux is small enough. The ridged waveguide section can be placed inside the cryostat because of its compact size.
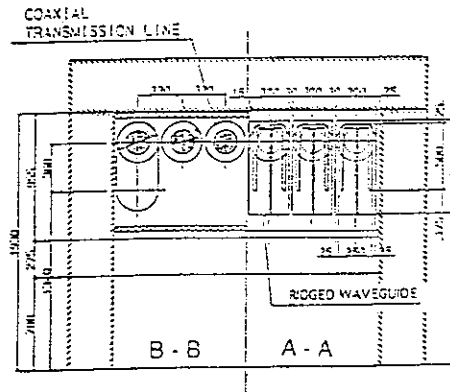
Fig. 1b Cross section of coax. and support section
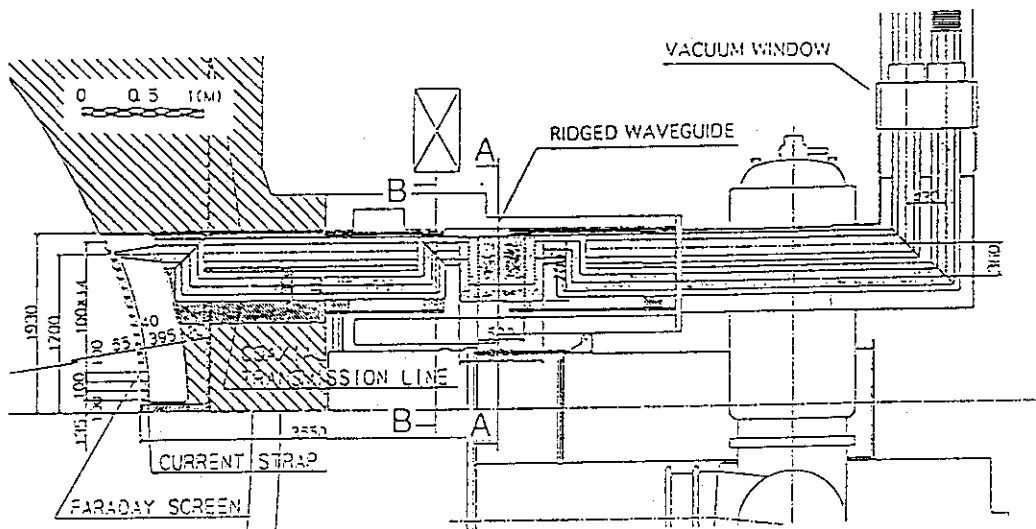
Fig. 1a Schematic view of the antenna designed for ITER employing ceramics free feeder line. Inner conductor is supported mechanically by ridged waveguide section.

Mock-up model and impedance calculation

One fourth mock-up model of the all metal waveguide designed for the ITER ICRF system is fabricated (Fig. 2). Analysis of the electrical characteristics of the ridged waveguide has already been done by a calculation with finite element method). However it is not easy to calculate the effect of the junction to a coaxial line because the structure is not simple. We intend to analyze the electrical characteristics of the all metal waveguide including the connection by means of measurements with the mock-up model. The model consists of a TEM waveguide supported mechanically by a T-shaped ridged waveguide, junctions to an coaxial line which is called "coax-waveguide converter", coaxial lines with the same impedance of the TEM waveguide, coaxial λ/4 impedance transformers and 50Ω coaxial lines for measurement. The cut-off frequency and the length of the ridged waveguide can be varied according to the choice of arms and supports of the waveguide. The length and the vertical position of the coax-waveguide converter can be varied as well.
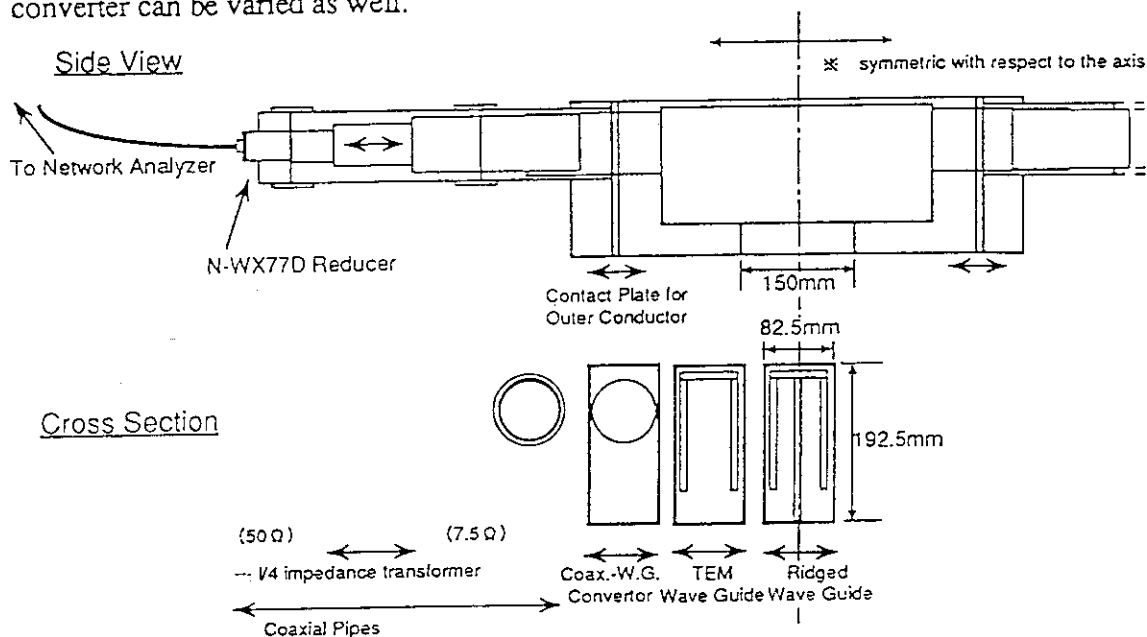
Fig. 2 Schematic view of the one-fourth mock-up model of the all metal waveguide designed for ITER ICRF system.

RF transmission properties of the model are measured in 54.5 - 291 MHz corresponding to 15 - 80 MHz with a network analyzer. Measured data is compared with calculation on the basis of the transmission line model (Fig. 3). The cut-off frequency and the characteristic impedance of the ridged waveguide were calculated by the finite element method.

	1	2	3	4	5	6	7	8
Part	Reducer	λ/4 Impedance transformer			Coax.	Coax.-WG Converter	TEM WG	Ridged WG
Impedance	50Ω	19.34Ω	14.83Ω	19.39Ω	7.54Ω	ZCON	7.54Ω	
Length	145mm				238mm	LCON(7mm)	135mm	150mm

· Symetric with respect to axis B
· The other side of A is terminated with 50 Ω
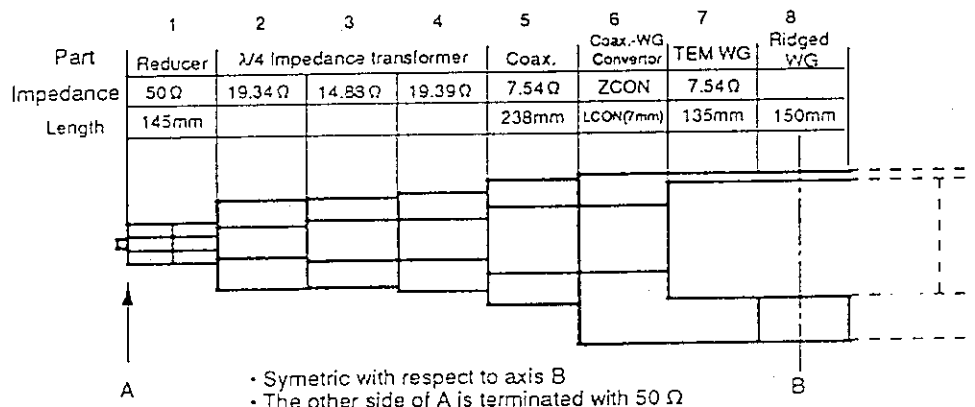
Fig. 3 Transmission line model for impedance calculation.

Measurement and analysis

Measured and calculated power reflection coefficient of the whole model is shown in Fig. 4. Relatively high reflection coefficient especially below the cut off frequency of 107 MHz or discontinuity comes from imperfect impedance transformer. The 1/4 impedance transformer has sliding part which has slightly different impedance from $(Z_1 \times Z_2)^{1/2}$, moreover, because of wide frequency range, we use three impedance transformers which cover 1/3 of whole frequency range respectively. In the calculation which shows good agreement with the measurement, we assume the coax-waveguide converter as a very short TEM line whose characteristic impedance is estimated (~45Ω) referring to Fig. 5. In Fig. 5, frequency dependence of the measured reflection coefficient with fixed length of impedance transformer is compared with the calculation for some values of characteristic impedance of the coax-waveguide converter which is assumed as a TEM line. In the case of 45Ω, the calculation is most close to the measurement.
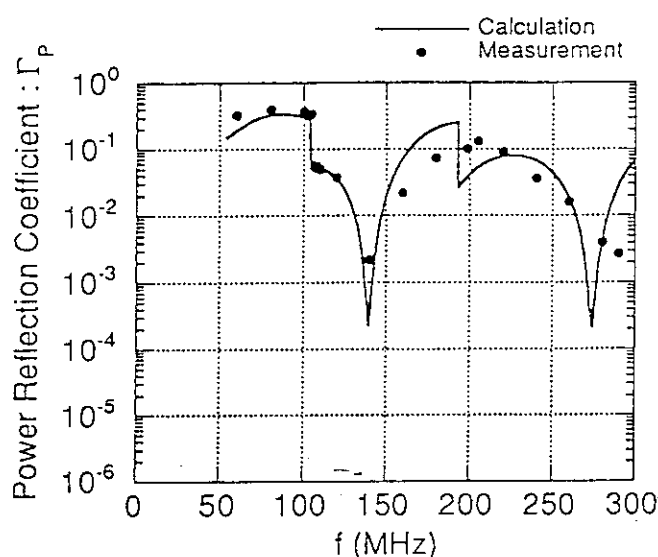
Fig. 4 Measured and calculated power reflection coefficient of the whole model with impedance transformers.
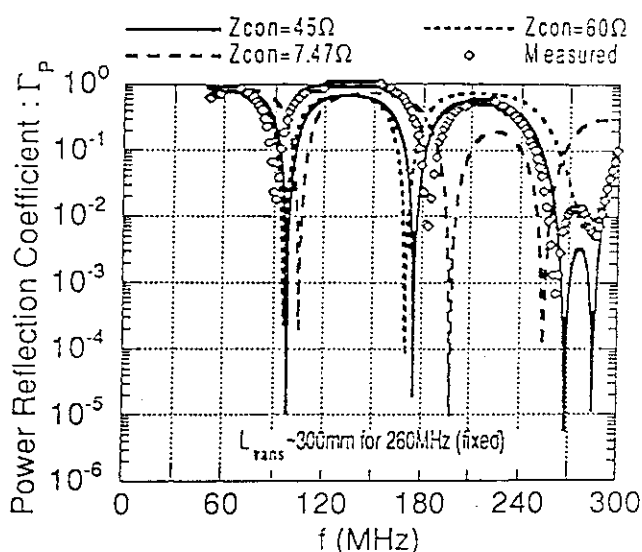
Fig. 5 Calculation for various values of impedance of the coax-waveguide converter which assumed as a very short TEM line. In the case of 45Ω, the calculation is most close to the measurement.

We obtain the power reflection coefficient of the model excluding the impedance transformer by means of assuming a perfect impedance transformer (Fig. 6). Power reflection coefficient of the model including the coax-waveguide converter to the input coaxial line is estimated less than 15% below the cut-off frequency of 107 MHz and less than 3 % above the cut-off frequency. The reflection coefficient is low enough for the antenna support which will be located at relatively high VSWR section between the matching circuit and the antenna. Power reflection coefficient of the model without coax-waveguide converter is shown as a dotted line as a reference.

Near cut-off frequency of the ridged waveguide, the reflection coefficient is close to 1.0 in the calculation as shown in Fig. 7. We cannot find such a high reflection coefficient in careful measurements, however it is better to avoid the frequency band near the cut-off frequency.
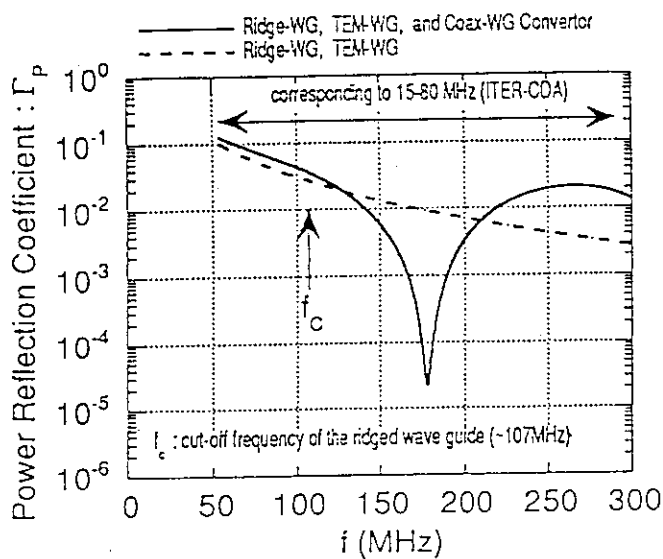
Fig. 6 Power reflection coefficient of the mock-up model of the ceramics-free antenna support with coax.-waveguide converter. Effect of the imperfect impedance transformer is removed by calculation. The reflection coefficient is low enough for a antenna support even below the cut off frequency of the ridged waveguide.
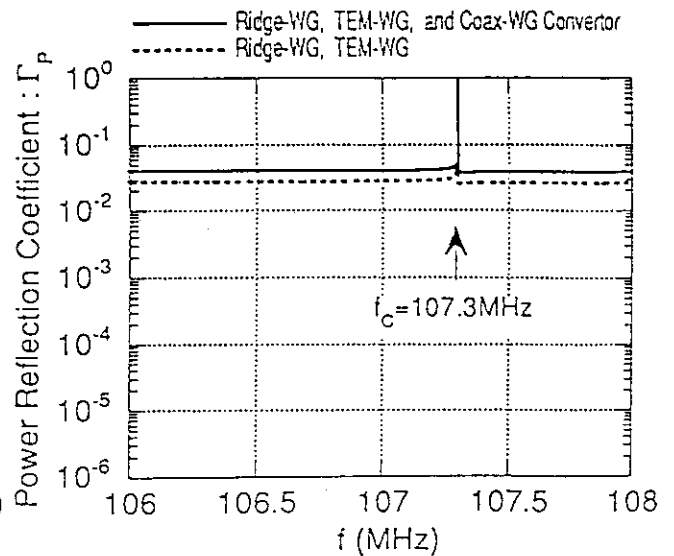
Fig. 7 Enlargement near the cut-off frequency of the ridged waveguide. In calculation, the reflection coefficient is ~1.0 near the cut-off frequency.

Summary

We have proposed a ceramics-free antenna feeder line employing a ridged waveguide as a local support for IC antenna of next-generation tokamaks. One fourth mock-up model of the all metal waveguide designed for the ITER ICRF system is fabricated and electrical characteristics of the model including the coaxial line - waveguide converter are measured. Power reflection coefficient of the model including the coax-waveguide converter to the input coaxial line is estimated to be less than 15% below the cut-off frequency of 107 MHz and less than 3 % above the cut-off frequency. It is found that this ceramics-free antenna support employing a ridged waveguide is quite available for IC antenna of next-generation tokamaks.

Reference

1) H. Arai, H. Kimura, T. Fujii, M. Saigusa, and S. Moriyama, "A Ceramics-Free Waveguide for ITER Ion Cyclotron Wave System," IEEE Trans. Plasma Sci., vol. 21, pp. 265-270, June, 1993.

2. Lower Hybrid Range of Frequecies

2. 1   Performance of LHCD Launchers on JT-60U

Y. Ikeda, M. Seki, O.Naito, S.Ide,T.Kondoh, S.Maebara, K.Ushigusa and T.Imai

JAERI, Naka Fusion Research Establishment
Naka-machi, Naka-gun, Ibaraki-ken,Japan

Abstract

A 48x4 multijunction launcher (CD-2) has been operated to drive plasma current up to 3.6MA on JT-60U in addition to the 24x4 multijunction launcher (CD-1'). The CD-2 launcher employs the oversized waveguides to simplify the LH launching structure. A maximum power density at $25MW/m^2$ has been achieved on the CD-2 launcher after a few weeks operation without differential pumping system. The total injected power is up to ~7MW using the CD-2 and CD-1' launchers. A good coupling is obtained on the CD-2 launcher around 1~5% when the plasma-wall distance is around 100mm. The current drive efficiency and profile controllability are well explained by the designed wave spectra without taking account of higher modes in the oversized waveguide. The maximum drive efficiency is $3.5x10^{19}A/m^2W$. Thus, the availability of the simple LHCD launcher has demonstrated to perform high power LHCD experiments on JT-60U.

1. Introduction

The required LH power in the next step tokamak is in the range of ~50MW at the frequency of ~5GHz. The number of several thousands waveguides is demanded for the LH launcher, because the empirical power density of the launcher is in the range of 30~50MW/m^2[1]. Therefore, it is very important to simplify the LH launching structure. A application of the oversized waveguide to the launcher is one of the most promising method to simplify the LH system. On JT-60U, a new 48x4 multijunction launcher (CD-2) with oversized waveguides has been developed to carry out high power LHCD experiments up to ~10MW in addition to a 24x4 multijunction launcher (CD-1') [2][3]. The CD-2 launcher consists of 4 (toroidal) x 4 (poloidal) multijunction modules, in each of which the RF power is divided toroidally into 12 sub-waveguides at a junction point through a oversized taper waveguide. Each module is driven by a klystron without circulator and power dividers in the transmission system.

2. CD-2 launcher

2.1 LHCD system of JT-60U

The LHCD system of JT-60 was established to generate the RF power up to 24 MW by using three amplifier units (unit A,B,C)[4]. On JT-60U, the maximum available power has been reduced to be in the range of ~15MW because the klystron often suffers from the degradation of stand-off voltage in the electric gun due to the evaporation of cathode material after long operational period. The frequency and power can be independently controlled on each unit. The unit C feeds the RF power to the CD-1' launcher, in which the RF power is divided into 4 lines in transmission line and is divided into three in the multijunction module. The unit A and B feed the RF power to the lower and upper 8 multijunction modules of the CD-2 launcher without power divider in the transmission line as shown in Fig.1.

2.2 Characteristics of the CD-2 launcher

The CD-2 launcher is featured by the simple multijunction structure with oversized waveguides. The RF power in the module is guided from the standard waveguide to a taper-oversized waveguide and then divided toroidaly into 12 sub-waveguides. The effect of higher modes in the oversized waveguide has been studied in a mock-up test module and shown that RF properties of the module is well explained by the theory without taking account of higher modes as far as reflection coefficient of the sub-waveguide is lower than ~10%. The sharp wave spectra are expected as $N_{//}{}^{peak} = 1.5$, 1.7 and 2.3 at f=2.23, 2 and 1.74GHz as shown in Fig.2. The wave spectrum of the CD-2 launcher, where the number of sub-waveguide in toroidal direction is considerably

larger than that of the multijunction module, is well understood as the combination of the wave spectrum of a 12-divided multijunction module and a 4-waveguide array.

The other feature of the CD-2 launcher is to disuse a differential pumping system. A high baking up to 250°C is available during operation to reduce the outgassing from the launcher. The launcher is protected against RF breakdowns by two alarm systems as shown in Fig.3. One is to detect RF breakdowns by a large mount of reflected power to the klystron from the launcher. Each RF power of the klystron is turned off when the reflection power beyond 100~200kW, and is restarted after 100ms interval. The other is to detect RF breakdowns in the launcher by a lightning. There are two light detectors on the module (L_1 and L_2). The L_1 turns off whole RF power of the unit when it detects the lightning at the windows. The L_2 is used in the case of RF conditioning without plasma, because it sometimes misdetects the light from plasmas without RF breakdowns.

3. Operational results

3.1 Power handling and outgassing

A very quick conditioning has been obtained up to 3.4MW on unit B within 2-week operation. The maximum injected power is limited by the stable output power of the klystron. The injected power of the unit A is limited by a poor coupling. The total injection power is achieved up to ~7MW using CD-1' and CD-2 launchers. The corresponding power density of the CD-2 launcher is 25MW/m^2 for the unit B even though there is no differential pumping system. Table I shows the summary of the power handling achieved in 1993.

The outgassing was measured by an ion gage equipped on the vacuum waveguide near the window. The outgas from the waveguide flows to JT-60U tokamak. The pressure rise is considerably reduced shot by shot. The strong power dependence of the outgassing was observed at the initial stage. On the contrary, the power dependence become week after enough RF conditioning as shown in Fig.4. Finally, the pressure rise is saturated within 1~2 sec. during long pulse injection. The outgassing rate is estimated around 10^{-5}~10^{-6}Pam^3/sm^2 at the operational temperature of 250°C. This value is in the same level as that of the test modules of CEA-JAERI and TdV[5]. This results indicates that a small pumping system is enough to evacuated the LHCD launcher

3.2 Coupling

The coupling was studied by changing the plasma and launcher positions. A good coupling of the reflection coefficient ρ~2% is obtained on Unit B (upper modules) when the plasma-wall distance is around 100mm at the launcher position of ~10mm behind the wall. However, A poor coupling of ρ~20% is observed on Unit A (lower modules) at

the same conditions. This is due to the discrepancy of the curvature of launcher mouth and the wall, because a coupling is improved by moving launcher ~5mm ahead.

The phase dependence of the coupling is well explained by the theory without higher modes in the oversized waveguides when the coupling is good. Figure 5 shows the reflection coefficient of Unit B as a function of phase between adjacent modules, where Ip=1.2MA, ne=1x10^{19}m^{-3}. The density profile in front of the launcher are assumed as $n_{e,edge}$ = 5x10^{17}m^{-3}, $\nabla n_{e,edge}$ = 5x10^{19}m^{-4} in thoery.

A degradation of coupling in H-mode is observed, however, a good coupling is obtained at ρ~3% in the case of high frequency ELMy phase.

3.3 Heat load

The infrared TV and visible CCD TV camera systems are used to investigate heat load and RF breakdowns on the launcher mouth. The CD-2 launcher is located at the mid-plain, so the infrared view is obtained by using two mirrors. To obtain a whole view of the launcher mouth, the surface of the 1st mirror is designed to be sharped. Since the temperature calibration has not been done, the absolute heat load has not been obtained. However, it is very useful to investigate the thermal condition of the launcher operation.

On the LHCD experiments, bright is usually observed in front of the launcher in the visible camera. The temperature of the launcher mouth is in proportion to the pulse duration. When the temperature locally increases on the launcher mouth, the local brightening is also observed on visible view, and then RF breakdown occurs. It is not clearly understood that the temperature effect on the RF breakdown, it may be important to reduce the hot spot on the launcher mouth. On the contrary, the temperature rise depend on the plasma density and the LH injected power in the case of no RF breakdown. Figure 6 shows the temperature rise rate normalized by the P_{LH} and density.

In the case of the combination experiments of LH and ICRF, the temperature increases on the ion side of the launcher. The temperature rise rate normalized by the injected ICRF power is much higher than that of the LH alone. Moreover, strong brightening is not observed on the high temperature point. Therefore, this temperature may be due to the bombardment of fast ion. The toroidal ripple effect of the JT-60U is around 2% near the LH launcher mouth, therefore, a large heat load mainly occurs due to the ripple effect.

4. LHCD experiments

4.1 Wave spectrum controllability

On the CD-2 launcher, the wave spectra can be controlled by changing phase between adjacent module and frequency. At first, we investigate the wave spectrum of

the multijunction module with oversized waveguide. The $N_{//}^{peak}$ is expected 2.3, 1.7 and 1.5 at the frequency of 1.74, 2,and 2.23GHz, respectively. Figure 7 shows the change of the internal inductance Δli deduced from Shafranov lambda and diamagnetic βp during LH injection. Since the peaked current profile was obtained by injecting LH wave with lower $N_{//}$ at higher frequency, the wave spectrum from the multijunction module is consistent with the designed wave spectrum.

The phase dependence of the current drive efficiency is also studied by using whole modules. Figure 8 shows the drive efficiency, the weighted $N_{//}$ spectrum $<N_{//}^{-2}>$ and Hard X-ray temperature as a function of the phasing, where the $<N_{//}^{-2}>$ is given by [6],

$$<N_{||}^{-2}> \equiv \frac{\int_{N_{1ACC}}^{+\infty} P(N_{||})/N_{||}^2 dN_{||} - \int_{-\infty}^{N_{1ACC}} P(N_{||})/N_{||}^2 dN_{||}}{\int_{-\infty}^{+\infty} P(N_{||})dN_{||}}$$

The phase dependence of the drive efficiency is well explained by the $<N_{//}^{-2}>$. These results indicate that the simple multijunction launcher surly excites the expected wave spectra.

4.2 High power LHCD

Figure 9 shows the performance of the current drive experiments on JT-60U. The maximum driven current is achieved up to 3.6MA with taking account of change of li. The current drive efficiency is improved by increasing plasma current and is $3.5 \times 10^{19} A/m^2 W$.

5. Future plan

We have started the concept study of the JT-60 super upgrade to demonstrate high efficiency steady state operation with high inject power[8]. The main feature is to drive plasma current up to 10MA for the pulse duration up to 200 sec. ~ 1hour. The LH system is one of the candidate to drive plasma current and control profile control. The technical key of the LH system is to develop the high heat resisting launcher against the heat load under the steady-state plasma.

We plan to deign the launcher which is composed of compact multijunction module with oversized waveguide. The septum plate of the module is of dispersion strengthen copper (DSC) to remove thermal load. The head of the septum is plan to use carbon material or Mo for high heat resisting property. We have succeeded to fabricate the brazing between carbon and copper plate, and diffusion bonding of DSC and SS.

Therefore, we will be able to fabricate the multijunction launcher using carbon or Mo, which will have reliability under the stead-state operation.

6 Conclusion

The performance of the CD-2 launcher is presented. This LH launcher is consists of 4x4 mulitijunction modules, in which RF power is divided into 12 sub-waveguides using oversized waveguide. The application of the oversized waveguide to the LH launcher considerably simplify the LH launcher. The power handling, coupling and wave spectrum of the CD-2 launcher show good values, therefore, it will be usefully in next step LH launcher. Moreover, the simple structure enable the application of high thermal resisting material such as carbon, Mo to the launcher septum for steady state operation.

Acknowledgement

References

[1] V. Parail et al., ITER Current Drive and Heating System, ITER Documentation Series No.32.

[2] Y. Ikeda et al., Proc. 14th SOFT, Vol.1 (San,Diego,1991) 122.

[3] M. Seki et al., Proc. 16th SOFT, Vol.2 (London,1990) 1060.

[4] T. Nagashima et al., Fusion Eng. Design 5(1987)121.

[5] G.Ray et al., Proc. 10th Topical Conf. on Radio Freq. Power in Plasmas, (Boston,1993).

[6] F.Lueterer et al., Nucl. Fusion 31(1991)2315.

[7] F.X.Söldner et al. Proc. 13th Int. Conf. on Plasma Phy. and Contr. Nucl. Fusion Res. (Washington, DC, 1990) 613.

[8] M.Nagami, et al., 17th SOFT, (Rome,1992).

Table I

		Max. injected power [MW]	power density [MW/m^2]	limitation	total injected power [MW]
CD-2	Unit A	2.5	18	poor coupling	1.8
	Unit B	3.4	25	klystron	3.3
CD-1'	Unit C	2.6	22	breakdown (no-baking)	1.8
Total					~7
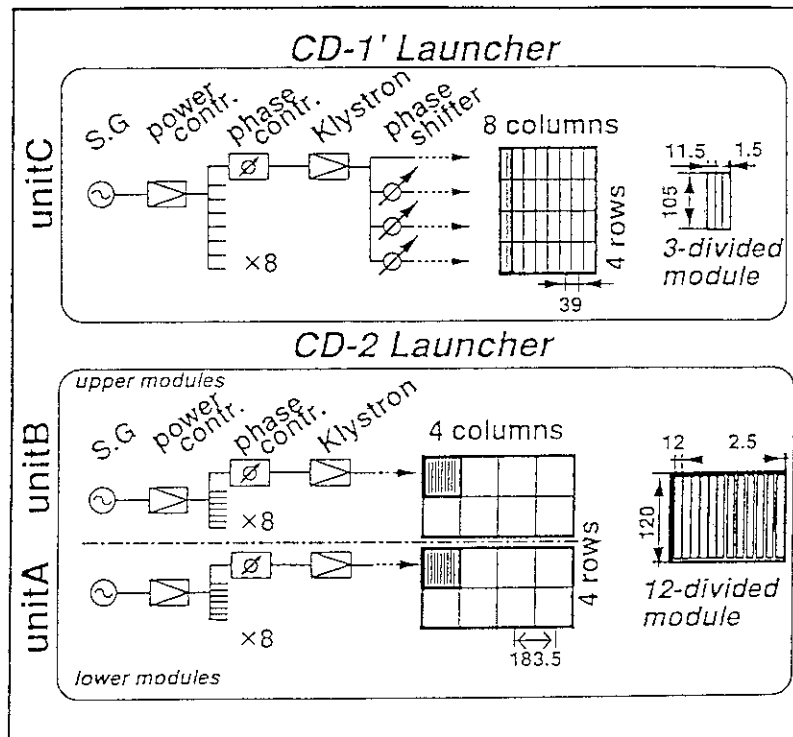
Fig. 1: LHCD system of JT-60U
Unit C feeds RF power to CD-1' launcher,
Unit A,B feed RF power to CD-2 launcher.
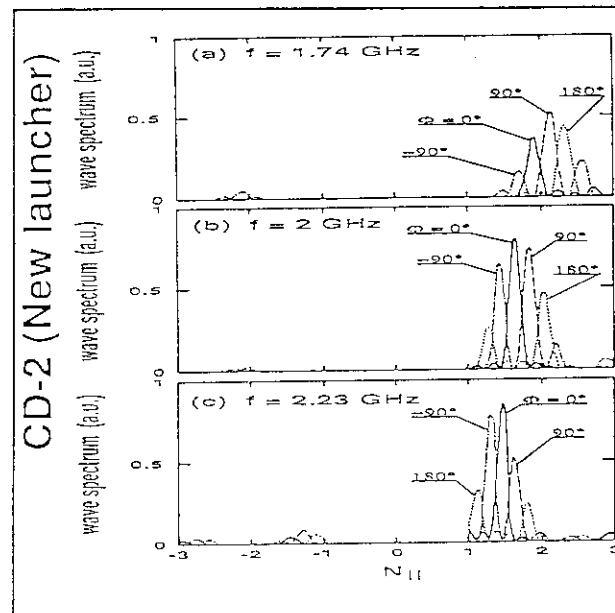
Fig. 2 : Wave spectra of CD-2 launcher
N//peak is widely controlled by frequency
with high directivity.
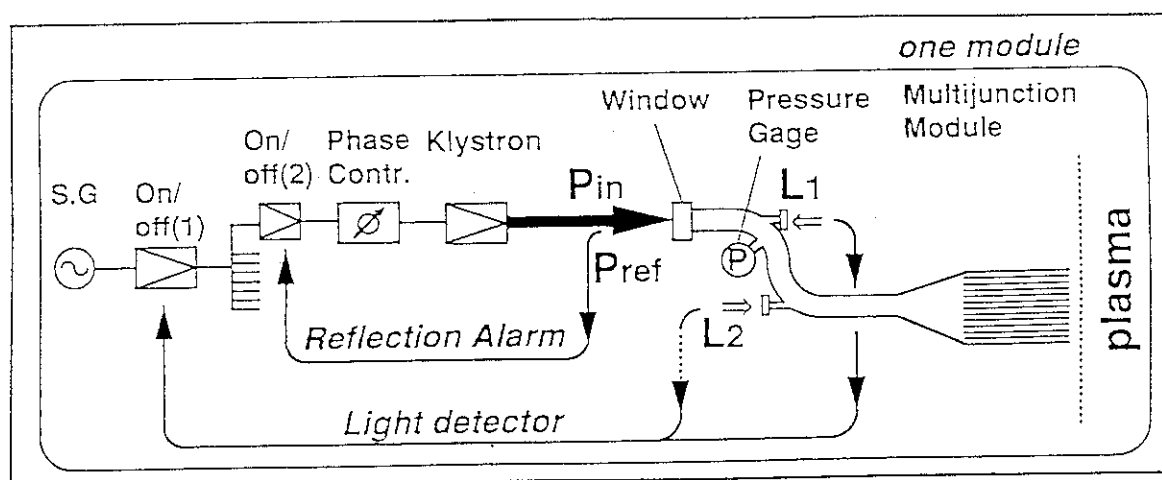
Fig. 3: Alarm system of CD-2 launcher
Reflection alarm and two light detectors protect
launcher against RF breakdowns.
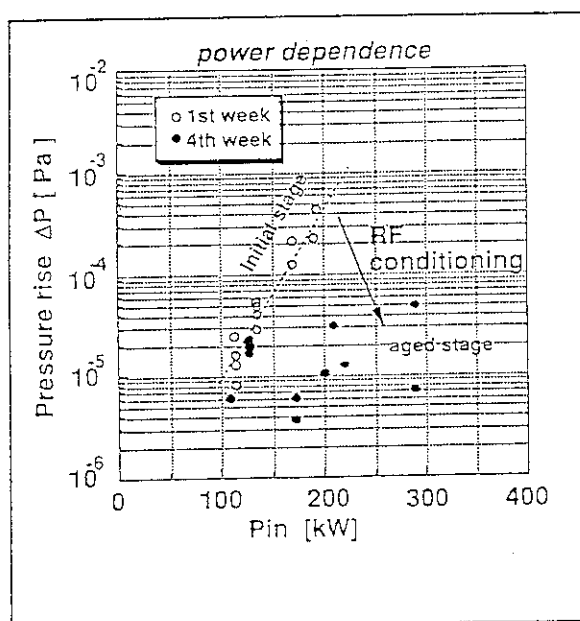
Fig. 4: RF conditioning of outgassing
○; initial stage, ●; aged stage
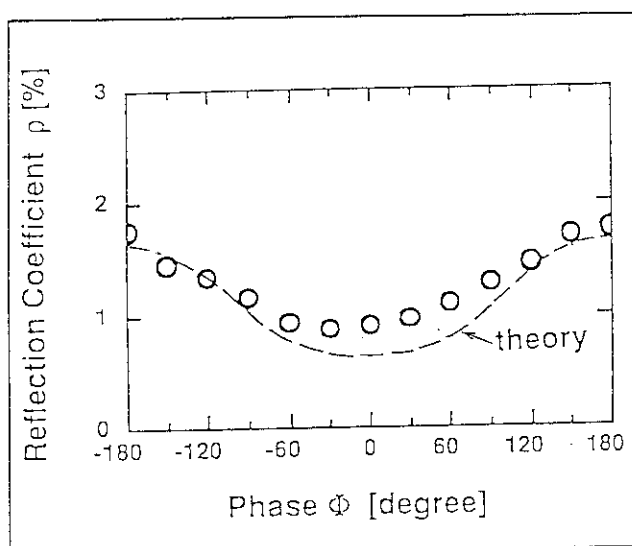
Fig. 5: Phase dependence of coupling
$n_{e,edge} = 5 \times 10^{17} m^{-3}$, $\nabla n_{e,edge} = 5 \times 10^{19} m^{-4}$
are assumed in theory.
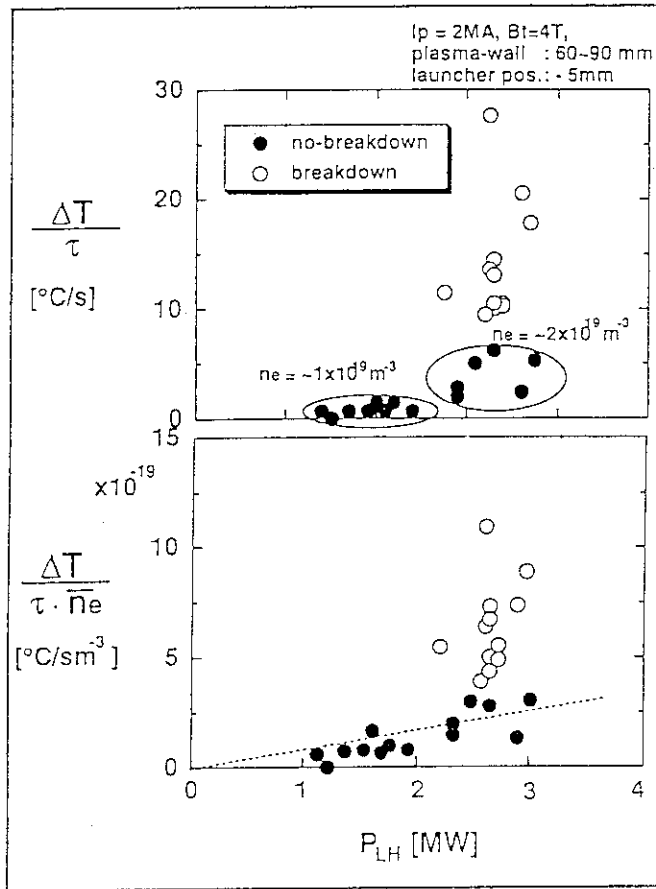
Fig. 6 Temperature rise rate during LHCD
● ; no-breakdown at mouth,
○ ; breakdown at mouth
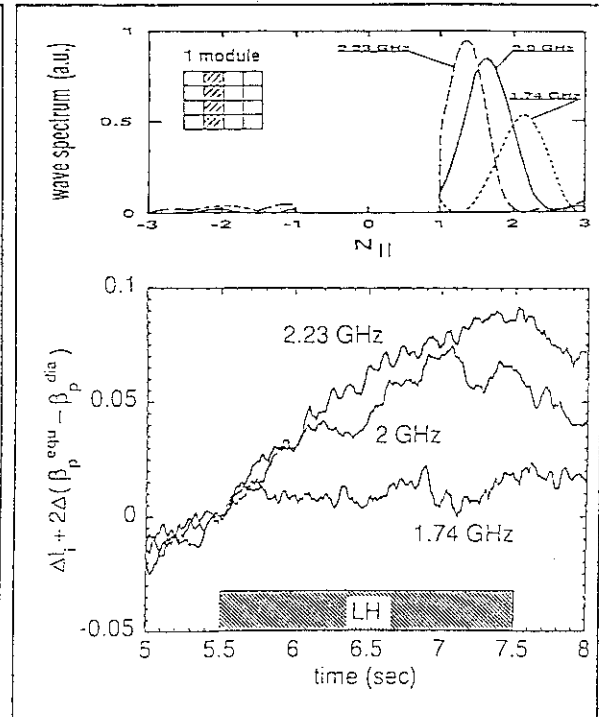
Fig. 7: Change of Δli during LHCD
One module in toroidal direction is used to inject RF power. Wave spectra are controlled by frequency.
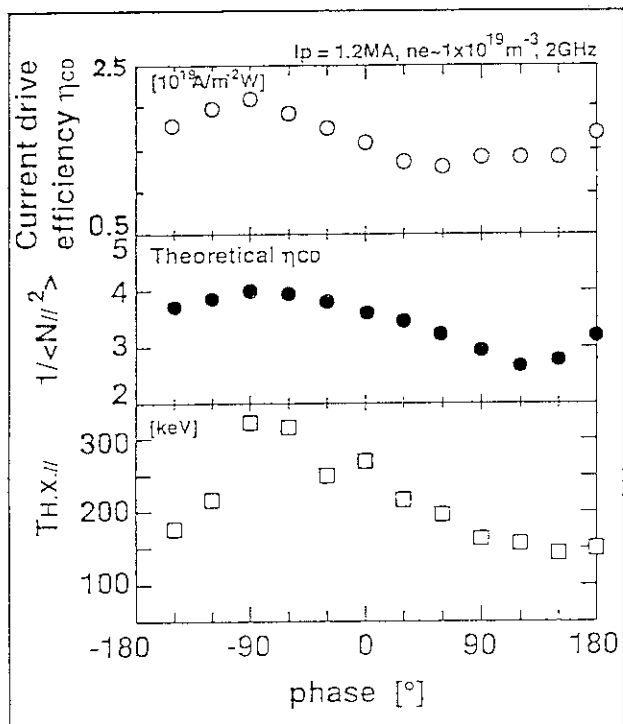
Fig. 8: Phase dependence of current drive efficiency
○ ; drive efficiency,
● ; $<1/N_{//}^{-2}>$,
□ ; X-ray temperature.
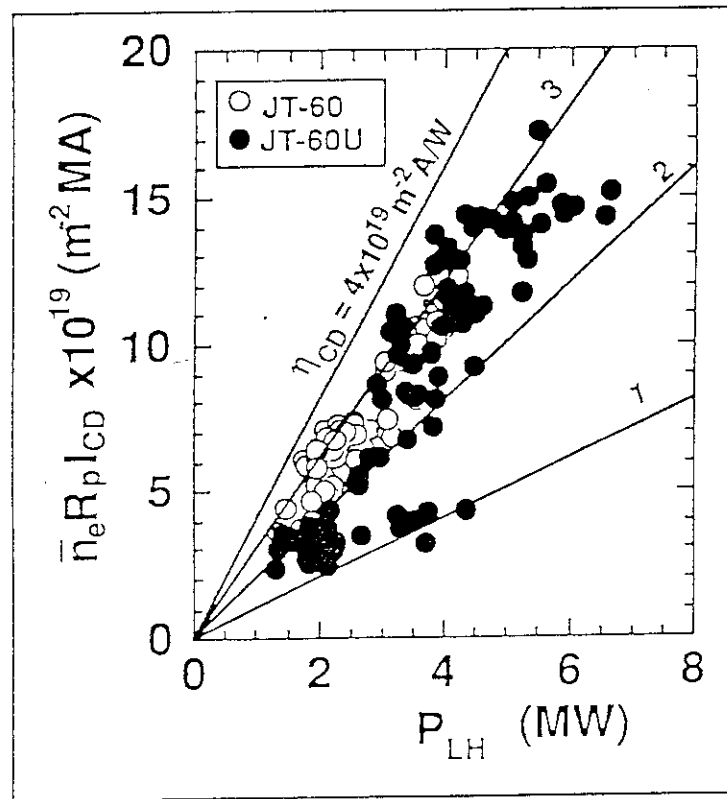
Fig. 9: Pregress of LHCD

2. 2　Full-Wave Theory
of a Quasi-optical Launching System
for Lower-hybrid Waves

F. Frezza[*], F. Gori[○], M. Santarsiero[○], F. Santini[□], G. Schettini[*]

[*]　Dip. di Ingegneria Elettronica.Università "La Sapienza".Roma. Italy

[○]　Dip. di Fisica. Università "La Sapienza". Roma. Italy

[□]　Associazione EURATOM-ENEA sulla Fusione. C.R.E. Frascati. Italy

ABSTRACT

Numerical studies on the use of a quasi-optical grill to couple lower-hybrid waves to a plasma, for current drive in tokamaks, are currently under development. The study of the coupling has been carried out in a rigorous way, through the solution of the scattering from cylinders with parallel axes in the presence of a plane of discontinuity for electromagnetic constants. Here we restrict our attention to the case of a plasma with a step density profile, and report some results on launched spectra, coupled power, and directivity.

1. INTRODUCTION

When a beam of radiofrequency radiation is to be injected into a plasma for current drive purposes at the lower-hybrid frequency [1], one is faced with the problem that a propagating plane wave is completely reflected by the plasma. The solution is to use a coupling mechanism via slow waves. This is generally accomplished by a sophisticated arrangement of waveguides [2]. An alternative approach that has been proposed not long ago [3] is to produce slow waves by scattering at a grating made of, e.g., conducting cylinders.

A rigorous analysis of such a system is not easy because it entails the solution of a heavy scattering problem. The main difficulty arises from the presence of the plane reflecting surface. Indeed, solutions of the scattering problem from circular section cylindrical structures in homogeneous media are available [4,5]. In presence of plane interfaces solutions that hold in the limit of wires [6] are known. It is not possible to apply this approximation to the present case, because the radii of the cylinders are comparable with the operating wavelength.

It is possible to get a rigorous solution of the problem for an arbitrary plasma density profile by using the plane wave expansion of cylindrical functions [7]. The general features of the method have been presented elsewhere [8].

In the next paragraph the solution in the case of a constant density plasma is obtained; this approach leads to remarkable numerical simplifications with respect to the general formulation [8]. Numerical results will be given in the third section, while the last one is dedicated to future developments and conclusions.

2. N CYLINDERS IN FRONT OF A PLANE PLASMA SURFACE

Owing to the various geometrical features of the interacting waves and bodies, the imposition of the right boundary conditions is not a trivial task. To solve this problem it is customary to expand the diffracted field in terms of cylindrical functions, i.e., the product of a Hankel function of integer order H_n times a sinusoidal angular factor ($\exp(in\vartheta)$).

The problem consists in calculating the coefficients of the expansion of the field diffracted by every cylinder, in the presence of a plane surface with reflection coefficient $\Gamma(n_{//})$, in terms of the cylindrical functions. Such coefficients .can be determined imposing the right electromagnetic boundary conditions on the conducting surfaces; to this aim it is convenient to express the field in terms of cylindrical functions centered on the different cylinders.

Since the reflection properties of a plane of discontinuity for electromagnetic constants are generally known for incident plane waves [2,4], in order to get the rigorous solution it is essential the use of the analytic plane wave expansion of the above-mentioned cylindrical functions [7,8]. However, dealing with a constant plasma density n_o, the reflection coefficient Γ is independent from $n_{//}$ ($\Gamma=[(1-n_o/n_c)/(1+n_o/n_c)]^{1/2}$, with n_c = critical density) and it is possible to use a simplified formulation. In this case, it can be shown that the field is given by the diffraction of an incident wave on a structure formed by the real cylinders together with an arrangement of virtual cylinders specularly placed beyond the plasma surface, without taking into account the discontinuity surface (image method).

In this paper we consider a plane wave with wavevector k^i as the incident field. The linear polarization with the magnetic vector parallel to the axes of the cylinders has been chosen to properly launch a lower-hybrid slow wave. The notations used throughout the paper are those shown in fig. 1.

The magnetic field H_{tot} can be expressed as the sum of the following fields:

H_i: field of the incident plane wave;
H_r: field due to the reflection of H_i from the plane surface;
H_d: field diffracted by the cylinders;
H_{dr}:   field due to the reflection of H_d from the plane surface.

The H_i e H_r fields can be expanded in terms of Bessel functions J_n [4], while the diffracted field can be expressed as a sum of cylindrical functions with unknown coefficients c_{sn} (s=1,...,N where N represents the total number of cylinders). Moreover, the use of the image method
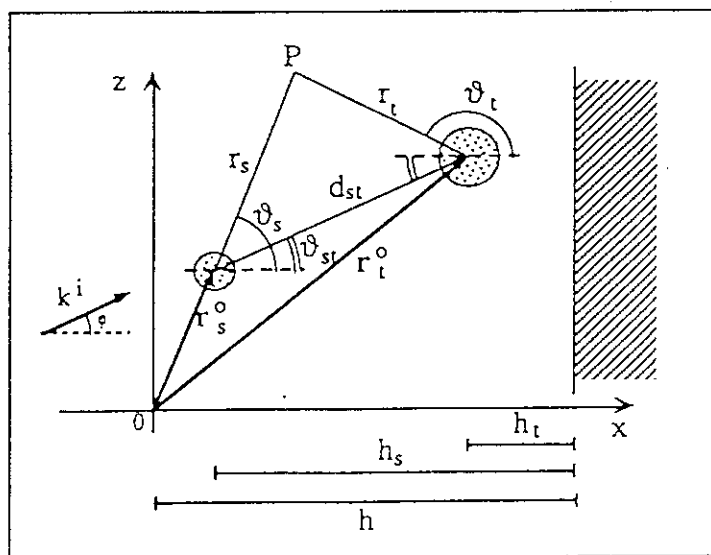
Fig.1. Geometry and notations used in this paper

allows to write:

$$H_{dr}(x_s, z_s) = \Gamma \, H_d(2h_s - x_s, z_s) \ . \tag{1}$$

By imposing the vanishing of the tangential component of the electric field on the cylindrical surfaces, we find the following linear system:

$$i^m \, e^{ik_{//}^i z_s^0} \left[e^{ik_{\perp}^i x_s^0} e^{-im\varphi} + \Gamma \, e^{-ik_{\perp}^i x_s^0} e^{im(\varphi-\pi)} \right] +$$

$$+ \sum_{t=1}^{N} \sum_{n} \left\{ \left[H_{m-n}\left(kd_{st}^{(1)}\right) e^{-i(m-n)\vartheta_{st}} + H_{m+n}\left(kd_{st}^{(2)}\right) e^{-i(m+n)\vartheta_{st}} \right] \left(1 - \delta_{s,t}\right) + \right.$$

$$\left. + \, G_n(ka_s)\delta_{m,n}\,\delta_{s,t} \right\} i^n \, e^{-in\varphi} \, c_{tn} = 0 \ , \tag{2}$$

where a_s is the radius of the sth cylinder, $\delta_{i,j}$ is the Kronecker symbol, $d_{st}^{(1)}$ is the distance between the sth and the tth real cylinder, $d_{st}^{(2)}$ is the distance between the sth real cylinder and the tth virtual one, and

$$\alpha = \sin^{-1}(n_{//}) \ , \qquad G_n(\xi) \equiv \frac{J'_n(\xi)}{H'_n(\xi)} \ . \tag{3}$$

The solution of such a system leads to the evaluation of the unknown coefficients c_{sn}; therefore the total magnetic field H_{tot} is fully determined.

To calculate the power flux toward the plasma core, i.e.

$$\Phi_x = \frac{kZ_0}{4\pi}\left\{ \int\limits_{|n_{//}|<1} |\sigma_H|^2\left(1-|\Gamma|^2\right)n_\perp dn_{//} - 2\int\limits_{|n_{//}|>1} |\sigma_H|^2 \Im m[\Gamma]|n_\perp|dn_{//}\right\} \quad , \quad (4)$$

we need the Fourier spectrum σ_H of the launched waves. The analytic evaluation of σ_H can be performed by using the plane wave expansion of the cylindrical functions [7].

In order to optimize the coupling efficiency it has to be defined the power of the incident wave. Since an ideal plane wave carries an infinite power, we consider only the power due to the portion of the plane wave corresponding to the width of the array of cylinders along the z-axis.

3. NUMERICAL RESULTS

The method outlined in the previous section has been applied to the evaluation of the diffracted field, the launched spectrum, and the coupled power in different experimental configurations.

As an example we consider an alignment of N identical cylinders of radius a with periodicity d and distance between the axes of the cylinders and the plasma surface D.

The shape of the coupled power spectrum is reported in fig. 2 for $N=20$, $ka=0.85$, $kd=2.9$, $\varphi=45°$, $n_0=2n_c$, $kD=1.1$: as can be seen, only the -1 and +1 orders carry a significant amount of power.
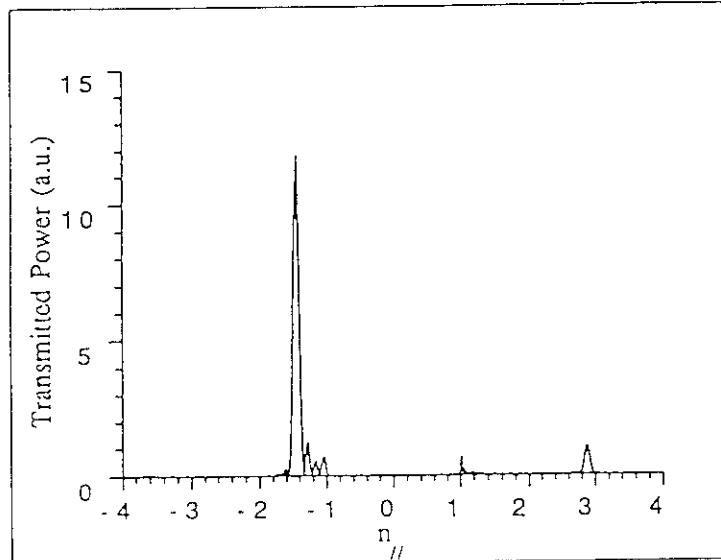
Fig. 2. Power spectrum ($N=20$, $ka=0.85$, $kd=2.9$, $\varphi=45°$, $n_0=2n_c$, $kD=1.1$)

In figs. 3,4 are reported the power reflection coefficient and the selectivity vs. the total number of cylinders (N) for different values of the periodicity of the grill. The selectivity has been defined as the ratio between the power coupled in the -1 order and the total coupled one.
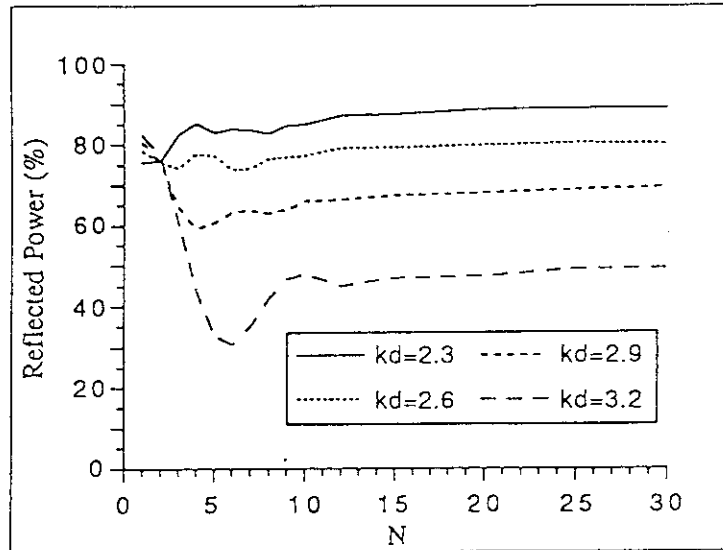
Fig. 3. Reflected power (ka=0.85, φ=45°, n_o=2n_c , kD=1.1)
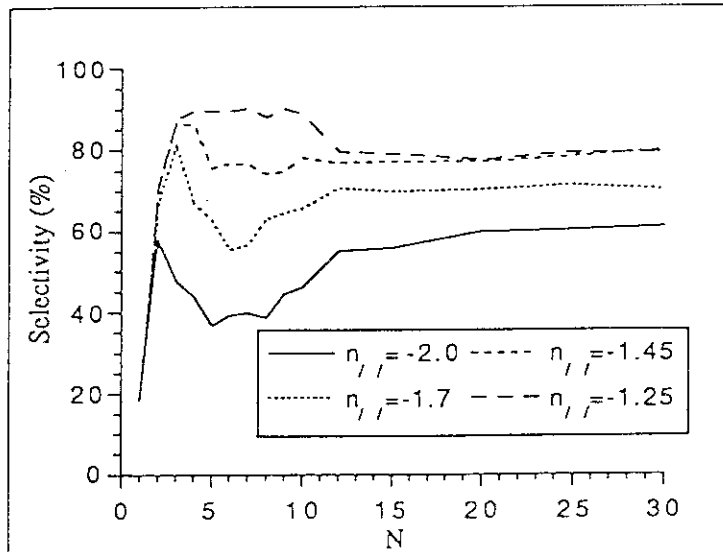
Fig. 4. Selectivity (ka=0.85, φ=45°, n_o=2n_c , kD=1.1)

In fig. 5 reflected power and selectivity of a single layer quasi-optical grill vs. the angle of incidence are shown, while in fig. 6 the same parameters are plotted vs. the normalized density n_o/n_c.

4. CONCLUSIONS

The numerical results of this work are relevant to the optimization of the single layer quasi-optical grill: the use of rods shaped in a different way could give better coupling results [9]. The aim of our analysis is a more realistic modeling, which needs the use of incident fields different from plane waves and the presence of metallic side walls. For instance, a gaussian beam can be assumed as the incident wave: such a beam can actually be transmitted from a radiofrequency generator to the grill in the form, e.g., of a HE_{11} mode of a corrugated waveguide. On the other hand, metallic walls can be simulated by means of a suitable set of wires [10], thus allowing us to use the method outlined in this paper.
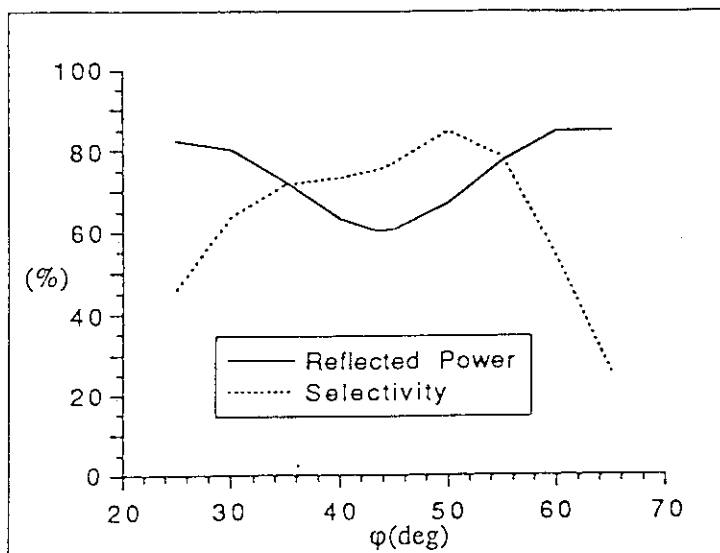
Fig. 5. Coupling parameters (N=5, ka=0.85, kd=2.9, $n_o=2n_c$, kD=1.1)
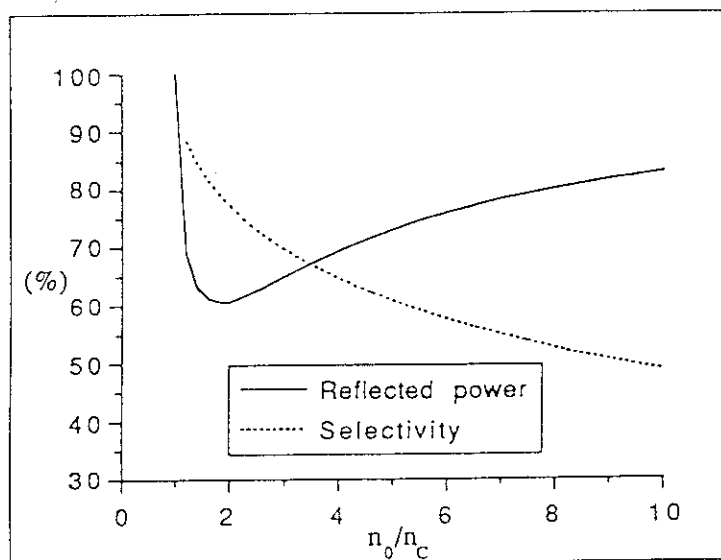
Fig. 6. Coupling parameters (N=5, ka=0.85, kd=2.9, $\varphi=45°$, kD=1.1)

REFERENCES

1. R.A. Cairns, *Radiofrequency Heating of Plasmas*, Adam Hilger, Bristol 1991
2. M. Brambilla, Nucl. Fusion **16**, 47 (1976)
3. M.I. Petelin, E.V. Suvorov, Sov. Tech. Phys. Lett. **15**, 882 (1989)
4. C.A. Balanis, *Advanced Engineering Electromagnetics*, J.Wiley & Sons, NY 1989
5. H.A. Ragheb and M. Hamid, Int. J. Electronics **59**, 407 (1985)
6. J.R. Wait , Can. Journal of Physics **32**, 571 (1954)
7. G. Cincotti, F. Gori, M. Santarsiero, F. Frezza, F. Furnò, G. Schettini, Optics Comm. **95**, 192 (1993)
8. G. Cincotti, F. Gori, M. Santarsiero, R. Serrecchia, F. Frezza, G. Schettini, and F. Santini, Proc. of the 10th Topical Conference on RF Power in Plasmas, Boston 1-3 April 1993
9. E.V. Suvorov, N.F. Kovalev, private communication
10. J.H. Richmond, IEEE Trans. MTT-13, 408 (1965)

2. 3   Lower Hybrid Launcher on JET

F.X. Söldner, M. Brusati, A. Ekedahl, Ph. Froissard, C. Gormezano, J. Jacquinot,
A. Kaye, M. Lennholm, J. Plancoulaine, F. Rimini, Ph. Schild

JET Joint Undertaking, Abingdon, Oxfordshire, OX14 3EA, UK

ABSTRACT

Lower Hybrid current drive (LHCD) experiments were performed in JET in a first stage with one third of the final LHCD system. Good coupling with reflection coefficients as low as 1% and a power density of ~4 kW/cm^2 on the plasma interface were obtained with the prototype launcher. The complete LHCD system with a total power of 12 MW (20 s) in the generator will start operation with the begin of JET divertor experiments in early 1994. The full launcher contains an array of 384 waveguides, built up from 48 multijunctions with internal power splitting. Three different LH wave spectra can be radiated simultaneously into the plasma, applying different phase settings to the three independent sections of the grill type antenna. Testbed experiments have started on a new concept for a compact LH launcher, using a hyperguide as connection between an array of standard size waveguides and the plasma facing antenna structure which forms the slow wave LH spectrum.

1. INTRODUCTION

Lower Hybrid current drive (LHCD) on JET aims at active control of the plasma current profile. It provides the potential for steady state operation in high confinement modes, together with the other sources for noninductive current drive (Fast Wave Current Drive, Neutral Beam Injection, Bootstrap Current). An LH system with a total power of 15 MW in the generator was built up with 24 klystrons at a frequency of 3.7 GHz /1/. First experiments were performed with a prototype launcher (L0), delivering up to 2.4 MW power coupled to the plasma from 8 klystrons. With the addition of 1.5 MW LHCD power during the Ohmic current ramp-up a flux of 2 Vs could be saved. The full plasma current was driven by LHCD alone in a 0.4 MA discharge. In combination with Ion Cyclotron Heating (ICRH) a discharge with 2 MA plasma current could be sustained for 1 minute. Record current drive efficiencies were obtained due to synergy with ICRH, with values up to $\eta_{CD} = 0.44$ (10^{20} Am^{-2}W^{-1}) /2/. This comes already close to the requirements for an application of noninductive current drive to reactor grade plasmas like in ITER. Future systems with a large number of rf tubes at high power, however, need also a further simplification in the power transmission and the coupling structure.

This paper describes the layout of the LH launcher system, operational experience with the prototype antennae and new technical developments of a compact power transmission system on JET.

2. LAYOUT OF THE JET LHCD LAUNCHER SYSTEMS

The LH power is supplied by a plant of 24 klystrons with a maximum power output of 650 kW each, at 3.7 GHz /3/. The launcher is fed through 40 m transmission lines containing slightly oversized waveguides (77.2 x 38.6 mm). At the front end an array of narrow waveguides (72 x 9 mm internal dimensions, 2 mm walls), the so-called grill, radiates slow LH waves with a parallel refractive index $N_\parallel > 1$ into the plasma. The design of the LH system on JET is heavily influenced by the constraints arising from the final tritium phase. All penetrations into the primary torus vacuum need double tritium tight barriers. No electronics can be used inside the torus hall. All components in the torus hall have to be radiation resistant. All maintenance and repair has to be carried out remotely by robots. Specific solutions had to be developed therefore for many parts. A high degree of reliability is required for all systems and operations control is being automated to a maximum.

2.1. General Features of the JET LH Launcher

The different components are seen from Fig. 1. The power of each klystron is split after the penetration into the torus hall into 2 lines in a hybrid junction, with high power (250 kW/dc) loads on the fourth port. Three flexible joints in each transmission line provide a stroke of 300 mm for displacements in the radial direction of the JET torus. Double BeO pill box windows of a quarter wavelength thickness separate the pressurised transmission lines (2 bar SF_6) from the torus vacuum (10^{-7} mbar). The interspace is kept at UHV by ion getter pumps. Arc detectors monitor the vacuum side of the rf windows. A focusing optics transmits eventual light emission from the window surface through a fiber onto diodes outside the torus hall. After the vacuum transition the power is split from each input waveguide into 8 narrow size output waveguides within multijunction modules as shown in Fig. 2. The incoming forward power is first split vertically into two superposed lines in an H-plane junction and then further divided horizontally in each level into 4 narrow waveguides by E-plane junctions. The phase between horizontally adjacent waveguides is set at 90° by step transformers. The fourth port in the H-plane junction is fitted with a vacuum matched load in order to maintain equal vertical power distribution in the case of imbalanced reflection. The multijunctions are manufactured from stainless steel and internally coated with a 15 μm Cu layer. The whole stack of multijunctions is tightened together by a rigid frame inside a vacuum vessel connected to a main port (0.9 m high x 0.4 m wide) of the JET torus vessel by 1.5 m diameter double-walled inconel bellows. This allows a radial movement of the whole launching structure. The front end of the launcher is curved toroidally and poloidally to match the shape of the plasma surface. The plasma facing waveguide walls are protected against excessive energy deposition from direct plasma contact by a surrounding frame of shaped carbon tiles. They protrude the waveguides by 2.5 mm. The details of the waveguide array are described in sections 2.2 and 2.3 for the different types of launchers used on JET. The whole launcher is bakeable to 500° C for outgassing. Gas released from the inner walls of the waveguides during LH power transmission is removed through holes in the waveguides by a cryopump with 100 000 l/s pumping speed.

Coupling of the LH waves is determined by the electron density and the density gradient in front of the launcher. Therefore the proper distance between plasma and antenna structure has to be adjusted. This is obtained on JET by separate control of the launcher position and the plasma position. The launcher can be moved radially with a stroke of 210 mm during shots by means of a hydraulic position control system /4/. Hydraulic actuators move the launcher against a reaction flange fixed onto the main torus port (Fig. 1). Fail-safe operation is provided by three independent systems: An offset system consisting of three cylinders equally spaced around the launcher balances a 20 t vacuum load tending to pull the launcher (weight: 15 t) into the port. A servo system of 2 cylinders accelerates the launcher radially. A protection system of three adjustable legs buffers excessive travels and limits the innermost position. The launcher can be positioned through pre-programmed waveforms or in feedback controlled operation, using the reflection coefficient from selected waveguides or an average value for the error signal. With the active position control working in a closed loop, a static position accuracy of 0.3 mm is achieved. The system has a closed-loop resonant frequency of ~4.5 Hz, a maximum acceleration of 5 ms^{-2}, a maximum velocity of 100 mms^{-1} and a response time of 0.2 s to small amplitude steps. Fast changes of the plasma parameters in front of the launcher can be accommodated also by a second feedback loop which acts on the plasma position instead of the launcher position. Both loops operate with different time constants. They can be nested in order to provide flexible real time coupling control in a wide range of plasma discharge parameters.

2.2. The JET Prototype LH Launcher (L0)

The prototype launcher consists of two different stacks of multijunctions, denoted module L0C (Launcher Zero Cadarache, built by CEA Cadarache) and module L0P (Launcher Zero Physics, built by JET) /5/. The characteristics are summarised in Table 1. The multijunctions of module L0C are manufactured of zirconium copper. The multijunctions of module L0P are made of copper plated stainless steel. The internal walls of both types of multijunctions are coated with anti-multipactor layers of carbon. During operation the front ends were also coated with a beryllium layer by the evaporators located inside the JET vessel near the LH launcher. The plasma facing front end of module L0P is radially 5 mm behind that of module L0C. All multijunctions contain phase shifters which provide $90°$ fixed retardation between adjacent waveguides. Phase adjustment with a high precision of $10°$ was achieved for the whole system by careful control of all mechanical dimensions and by feedback control of the phase on each klystron. One third of the final LH generator was used for the experiments with the prototype launcher. Each module is powered by four klystrons, with the two superposed multijunctions fed by the same klystron each. Adjacent multijunctions each are connected to different klystrons. The phase between multijunctions is regulated with electronic phase control on the drivers in the low power stage. It was kept at $0°$ in all experiments with the prototype launcher. A directional wave spectrum with the maximum of the main lobe at $\overline{N}_\parallel = 1.84$ and a full width of $\Delta N_\parallel = 0.92$ between the minima on both sides of the main lobe is then radiated from module L0P. The wave spectrum of module L0C is shifted to slightly lower $N_\parallel$ values with the maximum of the main lobe at $\overline{N}_\parallel = 1.78$, due to 2 mm gaps between adjacent multijunctions. No vacuum pump was used yet on the vacuum vessel of the LH launcher during the first experimental campaigns with the prototype modules.

2.3. The JET full size LH Launcher (L1)

The first full size LH launcher (L1) for the LH system on JET has been completed now. It will be put into operation early 1994 with begin of the experiments in the new JET divertor configuration. The features of the launcher L1 are given in Table 1. The launcher is built up from 48 multijunctions of the same type as used in module L0P of the prototype launcher, but without C coating of the internal walls. All multijunctions were tested individually in vacuum up to 100 kW in 2s pulses. The multijunctions are put together into a rectangular array without leaving gaps in between on the plasma facing front end, to form a large grill type antenna occupying the whole surface area of one main port (0.9 m high x 0.4 m wide) on JET. The whole array contains 384 waveguides total, grouped in 12 rows with 32 waveguides per row. Six rows of multijunctions are stacked vertically, with eight multijunctions per row. The eight multijunctions in a row are fed by eight different klystrons. Two superposed multijunctions each are powered by the same klystron. The electronic phase control of the klystrons provides the possibility to vary the launched wave spectrum by adjusting the phase between the multijunctions in a row. With a variation of $\Delta\Phi = -90° - +90°$, the maximum of the main lobe of the spectrum is shifted in the range $\overline{N}_\parallel = 1.4 - 2.3$. Narrow spectra with a full width of $\Delta N_\parallel = 0.46$ are produced. Three different wave spectra can be launched simultaneously by applying three different phase settings to each of the two vertically linked rows of multijunctions each. A combination of three different spectra, launched with equal power at $\Delta\Phi = -90°$, $0°$, and $+90°$ is shown in Fig. 3. The spectral power density is plotted in section a, the running integral power in section b, and the running integral power weighted with $1/N_\parallel^2$ in section c. The latter quantity is proportional to the LH-driven current. The spectrum with $\Delta\Phi = -90°$ ($\overline{N}_\parallel = 1.4$) drives a plasma current about a factor 3 larger than the one driven by the spectrum with $\Delta\Phi = +90°$ ($\overline{N}_\parallel = 2.3$), as seen from Fig.3, section c.

3. OPERATIONAL EXPERIENCE

The launcher L0 was used on JET during a total of 12 months of LH experiments. The LHCD system operated in a wide range of plasma conditions, in limiter and X-point plasmas, in L and H modes, with plasma currents in the range 0.4 - 7 MA.

3.1. Power Handling

Baking of the narrow waveguide sections in the multijunctions by high duty cycle long rf pulses into vacuum turned out to be an efficient method of conditioning. Temperatures well above the normal values of 300° C during JET operation forced the outgassing of the internal walls of the waveguides. After a sequence with rf baking good power handling could be achieved. The conditioned status was maintained in the L0P multijunctions even after major vacuum leaks in the JET torus broken up during operation at around 300° C. The multijunctions of module L0C, on the other hand, did not recover to their previous status after the occurrence of the leaks. The rf losses in the multijunctions and the power absorbed in the loads in the fourth ports of the H-plane junctions were determined from the temperature increase measured with thermocouples in these sections. About 20% of the power reflected in the multijunctions back towards the transmission line is absorbed in the loads. The measured values of the losses agree well with the calculations for module L0P. In module L0C, however, about a factor four higher values than expected were found. This could be caused by imbalanced power distribution in the multijunctions due to the short circuit in the fourth port of the H-plane junction. The level of power transmitted without breakdown increased steadily during the twelve months of operation. The status of conditioning achieved was not lost during an intermittent period of seven months shutdown. At the end of the experimental campaign the maximum generator power of 600 kW could be transmitted with several klystrons. Launcher module L0P reached a total of 2 MW of 2.4 MW installed generator power.

3.2. Coupling

Coupling of LH waves from slow wave antenna structures into a plasma depends critically on the density and the density gradient in front of the antenna. The coupling of LH waves to JET plasmas was studied with launcher L0 in limiter and double null X-point configurations. The front end position of the grill was varied with respect to the position of the toroidal belt limiters and the protection limiters of the ICRH antenna next to the LH launcher in order to minimise the reflected power. Optimum coupling is expected for a density of $n_e = 1 \times 10^{18}$ m^{-3} in front of the launcher. The edge density profiles and the density decay length in the scrape-off layer differ strongly in the various plasma configurations, especially between limiter and X-point plasmas. The optimum distance between antenna front end and plasma boundary (last closed flux surface) depends therefore critically on the magnetic configuration. Higher reflection is found for launcher module L0P than for L0C. Module L0P is mounted 5 mm radially behind module L0C. A short density decay length is then expected in this region. The variation of the reflection coefficient with plasma - launcher distance is shown in Fig. 4 for different scenarios with launcher module L0P. Most favourable for good coupling are X-point plasmas. The weak dependence of the reflection on the antenna position in this case is due to the wider scrape-off layer and the longer radial density decay length. Reflection coefficients as low as 1% were then attained. In a 1MA H-mode discharge stable operation with low reflection of 3% on both modules L0P and L0C was maintained.

The radial electron density decay length is determined essentially by the parallel connection length $L_\parallel$ of the magnetic field line to the strike zone on limiters or divertor plates. For conditions with the launcher in front of the ICRH antenna, the connection length varies from $L_\parallel \approx 9$ m in the limiter configuration to $L_\parallel \approx 40$ m in the double null X-point configuration. In the

limiter plasmas the connection length is given by the distance along a field line between top and bottom belt limiters. In the X-point plasmas the connection length is given by the distance along a field line between two X points. With the launcher in the shadow of the ICRH antenna, the connection length between the two neighbouring ICRH antennae side limiters determines the density in front of the LH antenna. This results in low values of $L_{\parallel} \approx 4$ m. All dependences of the reflection coefficient on the launcher position can be represented in a universal curve if the radial density decay length in front of the LH launcher is related to the parallel connection length through perpendicular particle diffusion and parallel flow with the ion sound speed /6/. The reflection coefficient is then plotted versus the ratio of plasma - antenna distance d to the square root of the connection length $L_{\parallel}$ as shown in Fig. 5. The measured values of R are well reproduced by calculations with the SWAN coupling code as shown by the dashed curve, Fig.5.

Feedback control of the reflection coefficient could be achieved by controlling the position of launcher L0 in a closed loop. The temporal evolution injected power, reflection coefficient, line averaged density and launcher position in such a discharge are shown in Fig. 6. The requested reflection coefficient there was set to 10%. The launcher position could be adjusted by the feedback system within a range of $\pm$ 3 mm around the pre-set location of 4 mm behind the ICRH antenna. The gradual increase of the plasma density would have reduced the reflection coefficient. This was corrected for by retracting the launcher backward away from the plasma. The plasma position was kept constant in this case.

4. COMPACT LAUNCHER DEVELOPMENT

The new JET divertor configuration gives large flexibility in plasma shaping. Slim elongated plasma configurations, however, can not be matched with the actual LH launcher. The stroke of the radial movement is not large enough to approach the plasma boundary sufficiently for good coupling. This led to the development of a new concept of a compact launcher system which would allow the application of LH to a wide class of plasma configurations in JET. Design principle was the mechanical decoupling of the transmission line and the antenna structure in order to facilitate modifications of the front end and adjustment to the various plasma configurations. An extremely oversized waveguide, a so-called hyperguide, shall provide power transmission between an array of standard size waveguides and a plasma facing antenna structure which forms the slow wave spectrum radiated into the plasma /7/. The hyperguide cavity is strongly coupled to the emitting and receiving surfaces. It transfers power between the fundamental propagating TE_{01} modes on both sides through a TE_{0N} mode inside the hyperguide (N = number of rows of waveguides on both ends of the hyperguide). A high transmission coefficient into the TE_{0N} mode is required.

A code has been developed for the calculation of the wave propagation in the hyperguide. Arrays of waveguides are used for the emitter and the receiver. Both arrays have similar overall dimensions. They contain the same number of rows . The number of waveguides per row is larger on the receiver side, with smaller width than on the emitter side. Up to 200 modes (TE and TM) are treated in the hyperguide and up to 6 modes in each of the receiver waveguides. The properties of the hyperguide are characterised by the overall transmission coefficient Q_T and a mode quality factor Q_M defined as the ratio of power in the TE_{0N} mode to total incident power. Calculations were performed for arrays with 4 columns x 12 rows on the emitter side and 16 columns x 12 rows on the receiver side. The single waveguides are 72 mm high each, 34 mm wide on the emitter side and 7.7 mm wide on the receiver side, according to the dimensions appropriate for the 3.7 GHz LH system of JET. The results of several case studies are shown in Table 2. The vertical phase difference between superposed rows is set at $\Delta\Psi =$ 180°, with a random phase error of 0° in cases 1-3, 10° in cases 4-6 and 60° in case 7. In the ideal case without reflection all power is transmitted in the TE_{012} mode, also in the case of 10° random phase error. With a random phase error of 60°, the transmission coefficient is still high with 0.9. The mode purity, however, is not maintained in these conditions, as only 24% of the power are coupled to the TE_{012} mode. With 10% reflection from the receiver array (cases 2 and

5), only 5 % are reflected back into the emitter. Tripping of parts of the generator is simulated by inhomogeneous power distribution across the rows. Only rows 1-4 and 7-12 are powered in cases 3 and 6. The fraction of power in the TE_{012} mode is then reduced to 71-75% and the power distribution between different rows is strongly perturbed. The global transmission coefficient, however, remains above 90% with homogeneous distribution across the rows. The calculations show that the hyperguide should provide high power transmission in the selected TE_{0N} mode also in nonideal conditions as to be expected in the experiment and even in certain fault cases.

Testbed experiments have started with a low power prototype assembly of 1:1 scale for JET. The set-up is shown in the upper part of Fig. 7. An emitter array of 96 waveguides in 8 columns x 12 rows is connected to a receiver array of 288 waveguides in 24 columns x 12 rows with a hyperguide of 1.5 m length. The hyperguide is slightly tapered from 1019 mm high x 418 mm wide on the emitter side to 944 mm high x 403 mm wide on the receiver side. The dimensions of the waveguides on the emitter side are 76 mm high x 42 mm wide with 6 mm walls. The receiver is 300 mm long with waveguides 72 mm high x 12 mm wide and 3 mm walls. Emitter and receiver are manufactured in aluminium. The hyperguide is made of stainless steel plates. Phase shifters are placed in the receiver array to give a phase difference of 120° between horizontally adjacent waveguides. The emitter array is fed through a power splitting network from 6 solid state amplifiers of the same type as used to drive the JET high power klystrons, with 17 W each at 3.7 GHz. Loads are inserted into the receiver waveguides on the front end. Phase and amplitude of the waves inside the receiver are measured with probes in front of the loads. The mode structure in the hyperguide is determined from recording of the temperature distribution on the side walls with an Infra-Red camera. First measurements with an absorber plate in the place of the receiver show low reflection back to the receiver. No hot spots are seen with the Infra-Red camera on the hyperguide walls. Homogeneous temperature distribution and the heating of the absorber indicate good power transmission through the hyperguide.

The design of a high power hyperguide can be envisaged for the JET LH system after successful tests of the low power prototype. The implementation into the launcher is shown in Fig. 7, lower part. The actual stack of multijunctions would then be replaced by one single TE_{012} mode hyperguide.

The hyperguide concept presents several advantages over multijunction power splitting for the application to Lower Hybrid launchers in a reactor environment:
a) Mechanical decoupling of the transmission line and the launching structure allows remote handling maintenance and repair, including exchange of the plasma facing front end.
b) Reduction of the surface area of internal waveguide walls in the vacuum section facilitates conditioning and reliable power handling.
c) Extension of the length of the hyperguide gives the possibility to place the vacuum windows outside the radiation shielding of the machine.

5. CONCLUSIONS

High power transmission at maximum generator power level was obtained with the prototype LH launcher on JET. Feedback control of the launcher position allows maintenance of good coupling through dynamic adjustment to slowly varying plasma conditions during a discharge. The full launcher available now can transmit up to three different independent wave spectra. The hyperguide concept under study actually in low power testbed experiments provides a way to a compact reactor compatible LH launcher.

Table 1: LOWER HYBRID LAUNCHERS ON JET

1. Prototype Launcher L0 (1990 - 1992)

2 different multijunction arrays: modules L0C and L0P, each with 8 multijunctions.

1.1. Common features of the modules:

2 rows of multijunctions superposed with 4 multijunctions in each row.

Multijunctions contain 2 rows of waveguides vertically superposed, 4 waveguides per row.

Total number of waveguides per module: 16 per row in toroidal direction x 4 rows = 64.
Dimensions of narrow waveguides: height = 72 mm, width = 9 mm, wall thickness = 2 mm.
Surface area per waveguide: 6.48 cm^2, total surface area per module: 415 cm^2.

Phasing: $\Delta\varphi = 90°$ between adjacent waveguides in a multijunction,
         $\Delta\Phi = -90° - +90°$ between multijunctions.

Spectrum: $\overline{N}_{||} = 1.84$ with $\Delta\Phi = 0°$, $\overline{N}_{||} = 1.4 - 2.3$ with $\Delta\Phi = -90° - +90°$.
         $\Delta N_{||} = 0.92$ (full width between minima on both sides of the main lobe).

1.2. Specific features of the modules:

a) Module L0C (CuZr with C coating, short circuits in the 4th ports of the H-plane junctions):

Vertical gap between the 2 rows and toroidal gaps of 2mm between multijunctions.

b) Module L0P (Cu plated stainless steel with C coating, loads in the 4th H-plane junction ports):

No vertical gap, no toroidal gaps between multijunctions. 2 passive waveguides on both sides of each row of waveguides.

2. Full Size Launcher L1 (1993 -)

6 rows of multijunctions superposed with 8 multijunctions per row.
No vertical gaps, no toroidal gaps.

Multijunctions contain 2 rows of waveguides vertically superposed, 4 waveguides per row.

Total number of waveguides: 32 per row in toroidal direction x 12 rows = 384.
Additional 2 passive waveguides on both sides of each row of waveguides.
Dimensions of narrow waveguides: height = 72 mm, width = 9 mm, wall thickness = 2 mm.
Surface area per waveguide: 6.48 cm^2, total surface area of the coupler: 2488 cm^2.

Phasing: $\Delta\varphi = 90°$ between adjacent waveguides in a multijunction,
         $\Delta\Phi = -90° - +90°$ between multijunctions.

Spectrum: $\overline{N}_{||} = 1.84$ with $\Delta\Phi = 0°$, $\overline{N}_{||} = 1.4 - 2.3$ with $\Delta\Phi = -90° - +90°$. $\Delta N_{||} = 0.46$.

TABLE 2: HYPERGUIDE POWER TRANSMISSION CHARACTERISTICS

Case	Phase $\Delta\Psi$	Reflection	Rows fed	Q_T	Q_M
1	$180° \pm 0$	0	1 - 12	0.998	0.997
2	$180° \pm 0$	10%	1 - 12	0.95	0.91
3	$180° \pm 0$	0	1 - 4, 7 - 12	0.91	0.75
4	$180° \pm 10°$	0	1 - 12	0.99	0.98
5	$180° \pm 10°$	10%	1 - 12	0.94	0.93
6	$180° \pm 10°$	0	1 - 4, 7 - 12	0.93	0.71
7	$180° \pm 60°$	0	1 - 12	0.90	0.24

REFERENCES

/1/ C. Gormezano, et al., Proceedings 12th Symp. on Fus. Eng., Vol. 1, p. 38, Monterey (1987).

/2/ C. Gormezano, et al., 14th Int. Conf. on Plasma Phys. and Contr. Nuclear Fusion, Würzburg, CN-56, E-1-1 (1992).

/3/ M. Pain, et al., Proceedings 13th Symp. on Fus. Eng., Knoxville (1989).

/4/ A. Kaye, et al., Proceedings Machine Actuators and Control Seminar, London (1993).

/5/ M. Brusati, et al., 9th Topical Conf. on RF Power in Plasmas, Charleston (1991)

/6/ A. Ekedahl, et al., EPS Topical Conf. on RF Heating and Current Drive of Fusion Devices, p. 221, Brussels (1987).

/7/ M. Pain, et al., Fus. Technology and Design 22, 251 (1993).

JET Plasma

LH Launcher

1. Waveguides
2. Hybrid junction
3. Load
4. Flexible joints
5. Vacuum window
6. Cryopump
7. Bellows
8. Reaction flange
9. Multijunctions
10. Protection frame
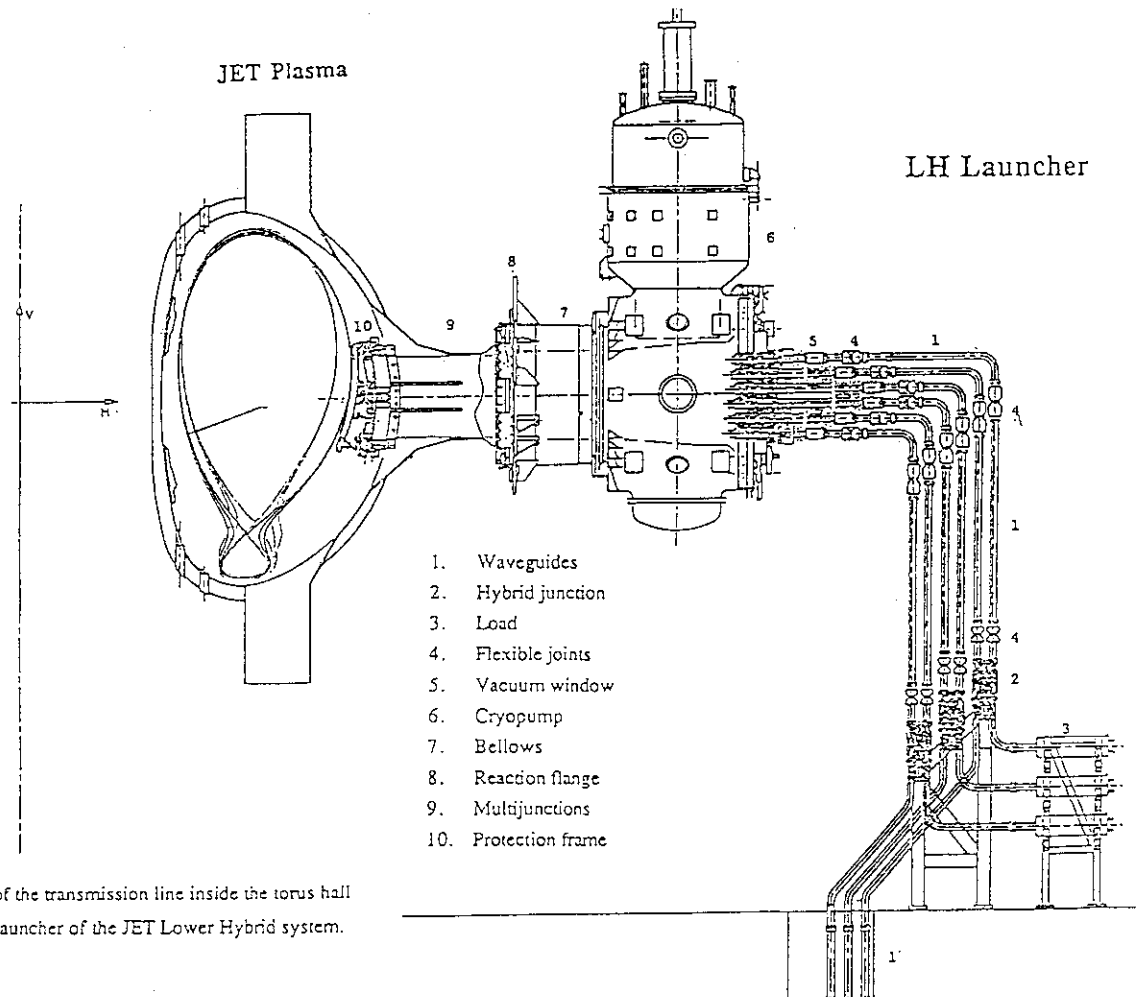
Fig. 1: Layout of the transmission line inside the torus hall
and the launcher of the JET Lower Hybrid system.

Multijunction module of the JET LH launcher

Phase shifters

Load

Output
to
plasma

E plane junctions

H plane junction

Input from
generator
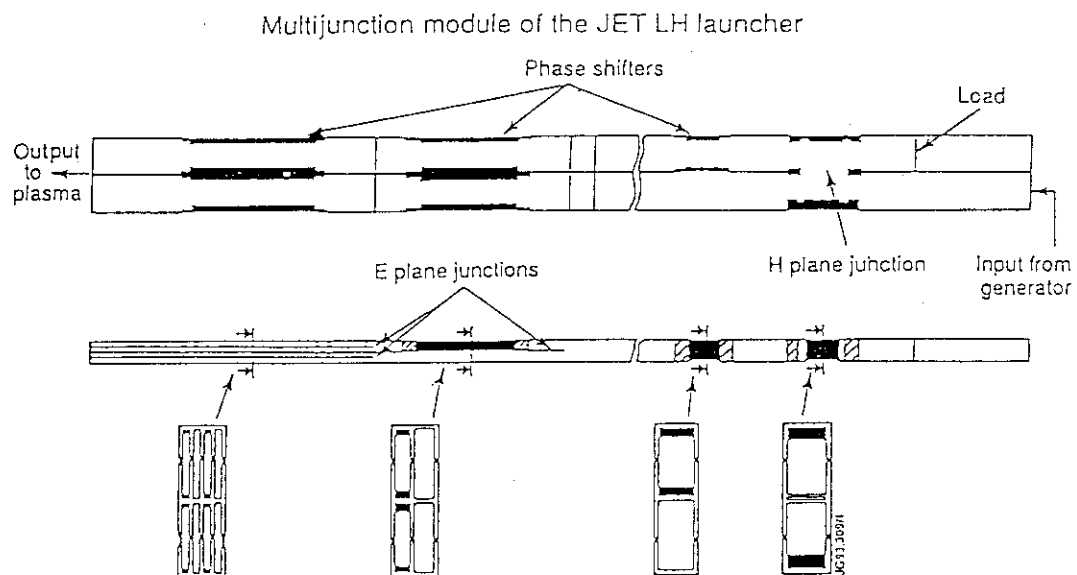
Fig. 2: Side and top view of a multijunction module of the JET LH launcher.

$N_{\parallel}$ Spectrum: $-90°/\ 0°/\ +90°$
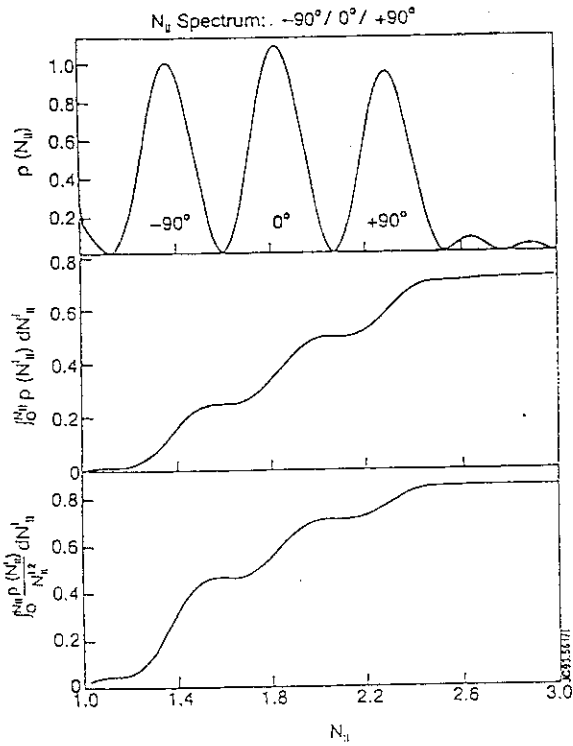
Fig. 1: LH wave spectrum for a combination of three different phase settings with equal power.
a) power density, b) integral power, c) weighted integral power.
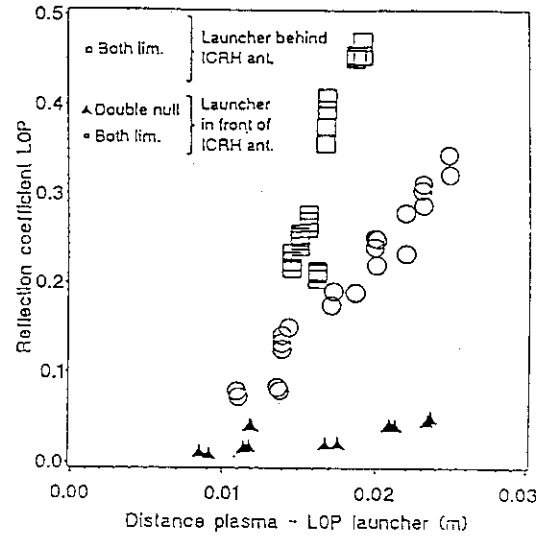
Fig. 4: Reflection coefficient versus plasma-launcher distance with the LOP module of the prototype JET LH launcher L0 for different plasma configurations and launcher positions.
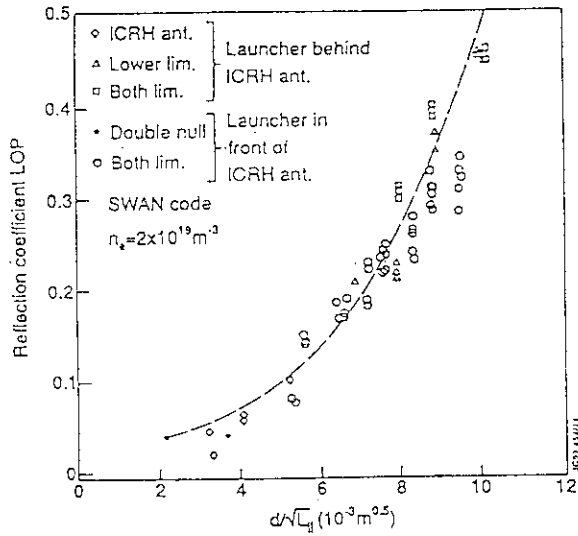
Fig. 5: Reflection coefficient versus the ratio of plasma-launcher distance to the parallel connection length with the LOP module of the prototype JET LH launcher L0 for different plasma configurations and launcher positions.
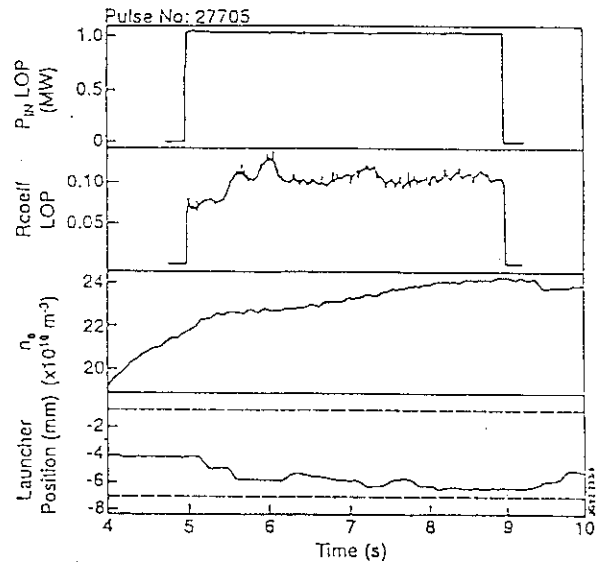
Fig. 6: Feedback control of the reflection coefficient by real time adjustment of the launcher position.

TE0,12 hyperguide

Mouthpiece with
phase shifters

Input waveguides
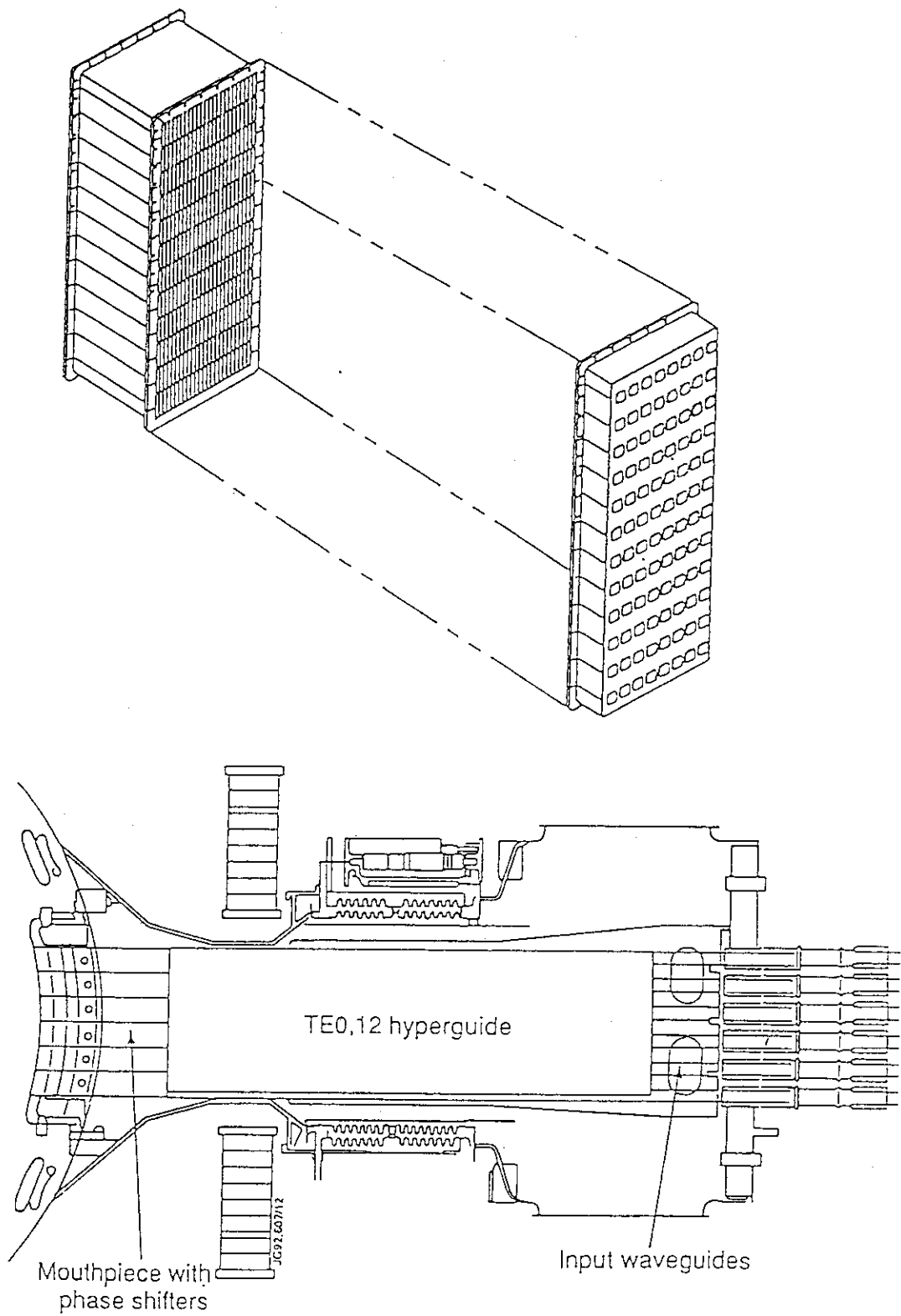
Fig. 7: a) Schematic view of the low power test module of a Hyperguide for JET with emitter and receiving grill surface.

b) Layout for the implementation of a Hyperguide into the LH launcher on JET.

2.4 Principle of a "Retro Reflecting" or "Backfire" LH Antenna: A Robust Efficiently Cooled Launching Structure for LH Waves in Reactor-Grade Plasmas

Ph. Bibet, X. Litaudon, D. Moreau

Departement de Recherches sur la Fusion Contrôlée
Association Euratom-CEA
Centre d'Etudes de Cadarache
13108 St Paul lez Durance, Cedex
FRANCE

1/ INTRODUCTION

Up to now Lower Hybrid Current Drive launchers have been made of waveguide arrays. Typically for a frequency around 5 GHz the power density is limited to less than 50 MW/m^2 for reliability, and taking into account that the necessary injected power is of the order of 50 MW or more for a steady-state reactor, the number of waveguides will be many thousands. To extrapolate present techniques despite the thermal power load and the mechanical stresses, it is therefore necessary to develop an advanced launcher concept both simpler and more robust.

To simplify the antennae between the RF vacuum windows and the plasma, studies have been carried out or are underway : the hyperguide (JET) [1], the toroidal oversized waveguide (JT60U) [2] and the poloidal mode converter [3] (Tore Supra).

For the plasma facing component it has been proposed to use diffraction through rod arrays [4] although this suffers from bad coupling per pass.

Here a new concept is given which seems to be robust and should leave enough space for efficient water cooling. The front part near the plasma can be easily replaceable by remote handling.

After a general description of the guiding principles which led to this new concept, the dependance of the spectrum power directivity and of the coupling upon the main plasma parameters will be studied.

2/ PRINCIPLE AND DESCRIPTION

One first idea to simplify the structure in front of the plasma is to use oversized waveguides in the poloidal direction. The phase shift between waveguides could be realized by using phase shifters which would act also as mode filters.

The main problem is then the cooling. For juxtaposed and independently fed waveguides, the $N_{//n}$ values of the different peaks of the radiated power spectrum are given by the relation :

$$N_{//n} = \frac{\varphi}{k\Delta} + n\frac{2\pi}{k\Delta} \quad (1)$$

with φ the phase shift between neighbouring waveguides, $k = 2\pi/\lambda$ the vacuum wavenumber, λ the wavelength, Δ the geometric periodicity. To excite a propagating slow wave, φ and Δ are chosen in such a way that $|N_{//0}|$ is greater than the accessibility limit at the launcher. For example for $N_{//0}=2$ and $\varphi=\pi/2$, then $k\Delta=\pi/4$ and the module of the $N_{//n}$ values are greater than 1. The geometric periodicity is then $\Delta=\lambda/8$, and therefore the wall thickness is too small to insert water cooling and is not robust enough to withstand strong mechanical stresses.

The second idea is therefore to realize an array of waveguides where each 2 neighbouring active waveguides labeled for instance 1 and 2 are separated by a short passive one which acts as a reflector (fig 1).

As a first order calculation, if the coupling coefficient through the plasma between 2 adjacent active waveguides is noted S_{12}, if the incident wave phase shift between 1 and 2 is equal to 2φ, the total electric field E in the passive waveguide calculated at the grill aperture is given by :

$$E = S_{12}\, e^{j\gamma}\, 2\cos\varphi\,(1 - e^{-j\frac{4\pi d}{\lambda}})\quad (2)$$

where d is the distance between the plasma and the short circuit placed inside the passive waveguide (fig 2).

Since the phase shift between the active waveguides is 2φ, the goal is to adjust the short circuit position in such a way that the phase of E noted $<E$ equals to φ (2π). Using relation (2) $<E$ satisfies the following condition :

$$<E = <S_{12} + \varphi - \frac{2\pi d}{\lambda} + \frac{\pi}{2} + \varepsilon\pi\quad (3)$$

where :

$\varepsilon=0$ if sign($\cos\varphi$) x sign ($\cos(2\pi d/\lambda)$) = + 1   (4)

$\varepsilon=1$ if sign($\cos\varphi$) x sign ($\cos(2\pi d/\lambda)$)= - 1   (5)

A solution of the equality :

$$<E = \varphi\ (2\pi)\quad (6)$$

is found for d if :

$<S12$ and $\varphi \in [\pi/2, 3\pi/2]$ (2π) or $<S12$ and $\varphi \in [3\pi/2, \pi/2]$ (2π) (7)

If condition (7) is satisfied the total electric field of the wave in passive waveguides are coherent with the one of active waveguides .

The geometric periodicity between active waveguides is 2Δ to allow for cooling between the active waveguides and behind the passive reflector waveguides. Without the reflected waves, the $N_{//n}$ values of the main peaks would then follow the relation :

$$N_{//n} = \frac{\varphi}{k\Delta} + n\frac{\pi}{k\Delta}\quad (8)$$

Thus, if the field amplitude in the reflector waveguides is too small, the main peaks will be more closely spaced than for a conventional grill. Computations which take into account the plasma admittance show that $<S_{12}$ is between $\pi/2$ and $3\pi/2$, and a good choice for φ seems to be $2\pi/3$. Then if the desired $N_{//}$ value is 2 for n=0 then $k\Delta=\pi/3$ and $N_{//n}$ equals to (2 + 3 n). The depth of the passive waveguides must therefore be adjusted in such a way that the coherent addition of incident and reflected fields inhibit the parasitic peak at $N_{//} \approx -1$ in order to build up a highly directive power spectrum with a small reflection coefficient.

3/ NUMERICAL RESULTS

The coupling properties of the proposed structure have been studied using the SWAN code [5]. Good agreement between the SWAN calculations and the coupling measurements performed on Tore Supra has been previously reported [6]. The calculations are made at a frequency of 3.7 GHz for an antenna composed of 12 waveguides : 6 active waveguides

supposed to be fed independently with a phase shift of $4\pi/3$ and 6 short passive waveguides depending on the short circuit position, the electron density and the density gradient. For the study the chosen periodicity is $\Delta=16.2$ mm and 2 evanescents modes have been considered to satisfy the continuity limits at the interface grill-plasma.

3-1/ The short circuit position (fig 3)

The short cicuit position is the same in all the passive waveguides. Its effect is very important on the mean reflection coefficient R of the active waveguides . As expected , when (6) is satisfied the coherence destroys the peak corresponding to $|N//|<1$ which is one of the main source of reflected power. The effect on the power directivity δ is weak. Only in this case the periodicty Δ is equal to 14.6 mm . The same study has not been done with $\Delta = 16.2$ mm since the phase of the cross coupling S_{12} is the same .

3-2/ The electron density n_e (fig 4)

R decreases when the density is decreased to reach an optimum when the electron density is twice the cutoff density. In the meantime the directivity is always increasing. This is explained by the increase of the module of the coupling coefficient $|S_{12}|$ while its phase $<S_{12}$ stays nearly constant (fig 5).

3-3/ The density gradient ∇n_e (fig 6)

The power directivity variation is small with the density gradient, it stays around 76 %. The reflection coefficient R decreases when the density gradient ∇n_e increases. For a decay length $n_e/\nabla n_e$ of 5 mm, R is less than 3 % at an electron density of $2 \ 10^{11}$ cm^{-3}.

3-4/ Radiated $N_{//}$ spectrum

The spectrum has been plotted on fig 7 for an array of 12 waveguides, 6 active ones and 6 passive ones. The electron density is $2 \ 10^{11}$ cm^{-3} and the linear density gradient is $4 \ 10^{11}$ cm^{-4}. The obtained mean reflection coefficient in active waveguides is 2.2 %. Two peaks are observed on this plot, the main one at $N_{//} = 1.63$ and a secondary one at $N_{//} = - 3.3$.

4/ CONCLUSION

Based upon a principle somewhat similar to the "backfire arrays" used in TV antennae, the new concept of a "backfire" or "retro-reflecting" LH antenna is suggested for the plasma facing component of an advanced LH launcher. It falls into the general category of reflector antennae and it has been shown in our preliminary studies that the power spectrum radiated by such a structure has a power directivity and a coupling efficiency similar to classical LHCD antennae. Moreover, it has been shown that the coupling properties of such an antenna are optimized at low edge density where the thermal load is lower.

It can be fed in several ways, e.g. by an hyperguide, a mode converter or a quasi optical transmission. Multijunctions can be used to further reduce the reflection coefficient. It is a simplified and more robust antenna which can be easily water cooled through pipes situated in the thick wall behind the passive waveguides. It can therefore have some relevance for applying LH waves in the next step reactor-grade tokamaks.

AKNOWLEDGEMENT

We acknowledge Dr. G. Tonon for his strong interest and support for this study .

REFERENCES

[1] M. PAIN , M. BRUSATI et al. The Hyperguide : a new concept of Lower Hybrid
Launcher. JET-P(92)94 (Nov. 92)
[2]Y. IKEDA et al. The Upgrade of the 2 GHz LHCD system on the JT-60U. Proceedings of
the 17th Symposium on Fusion Technology. Rome Italy 14-18 sept 1992.
[3]Ph. BIBET, T.K. NGUYEN et al. Design of new antennae for LHCD on Tore Supra. This
conference.
[4] M.I. PETELIN , E.V. SUVOROV , Pisma v ZhTF (letters to Journal of Thechnical physics
1989 vol. 15 n°22 p23)
[5]D. MOREAU, T.K. NGUYEN. Couplage de l'onde lente au voisinage de la frequence
hybride basse dans les grands tokamaks . Rep. EUR-CEA-FC-1246 . CEN Grenoble (1984)
[6]X. LITAUDON et al, Nuclear Fusion . 32 (1992) 1883.
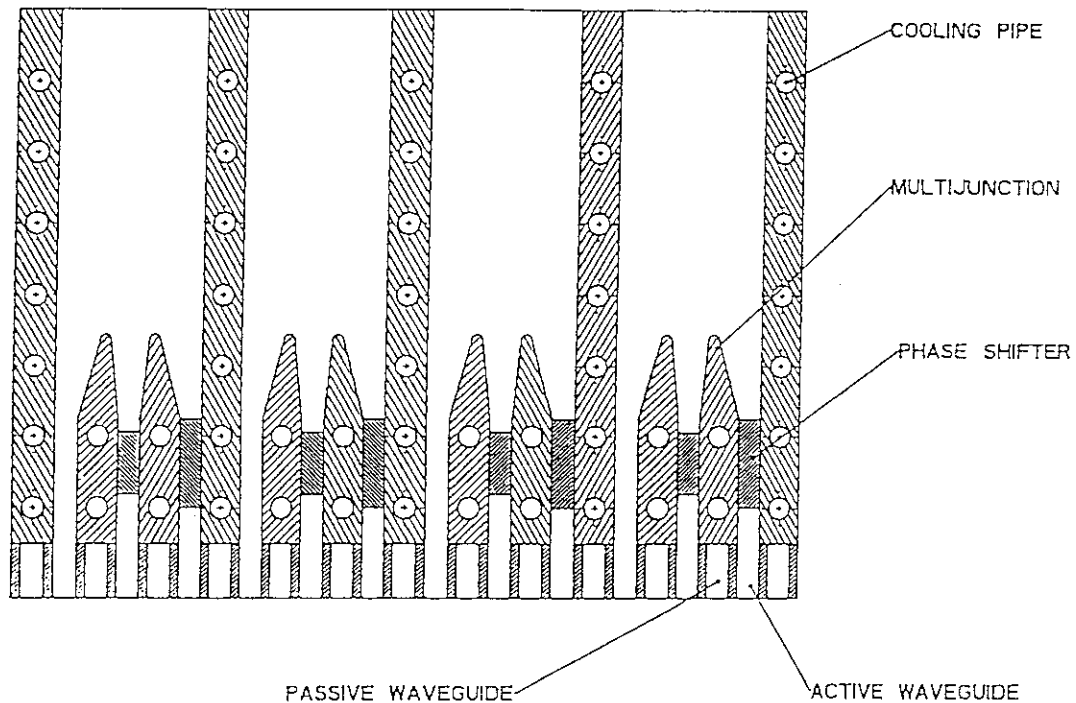
Fig 1 :Overview of the "retro-reflecting LH antenna"

Fig 2 : Principle of "the retro reflecting"LH antenna. S_{12} the cross coupling coefficient between an active and a passive waveguides, 2φ the wave phase shift between active waveguides, and d the distance between the short circuit in the passive waveguide and the plasma.

Fig 3 : Influence of the short circuit position d for an antenna made of 6 active and 6 passivewaveguides at a frequency of 3.7 GHz. The geometric periodicity Δ is 14.6 mm.

Fig 4 : Influence of the electron density. The geometric periodicity Δ is 16.2 mm . The short circuit distance d to plasma interface is 1.7 cm.
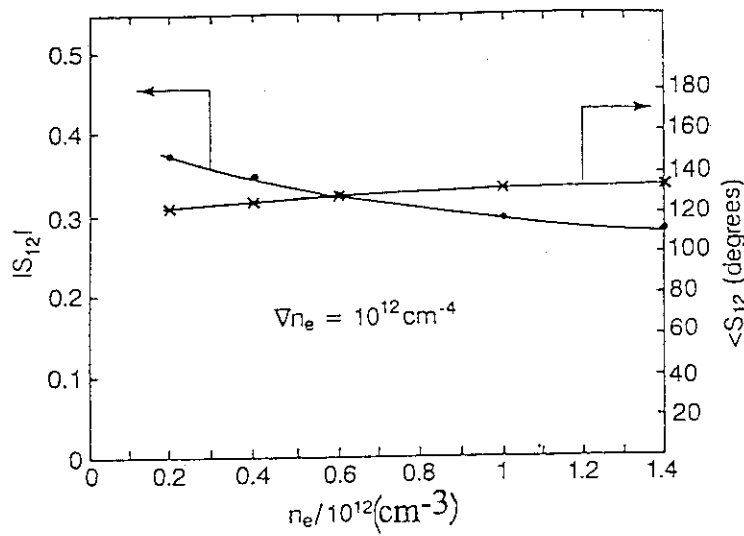
Fig 5 : Influence of the electron
density on the cross coupling
coefficient S_{12} (Δ=16.2mm ;
d=1.7cm)

Fig 6 : Influence of the electron
density gradient (Δ=16.2mm,
d=1.7cm).
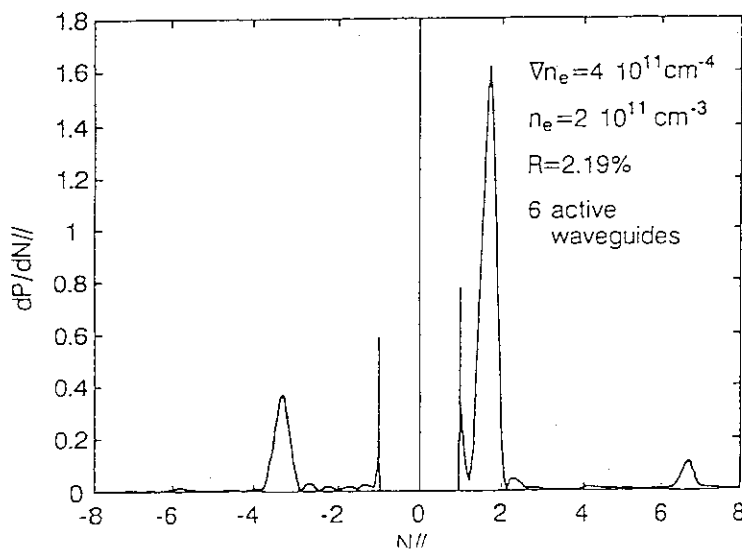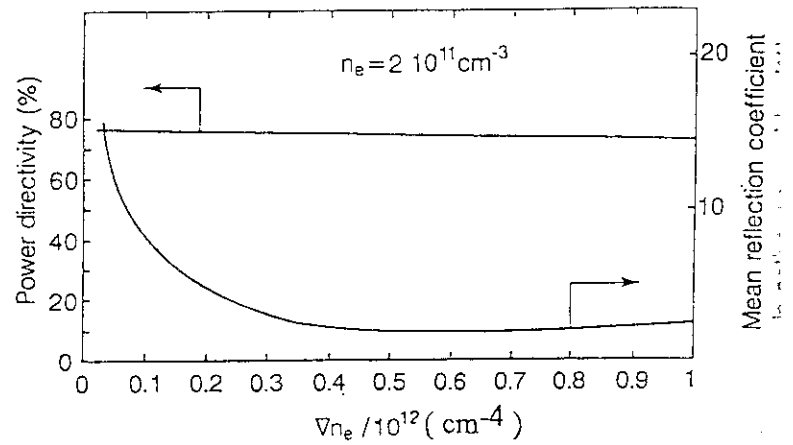
Fig 7 : Radiated $N_{//}$ spectrum
of a 6 active, 6 passive
waveguides. (Δ=16.2mm ,
d=1.7cm).

2. 5   Design of New Antenna for LHCD on Tore Supra

Ph BIBET, T.K. NGUYEN*
G. BERGER-BY, M. GONICHE, G. REY, G. TONON

Association Euratom-CEA
CE Cadarache
13108 St Paul lez Durance, France

* DSM/DRFMC/PSI
CE Grenoble
38041 Grenoble Cedex, France

1/ INTRODUCTION

To drive the TORE SUPRA total current 1.7 MA at an average density of $6 \ 10^{19} \ m^{-3}$ the total injected power must be more than 15 MW at a frequency of 3.7 GHz. Up to now two antennae allow to inject routinely 2.5 MW each. To upgrade the system 4 antennae injecting 4 MW each have to be built with an optimized use of the port area. Depending on the main peak N// value 1.93 or 2.57 the new antennae will be made of 16 modules of 3 x 6 waveguides in the first case, 3 x 8 waveguides in the second one. It will lead at the mouth to an array of 6 x 48 waveguides or 6 x 64 waveguides. Each klystron will feed 2 modules . Each module will have one input port which must be divided poloidally in 3 ports . For this purpose a mode converter which transform the TE_{01} mode into the TE_{03} mode has been developped and the poloidal junction between the oversized waveguide at the output of the mode converter and the 3 ports has been studied.

After a small description of the module, the method of computation of the different part is given and then the main results are shown . The interest of such components in the future is finally given.

2/ THEORETICAL DETERMINATION OF THE MODULE SIZES

The module will be made of four parts (fig 1) :
- a raised cosine taper connected to a mode converter to convert the TE_{01} mode into TE_{03} mode.
- a poloidal junction with one main oversized waveguide and 3 output waveguides.
- a E plane linear taper.
- E plane multijunctions.

2-1/ THEORETICAL MODEL FOR THE DEFINITION OF THE TAPER AND THE MODE CONVERTER

To compute the taper and the mode converter the telegraphist equation which is derived from Maxwell equations has been solved using Unger method [1]. Due to the symmetry and also to the choice of the small size of the waveguide ,only the TE_{0n} modes have to be taken into account with n odd . If the amplitude of the forward and the backward waves for the different modes are noted A_n and B_n, the wavenumber k , the pulsation ω and the magnetic permeability μ and a the larger size of the waveguide , the telegraphist equation is the following:

$$\frac{dA_n}{dz} = -j\beta_n A_n - \frac{1}{2K_n}\frac{dK_n}{dz}B_n + \sum_{m \neq n}(k_{nm}^+ A_m - k_{nm}^- B_m) \quad (1)$$

$$\frac{dB_n}{dz} = j\beta_n B_n - \frac{1}{2K_n}\frac{dK_n}{dz}A_n + \sum_{m \neq n}(k_{nm}^+ B_m - k_{nm}^- A_m) \quad (2)$$

with :

$$k_{nm}^{\pm} = \frac{k_n k_m}{k_m^2 - k_n^2}(\sqrt{\frac{K_n}{K_m}} \pm \sqrt{\frac{K_m}{K_n}})\frac{1}{a}\frac{da}{dz}(-1)^{\frac{m-n}{2}}$$

$$k_n = n\pi \quad K_n = \frac{\omega\mu}{\beta_n} \quad \beta_n^2 = k^2 - (\frac{n\pi}{a})^2 \quad (3)$$

To avoid numerical divergence the different components have been divided in many parts depending on the number of propagating modes [2]. The scattering matrix which links the electric field of the output waves to the input ones is given by solving (1) (2) with 2 N boundary conditions for N propagating modes.

2-2/ THEORETICAL MODEL FOR THE POLOIDAL JUNCTION AND THE MULTIJUNCTIONS.

The poloidal junction and the multijunctions have been studied considering the TE_{0n} modes in the first part and the LSE_{1n} modes [3] in the second part. If N modes are considered in the main waveguide , and M modes in each of the P secondary waveguides, to write the continuity of the tangential component of the electric and magnetic fields leads to a scattering matrix S of size (N+MxP,N+MxP) given by :

$$S = \begin{pmatrix} -I^0 + \sqrt{Y^0}\,G^0\,Y^{-1}\,{}^tG^0\sqrt{Y^0} & \sqrt{Y^0}\,G^0\,Y^{-1}\sqrt{Y^1} \\ \sqrt{Y^1}\,Y^{-1}\,{}^tG^0\sqrt{Y^0} & -I^1 + \sqrt{Y^1}\,Y^{-1}\sqrt{Y^1} \end{pmatrix} \quad (4)$$

with $Y = \frac{1}{2}({}^tG^0\,Y^0\,G^0 + Y^1)$ and Y^0 and Y^1 the diagonal matrix of the characteristic admittance of the chosen modes , I^0 and I^1 the matrix identity and G^0 the matrix of general term $G_{mm'}^{pp'} = \iint \vec{e}_m^{p'} \times \vec{h}_m^p\, d\vec{S}$ where $\vec{e}_m^{p'}$ and $\vec{h}_m^p$ are the tangential components of the normalized electric and magnetic vectors of the p', p th waveguide considering the m' , m th mode.

3/ NUMERICAL RESULTS

3-1/ THE RAISED COSINE TAPER

To realize a change of section a 150 mm long raised cosine taper has been computed. The coupling coefficient from TE_{01} mode to TE_{01} mode is estimated to be 99.6 % and the coupling to the TE_{03} mode is less than 26 dB. The Voltage Standing Wave Ratio is

better than 1.01 . The total scattering matrix for the region where 2 modes are considered which gives the relations between the input waves to the output waves for the TE_{01} and the TE_{03} modes is written in tab 1 .

3-2/ THE MODE CONVERTER

Using [4] a 3.5 period mode converter has been defined . Its estimated conversion efficiency from the TE_{01} mode to the TE_{03} mode is 98.7 % . 1% of the total power stays in the TE_{01} mode . The VSWR for the TE_{01} mode and the TE_{03} mode are found to be 1.38 and 1.1 . In fig 2 the amount of power in the 2 propagating modes for the forward and backward waves are plotted depending on the length inside the mode converter when the power at the input is 100 % TE_{01} mode . It has been checked that the conservation of energy is verified all along the mode converter . The total matrix of scattering is given in tab 2 .

3-3/ THE POLOIDAL JUNCTION

On fig 3 the reflection coefficient and the coupling coefficient from the TE_{03} mode in the main waveguides to the 3 output waveguides are plotted depending on the thickness e of the septums separating the 3 waveguides. The reflection coefficient is small and the power is divided by 3 into the 3 secondary waveguides even for a septum thickness of 4 mm.

On fig 4 the reflection coefficient of the TE_{01} mode in the main waveguide is high , about 70 % and the coupling coefficient from the main waveguide to the 3 secondary waveguides is 2 times higher in the central waveguide compared to the extremes ones.

On fig 5 the coupling coefficient and the reflected coefficient are given for the secondary waveguides . The coupling between the secondary waveguides is less than 10 %.

3-4/ THE MULTIJUNCTIONS

In the 2 cases defined in the introduction 90 degrees multijunctions are considered at the mouth . The main peak N// value is given by the relation [5] :

$$N_{//} = N_{//0} \left(1 + \frac{\delta\Phi}{N.\Phi} \right) \qquad N_{//0} = \frac{\Phi}{k\Delta} \qquad (5)$$

where Δ is the geometric periodicity , Φ the geometric phase shift inside the module (90 degrees) , $\delta\Phi$ the phase shift between each module and N the number of waveguides per module .

The $N_{//}$ flexibility $\delta N_{//}/N_{//}$ for $\delta\Phi$ changing from -90 to + 90 degrees is $\pm$ 16 % in the first type and $\pm$ 12.5 % in the second one . The reflection coeffcient at the input depending on the reflection at the output ρ can be as low as ρ^6 to ρ^8 if 120 degrees multijunctions are set in serie with 90 degrees multijunctions for the first case, and 3 steps of 90 degrees multijunctions in the second case . This reduction of the reflection coefficient is obtained at the expense of an increase of the total electric field near the mouth by a factor $(1+\rho)^2(1+\rho^2+\rho^4)$.

4/ CONCLUSION

The different parts of the modules for next Tore Supra antennae have been computed . After an experimental checking on low level mock-up , a module will be realized for high power tests . Then the antennae will be designed.

The main concept which has been used in these new antennae is the mode converter to feed a poloidal junction. This device can be relevant for ITER to feed for example an hyperguide which can radiate on a new concept of antenna, the "retro-reflecting LH antenna" [6].

BIBLIOGRAPHY

[1] H-S Unger . Circular waveguide taper of improved design . The bell system technical journal , july 1958 .(p 899 - 912)

[2] H. Flugel . Taper analysis of the 150 GHz KfK gyrotron including the electron beam . Int. J. Electronics ,1988,vol 64,n°1 p 95 - 106

[3] R. E. Collin . Field Theory of guided waves . IEEE press p 569

[4] M. J. Buckley , R. J. Vernon . Compact quasi periodic and aperiodic TE_{0n} mode converters in the overmoded circular waveguides for use with gyrotrons . IEEE Transactions on microwave theory and techniques , vol 38 ,n° 6 ,june 1990,p 712 - 721

[5] X. Litaudon , D. Moreau . Coupling of slow waves near the lower hybrid frequency in JET . Nuclear Fusion , Vol. 30, N° 3 (1990) , p 471 - 483

[6] Ph. Bibet, X. Litaudon, D. Moreau. Principle of a "retro-reflecting LH antenna " : a robust , efficiciently cooled launching structure for LH waves in reactor grade plasmas . This conference.

Tab 1 : amplitude | S | and phase < S (degrees) of the scattering matrix of the raised cosine taper of sizes at the input (40 x 76 mm^2) and (40 x 130 mm2) at the output (part where 2 modes are propagating)

$$
\begin{vmatrix} \overline{b_1} \\ \overline{b_2} \end{vmatrix} \begin{matrix} TE_{01} \\ TE_{03} \\ TE_{01} \\ TE_{03} \end{matrix} = \underset{=}{S} \begin{vmatrix} \overline{a_1} \\ \overline{a_2} \end{vmatrix} \begin{matrix} TE_{01} \\ TE_{03} \\ TE_{01} \\ TE_{03} \end{matrix}
$$

| S | =

0.0017	0.0305	0.999	0.034
0.0306	0.776	0.0452	0.6327
0.9989	0.0453	0.0018	0.0073
0.0341	0.633	0.0072	0.7771

< S =

69.2	-31.6	-175.8	99.7
-31.66	176.2	-147.1	-50.8
-175.8	-147.2	91.4	170.2
99.7	-50.8	170.2	-97.9

Tab 2 : amplitude | S | and phase < S (degrees) of the scattering matrix of the mode converter .

| S | =

0.1563	0.0197	0.0998	0.9829
0.0197	0.0475	0.9935	0.1008
0.0997	0.9937	0.0424	0.0326
0.982	0.1008	0.0326	0.1534

$$< S = \begin{vmatrix} -142.6 & -28.2 & 105.9 & 113.7 \\ -28.2 & -7.3 & -64.9 & 120.8 \\ 106 & -64.9 & 58 & -132.6 \\ 113.7 & 120.9 & -132.6 & 171.4 \end{vmatrix}$$
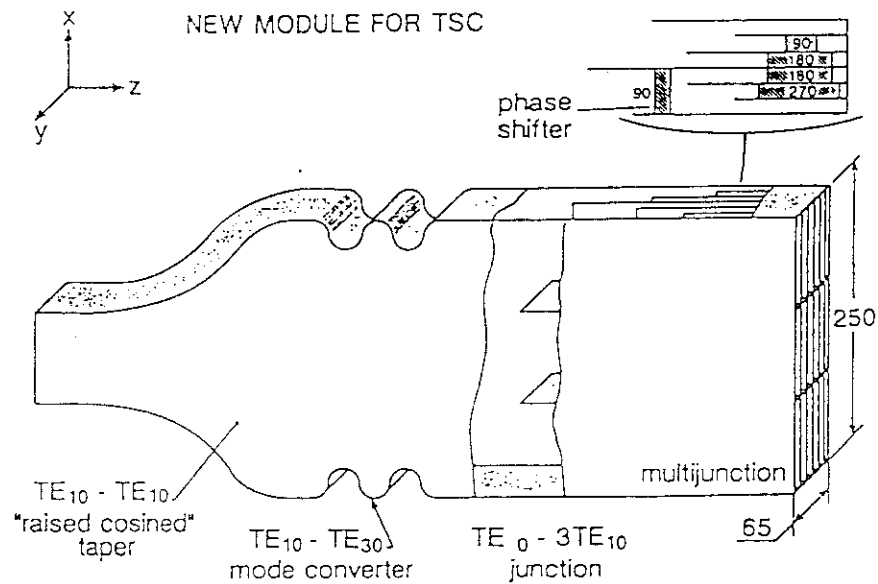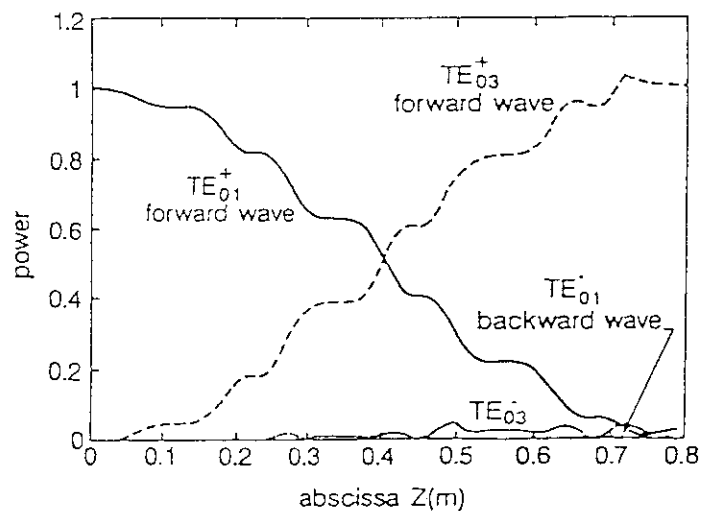

Fig 1 : New module of antenna for Tore Supra.

Fig 2 : Power in forward and backward waves for the TE_{01} and the TE_{03} modes in a 3.5 period rectangular mode converter of larger section ($40*192mm^2$) at a frequency of 3.7 GHz vs the propagating length inside the mode converter.
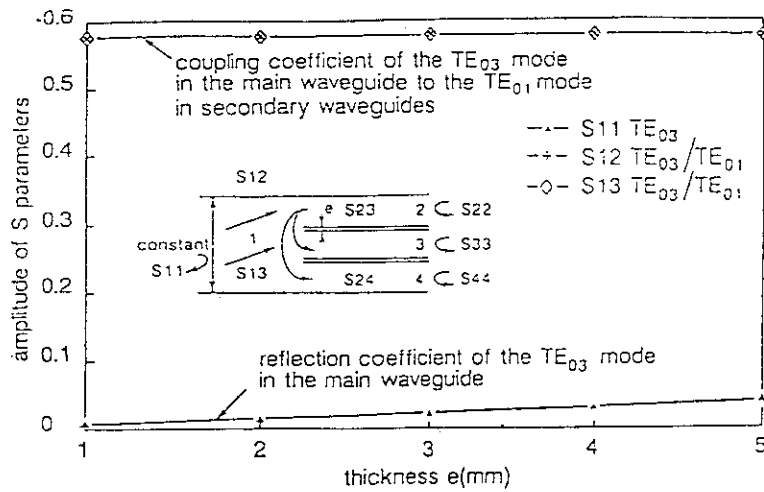
Fig 3 : Amplitude of the S parameters
involving the TE_{03} mode in the main
waveguide of the poloïdal junction
at a frequency of 3.7 GHz for a section
of the main waveguide of (40*192 mm^2

Fig 4 : Amplitude of the S parameters
involving the TE_{01} mode in the main
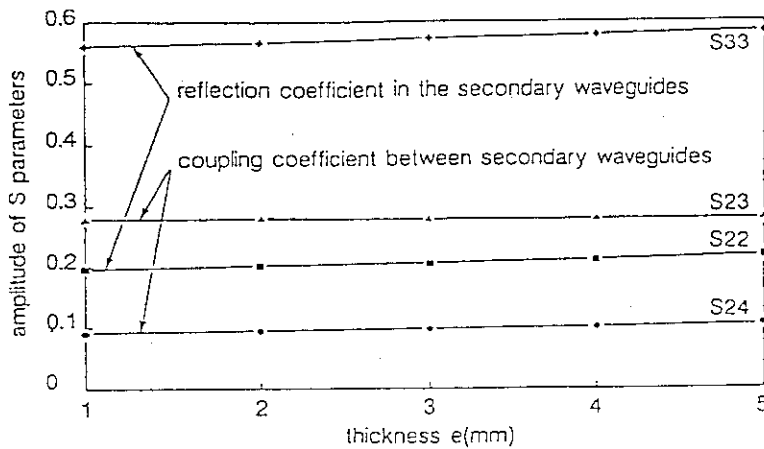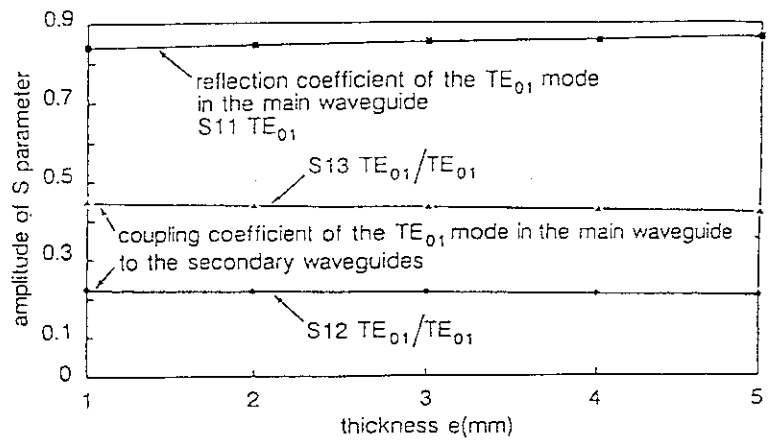waveguide of the poloïdal junction.

Fig 5 : Amplitude of the S parameters
of the reflection coefficient and of the
coupling of the secondary waveguides
of the poloïdal junction.

2.6 Development of LHCD Launcher for Next Stage Tokamak

I. Demonstration of long pulse rf injection

< from the first joint JAERI - CEA experiment >

M. Seki, K. Obara, S. Maebara, Y. Ikeda, T. Imai, T. Nagashima
Naka Fusion Research Establishment, JAERI

M. Goniche, J. Brossaud, C. Barral, G. Berger-By,
Ph. Bibet, S. Poli, G. Rey, G. Tonon
DRFC, Centre d'Etudes de Cadarache, CEA

1. Introduction

In the next stage LHCD experiments, long pulse rf injection is required for study of quasi steady state tokamak. Suppression of outgassing from waveguides is one of main issues for LHCD launcher to transmit rf power in the waveguide continuously and stably. In order to know the parameter which control outgassing rate and to investigate how to reduce outgassing rate, JAERI and CEA had performed outgassing experiments using 4-divided waveguide.

2. Experimental set-up

The feature of this experimental system is the ability of quasi-CW operation, that is needed to study outgassing behavior in a long pulse. A source power up to 500 kW is available at a frequency of 3.7 GHz. The rf power is transmitted in the 4-divided waveguide (test module) as shown in fig.1, and is terminated into water dummy load. No reflection rf power makes no standing wave in the waveguides so that the temperature gradient is small. The uniform temperature is important to obtain the temperature dependence on outgassing rate. Figure 2 illustrates structure of the test module. The test module is made of copper-plated stainless steel and dispersion strengthen copper, which are composed by diffusion bonding in Hot Press Machine, and is bakable at high temperature up to 500°C. The test module has a cooling channel to remove heat load due to rf losses. The cooling channel is designed to maintain the maximum temperature less than 100°C with transmitting power of 200 kW. The main effort in design is that homogeneous temperature of the test module will realize in order to investigate temperature dependence of outgassing rate. It should be mentioned that the temperature increase due to rf losses in test module is larger than that in connection waveguides.

Incident and reflective power are measured and temperature at some points are monitored by thermo-couples. Total pressure in vacuum tank and partial pressure are measured. The outgassing rate is estimated from the increase of pressure during rf injection. Temperature dependence of the outgassing can be obtained in one shot, as temperature increases due to rf losses.

3. Experimental results

Before high power injection, voltage standing wave ratio (VSWR) was measured to be less than 1.2. Rf conditioning was easily finished up to ~ 400 kW (20 kW/cm^2 in the test module) and this high power density is enough for next stage LHCD launcher.

Some thermal treatments were performed. In order to investigate dependence of outgassing rate on baking temperature, baking temperature was raised up to 450°C. Thermal treatment was carried out under atmosphere of hydrogen and/or deuterium gas, which made deoxidization on the surface of test module. An air exposure of 8 hours was used to set initial surface condition before thermal treatment.

Outgassing flux at 400°C is shown as a function of injected rf energy in fig.3 in which thermal treatments are indicated. As known from the figure, outgassing rate decreases with input energy (conditioning effect). The outgassing rate is reduced by means of baking at higher temperature of 450°C. On the other hand, gas treatment using H$_2$/D$_2$ gas does not affect on outgassing rate. According to experiments carried out at different rf power densities, the outgassing rate depends strongly on working temperature of waveguide, but it is independent of rf power density as shown in fig. 4. These results suggest that the outgassing rate is controlled by changing temperature after good conditioning.

It is found out using a calculation model that the desorption mechanism can not explain these outgassing phenomena unless activation energy of desorption is assumed to be relatively high of 1eV, but the desorption with adsorption mechanism explains well with proper physical values. At high temperature than 450°C, diffusion process from bulk is important, especially for CO, CO$_2$.

4. Demonstration of long rf injection

The steady state outgassing is observed in the long duration up to 1800 sec as shown in fig.5, when a water cooling removes the rf heat load. The rf power density is 15 kW/cm^2 (~270kW), the maximum temperature is around 100°C at the center part of test module. The outgassing rate level of ~10^{-7} Pa m^3/m^2 sec is low enough to design a vacuum system with a reasonable dimension. It seems that the desorption and adsorption mechanism realize the steady state outgassing. This demonstration serves design database for a vacuum system of next LHCD launcher.

5. Summary

The outgassing property has been studied by using 4-divided waveguide during rf power pulse. It is found that outgassing rate depends on working temperature and is independent of rf power density. And it should be pointed out that the baking at higher temperature is effective for reduction of outgassing flux, moreover outgassing rate is controlled by changing the working temperature.

The steady state rf injection, with low outgassing due to water cooling, was demonstrated.

II. Development of rf power dividing into waveguides lined in the poloidal direction using mode converter concept

< for the second joint JAERI - CEA experiment >

M. Seki, S. Maebara, Y. Ikeda, T. Imai
Naka Fusion Research Establishment, JAERI

1. Introduction

The next generation LHCD launcher should be demanded to launch the high-directive and sharp spectrum, and to be simple and compact structure. But these spectrum requires many waveguides in front of plasma and this situation is not consistent with compact structure which is needed for low cost and easy maintenance. Moreover the launcher will be advantageous if $N_{//}$ controllability is wide for various spectra by changing adjacent phase. And a low rf power density at grill mouth makes power launching easily.

2. Poloidal rf dividing concept

In order to realize features mentioned in introduction, a new type launcher is considered. As the conceptual structure is illustrated in fig.6, an rf power is divided into many waveguides in lined toroidally (6) and poloidally (3). In former multijunction module, the rf power is mainly split into sub-waveguides lined in the toroidal direction only. Mode converter concept is used to distribute rf power in the poloidal direction.

3. Rf property

Basic rf properties are obtained by using many mock-ups with matched load. The main R&D item is to divide rf power into 3 waveguides lined in the poloidal direction, because the features of E-plane multijunction are well known in the previous multijunction launcher. The structure of mode converter is optimized by experimentally and analytically. The optimized mock-up is shown in fig.7. This mock-up shows low VSWR (1.4%) in main waveguide and good dividing ratio (33 +/- 5 %) in 3-divided waveguides as drawn in fig.8. It is pointed out that although the mode converter is short, the length is enough to obtain low VSWR so that the launcher composed of the mode converter will be compact. According to the simplified calculation result, each amplitude of main modes for TE01, TE03, TE05 is ~ 0.5, 0.4, 0.3, respectively at outlet of mode converter.

The rf property with reflection wave is estimated from S-parameters, are measured by using reducers (waveguide/coaxial cable converter) located at each ports. The two-case calculations are performed for the launcher composed of the mode converter and multijunction section. For the usual coupling condition case, main rf parameters show the validity of the multijunction launcher. Moreover for the coupling under in-homogeneous

plasma poloidally, it seems that the performance does not so degrade as known from fig.9.

4. Conclusion

The poloidally power dividing waveguide is newly developed by using mode converter concept. This waveguide will be used as a main part for the next LHCD launcher which is featured by $N_{//}$ controllability.

The rf property is studied by mock-up test, measured data show good power dividing ratio with low VSWR. The calculation from S-parameter suggests that this new type multijunction launcher allows successful performance under usual plasma conditions.

High power long pulse test will be performed using the new multijunction module at Cadarache LH test facility in 1994.

Figure captions :

Figure 1 ; The test module and connection waveguides are installed in the vacuum tank. The waveguides are baked by radiation from the heated tank in thermal treatments. Temperatures are monitored by thermo-couples, pressure is measured by ionization gauge.

Figure 2 ; Rf power is divided into 4 sub-waveguides. Septum plate is made from dispersion strengthen copper, and rod from copper-plated stainless steel. The septa and rods are fixed by diffusion bonding method under the high temperature of 850°C. The test module has a cooling channel on the top and bottom side. The pumping holes yield conductance of ~96 l/sec.

Figure 3 ; Outgassing flux at 400°C is shown as a function of integrated rf energy. The thermal treatment is also indicated. Outgassing is calculated from increase in pressure during rf injection. The outgassing flux estimated from the build-up method is consistent with these values calculated from the dynamically method. One circle stands for one shot. Closed circle presents outgassing flux in the first shot just after each thermal treatment. The outgassing flux decreases with rf shot.

Figure 4 ; Dependence of inject rf power density on outgassing flux is investigated after good conditioning. High rf power density leads the temperature to increment faster. The outgassing flux is the same for rf power densities from 5 to 15 kW/cm² at the same working temperature. This means that the outgassing rate is controlled by changing of temperature.

Figure 5 ; This figure shows the demonstration of long pulse rf injection with water cooling. The power density is 15 kW/cm², the temperature in the center of test module saturates around 100°C, (the temperature in the down-stream side is higher than that of center, because heat exchange of cooling channel is not sufficient in the down-stream connection waveguide). The steady state outgassing is observed. The demonstration suggests the possibility of steady state rf injection in the waveguides.

Figure 6 ; The conceptual design is illustrated for the new type multijunction launcher. This launcher is featured by the rf power dividing in the both toroidal and the poloidal direction at one junction point. The $N_{//}$ controllability will be available

by changing adjacent phase using this launcher. In order to distribute rf power into the poloidal waveguides, the mode converter method is used.

Figure 7 ; The mock-ups are mainly used to investigate whether VSWR is low in main waveguide and the power dividing ratio is the same in each 3-divided waveguide. The final mock-up is shown after optimization by experimentally and theoretically. The mode converter has symmetry and no septum inside.

Figure 8 ; The rf properties are measured by pick-up probe under the matching condition (no reflection wave) at a frequency of 2.2 GHz. The main results are as follows : return loss in main waveguide is 1.4%, power dividing ratio ~33 +/-5%.

Figure 9 ; The rf property is estimated using measured scattering-parameters in the case that reflective wave exists in the usual coupling conditions. For the homogeneous plasma in the poloidal direction, the main rf property does not change from no-reflection case. For the in-homogeneous plasma, the calculation results are pictured. In this case the reflection coefficient in each 3-div waveguide is different due to the length of vacuum gap Xp. Although the power dividing ratio is small affected, the rf performance is seemed to be available.
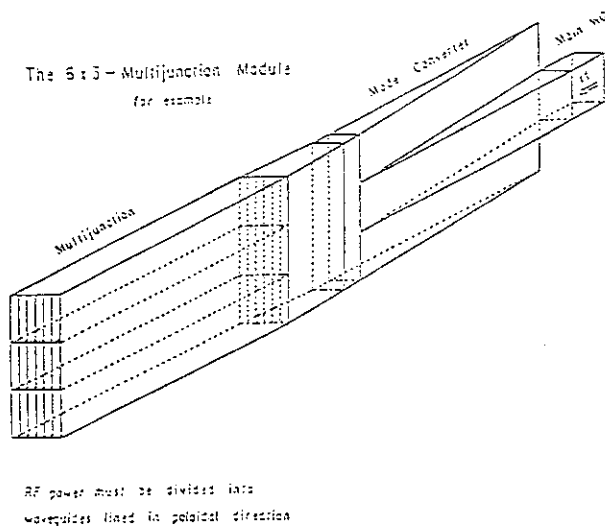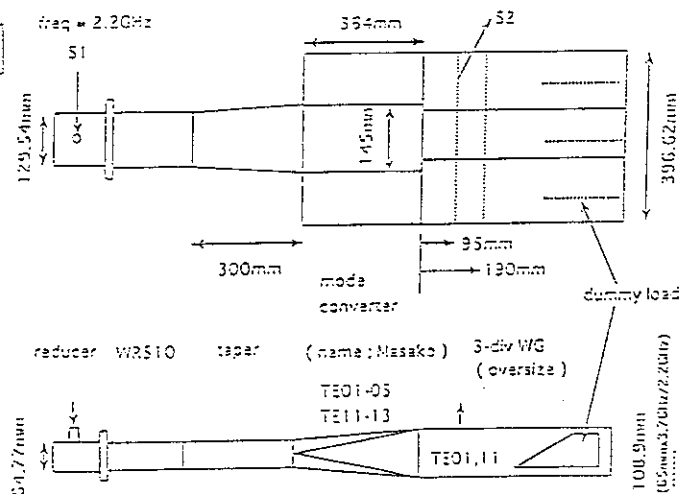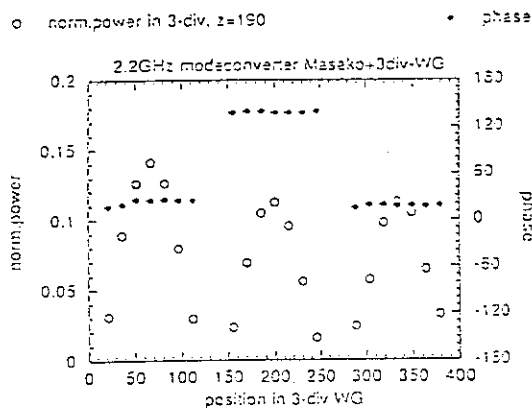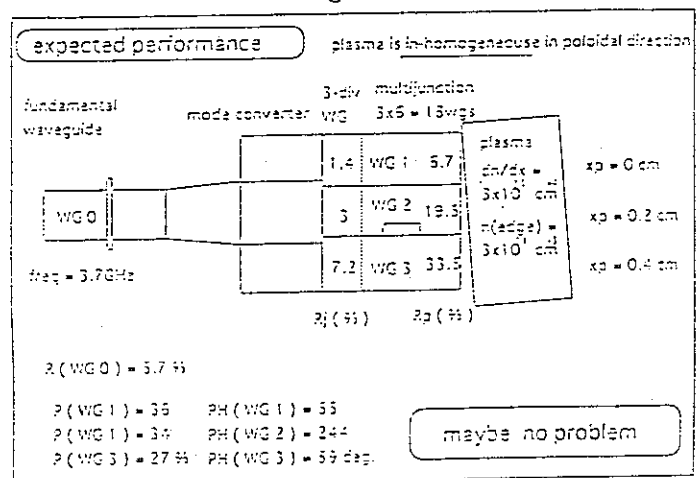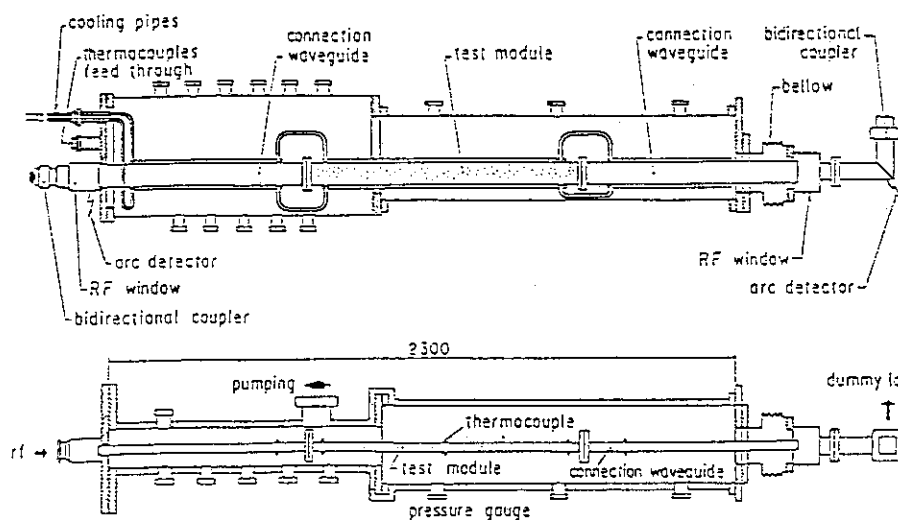

Figure 6

Figure 7

Figure 8

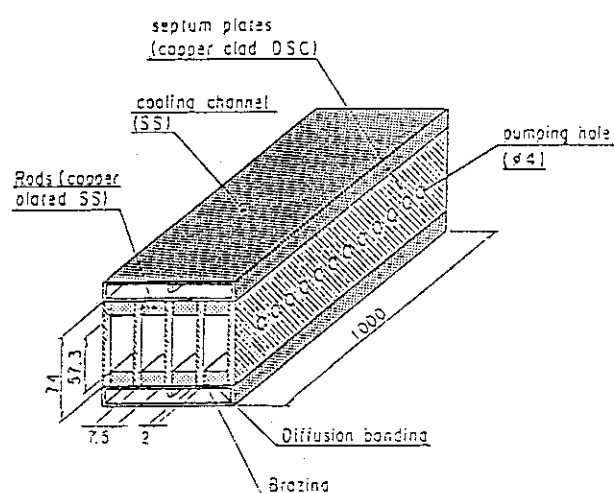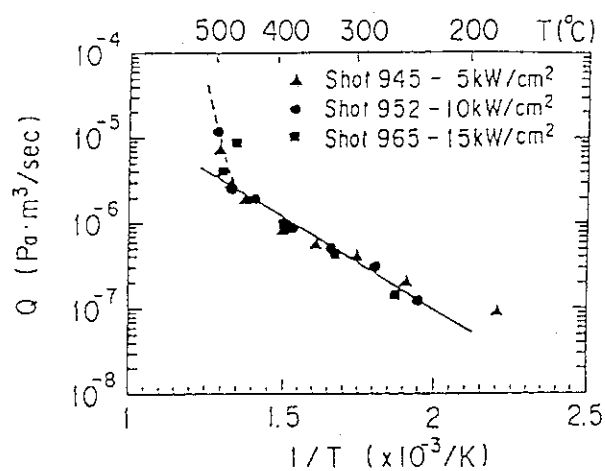
Figure 9

Figure 1

Figure 2
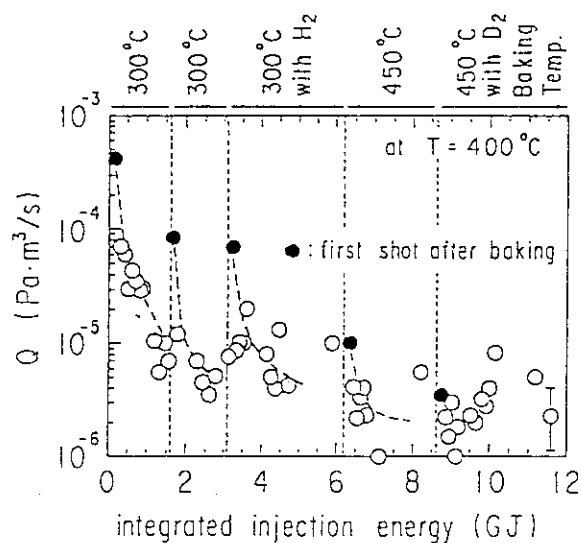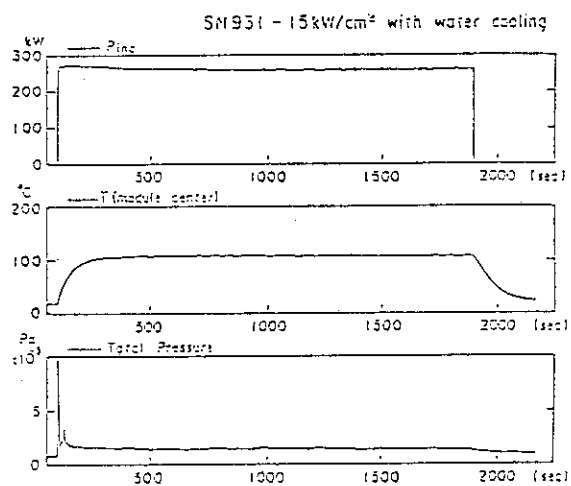

Figure 3

Figure 4

Figure 5

2. 7 Quasi Optical Antenna using a Strip Array
for
Lower Hybrid Current Drive

J.P. CRENN , Ph. BIBET , G. TONON

Département de Recherche sur la Fusion Controlée
Association EURATOM-CEA
Centre d'Etudes de Cadarache
13108 St Paul lez Durance
. FRANCE

1/ INTRODUCTION

In a future tokomak like ITER the amount of power needed to generate a current of 2 MA using Lower Hybrid Wave is evaluated to be about 50 MW at 5 GHz [1] . If the antenna is built using up to now concept , it leads to a total number of waveguides which is more than one thousand due to a power density chosen less than 5 kW/cm^2 [2] . Therefore the concept of PETELIN and SUVOROV using quasi optical antenna [3] seems to be attractive . The main principle consists in the diffraction of a plane wave by a rods array . A vacuum layer is used between the array and the plasma to filter the n = -1 order which is used to built a slow wave at the rigth n// value .

Here the antenna which is studied is an infinite array of strips of normalized width 2 ka , of periodicity kd and separated from the plasma by a distance kD (fig 1) (k is the free space wavenumber). The ratio η_{-1} of the power going into the n = -1 order to the total incident power is given depending on the different parameters . Then the problem of the reflected power is discussed . And finally the problem of a resonant cavity for decreasing the reflected power is considered .

2/ THEORITICAL MODEL

The incident plane wave is taken into account by its characteristic impedance $Z_c = Z_0 k_\perp /k_0$ where Z_0 is the vacuum impedance and k_0 is the free space wavenumber ,$k_\perp$ is the perpendicular wavenumber defined by $k_\perp = k_0 \cos \alpha$, α is the angle of incidence of the plane wave . The coupling coefficient c_n of the plane wave to an order of diffraction n is computed using the expression from [4] which gives the coefficient of diffraction of a plane wave by an infinite array of strips . It leads to :

$$\frac{C_n}{C_0} = \frac{\sin(n\pi h / d)}{(n\pi h / d)} \quad (1)$$

The plasma impedance for each diffraction order Z_{pn} for a step of density or a linear density gradient [5] (fig 2) is brougth back to the strip array using characteristic impedance of the diffraction order in free space Z_{cn}. It leads to a reflection coefficient ρ_{Dn} given by :

$$\rho_{Dn} = \frac{Z_{pn} - Z_{cn}}{Z_{pn} + Z_{cn}} \exp\left(-2\left|k_{\perp n}\right|D\right) \quad (2)$$

Z_{cn} is equal to $Z_0 k_{\perp n}/k_0$ with $k_{\perp n}$ the perpendicular wavenumber for each diffraction order which is given in free space by :

$$\frac{k_{\perp n}^2}{k_0^2} = 1 - \frac{k_{//n}^2}{k_0^2} \quad (3)$$

with $k_{//n}$ the parallel wavenumber for each order which depends on the angle of incidence and the periodicity of the strip kd :

$$n_{//n} = \frac{k_{//n}}{k_0} = \sin\alpha + n\frac{2\pi}{kd} \quad (4)$$

The normalized periodicity kd is chosen less than π, therefore only the n=0 order is propagating in free space, the others are evanescents. The transmission coefficient t through the strip array is computed using the equivalent circuit given by [6]. It leads then to an efficiency of absorption η_n per passage for each diffraction order n given by :

$$\eta_n = t\frac{C_n^2/C_0^2}{\cos\alpha}\frac{Z_0\,\mathrm{Re}(Z_{Dn})}{\left|Z_{Dn}\right|^2}\left|\frac{k_{\perp n}}{k_0}\right|^2 \quad (5)$$

with Z_{Dn} given by :

$$Z_{Dn} = Z_{cn}\frac{1 + \rho_{Dn}}{1 - \rho_{Dn}} \quad (6)$$

3/ NUMERICAL RESULTS
3-1/ EFFICIENCY PER PASSAGE

The main conclusions are that the parameters taken by PETELIN and SUVOROV α=45 degree , kd=2.9 and the ratio of density at the step over cutoff density n_0/n_c=2 appear to be an optimum . On fig 3 the efficiency η_{-1} is plotted depending on the parameters ka and kD . The figures from [3] have been superposed . For the rods arrays D is

the distance between the rods axis and the plasma . One can see a good agreement between the 2 models. The region kD<1 must not be considered because spurious space harmonics of order n ≠ -1 are not neglegible . For ka = 0.8 and kD = 1.1 the efficiency per passage for a step of density is 15 % . On fig 4 the influence of a linear density gradient ∇ne is studied , it is shown that the maximum value is obtained for ∇ne=0 which is the step of density case and that it is decreasing reaching for example for a decay length ne/∇ne of 1 cm ,which is a realistic case an efficiency of 10 %.To decrease the reflected power a resonant cavity must be studied .

3-2/ THE RESONANT CAVITY

In paper [3] it has been suggested to use 2 arrays distant from a normalized length kl . On fig 5 the reflection coefficient has been plotted depending on the angle of incidence and on the distance kl and using the geometrical optics assumption . It is supposed here that there is no reflection coming from the plasma . The reflected coefficient must be 10 times less than the efficiency per passage leading to a value of 1 % . This has for consequence that the angle of divergence of the incident beam must be less than 3.5 degrees . It means also that to have a certain n// flexibility the 2 arrays must be moveable . Due to the efficiency of 10 %, if the reflector is supposed perfect it is shown on fig 6 that 30 multipassages are necessary leading to a high increase of the total electric field .

But in order to built an efficient resonant system 4 problems have to be solved :

- How to excite the plane wave ? . One way should be to use a gaussian beam radiated for example by an oversized corrugated cylindric waveguide . To satisfy the condition of low angle of divergence on fig 7 the angle of divergence of a gaussian beam has been plotted depending on the distance to the waist and of the diameter in which 99 % of the total power is radiated . For 3.7 GHz for example it leads to a beam diameter which is about 2 meters .

- When the number of strips is finite the diffraction of the plane wave leads to a change of polarisation . The E polarisation is changing from tranverse to longitudinal to the incident wavenumber vector , this process is smaller when the number of strip is larger . On fig 8 the ratio of the power of the longitudinal polarization to the transverse one is plotted versus the distance from the strip array and for a number of strips of 100 . It is shown that even with 100 strips this ratio is more than 2 % .

- If the distance between the 2 arrays is only around one wavelength like in fig 5 for kl=6.2 there will not be any more a quasi optical propagation and therefore it will be a propagation with waveguide modes . The memory of the angle of incidence will be lost and the angle φ of the equivalent optical rays to the waveguide axis will be given by the cutoff wavenumber kc and the guided wavenumber kg for each propagating mode by the relations :

$$k_c = k \sin \varphi$$
$$k_s = k \cos \varphi \quad (7)$$

- Due to the width of the incident beam to satisfy a necessary condition to have small reflection , due also to the bad efficiency per passage $\eta\text{-}1 = 10\ \%$ which leads to a large number of multipassages and also taking into account the distance kl between the 2 arrays , the size in the toroidal direction of the antenna which is drawn on fig 9 will be very long more than 100 wavelengths .

4/ CONCLUSION

Up to now 3 laboratories have worked on this worked on this subject NizhnyNovgorod(Russia), Frascati (Italy), Cadarache (France). In [3] where an array of cylindric rods has been considered and with a plasma density step the maximum obtained efficiency η_{-1} is 15 % . In [7] where a finite array of cylindric rods has been taken into account and also with a step of density the global obtained coupling efficiency is 25 % with a directivity of 90 % .The product of these 2 numbers can be compared to η_{-1}. In this present paper where an infinite array of strips is considered the computed efficiency η_{-1} is in agreement with the first value and it is shown that when a realistic linear density gradient is taken into account this efficiency decreases to about 10 % .

Therefore to be relevant for a machine the efficiency η_{-1} must be improved by for example changing the shape of the rods . The design of an efficient resonant cavity and its computation is shown to be a difficult problem and has still to be realized .

BIBLIOGRAPHY

[1] NET Predesign report by the NET Team . Fusion Engineering and Design . vol . 21 Feb 93 p 298

[2] G . TONON et al . SOFT 1990 . Proceeding of the 16 th SOFT London U.K.

[3] M.I. PETELIN , E.V. SUVOROV ,Pisma v ZhTF (letters to Journal of Technical physics 1989 vol. 15 N°22 p 23)

[4] M. BORN and E. WOLF . Principle of optics . Pergamon press 1970

[5] J. STEVENS et al Edge density profile effects for lower hybrid waveguide coupling .Nuclear Fusion vol 21 n° 10 (1981)

[6] N. MARCUVITZ Waveguide Handbook Mc GRAW HILL 1951 p 280

[7] G. CINCOTTI et al . Full wave theory of a quasi optical launching system for Lower Hybrid Wave : preliminary results . 10 th Topical Conference on Radio Frequency power in plasmas . (1-3 April 1993)
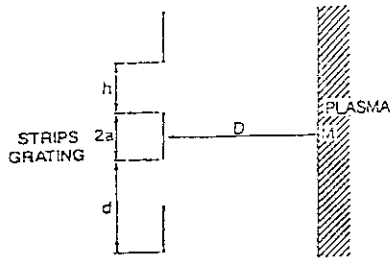
Fig 1 : Strips grating;

Fig 3 : Efficiency η_{-1} for an angle of incidence α=45 degrees, a normalized periodicity kd=2.9, $\frac{n_o}{n_c}$=2, with a step of density.
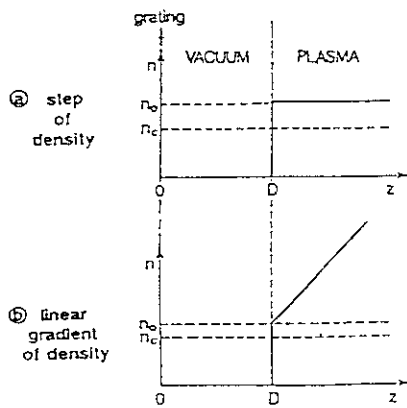
Fig 2 : Considered density profile
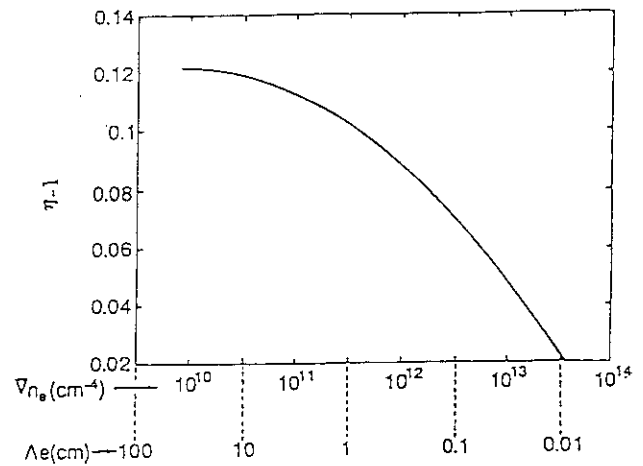
Fig 4 : Efficiency η_{-1} vs the linear density gradient ∇_{ne} with ka=0.8, kd=2.9, $\frac{n_o}{n_c}$=2, α=45 degrees, kD=1.1
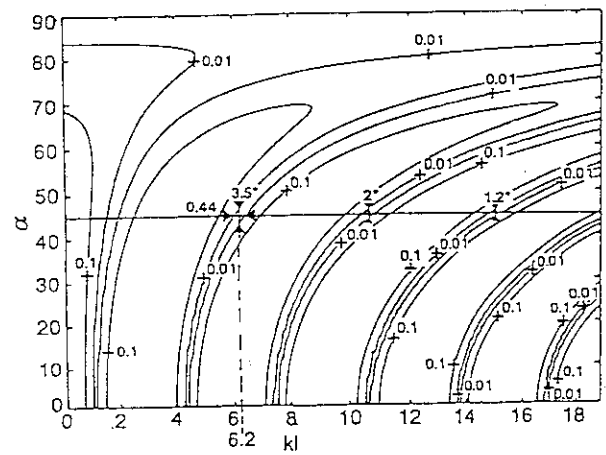
Fig 5 : Power reflection coefficient for kd=2.9, ka=0.8 The plasma is supposed to be a perfect load
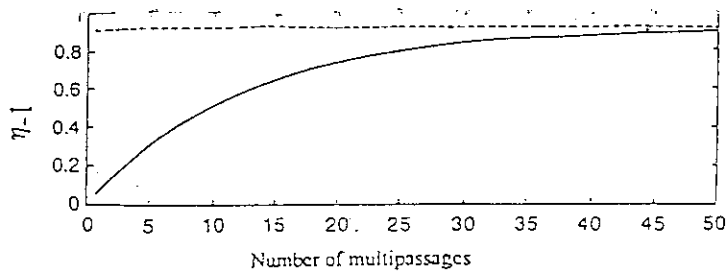
Fig 6 : Efficiency η_{-1} vs the number of passages. The coupling per pass is supposed to be 10%; the reflector is considered to be perfect.

Fig 8 : Ratio of the power in the longitudinal polarisation to the transverse one of the incident wave.

BEAM DIVERGENCE ε (z)

Fig 7 : Divergence of a gaussian beam.

Fig 9 : Size of the resonant cavity.

3. Electron Cyclotron Range of Frequencies

3. 1 FWCD and ECCD Experiments on DⅢ-D

R Prater, M Austin*, F W Baity†, R W Callis, S C Chiu,
J S deGrassie, R L Freeman, C B Forest, R H Goulding†,
R W Harvey, D J Hoffman†, H Ikezi, J Lohr, R A James‡,
K Kupfer‖, Y R Lin-Liu, T C Luce, C P Moeller, C C Petty,
R I Pinsker, M Porkolab♭, J. Squire‖ and V. Trukhin♮

General Atomics, San Diego, California, USA

Abstract. Fast wave current drive and electron cyclotron current drive experiments
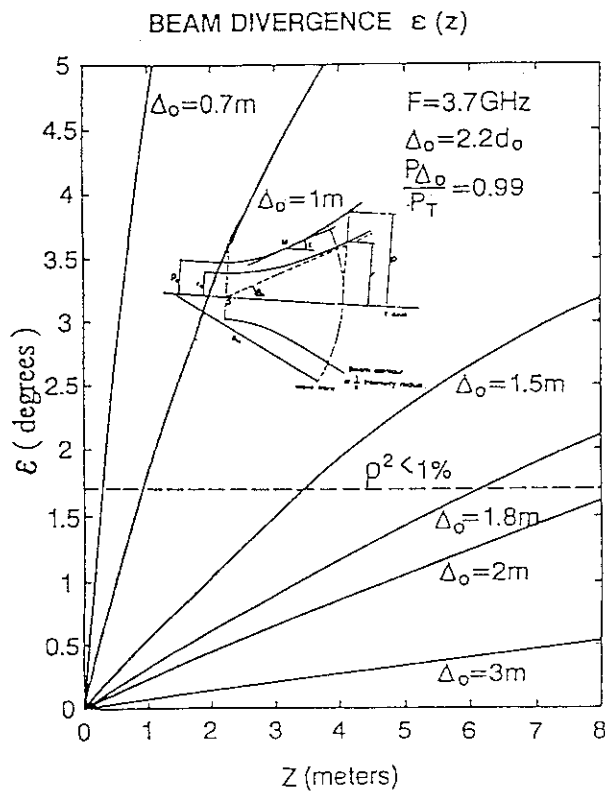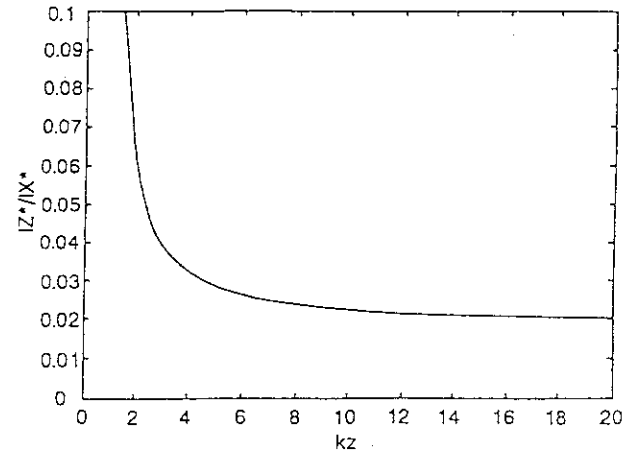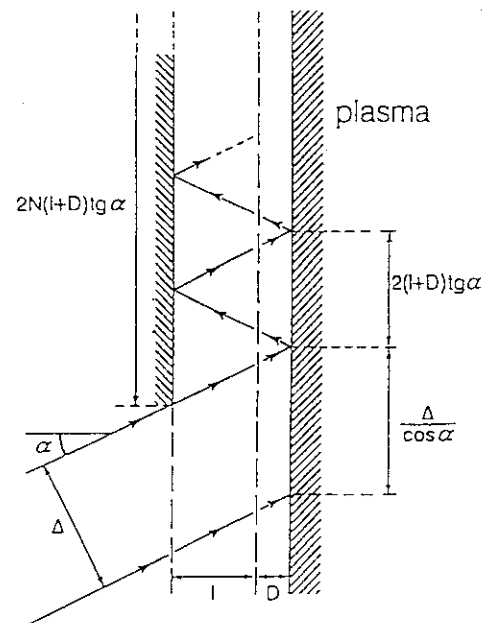have been performed on the DIII-D tokamak as part of the advanced tokamak program.
The goal of this program is to develop techniques for controlling the profile of the
current density in order to access regimes of improved confinement and stability. The
experiments on fast wave current drive used a four strap antenna with $90°$ phasing
between straps. A decoupler was used to help maintain the phasing, and feedback control
of the plasma position was used to keep the resistive loading constant. RF pickup loops
demonstrate that the directivity of the antenna is as expected. Plasma currents up to
0.18 MA were driven by 1.5 MW of fast wave power. Electron cyclotron current drive
experiments at 60 GHz have shown 0.1 MA of plasma current driven by 1 MW of power.
New fast wave and electron cyclotron heating systems are in development for DIII-D,
so that the goals of the advanced tokamak program can be carried out.

Current drive program on DIII-D

An active program is underway on the DIII-D tokamak to develop means of control of the
current profile. This program is motivated by observations on DIII-D (Lao et al., 1993; Ferron
et al., 1993) and some other tokamaks that both energy confinement and beta limits can
be improved through the proper choice of the current profile. On DIII-D, this has been
demonstrated in a series of experiments in which the current profile has been modified through
techniques which are inherently transient in nature: dynamic ramping of the plasma current
or elongation. By these means, discharges with a peaked current profile characterized by high
internal inductance ℓ_i have been generated. These discharges have energy confinement times
up to 3.6 times the L–mode scaling and beta values up to twice the Troyon limit. The improved
energy confinement is manifested as an increase in both the density and temperature of the
plasma. Other regimes of improved confinement have also been achieved, such as the VH–mode,
in which the current near the edge of the plasma generated by the bootstrap effect appears to
play a crucial role; the second stable core; and the high β_p discharge, in which the safety factor
on axis $q(0)$ can rise above 2.

The purpose of the current drive program on DIII-D is to achieve the confinement improve-
ment in a manner which can be projected to true steady state. If successful, this can lead to
reactors which require less plasma current to provide satisfactory confinement for ignition and
which can operate at higher beta than expected from the usual limits on tokamaks. The
reduction in plasma current also leads to reduced sensitivity of the power balance to the

*University of Maryland, College Park, Maryland, U.S.A.
†Oak Ridge National Laboratory, Oak Ridge, Tennessee, U.S.A.
‡Lawrence Livermore National Laboratory, Livermore, California, U.S.A.
‖Oak Ridge Associated Universities Postdoctoral Fellow.
♭Massachusetts Institute of Technology, Cambridge, Massachusetts, U.S.A.
♮Kurchatov Institute, Moscow, Russia.

efficiency of the current drive technique. Bootstrap current is projected to provide a large fraction of the total current without a cost in power.

Experimental programs are underway on DIII–D on fast wave current drive (FWCD) (Prater et al., 1993; Pinsker et al., 1993a) and electron cyclotron current drive (ECCD) (James et al., 1992) to develop means of controlling the current profile. The FWCD tends to be deposited where the electron temperature is highest, which is near the center of the discharge. FWCD is therefore particularly useful for generating discharges with high ℓ_i, in which the current is highly peaked on axis. ECCD has the highest efficiency when it is localized near the axis, but it can be conveniently placed well off axis by aiming the antennas toward the desired location or by changing the frequency or magnetic field to move the resonance to the right place. This is important for generating discharges in which the core is in the second stable regime. The combination of FWCD and ECCD will provide a unique degree of control over the current profile in DIII–D.

Fast wave current drive

The DIII–D tokamak has a flexible poloidal coil system which provides discharges in many configurations, including single and double null divertor and inside and outside wall limited. The experiments described in this paper were performed in double null configuration with major radius of 1.68 m, minor radius of 0.68 m, and elongation near 2. The working gas was deuterium. The walls of the vacuum vessel were fully covered by graphite tiles, and the vessel was boronized to reduce the gas recycling at the wall. Glow discharge cleaning in helium was also performed between discharges to reduce recycling. These techniques were effective in reducing the density increase which usually accompanies the application of fast wave power.

The fast wave current drive antenna (Hoffman et al., 1992) is located on the outer midplane of the vessel, as shown in the midplane cross section view of Fig. 1. It has four current straps spaced 22 cm between centers. Each strap has a vacuum feedthrough to provide for independent phasing. The straps are 45 cm high and 11 cm wide. The antenna is powered by a 2 MW source operating at 60 MHz. The maximum power delivered to the plasma is 1.6 MW.

The Faraday screen used in these experiments is a single layer of inconel rods which are tilted to be parallel with the total magnetic field for plasma current of 0.5 MA and toroidal field of 1.0 T. The rods are plasma sprayed with a boron carbide coating approximately 0.1 to 0.3 mm thick, depending on the location of the measurement. This Faraday screen replaced a double layer, optically opaque, titanium carbide/nitride coated Faraday screen which was used in previous experiments.

Since the FWCD antenna is powered by a single power source, the power must be split in such a manner that the phase and current of each strap is that necessary to produce the desired spectrum in $k_{\parallel}$. In the case of current drive, the desired phasing of the antenna is 90° with equal currents in each strap to produce a spectrum which is highly directional. At the same time, the impedance of the antenna must be matched to the transmission line in order to couple the power.

A major difficulty with current drive phasing is the mutual inductance which couples the straps of the antenna array. This inductance tends to make the phase control at 90° unstable and inhibits effective splitting of the power due to the toroidally directed power flow from one strap to another. In order to correct this, a decoupler was added to the transmission system (Pinsker et al., 1993b). The decoupler, shown schematically in Fig. 2, introduces a reactance between points A and B of Fig. 2 which cancels the reactance due to the coupling of the straps. The decoupler has proved very successful in generating the desired currents and phasing over a wide range of plasma conditions in DIII–D. The changes in the mutual reactance of the straps
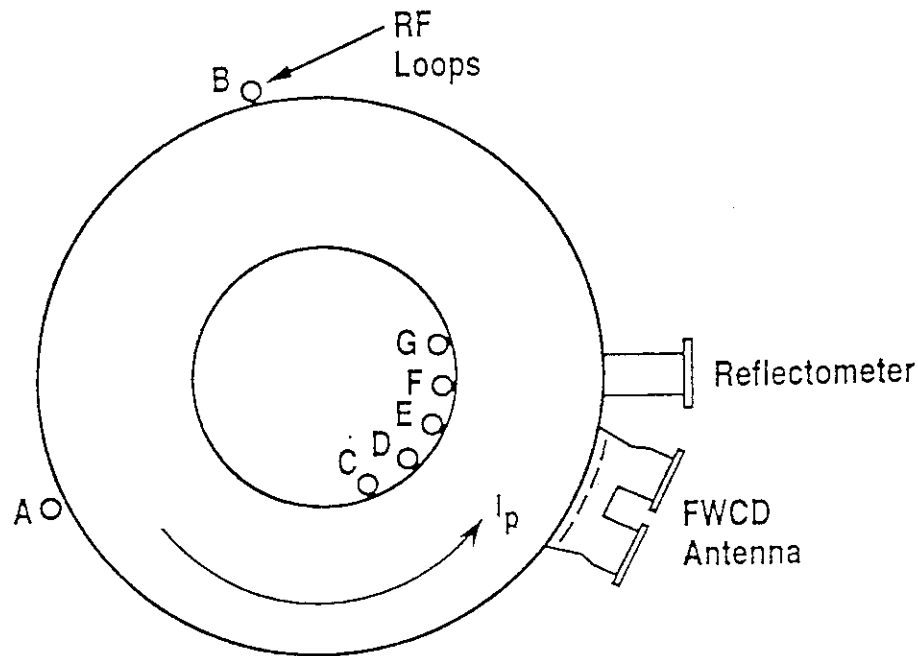
FIG. 1. A cross section at the midplane of DIII-D showing the FWCD antenna, the rf pickup loops labeled A through G, and the reflectometer.

due to varying plasma conditions has not caused problems provided the resistive loading is above about 1 Ω.

In order to further simplify the tuning process, feedback control of the plasma position was used to keep the loading constant at a preset value. Since the equilibrium in DIII-D is now fully controlled through feedback mechanisms implemented in real time by a digital computer, it was relatively easy to add an algorithm to shift the gap between the plasma and the antenna to keep the resistive component of the antenna loading fixed during a discharge. By this means, it was possible to keep the fast wave power at a constant high level through a transition from L-mode to H-mode and during the ELM-free phase of the H-mode. (ELMs are MHD activity localized near the edge of the plasma which cause large fluctuations in density at the edge of the plasma during H-mode discharges.) However, this system is not fast enough to correct for the loading changes caused by giant ELMs, so that at high power the transmitter rolls back due to excessive reflected power. But position control can compensate for the average change in the density profile caused by small, frequent "grassy" ELMs, and over 1 MW has been coupled under this condition in initial FWCD experiments in H-mode discharges with high power heating by neutral beams.

Fast wave power up to 1.6 MW was coupled to the plasma. At moderate rf power, the antenna was found to emit visible light from the Faraday screen, and at high power bright incandescent spots were found to occur at fixed locations on the screen. In extreme cases of high power and long pulses, incandescent chips of the boron carbide coating were emitted into the plasma. Visual inspection of the antenna after several days of operation showed that at some locations the boron carbide coating had come loose from the inconel substrate. This was mostly in locations where the coating had been applied too thickly. It is conjectured that experiments with intense neutral beam heating at low plasma current (< 0.6 MA) caused excessive localized heating of the antenna by fast beam ions with unconfined orbits, which caused some of the boron carbide to disadhere. At these locations the thermal capacity became poor, and rf
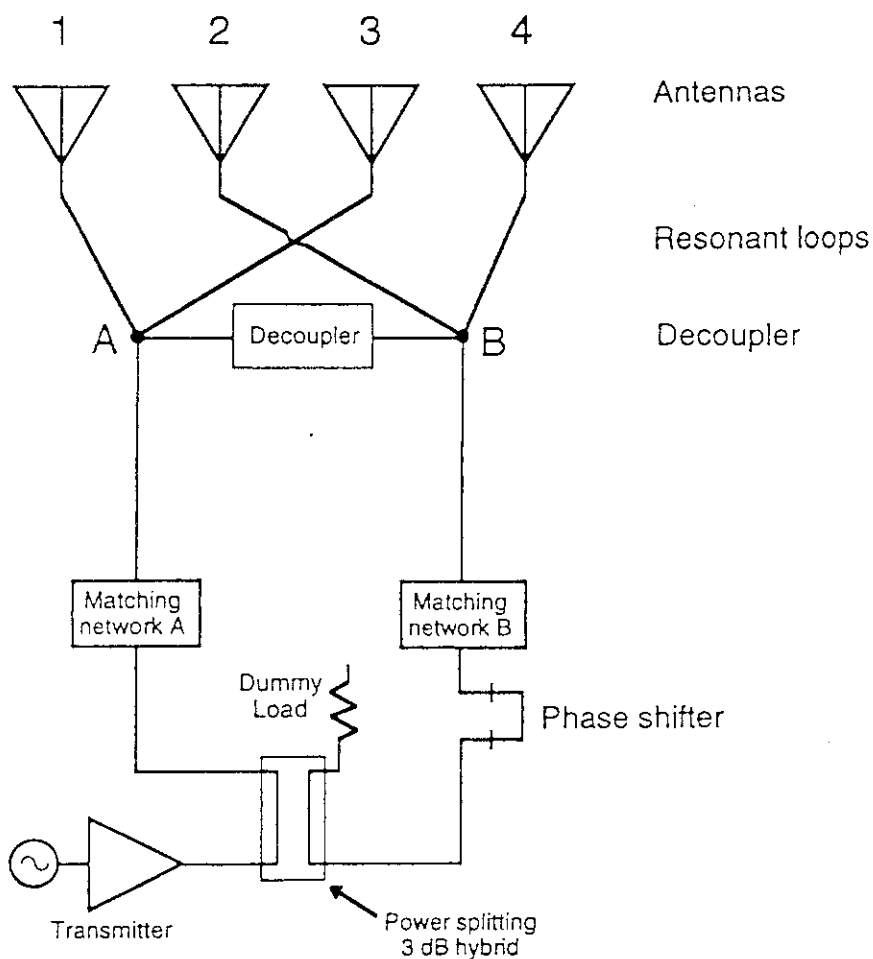
FIG. 2. The transmission line for the FWCD antenna. The decoupler which was inserted between points A and B provides a reactance which effectively cancels the mutual inductance between the straps.

combined with radiated power from the plasma caused overheating of the flakes. In spite of this problem, and without much conditioning, the antenna was successfully operated at the power limit of the rf source for pulses of several seconds.

The bars of the Faraday screen were tilted to be aligned with the magnetic field, following work on JET and elsewhere which suggested that alignment of the screen with the field resulted in reduced impurity generation. This was attributed to a reduction in the rf sheaths which form where the field lines intersect the bars of the Faraday screen. However, in extensive experiments on DIII-D in which the direction of the toroidal field was reversed, very little difference was found in the performance of the antenna, even though for the normal polarity the field lines were approximately parallel to the bars and for the reversed polarity the angle of the field lines to the bars was about 24°. Under both conditions, very little problem was found with the generation of impurities. From these results, we conclude that that the importance of tilting the bars is not very great. It is possible that the difference in these results from those on JET are related to the thorough boronization of the antenna on DIII-D.

A newly installed array of rf pickup loops was placed at several locations (shown in Fig. 1) to study the propagation and absorption of fast waves. The loops on the centerpost were

placed behind the tiles, and the loops on the outer wall were in port cavities. The outer wall probes A and B were placed above and below the midplane in order to lie approximately along a field line from the antenna. In all locations, measurements of both the fluctuating poloidal magnetic field $\bar{B}_p$ and the toroidal field $\bar{B}_t$ were made. Each magnetic fluctuation signal was beat with the applied rf and detected in quadrature, giving $|\bar{B}_{p,t}|\sin\phi$ and $|\bar{B}_{p,t}|\cos\phi$, where ϕ is the phase angle. Therefore, the phase, amplitude, and polarization of the detected wave are available as a function of time at the location of each loop.

The rf pickup loops illustrate some properties of the launched wave. Figure 3 shows an example for the beginning of a discharge. The antenna is phased $(0,0,0,0)$ and the fast wave power is very low, about 10 W. The signal in Fig. 3(d) is $|\bar{B}_t|\sin\phi$ from the loop directly across the plasma from the antenna (loop E in Fig. 1), and Fig. 3(e) shows the signal in quadrature to that in Fig. 3(d), from the same probe. These signals show a low frequency variation, which is due to the change in the phase at the pickup loop relative to the phase of the signal applied to the antenna caused by the gradual rise in density, Fig. 3(c). There is superimposed a high frequency component, which is due either to fluctuations in density or to components of the wave which travel a longer distance, maybe once around the torus, on the way to the pickup loop. The signal picked up on loop A, shown in Fig. 3(f), shows that the wave travels toroidally as well as directly across the plasma for 0° phasing. This can be understood from a study of the dispersion relation at high ω/Ω_i.

The pickup signals like those shown in Fig. 3 indicate the delay between the launched and the detected waves. The phase delay is proportional to the speed of the wave between the launcher and the detector. The phase velocity across the plasma is expected to be the Alfvén speed, $v_A = (B^2/M_i n)^{1/2}$, where M_i is the ion mass and n is the ion density. From this expression, $n = B^2\phi^2/\omega^2 L^2 M_i$, where L is the path length of the wave across the plasma. Figure 4 shows the right hand side of this equation as a function of time for loop E for the discharge of Fig. 3. Also shown is the density derived from the CO_2 interferometer. A correction factor of order unity has been applied to get the best agreement, since the average ion mass is not well known early in the discharge. Figure 4 shows that the Alfvén speed is an excellent description of the propagation speed of the wave.

The directionality of the antenna can be clearly seen from the signals from pickup loops A and B. Figure 5 shows a discharge at high power, 1.5 MW, in which the antenna phasing is $(0,0,\pi,\pi)$. For this antisymmetric phasing, the wave is launched with equal power in the forward and backward toroidal directions. The large size of the low frequency components of Fig. 5(e) and 5(f), representing the signals from probes A and B, show that the wave travels directly from the antenna to those locations. The signal from directly across the plasma, however, has only a high frequency component, which indicates that the wave arrived there only after traveling a path much longer than the distance from the antenna to loop A or B.

For current drive phasing, $(0,\pi/2,\pi,3\pi/2)$, the wave should travel in a single toroidal direction. This is shown in Fig. 6, for much the same conditions as for Fig. 5 except the antenna phasing. For current drive phasing, the direct pickup on loop B has disappeared, but the low frequency component, representing pickup after a short path length, remains on loop A. This is direct evidence that the spectrum is strongly weighted in the expected toroidal direction. Note that for these two discharges there was no ECH heating applied, so the electron temperature was low, about 1.5 keV, which makes the damping of the fast wave weak.

Experiments on FWCD using the directional current drive spectrum showed that up to 0.18 MA of the current was driven noninductively in discharges with 0.3 MA total plasma current, using 1.5 MW of fast wave power plus about 1 MW of ECH power. The plasma was scanned from 0.2 MA to 0.5 MA to determine the current at which the noninductive fraction (FWCD, ECCD, plus bootstrap) was maximum. The divertor cryopump was used to help control the density rise which normally accompanies the application of fast wave power; by this means, the density rise was held to a few times 10^{18} m^{-3}. These results represent a moderate
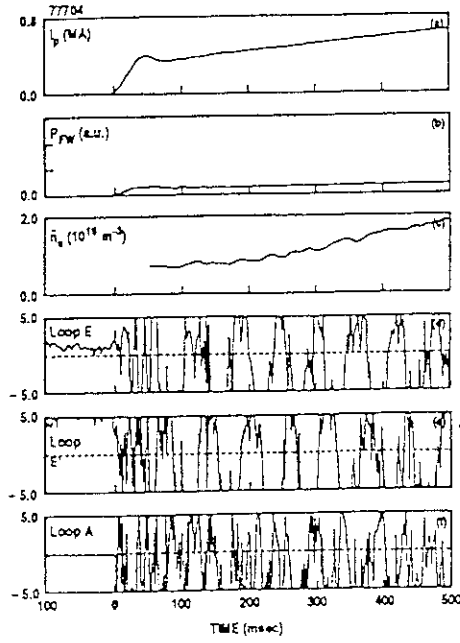
FIG. 3. Data from startup phase of discharge with very low power FW power in $(0,0,0,0)$ phasing. (a) Plasma current, (b) fast wave power, (c) line averaged density from CO_2 interferometer, (d) signal $|\tilde{B}_t| \sin \phi$ from pickup loop E of Fig. 1, (e) signal $|\tilde{B}_t| \cos \phi$ from same loop, and (f) signal $|\tilde{B}_t| \sin \phi$ from loop A.

FIG. 4. Line averaged density, from the discharge of Fig. 1. Also shown is the quantity $c\phi^2$, where c is a constant. Here, ϕ is derived from the signals shown in Fig. 3(d) and 3(e).
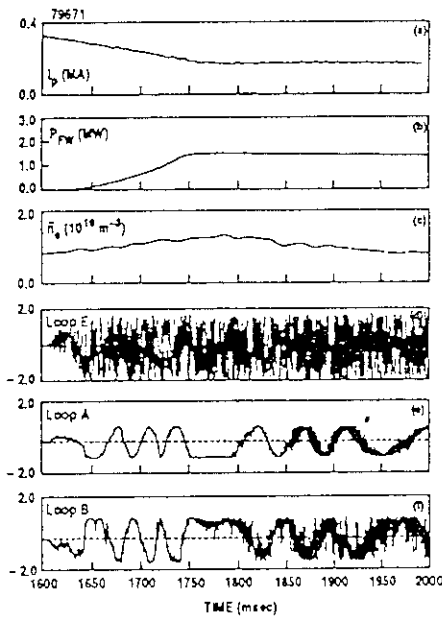

FIG. 5. Data from a discharge with 1.5 MW of fast wave heating with antisymmetric phasing $(0,0,\pi,\pi,)$. (a) Plasma current, (b) fast wave power, (c) line averaged density, and the signals $|\tilde{B}_t| \sin \phi$ (d) from pickup loop A of Fig. 1, (e) pickup loop A, and (f) pickup loop B.
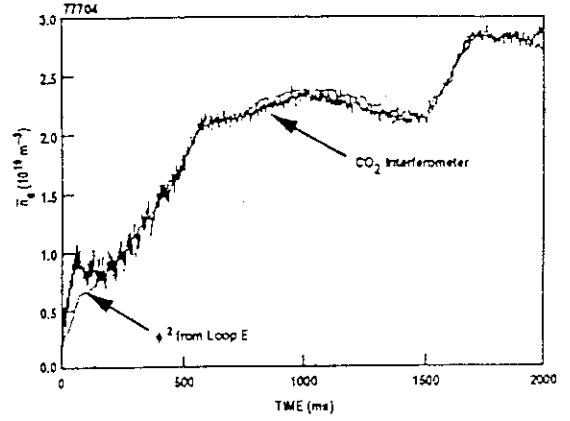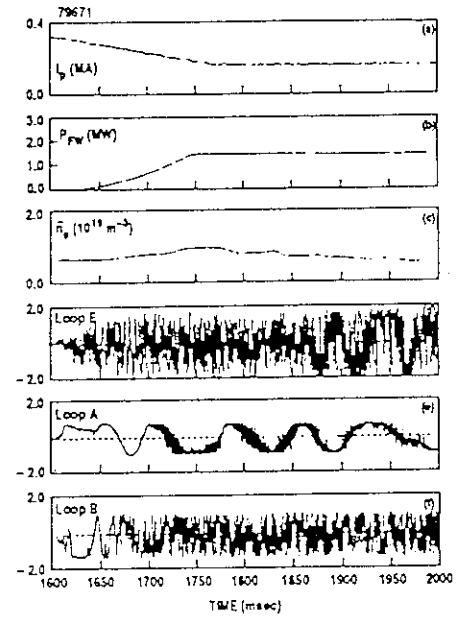

FIG. 6. Same as Fig. 5, except the antenna phasing is the directional current drive phasing $(0,\pi/2,\pi,3\pi/2)$.

improvement over results presented previously (Prater et al., 1993; Pinsker et al., 1993a), due primarily to increased rf power.

Another set of experiments in which FWCD was combined with a ramp-down of the plasma current demonstrated full current drive. For these experiments, the plasma current was ramped down from 0.4 MA to around 0.2 MA during combined FWCD and ECH injection. The purpose of the current ramp was to generate a discharge with high confinement relative to that of a steady discharge of the same current, due to the improved current profile (high ℓ_i) which is generated when current is removed preferentially from the outer part of the discharge.

After the current ramp down, the surface loop voltage was observed to remain negative for as long as the high power FWCD and ECH were applied, as shown in Fig. 7. Changing the FWCD antenna phasing from co-current to a nondirectional phasing $(0, \pi, \pi, 0)$ resulted in a more positive loop voltage, the analysis of which found no measurable current drive. These results indicate that complete current drive was achieved, albeit for a short period, and the amount of current drive depends upon the phasing of the FWCD antenna. The measured FWCD efficiency for full current drive cases is in reasonable agreement with theoretical calculations.

Electron cyclotron current drive

Experiments on DIII-D have found currents of up to 0.1 MA driven by ECCD, using about 1 MW of power at 60 GHz (James et al., 1992). The experiments were performed in discharges with total current of 0.3 to 0.5 MA, densities of 1 to 2×10^{19} m^{-3}, electron temperatures of 2.0 to 3.6 keV, Z_{eff} of 2.5 to 5.5, and toroidal field of 2 T. In these discharges, the electron distribution function is nearly Maxwellian, with no strong superthermal features.

In all cases, the current driven by ECCD is less than the total plasma current. This implies that an electric field remains in the plasma, and the modification of the distribution function due to the electric field has a measurable effect on the current driven by the electron cyclotron waves. At the same time, the ECH can generate a perpendicular tail which can pitch angle scatter into the parallel direction and increase the conductivity of the plasma even for fixed temperature of the bulk of the distribution. For these reasons, it is important to perform the analysis of the data using a Fokker-Planck code which includes these effects. Good agreement is obtained between the Fokker-Planck code and the experiment.

Future plans

In order to support full quasi-steady state current drive with control over the profile of the current, new fast wave and ECCD systems are being prepared for DIII-D as part of the advanced tokamak program. These systems will provide the needed flexibility and power to support the development of discharges with improved confinement and beta limits.

The fast wave current drive system for DIII-D is being upgraded by 4 MW in the 30 to 120 MHz frequency range (deGrassie et al., 1993), in addition to the existing 2 MW 30 to 60 MHz system. Two new ABB transmitters will be used to drive two new four-strap antennas. The transmitters have been installed, and installation of the antennas is scheduled for early 1994. The antennas will have recessed side walls, which improves the $k_{\parallel}$ spectrum but increases the mutual inductance, making the decoupler more important. The transmission and matching lines will be similar to those now installed on DIII-D, but with some important improvements. Resonant loops and a decoupler will be used in a manner very similar to that shown in Fig. 2, except that the resonant loops and decoupler will have elements to support operation over a range of frequencies. Another improvement is to use ceramic insulated, pressurized coaxial transmission lines. This system should be operable in mid-1994.
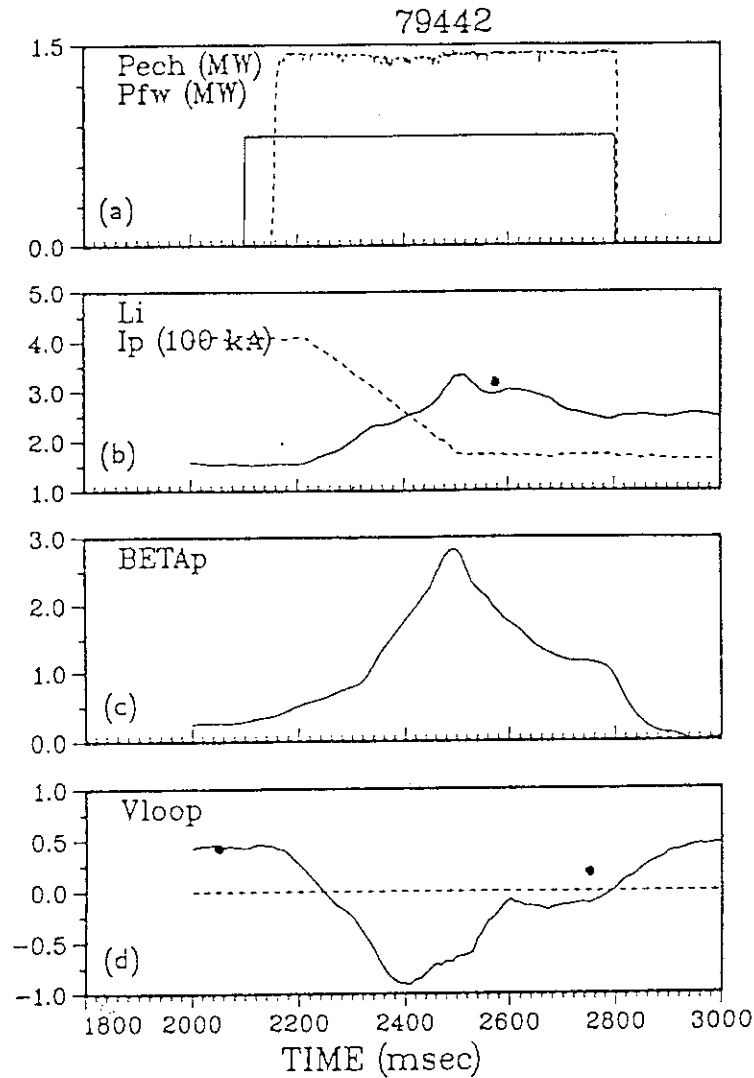
FIG. 7. Data from a discharge with high power FWCD in $\pi/2$ phasing and ECH, with a ramp down of the plasma current. Toroidal field is 1 T. (a) Fast wave power (dashed line) and ECH power (solid line), (b) plasma current (dashed line) and internal inductance ℓ_i(solid line), (c) beta poloidal, and (d) loop voltage at the surface of the plasma. The solid dots on (d) represent the calculated loop voltage for the measured profiles of T_e, n_e, and Z_{eff}.

A new high power ECH system is also under development for DIII-D (Callis et al., 1992). This system will operate at 110 GHz, using gyrotrons in the power range 0.5 to 1 MW. Such gyrotrons are being developed by Varian and by Gycom, and both types will be tested on DIII-D. A prototype transmission line has been installed for tests which will take place when a long pulse gyrotron is ready. The small diameter (31.75 mm) corrugated evacuated transmission line is expected to be suitable for powers well in excess of 1 MW. Bends are made through phase-corrected mitre bends. The antenna is a copper plated graphite plate which focuses and steers the beam with external control over the direction of the beam in the vertical plane.

Modeling of transport and current drive in DIII-D shows that 4.6 MW of fast wave power plus 2.5 MW of neutral beam power or ECH power can support a fully noninductive high ℓ_i

discharge with average beta of 2% and total current of 1 MA (deGrassie et al., 1993). In order to achieve a second stable core configuration, it is necessary to drive current well off axis, and ECH is suitable for this purpose. With 8.5 MW of ECCD, 0.4 MA of current can be driven near $r/a \approx 0.5$, which supports the current profile expected to be stable to a beta above 5.7%.

Acknowledgements

References

Lao L L, Ferron J R, Taylor T s et al. 1993 *Phys. Rev. Lett.* **70** 3435.

Ferron J R, Lao L L, Taylor T S et al. 1993 *Phys. Fluids B* **5** 2532.

Prater R, James R A, Petty C C et al. Plasma Phys. and Contr. Fusion **35** (1993) A53.

Pinsker R I, Petty C C, Porkolab M et al. 1993a *Plasma Physics and Controlled Nuclear Fusion Research, Würtzburg, 1992* (Vienna: International Atomic Energy Agency) Vol 1, p 683.

James R A et al. 1992 *Phys. Rev. A* **45** 8783.

Hoffman D J, Goulding R H, Ryan P M et al. 1992 *Proc. IAEA Technical Committee Meeting on Fast Wave Current Drive in Reactor Scale Tokamaks, Arles, 1991* (St Paul lez Durance: EURATOM–CEA) p 456.

Pinsker R I, Petty C C, Cary W P et al. 1993 "Experimental test of a two-port decoupler in the DIII–D fast wave current drive system" (General Atomics Report GA-A21498); to be published in *Proc. 15th IEEE/NPSS Symp. on Fusion Engineering, Hyannis, 1993.*

deGrassie J S, Lin-Liu Y R, Petty C C et al. 1993 "Simulation of enhanced tokamak performance on DIII–D using fast wave current drive," to be published in *Proc. 20th EPS Conference on Controlled Fusion and Plasma Physics, Lisbon, 1993.*

Callis R, Cary W, Moeller C et al. 1992 *AIP Conference Proceedings 244 Radio Frequency Power in Plasmas, Charleston, 1991* (New York: AIP) p 25.

3. 2   ECH Experiments on WT-3 by a Focusing Launcher

Y. Terumichi, S. Yoshimura, K. Hanada,
T. Maekawa, M. Nakamura,* T. Maehara,
S. Tabuchi, K. Nakamura and T. Iinuma
Department of Physics, Faculty of Science, Kyoto University
·Kyoto, Japan

1: Heat transport in Lower Hybrid Current Drive Plasma
A short electron cyclotron heating ($2\Omega_e$ECH) pulse can locally perturb the electron temperature. The temperature perturbation can be observed in the soft X-ray signal intensity. The radial thermal diffusion coefficient, χ_e, is estimated by propagation delay of the perturbed signal. It is found that there is a threshold of lower hybrid power above which χ_e falls to 1/2 - 1/3 times that of the target ohmic heating plasma. The improvement of χ_e is confirmed as effective $2\Omega_e$ECH that the central electron temperatuire rises up to 3 times that of the target plasma.

2: Stabilization of m=2 MHD Activity by $2\Omega_e$ECH
The stabilization or destabilization of the m/n=2/1 MHD activity by local $2\Omega_e$ECH was studied systematically in the WT-3 tokamak. The toroidal magnetic field was carefully scanned for signs of suppression or enhancement of the activity. It is found that the m/n=2/1 and 1/1 activities can be suppressed simultaneously when the electron cyclotron resonance in the equatorial plane is located in the narrow region near q=2 or 1 surface and the width of the region near q=1 depends on ECH power and the region spread inward q=1 surface with ECH power.

---

*On leave from Osaka Institute of Technology, Osaka, Japan

1 Experimental apparatus

Schematic diagram of the experimental setup is shown in Fig.1. WT-3 is a small standard tokamak which has a circular cross section. The major radius R_0 is 65cm, minor radius a=20cm, maximum toroidal field B_T=1.75T, the maximu plasma current I_p=150kA and discharge duration is about 100ms. LHCD power source is a 2GHz, 350kW, 100ms klystron. LH power is launched by a two stacked 4 waveguide arrays. ECH power source is a 56Ghz, 200kW, 100ms gyrotron. EC power is launched from the low field side by a focusing antenna which is consisted of a Vlasov converter, eliptical and plane reflectors (Fig.2). Microwave is injected into plasmas nearly perpendicular (84 degrees) to the toroidal magnetic field in the extraordinary mode.

Main diagnostics used in this experiment are two sets of soft X-ray computerized tomography (CT) systems, soft X-ray pulse height analyzer for electron temperature measurement and pickup coils (magnetic probe). One of the CT systems is consisted of 3 soft X-ray pin hole cameras located at the top, bottom, and horizontal port in a poloidal cross section (3 port soft X-ray detector array). The spatial resolution of this system is 1.5cm and time resolution is 5μs. Another has 5 cameras (5 port soft X-ray detector array) and the arrangement is shown in Fig.3. Each camera has 20 detectors on the movable image plane which are sensitive to soft X-ray in the range of 0.2-27keV and has changable Be absorber foils (5, 15 and 100μm). The spatial resolution of this system is 1 - 2cm depending on the sweep range and the time resolution is 5μs. The sweep range of the pin hole camera can be changed by changing the distance between the pinhole and the imaging plane. This helps to observe the wide range of the plasma cross section. Magnetic signal is detected by 12 pickup coils which sorround the plasma in a poloidal cross section. There are 4 sets of pickup coils and they are located 90 degrees apart each other in toroidal direction.

2 Heat transport in Lower Hybrid Current Drive Plasma

When LHCD is superimposed on Ohmic heating plasma with sawtooth oscillations, sawtooth oscillations can be stabilized above the threshold power level of lower hybrid power P_{LH}. It is interesting to investigate the thermal diffusion coefficient with sawtooth and without sawtooth. Thermal perturbation is generated by short (0.2-1ms) $2\Omega_e$ECH pulse injected into the center of the plasma. The temperature perturbation can be detected as perturbation of soft X-ray signal intensity on the detectors of 3 port CT system. The waveform of the detected signals are shown in Fig.4. Each trace in Fig.4 shows a signal intensity of different viewing chord and 'r' shows the distance from the plasma center. The heat pulse propagation can be seen in Fig.4(a) in OH plasma with sawtooth oscillations and in Fig.4(b) without them. There are apparent difference of the propagation velocity of the thermal pertubations (see r=10.1cm curves). It seems that χ_e with sawtooth is larger than χ_e without sawtooth. It is interesting in the P_{LH} dependence of χ_e. So, χ_e is estimated from the propagation delay in various P_{LH} level. χ_e is plotted versus P_{LH} in Fig.5. χ_e of OH plasma with sawtooth is about 6m^2/s. Sawtooth can be stabilized above P_{LH}=40kW and simultaneously χ_e decreases and is about 2m^2/s above P_{LH}=100kW. In the range of P_{LH}=50-90kW, sawtooth is stabilized but m=1 MHD oscillation appears. Above 100kW, there is no sawtooth and no m=1 oscillation. To confirm the improvement of χ_e, $2\Omega_e$ECH is applied to the plasma with χ_e=2m^2/s at the plasma center. Waveform of soft X-ray signal intensity of the central chord is shown in Fig.6. Open and solid circle shows the electron temperature measured by soft X-ray pulse height analysis. Electron temperture at the center increase up to 0.75 keV which is about 3 times that of the target plasma.

To confirm whether the improvement of χ_e depends on sawtooth stabilization or not, a plasma with high safety factor, q_L=7.5, is selected as a target plasma. There is no sawtooth in OH target plasma. LHCD is superimposed the sawtoothless plasma. Power

dependence of χ_e is found to be similar to the low q_L=3.7 plasma with sawtooth. There is a threshold power level of about 100kW above which χ_e can be improved. χ_e of OH plasma is about $8m^2/s$ and that of the LHCD plasma with $P_{LH} > 100$kW is about $3.5m^2/s$. It can be concluded that sawtooth stabilization is not essential for the improvement of χ_e. The mechanism is not known yet, but LHCD makes the current profile rather broad. $2\Omega_e$ECH at the center also raises the central temperature in this case.

3 Stabilization of m=2 MHD Activity by $2\Omega_e$ ECH

Stabilization and enhancement of m=2 MHD activity by $2\Omega_e$ ECH are studied systematically. Stable m/n=2/1 MHD activity can be observed in a plasma with q_L=2.7. Identification of the oscillation mode is made by getting the phase difference of magnetic probe signal detected 2 sets of magnetic probes located 180 degree apart each other in toroidal direction. To change the location of $2\Omega_e$ECR layer, toroidal magnetic field is scanned with keeping q_L constant. Fig.7 shows the typical waveforms of the magnetic probe signal. The upper left diagram shows the location of the ECR layer in the poloidal cross section where (1), (2) and (3) correspond to the waveform (1), (2) and (3) respectively. The most inner thin circle shows q=1 surface and the next one shows q=2 surface estimated by 5 port CT system. Waveform (1) and (3) show that the magnetic fluctuations can be stabilized when the ECR zone in the equatorial plane is located near q=2 or q=1 surface. Enhancement of the oscillation can be observed when ECR layer is located in the region between q=1 and 2 surfaces. The oscillation can be observed in the soft X-ray signal detected by the 5 port CT detectors. The frequency is the same as the magnetic signal. The contour map of the amplitude of the oscillation in the polodal cross section is reconstructed by CT method for OH plasma and the temporal evolution every $10\mu s$ is shown in Fig.8. There can be seen something like islands. One island can be seen in th inner space and two islands about 180 degrees apart each other are in the

periphery. The inner island rotates faster than the peripheral islands. Rotating velocity of the inner one is 2 times that of the peripheral one. The inner island shows m=1 MHD oscillation. From this figure, q=1 surface is estimated as the trace of the most inner maximum amplutude and q=2 surface is estimated as that of the peripheral one. In Fig.9, signal ratio of ECH case to OH case for magnetic probe, soft X-ray signal detected on the chord tangential to near q=2 (r/a=0.75) and q=1 (r/a=0.3) surfaces are plotted versus position of the ECR in the equatorial plane. All signal amplitudes are suppressed when the ECR zone is near q=1 and 2 surfaces. This clearly shows that m=2 and m=1 modes are strongly coupled each other. Coupling mechanism is not yet clear experimentally but toroidal coupling seems to be the most available mechanism.

Summary

Heat Transport in Lower Hybrid Current Drive Plsma

1:χ_e of LHCD plasma is measured at first by using ECH heat pulse propagation.

2:There are some threshold power level for improvement of χ_e.

3:Stabilization of the sawtooth oscillation is not essential for improvement of χ_e.

4:Improvement of χ_e is confirmed by effective ECH of central electron temperature.

Stabilization of m=2 MHD Activity by $2\Omega_e$ECH

1:Stabilization and enhancement of m=2 MHD activity by $2\Omega_e$ ECH are studied systematically.

2:m/n=1/1 and 2/1 MHD activities can be simultaneously stabilized when $2\Omega_e$ECR is located in the narrow region near the q=1 and 2 surfaces in the equatorial plane.

3:The width of the region near q=1 surface depends on the ECH power and the region spreads inward q=1 surface with ECH power.
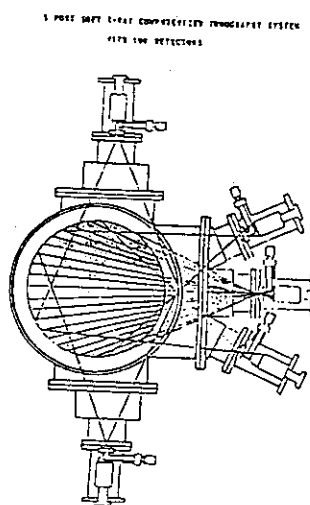
4:m=1 and m=2 activities are strongly coupled each other.
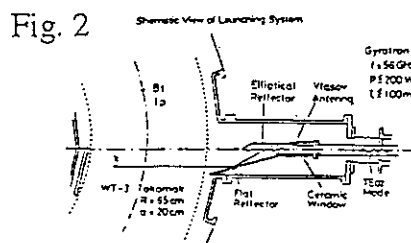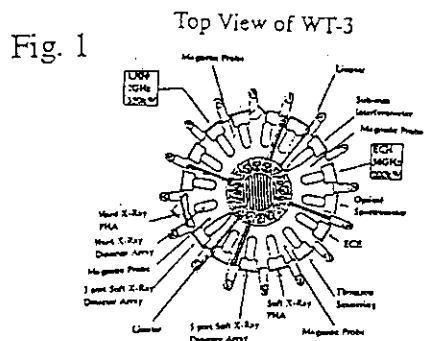
Top View of WT-3

Fig. 1

Fig. 2
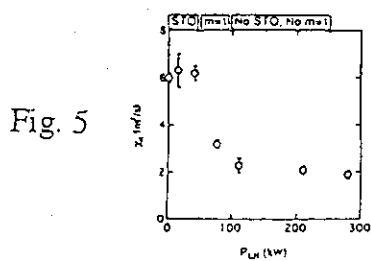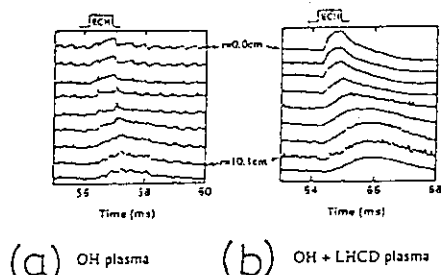
Fig. 3

Fig. 4 ECH heat pulse propagation in STO and no STO plasmas
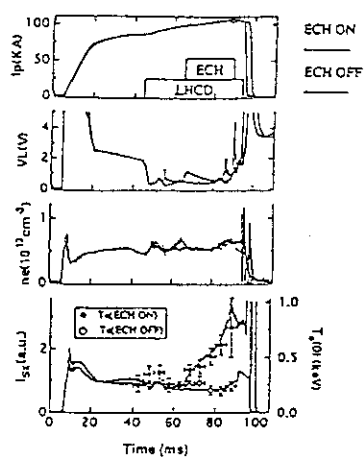
Waveforms of LHCD+ECH plasma

(a) OH plasma
(b) OH + LHCD plasma

Fig. 5

Fig. 6

Fig. 7
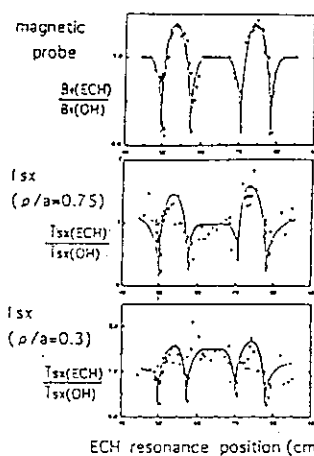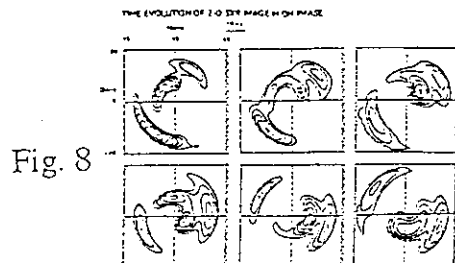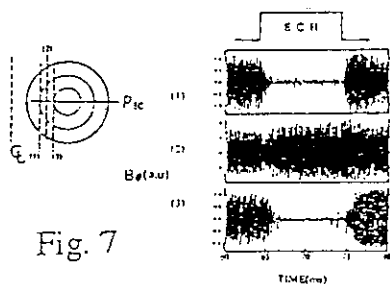
Fig. 8

magnetic
probe

Fig. 9

ECH resonance position (cm)

3. 3   Recent Results with 140GHz ECRH at the W7-AS Stellarator

V. Erckmann, U. Gasparino, H. Maaßberg, W7-AS Team, NBI Team
Max-Planck-Institut für Plasmaphysik, EURATOM Ass., Garching, Germany

W. Kasparek, G.A. Müller, P.G. Schüller
Institut für Plasmaforschung, Universität Stuttgart, Germany

A. Borschegovsky, V.I.Il'in*, V.I.Kurbatov, S.Malygin**, N.Alexandrov,
V.I.Malygin***
* Kurchatov Inst., Moscow, Russia, ** SALUT, Nizhny Novgorod, Russia,
*** Inst. for Applied Physics, Nizhny Novgorod, Russia

ABSTRACT

A new 140 GHz ECRH system with 0.9 MW power at up to 0.4 s pulse duration (alternatively 0.5 MW, <1.1 s) is running at the W7-AS Stellarator. The Gaussian output mode of a russian gyrotron is transmitted via an optical transmission line and launcher. A comparison of this advanced 140 GHz ECRH-system with the conventional 70 GHz system (0.8 MW, 3 s) is given with emphasis on technological aspects and investment-costs. Plasma experiments on combined heating with 70 GHz ECRH at moderate densities $\leq 6 \; 10^{19} \, m^{-3}$ or with NBI at high densities $\leq 1.1 \; 10^{20} \, m^{-3}$ are presented.

1.   INTRODUCTION

ECRH experiments in the last decade followed closely the technological progress in the development of high power microwave sources. The source availability was setting the leading constraint on the ECRH systems with respect to installed power, frequency and pulse length. Frequencies in the range of 100 - 160 GHz extend the accessible plasma density towards $1 - 5 \cdot 10^{20} \, m^{-3}$ (depending on the launched mode and resonant field), which matches the experimental needs for present-day and next-step fusion devices and removes the density constraints of previous ECRH systems at lower frequencies. The first 140 GHz plasma experiments were performed at W7-AS in 1991 with a prototype gyrotron from the development line at KfK with 0.1 MW power and the basic features predicted by linear theory (e.g. wave absorption, power deposition profile, cut-off density) were verified experimentally. Severe technological problems arose, however, by pushing theconventional gyrotron design towards the design target of 1-2 MW and CW operation and new approaches were sought. Advanced gyrotrons with 0.9 MW output power at 0.4 s pulse duration or, alternatively, 0.5 MW at >1 s pulse duration as an intermediate step towards the target requirements became available recently and plasma experiments were performed at W7-AS /1/ and T-10 /2/, which mark a qualitative step forward in both, the experimental application of ECRH and the technological progress in the source development. ECRH is of particular importance for Stellarators because of the capability to provide net current free plasma built up and heating. A 10 MW, CW ECRH system at 140 GHz is planned for the next step stellarator W7-X and the presently

running system at W7-AS is considered a pilot system for W7-X. In Sec. 2 some experiments are reviewed to illustrate the capability of an advanced ECRH system. A comparison of advanced versus conventional ECRH-systems is given with emphasis on technological aspects and costs in Sec.3.

2. EXPERIMENTAL RESULTS

The linear theory of wave propagation and absorption is well developed and explaines the experimental results with high accur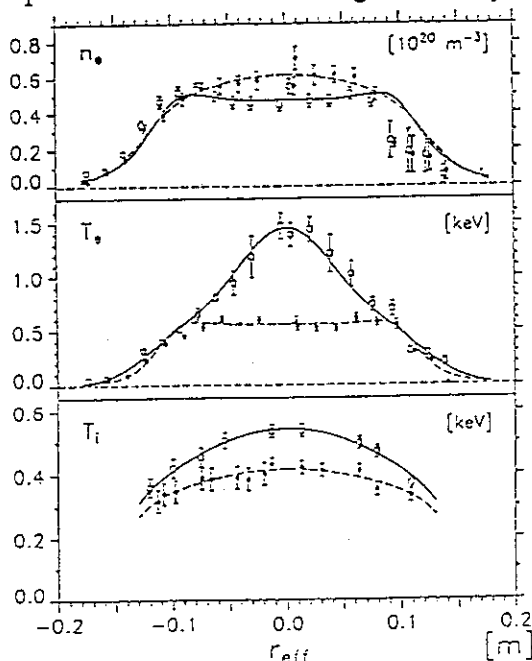acy, which indicates, that at the present day power densities of the order 10 MW/m^3 non-linear effects seem to play a minor role /3/. Ray-tracing calculations for determination of the power deposition profile in 3-D geometry became a routine method and the results could be verified experimentally. Among the various wave launching scenarios the low field side launch is the most favourable because of port accessibility in toroidal devices and comparatively easy remote maintenance in future contaminated devices. Although the cut-off density for a given frequency at O-mode, 1 harmonic is half that as for X-mode, 1st harmonic high-field side launch, the density accessible with 140 GHz is already $2.5 \cdot 10^{20}$ m^{-3} (for low field side launch) and thus may satisfy the requirements of next step plasma experiments. An example for profile shaping of temperature and density is given in Fig. 1. for on- and off-axis power deposition at $r_{eff} = 8$ cm, where the microwave beam was geometrically steered off-axis at constant magnetic induction. A discussion of the transport physics of

Fig. 1: Plasma profile response of the electron- (T_e) and ion temperature (T_i) and the electron density n_e to ECRH power deposition on axis (squares, # 23498) and off axis (dots, # 23515) in W7-AS.

W7-AS in comparison to off-axis heating in tokamaks (e.g. DIII-D off-axis ECRH) is beyond the scope of this paper and is discussed elsewhere /4,5/.

At high densities the collisional electron-ion coupling becomes strong and the ion transport plays a major role in contrast to previous experiments, which were restricted to low density due to the low cut-off density at lower ECRH-frequencies.
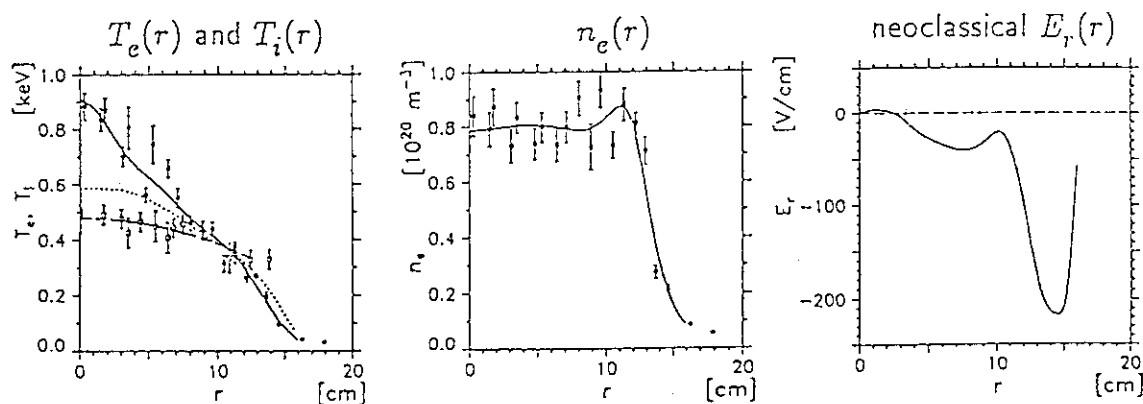
Fig. 2: Radial profiles of the electron- and ion temperature, the density and the calculated radial electric field for a high density H-mode discharge sustained with 0.4 MW ECRH power at 140 GHz (on axis deposition).

The profiles of T_i, T_e, n_e and the ambipolar radial electric field from neoclassical theory are plotted in Fig.2 for an H-mode discharge with 0.4 MW ECRH-power. The ions are closely linked to the electrons in the gradient region via collisional coupling and tend to dominate the energy balance /4,6/. The dotted line denotes the ion-temperature profile calculated for neoclassical ion-heat conduction taking into account the radial electric field distribution.

Experiments with combined ECRH and NBI-heating were performed in a wide parameter range at moderate densities around $n_{eo} \approx 5 \times 10^{19} \, m^{-3}$ and high densities around $n_{eo} \approx 1 \times 10^{20} \, m^{-3}$ with both, on- and off-axis power deposition of ECRH. An example is given in Fig. 3 with on axis ECRH at $n_{eo} \approx 5 \times 10^{19} \, m^{-3}$. The discharge is

started by a 70 GHz, 0.4 MW pre-pulse followed by a 140 GHz pulse, which is turned off at 0.95 s. NBI is added with 0.35 MW power at 0.6 s and turned off at 1.15 s, i.e. the final phase of the discharge from 0.95 to 1.15 s is heated by NBI only. During the ECR-heated prephase and the combined heating phase a pre-programmed constant density is maintained by feedback controlled gas puffing, whereas after switch off of ECRH the density increases, although the external gas feed is turned off by the feedback system. The density increase with pure NBI heating is a well known feature at W7-AS /7/ where beam fuelling and recycling fluxes have a comparable contribution to the overall density rise. Despite the beam fuelling (typically $1 \times 10^{20} \, s^{-1}$ for 0.35 MW beam power), the density can be controlled with combined heating. This is found also at high plasma densities and with combination of 0.75 MW ECRH and 0.7 MW NBI heating. As a rule, the density control could be maintained as long as the ECRH power was approximately equal or higher than the

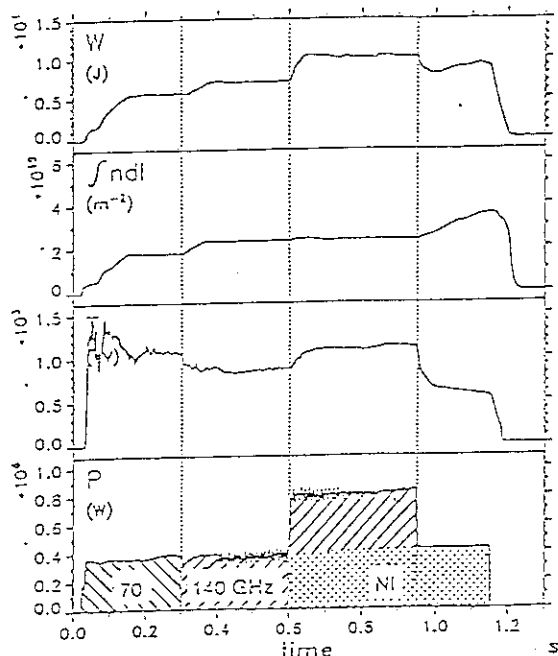Fig. 3: Time evolution of the total stored plasma energy W, the line integrated density $\int ndl$, the central electron temperature from SX-diagnostics and the cumulative input power P for combined heating with ECRH and NBI.

NBI power. For these combined heating discharges a degradation of the impurity confinement time for on axis ECRH as compared to off-axis ECR-heated discharges was measured by laser blow-off techniques with peaked electron temperature profiles which may offer a possibility for impurity control in combined heating discharges by proper profile shaping.

Experiments on ECCD were performed at several devices e.g./2,8,9/. In stellarators the EC-driven current can be measured with high accuracy because of the absence of large "obscuring" inductive currents as in tokamaks. ECCD-experiments at W7-AS could be well described by linear theory /10/, if trapped particle effects are taken into account. The influence of trapped particles on the ECCD efficiency was investigated in W7-AS with two different magnetic field configurations, which were controlled by the external coil currents. For case 1 a local magnetic field maximum is located in the wave-particle interaction region of ECRH, i.e. the trapped particle impact on the ECCD efficiency is mainly due to friction with the current carrying passing particles (standard case). In case 2 the minimum of the magnetic field is placed in the ECRH plane and consequently a considerable fraction of the injected ECRH power interacts directly with trapped particles, which do not contribute to ECCD. Both configurations have a comparable total trapped particle fraction of about 40 % on axis. The experiments were

performed at 2nd harmonic X-mode with a resonant magnetic field of 1.25 T. The plasma is heated by 0.4 MW ECRH power and 0.2 MW were used for current drive. Both the EC-driven current component and the bootstrap current component were compensated (Ip=0) by an inductively driven current (OH-transformer feedback). The required loop voltage is plotted at a function of the launch angle in Fig. 4 for both cases.
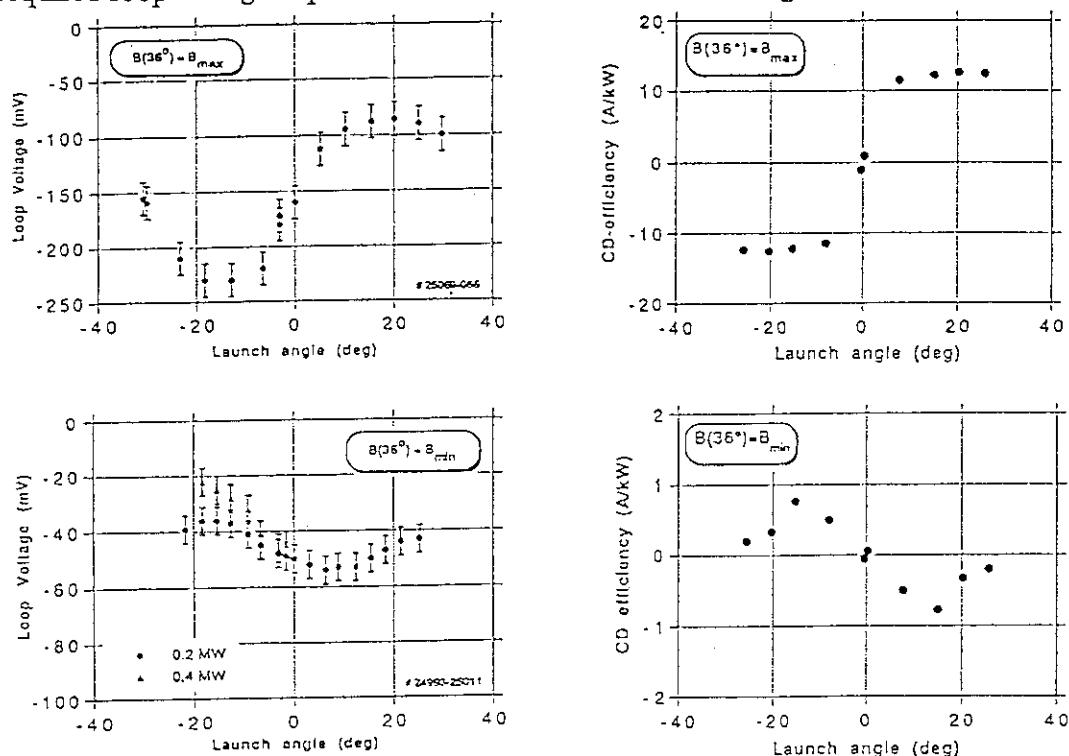

Fig. 4:   Left: Loop voltage response on a launch angle scan with plasma net-current I_p=0 for two magnetic field configurations. The discharges are heated with 0.4 MW ECRH, the launch angle scan is performed with 0.2 MW (dots) and 0.4 MW (triangles). Right: Modelling of the current drive efficiency for both cases.

The loop voltage at perpendicular launch ($\varphi = 0$, no ECCD) is nonzero and indicates the compensation of the bootstrap current alone. Two effects are clearly seen, i.e. the loop voltage and thus the driven current is much smaller in the case where the trapped particles are located mainly in the ECRH-plane (note the different scales) and the ECCD-efficiency even changes sign. This is in agreement with theoretical predictions as shown in Fig.4 using linearized theory in the long mean free path. The degradation of the ECCD efficiency is mainly due to the large fraction of the injected ECRH-power, which is directly absorbed by trapped particles without contributing to current drive. The reversal of the sign as compared to the usual current drive mechanism is a consequence of the ECRH-induced trapping of otherwise barely passing particles.

3.   TECHNOLOGICAL ASPECTS:
   ADVANCED VS. CONVENTIONAL ECRH SYSTEMS

The comparatively low power per gyrotron (0.1 - 0.2 MW) and the related complexity of the ECRH-systems limited the total installed ECRH-power to moderate values, the largest systems operating so far with conventional gyrotrons are installed at DIII-D (10 tubes, 2 MW, 60 GHz), at COMPASS (10 tubes, 60 GHz, 2 MW) and at W7-AS (5 tubes, 1 MW, 70 GHz). In order to satisfy the demands for multi-megawatt heating in next-step devices and to compete with present day heating installations at large machines, an increase of the unit-power towards 1-2 MW is mandatory. The technological gyrotron problems arising from these high power demands required new gyrotron concepts. An elegant solution was provided by the Russian research institute IAP, which followed the idea of high order volume mode cavities to tackle the problem of cavity loading and optical mode converters implemented in the gyrotron, which decouple the

microwaves and electron beam dump. A principle sketch of such a gyrotron is seen in Fig. 5.The cavity mode is converted directly into a Gaussian output mode, which can be easily transmitted through free space or in oversized corrugated waveguides. A further simplification with remarkable c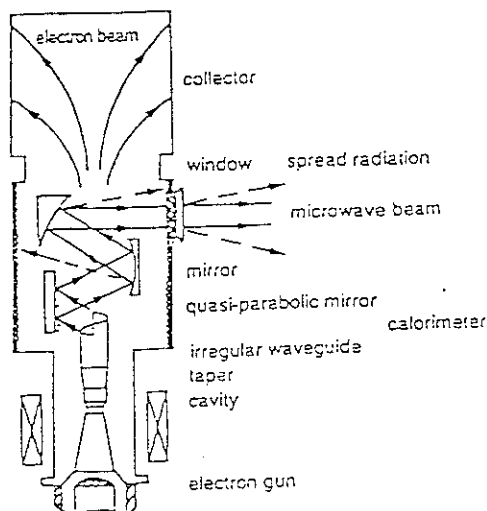onsequences is the absence of a control anode, which reduces the demands for the electronic control circuits and the DC-power supplies substantially.The Gaussian mode output of the advanced gyrotrons simplifies the transmission system design and technology. Whereas sophisticated waveguide transmission systems with special mode converters and rf-detection systems had to be developed in the past to match the individual gyrotron output mode mixture and transform the gyrotron mode to the wanted linearly polarised mode, the Gaussian radiation from advanced gyrotrons can be transmitted by simple optical mirror systems or with oversized HE_{11} waveguides with high power capability and low losses /11/. A cost comparison of advanced vs. conventional ECRH systems, which is based on the actual costs of the systems with 70 GHz and 140 GHz at W7-AS is given in Fig. 6. It should be noted, that the 70 GHz system is

Fig.5:   Lay-out of an advanced 140 GHz Gyrotron with built-in quasioptical mode converter and a lateral Gaussian microwave output beam.

capable of 3 s pulse duration, whereas the 140 GHz system is limited to 0.4 s in the high power (0.9 MW) operation. The costs for both systems do not take into account provisions for CW operation in order to allow for a comparison on the basis of existing systems. CW-operation is likely to be easier and thus cheaper with the optical transmission system at 140 GHz than with the waveguide system at 70 GHz, because the mirrors have a low power density and cooling is straight forward. So this aspect again favours the advanced concept. Cooling of in-vessel structures, which are esentially the same for both systems, do not indroduce additional criteria for the cost comparison. A cost reduction of the total system by more than a factor of 2 is achieved. The most pronounced savings are of course at the sources, it should be noted, however, that the cost savings at the peripheral systems are large also due to the
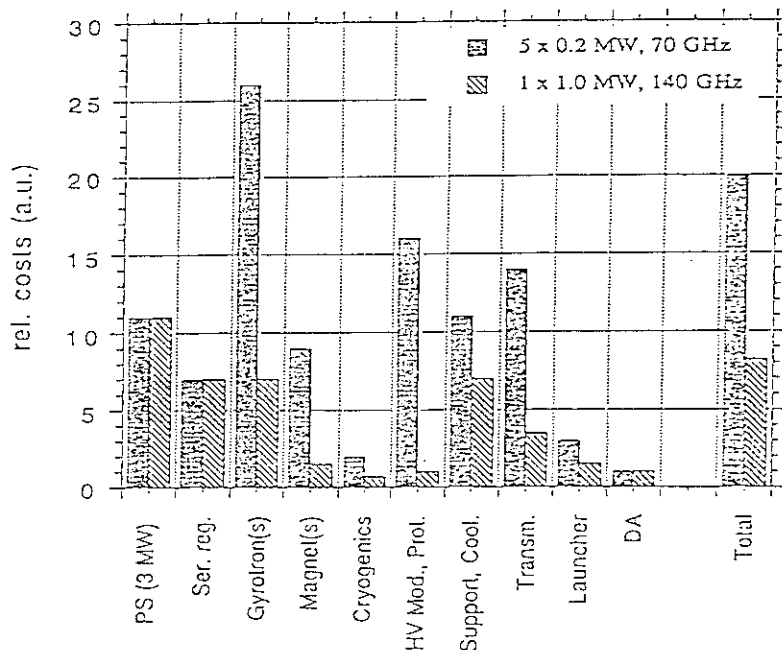

Fig. 6:   Cost comparison of components of a conventional (70 GHz) and an advanced (140 GHz) ECRH system in arbitrary units.

simplified protection system and the transmission line. In order to get an idea of the total costs per watt, the typical costs of conventional ECRH systems are comparable in many installations and of the order of 9-12 DM/Watt.

The most severe problems in pushing the existing pulsed systems towards CW operation were identified to be the gyrotron collector and cavity heat removal and the output window. As a consequence, some industries and laboratories proposed a partially (window at the gyrotron and no window at the torus) or fully (no windows at all) windowless solution, which requires evacuated waveguides with differential pumping and in- vacuum beam control and monitoring. Such a solution would introduce additional complexity and possibly jeopardize the progress achieved in both, simplification and cost reduction of ECRH-systems. It is questionable whether such a system is compatible with next step needs in an radioactive environment. We think, therefore, that windows at both, the gyrotron and the torus end of the transmission system are mandatory to maintain the advantages of the advanced gyrotron systems. There is strong effort in R&D under way to find proper technological solutions for windows, which can handle MW power levels in CW operation (e.g.distributed windows or cryo-cooled windows).

4. CONCLUSIONS

A qualitative step towards the goals of high frequency, high power ECRH systems was made by the development and experimental application of advanced 140 GHz gyrotrons from the Russian development line. Experiments with 140 GHz ECRH were successfully performed at W7-AS and show the expected benefits with respect to high density plasma operation and wide range applicability for heating, current drive and diagnostics. A thorough optimization of the ECRH system, which makes full use of the advantages of the new sources as compared to the conventional ones leads to a significant simplification and a cost reduction. The investment costs of such systems become comparable to other high power heating systems while the inherent ECRH advantages (narrow power deposition, remote launching) are maintained. CW operation at the MW level is still to be demonstrated and requires R&D efforts to solve the window and collector problems.

References:
[1]   V. Erckmann, et al., Phys. Rev. Lett.70, 14 (1993), 2086
[2]   V.V. Alikaev et al., Proc. 14 th Intern. Conf. on Plasma Physics and Controlled Nuclear Fusion Research, Würzburg, Germany, (1992), IAEA-CN-56/E-1-5
[3]   U. Gasparino, Proc. of the 8th Joint Workshop on ECE and ECRH,Gut Ising, Germany, (1992), p. 19
[4]   H.Maaßberg, 20 th EPS Conference on Controlled Fusion and Plasma Physics, Lisboa, Portugal, 1993, to be published.
[5]   C.C. Petty, et al., Proc. 18th EPS Conference on Controlled Fusion and Plasma Heating, Berlin, Germany, (1991), Vol.15 C, Part III, p 237.
[6]   M.Kick et al., 20 th EPS Conference on Controlled Fusion and Plasma Physics, Lisboa, Portugal, Vol. 17C, Part I (1993), p. 357
[7]   H. Renner, et al., Plasma Physics and Contr. Nucl. Fusion Research 1990, Vol. 2, IAEA, Vienna (1991) p. 439
[8]   V. Erckmann, U. Gasparino, H. Maaßberg, Plasma Physics and Contolled Fusion, Vol. 34, No.13, (1992), p. 1917
[9]   T. Luce, et al., Plasma Physics and Controlled Nuclear Fusion Research, 1990, Vol. 1, IAEA, Vienna (1991) p 631
[10]   V. Erckmann, et al., Plasma Physics and Controlled Nuclear Fusion Research, 1990, Vol. 2, IAEA, Vienna (1991) p 555
[11]   W. Kasparek, Proc. of the 8th Joint Workshop on ECE and ECRH, Gut Ising, Germany, (1992), p. 423

3. 4 Electron Cyclotron Resonance Heating for Controlling Potential and Transport along Open Field Lines

Y.Kiwamoto, T.Saito, Y.Tatematsu, I.Katanuma, Y.Yoshimura and T.Tamano

Plasma Research Center, University of Tsukuba
Tsukuba Ibaraki 305, Japan

1. Introduction

Transport of particles and energy in a plasma along magnetic field lines is a matter of great interest in connection with diverter operation in tori as well as in tandem mirror confinement. Contribution of electron cyclotron resonance heating (ECRH) has been recognized not only in heating but also in controlling plasma transport. In tandem mirrors ECRH is one of the major contributors to tailoring a potential profile, as exemplified in Fig.1, for increasing transport barrier atop magnetic mirror reflection. The outward transport of warm electrons is reduced by descending potential profiles either inside mirrors or along monotonically expanding magnetic field lines connecting to the machine wall.[1,2] However, the potential profile helps to increase an inward flux of colder electrons if they are produced at the machine end.[3] At every exchange of warm and cold electrons, the kinetic energy of a warm electron is lost to the end wall. A similar exchange process is expected along open magnetic flux connecting to a diverter in a torus.

Mirror reflection is not enough to reduce the influx of the colder electrons if the mirror ratio is not large or if the colder species is accelerated by the potential difference. A new role of ECRH has been proposed in a concept of thermal dike as a means to enhance the mirror reflection of colder electrons by increasing their pitch angles.[4] In this paper requirements to ECRH are discussed based on analyses of single particle dynamics in an open magnetic field. A scenario of a basic experiment of the thermal dike on the GAMMA10 tandem mirror is described.

FIG.1. Magnetic and potential profile along open field lines in tandem mirror.
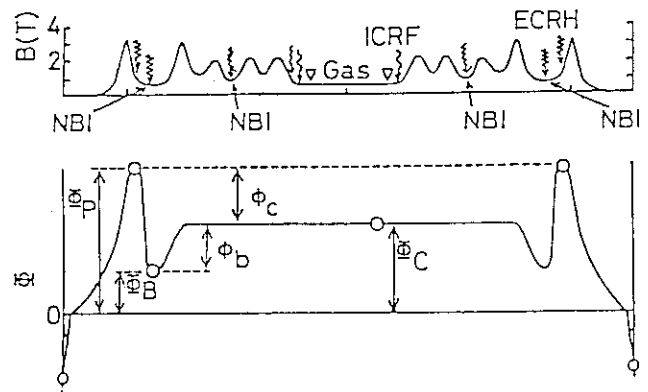
2. Power Loss Reduction by Thermal Dike

Let us consider particle transport in the magnetic and potential configurations as given in Fig.2. Cold secondary electrons are produced by impinging flux of ions (J_i) and electrons (J_1) with yield of γ_i and γ_e, respectively. They are accelerated by a potential difference $\Delta\phi = \Delta\phi_1 + \Delta\phi_2$ and reach the mirror throat $(B = B_m)$. Here the potential differences, $\Delta\phi_1$ and $\Delta\phi_2$, are separated at the location of ECRH with $B = B_R$.

FIG.2. Schematic profiles of potential and magnetic field strength along open field lines connecting to end plat. or diverter plate. Cold electrons are produced at $B = B_0$, and move to $B = B_R$ accelerated by a potential difference $\Delta\phi_1$. The potential difference across the point with B_R and the mirror throat with B_m is $\Delta\phi_2$. ECRH is applied at $B = B_R$.
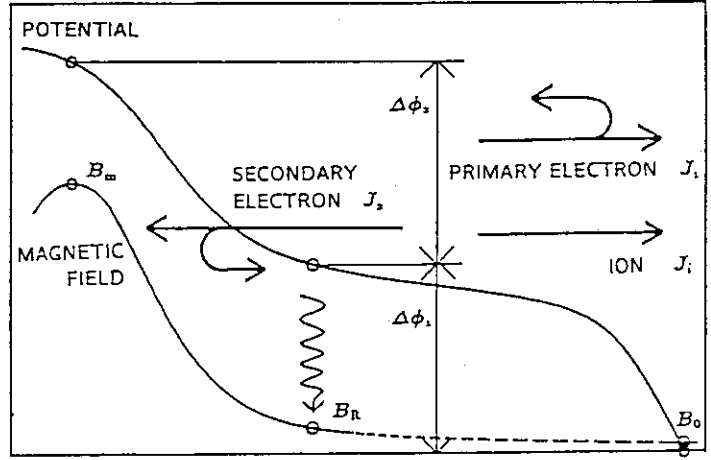
Without ECRH the flux J_{i0} of ions should balance with the net electron flux$J_{e0} = J_{10} - J_{20}$ composed of primary electrons (J_{10}) and secondary electrons (J_{20}) induced by J_{i0} and J_{10}. Therefore the electron flux are given as $J_{10} = J_{i0}(1 + \gamma_i)/(1 - \gamma_e)$ and $J_{20} = J_{i0}(\gamma_e + \gamma_i)/(1 - \gamma_e)$.

If the secondary electrons are reflected with a probability of R by a thermal dike, the current balance relations lead to $J_1 = J_i[1 + \gamma_i - R(\gamma_i + \gamma_e')]/[1 - \gamma_e + R(\gamma_e - \gamma_e')]$ for primary electrons and $J_2 = J_i[\gamma_e + \gamma_i]/[1 - \gamma_e + R(\gamma_e - \gamma_e')]$ for secondary electrons. Here γ_e' stands for the electron yield from the reflected secondary electrons. The transverse energy gain $\Delta W_\perp$ required for secondary electrons to be reflected at the mirror throat B_m is given as

$$\Delta W_\perp = e(\Delta\phi_1 + \Delta\phi_2)\left(\frac{B_m}{B_R} - 1\right)^{-1} = e\Delta\phi\left(\frac{B_m}{B_R} - 1\right)^{-1}.$$

The power loss to the end wall is written as $P_0 = T_{ew}J_{10}$ in the absence of thermal dike, and as $P_w = T_{ew}J_1 + \Delta W_\perp R J_2$ with its presence, where T_{ew} is the temperature of primary electrons. The ratio of the power losses is given by the following relation,

$$\frac{P_w}{P_0} = \frac{(1 - \gamma_e)[1 + \gamma_i - R(\gamma_i + \gamma_e') + \alpha R(\gamma_e + \gamma_i)]}{(1 + \gamma_i)[1 - \gamma_e + R(\gamma_e - \gamma_e')]}\frac{J_i}{J_{i0}},$$

where

$$\alpha = \frac{\Delta W_\perp}{T_{ew}} = \frac{e\Delta\phi}{T_{ew}}\left(\frac{B_m}{B_R} - 1\right)^{-1}.$$

Typical value of α is ≈ 1 in tori and ≈ 0.1 in the GAMMA 10 end region where a basic experiment on thermal dike is carried out.

Using a simplifying approximation that $\gamma_e = \gamma_i = \gamma = 2\gamma_e'$, the normalized end-loss power P_w/P_0 is evaluated as a function of γ and R for different value of α as in Fig.3. For small α, P_w/P_0 is substantially reduced with increasing R and with increasing γ. But for a larger value of α (≥ 1.5), a reduction in the power loss is expected with thermal dike only if a large amount of secondary electron yield is present.

The heating power required for thermal dike may be given by $P_H = \Delta W_\perp J_2$, so that if normalized with P_0 it is written as

$$\frac{P_H}{P_0} = \frac{\alpha}{1 + R(\gamma_e - \gamma_e')/(1 - \gamma_e)}\frac{\gamma_e + \gamma_i}{1 + \gamma_i}\frac{J_i}{J_{i0}}.$$

Therefore the required heating power is substantially small compared with the loss power P_0 in the absence of thermal dike if α is small and/or γ_e is close to 1.

FIG.3. Ratio of end-loss powers with and without thermal dike. The ratio P_w/P_0 is plotted as a function of secondary electron yield γ for different values of reflection probability R. Four plates correspond to different values of α.
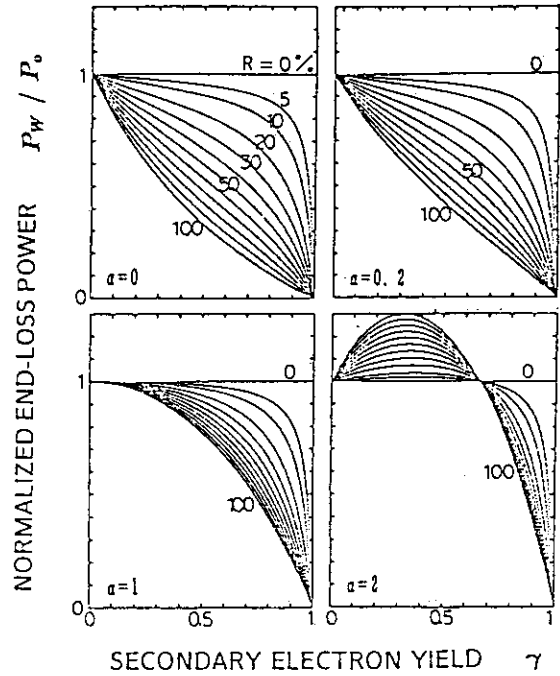
3. Requirements to ECRH

The reflection probability R is determined by ECRH, and $\Delta W_\perp$ is also affected by ECRH. We examine requirements to fundamental ECRH with a right-hand polarized monochromatic wave propagating along expanding magnetic field lines (magnetic beach). A single particle analysis is carried out numerically to determine the velocity distribution of electrons after a single passing through the ECRH zone.[5] The results are briefly summarized below.

Except few electrons which are reflected within the resonance zone, the velocity distributions, $F_i(W,\mu)$ before heating and $F_f(W,\mu)$ after heating, are connected by a heating response function $H(W,\mu:W',\mu')$ as,

$$F_f(W,\mu) = \int dW' \int d\mu'\ H(W,\mu:W',\mu')\ F_i(W',\mu').$$

Here

$$H(W,\mu:W',\mu') = P(W-W')\ \delta(\mu-\mu'-\frac{W-W'}{B_{R0}}),$$

where

$$P(\Delta W) = \frac{1}{\pi\sigma}\left[1-\left(\frac{\Delta W-u}{\sigma}\right)^2\right]^{-1/2},$$

for $u-\sigma < \Delta W < u+\sigma$, and $P(\Delta W)=0$ outside. The distribution parameters, u and σ, are determined by the following scaling equations,

$$u = 145\frac{L_B}{f}\tilde{E}^2 W_{\|R}^{-1/2},$$

$$\sigma^2 = 580\ \frac{L_B}{f}\tilde{E}^2 W_{\perp R}W_{\|R}^{-1/2}.$$

Here, the magnetic scale length $L_B = (dB/dz/B)^{-1}$ (in m) and the electric field strength $\tilde{E}$ (in kV/m) are evaluated at the location where the Doppler-shifted resonance condition $\omega - \omega_c = k_{\parallel} v_{\parallel}$ holds with the wave frequency at f GHz. The parallel and perpendicular energy, $W_{\parallel R}$ and $W_{\perp R}$, before heating should be evaluated at the location with $B = B_{R0}$ where the resonance condition $\omega = \omega_c$ holds. The above formulae can be applied to wide variety of heating configurations as far as adiabatic approximation holds in the absence of heating and a fraction of particles mirror-reflected in the resonance zone is negligibly small.

To simplify further analysis let us assume that at $B = B_0$ cold electrons have a distribution

$$F_0(W_{\perp}, W_{\parallel}) = \frac{1}{T_0} \exp\left(-\frac{W_{\perp}}{T_0}\right) \delta(W_{\parallel} - W_0).$$

Then the distribution at $B = B_{R0}$ before heating is written as

$$F_i(W, \mu) = \frac{1}{T_0} \exp\left(-\frac{B_0}{T_0}\mu\right) \delta(\mu - \frac{W - W_0}{B_0}).$$
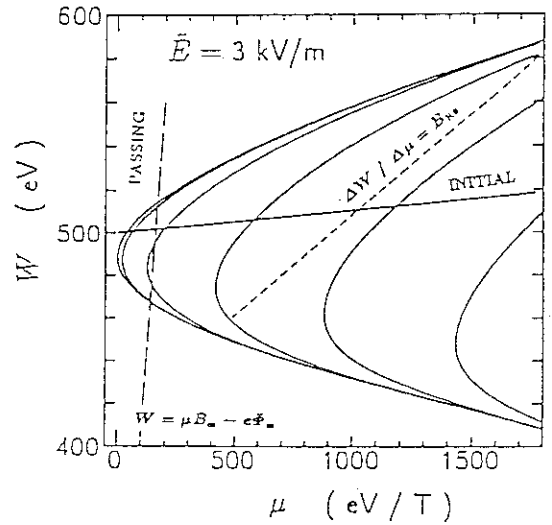
Using the heating response function, the distribution after ECRH with flat profile of wave field is obtained as

$$F_f(W, \mu) = \frac{B_0}{\pi T_0 \sigma_R (1 - B_0/B_{R0})}\left[1 - \frac{1}{\sigma_R^2}\left(\frac{W - W_0 - \mu B_0}{1 - B_0/B_{R0}} - u_R\right)^2\right]^{-1/2} \exp\left[\frac{B_0}{T_0}\frac{W - W_0 - B_{R0}\mu}{B_{R0} - B_0}\right].$$

Here,

$$\sigma_R = 24.08 \tilde{E}\left(\frac{L_B}{f}W_{\perp R}\right)^{1/2} W_{\parallel R}^{-1/4},$$

$$u_R = 145 \tilde{E}^2 \frac{L_B}{f} W_{\parallel R}^{-1/2},$$

$$W_{\parallel R} = W - \mu B_{R0},$$

$$W_{\perp R} = B_{R0}\frac{\mu B_{R0} - W + W_0}{B_{R0} - B_0}.$$

FIG.4. Velocity distribution of cold electrons after ECRH. Height of the contour increases by a factor e toward the left.

Contours of the final distribution are plotted in Fig.4 for the case of $W_0 = 500\text{eV}$, $T_0 = 10\text{eV}$, $\tilde{E} = 3\text{kV/m}$, $f = 2.45\text{GHz}$, $L_B = 0.566\text{m}$ and $B_0 = 0.01\text{T}$ as typical in the thermal dike experiment on GAMMA 10. The initial distribution which exponentially decreases along the straight line labelled "INITIAL " spreads along heating characteristics $dW/d\mu = B_{R0}$. The height of the contour increases by a factor of e toward the left and goes down to zero beyond the outermost contour on which the distribution is infinitely high. The singularity is due to the delta-function assumed for parallel velocity distribution.

For heated particles to be mirror-reflected before passing the mirror throat $B = B_m$, where the potential is $\Delta\phi_2 = \Phi_m$ above that at the resonance point $B = B_{R0}$, the coordinates (μ, W) should be below the dashed line $W = \mu B_m - e\Phi_m$. The probability R of mirror reflection is obtained by integrating the distribution below the boundary line. One of the double integral can be calculated analytically owing to the simplified initial distribution.

The probability of reflection is plotted in Fig.5(a) as a function of $\bar{E}$ for the case of GAMMA10 configuration. The potential Φ_m at the mirror throat $B = B_m = 3T$ is assumed to be 1000V, and the initial parallel energy W_0 which corresponds to the acceleration in the sheath surrounding the floating end wall is varied from 250 to 1000eV for temperature $T_0 = 2eV$. The increase of R with decreasing W_0 is due to increasing heating efficiency. The probability R increases as Φ_m decreases independently of heating. From these results the wave electric field is required to be more than 3 to 5kV/m to have noticeable contribution of thermal dike in the present configuration of the test experiment.

Same calculations are made for a tokamak case. A magnetic configuration with $B_0 = 1.5T$, $B_{R0} = 1.6T$, $B_m = 4.8T$ and (locally) $L_B = 20m$ can be created along the field lines connecting to a diverter plate by modifying an outer flux tube. By assuming $W_0 = 40$ eV and $T_0 = 20$ eV, R for different Φ_m is plotted against $\bar{E}$ in Fig.5(b). It is fortuitous that $R \sim 0.5$ can be achieved with $\bar{E} \leq$ 2-5kV/m similarly to Fig.5(a). Since required $\bar{E}$ scales with $L_B^{-1/2}$, its strength can be adjusted if tailoring L_B is available over several wavelengths.
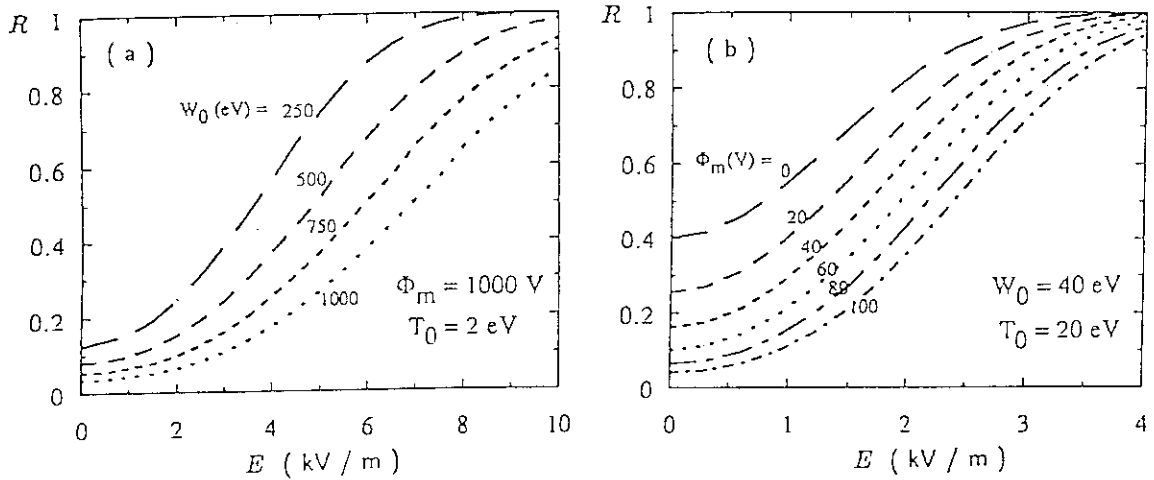

FIG.5. Probability of reflection is plotted as a function of wave field strength. Calculations are made for cases of tandem mirror (a) and tokamak (b).

4. Wave Launching System for Thermal Dike

It is well known that the absorption coefficient of wave power at the fundamental cyclotron resonance along a magnetic beach is close to 1. Calculations in the previous section indicate that the required strength of the wave field is not quite high. Therefore fundamental requirements to a wave launcher are to excite the right-hand polarized mode, to concentrate the power deposition within the associated magnetic flux tube and to avoid excessive heating much above required $\Delta W_\perp$. These do not present new difficulties, but an approproate tailoring of magnetic flux is required in connection with the wave launching.

In the basic experiment program of thermal dike on GAMMA10, we can expect observing a clear effect of thermal dike owing to small α. Because a large ratio of B_m/B_{R0} is advantageous to obtain small α, a magnetron source with frequency at 2.45 GHz is used, but the available power is limited to less than 5 kW. In order to have the wave field of 5 kV/m the wave power should be concentrated within a radius of 0.22 m. Therefore we are preparing a focusing hog-horn antenna as a lancher for this particular experiment. The experimental configuration is shown in Fig.6.

Due to spatial limitations the geometry of the antenna is made fat. But the closed wave-guide structure up to the opening mouth helps to prevent warm up of cryogenic pumping panels due to absorption of unwanted straying wave fields.
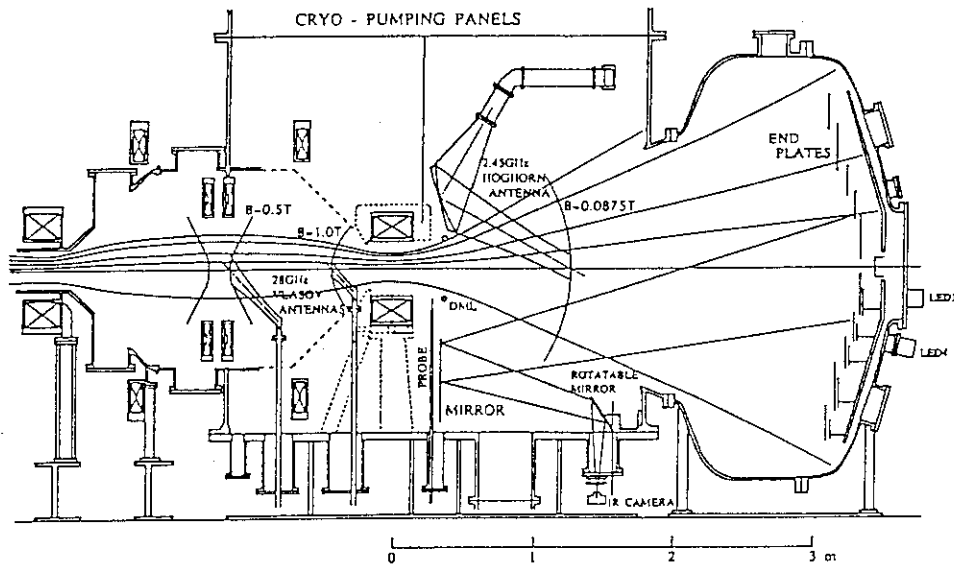

FIG.6. Schematic configuration of thermal dike experiment in an end region of the GAMMA 10 tandem mirror.

5. Conclusion

Thermal dike concept has appeared as a new application of ECRH technology. Theoretical analyses are made to define requirements to ECRH system. It is shown that the requirements can be moderated by properly tailoring magnetic field profiles. Basic experiment program of thermal dike on the GAMMA10 tandem mirror is described.

This research is supported by the Grant-in-Aid program of the Ministry of Education Science and Culture of Japan.

References

[1] K.Kurihara, Y.Kiwamoto, T.Saito, K.Yatsu, and S.Miyoshi, J. Phys. Soc. Jpn. 61, 3153 (1992).
[2] T.Saito, Y.Kiwamoto, K.Kurihara, T.Cho, M.Inutake, S.Miyoshi, T.Tamano and K.Yatsu, Phys. Fluids B 5, 866 (1993).
[3] K.Kurihara, T.Saito, Y.Kiwamoto and S.Miyoshi, J. Phys. Soc. Jpn. 58, 3453 (1989).
[4] T.Ohkawa, Kakuyugo-Kenkyu (J. Plasma and Fusion Research) 64, 305 (1990).
[5] Y.Kiwamoto, T.Saito, Y.Tatematsu, I.Katanuma, Y.Yoshimura and T.Tamano submitted for publication in Phys. Fluids B.

3.5 ECH Launching System for LHD and CHS

S. Kubo, K. Ohkubo, H. Idei, M. Sato, Y. Takita, and T. Kuroda

National Institute for Fusion Science
Nagoya, 464-01, Japan

INTRODUCTION

Electron cyclotron heating is a unique, reliable and indispensable method to produce and heat the plasma in the helical magnetic confinement system. High power ECH with total power up to 10 MW at 84GHz/168GHz is under design for the heliotron/torsatron type Large Helical Device (LHD). Experimental investigation of the ECH with both 200kW and 400kW gyrotrons at 53.2GHz is also underway in the similar magnetic field configuration but smaller machine, Compact Helical System (CHS). Recent experimental results indicate a clear advantage of the focusing beam. The design concept of ECH launching system for both CHS and LHD is reported.

INPORTANCE OF THE POWER DEPOSITION CONTROL

Normally, the port access to the plasma is bad in the helical system, because of the existence of a set of main magnetic field coils which helically turns around the torus. Furthermore, in the LHD, helical coil is superconducting magnet immersed in the bell jar which makes the port access worse. In the normal poloidal cross section, the mod-B surface structure is complicated as compared with that of tokamak, so that highly focused ECH beam is required to get well defined power deposition profile and to perform physically clear experiment.

Recent ECH experiment in CHS using Vlasov coupler, modified reflector, corrugated polarizer, and a steerable focusing mirror with 200 kW TE_{02} output gyrotron show a important effect of the power deposition profile and the polarization control [2].

Another feature to be stressed is that the ECH is realized as one of the powerful tools for the confinement investigation by using modulation technique [3]. In this sense, well defined power deposition profile is the critical prerequisite for performing the clear physical experiment.

ELLIPTIC GAUSSIAN BEAM

To get narrow power deposition profile, beams should be sufficiently focused on the mid-plane of the torus in the radial direction, but this strong focusing is not required in the toroidal direction because the slow change of mod-B structure along this direction. Gaussian optics indicates the narrow beam tends to expand faster than the wide one. Using this fact, adopting

elliptic Gaussian beam have a possibility to attain highly localized power deposition within the the port limitation. Using the elliptic Gaussian beam can reduce the peak power density at the heating region, keeping narrow power deposition profile. This fact might help to mitigate some unfavorable effects of the highly focused beam. To get this elliptic Gaussian beam with focusing mirror, the mirror surface is designed with the concept of the constant phase. The shape of the mirror surface can be derived from the matching condition of the waist size and phase front condition based on the elliptic Gaussian optics. This concept relies on the reflection law of the quasi-optical wave vectors, which is defined by the spatial gradient of the phase function of the Gaussian beam. For simplicity, consider the phase front of the symmetric Gaussian beams incoming and outgoing at the mirror in the e_{in}, and e_{out} direction The input and desired output phase function can be expressed by [4]

$$\Psi_{in}(r) = k\,r \cdot e_{in} - \eta\left((r - r_{w,\,in}) \cdot e_{in}\,,\, w_{0,\,in}\right) + \frac{k\left(\left|r - r_{w,\,in}\right|^2 - \left|(r - r_{w,\,in}) \cdot e_{in}\right|^2\right)}{2\,R\left((r - r_{w,\,in}) \cdot e_{in}\right)}\,,$$

and

$$\Psi_{out}(r) = k\,r \cdot e_{out} - \eta\left((r - r_{w,\,out}) \cdot e_{out}\,,\, w_{0,\,out}\right) + \frac{k\left(\left|r - r_{w,\,out}\right|^2 - \left|(r - r_{w,\,out}) \cdot e_{out}\right|^2\right)}{2\,R\left((r - r_{w,\,out}) \cdot e_{out}\right)}\,,$$

provided that the matching waist size $w_{0,\,in}$, $w_{0,\,out}$ and waist position $r_{w,\,in}$, $r_{w,\,out}$ for both beams are given. Here, the phase correction term and effective curvature radius is given by,

$$\eta(z, w_0) = \tan^{-1}\left(\frac{\lambda\,z}{\pi\,w_0^2}\right),$$

and

$$R(z) = z\left[1 + \left(\frac{\pi\,w_0^2}{\lambda\,z}\right)^2\right].$$

If the matching condition of the waist size at the mirror surface is satisfied, the shape of the mirror surface can be determined by the condition that $\Psi_i(r) + \Psi_o(r) = const.$, because the quasi-wave vector defined locally by taking the gradient of each phase front function like $k_i = \nabla \Psi_i(r)$, $k_o = -\nabla \Psi_o(r)$ for input and output beams, respectively. On the other hand, the local normal vector of the mirror surface can be defined by taking the gradients $n_r = \nabla(\Psi_i(r) + \Psi_o(r))$, which satisfies the reflection condition of the quasi optical wave vectors, $k_i - k_o = \alpha\,n_r$ on the mirror surface. These relations can be easily extended to the elliptic Gaussian beam by defining the independent waist size and position for two directions x, and y, perpendicular to the direction of propagation. The matching condition of the waist size can be determined numerically in the case that the input and output beam axis coincide. To guarantee the similar matching condition, the angle between input and output propagating axis

should be small. Actually, mirror configurations are determined by keeping this angle small under the given boundary condition.

The other method to get elliptic Gaussian beam is using the rectangular corrugated waveguide. The analysis and cold test show that the rectangular corrugated waveguide is one of the promising methods to get the elliptic Gaussian beam. The matching with the circular corrugated waveguide which is the most promising long distance transmission component, is also good[5].

DESIGN AND COLD TEST OF ELLIPTIC GAUSSIAN BEAM FOR CHS

Recently, 400 kW gyrotron is installed on the CHS in order to investigate the plasma confinement properties in the high electron temperature regime. This gyrotron generates Gaussian beam in contrast to the previous 200 kW gyrotron which oscillates TE_{02} mode. The quasi optical transmission system from these two gyrotron to the CHS is under construction. The launching system connected these quasi optical transmission line is designed with above mentioned concept. In Fig. 1 is shown the 1/e waist size evolutions of the designed beam along propagating direction. Solid line indicates that of radial direction. The waist in this direction is on the mid-plane of the CHS and is 15 mm in size. Dotted line indicates that of toroidal direction. From the requirement that the two well controlled beams must be injected from the same port of 300 mmϕ, the waist size of this direction should be optimized so that final focusing mirror width and beam width is minimized. Actually, the waist size of the toroidal direction is set 50 mm on the mid-plane. This size is selected so that the mirror size along toroidal direction become minimum under given distance from the mid-plane to the final mirror. In Fig.2a) and b) are shown the drawing of the new injection antenna system for CHS, here, two identical symmetric Gaussian beams from the quasi-optical transmission system generated by the 200 kW and 400 kW gyrotrons are injected from the vacuum window with the 1/e waist size of 25 mm and waist position on the window. The vacuum windows are made of 100 mmϕ C-face cut sapphire.
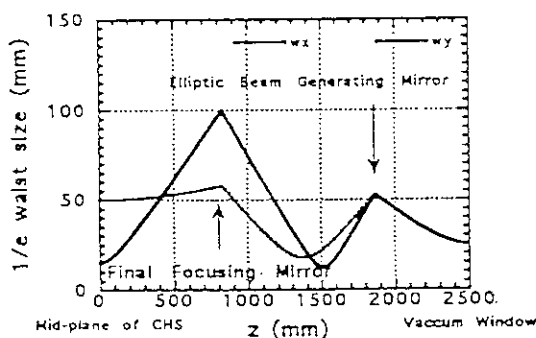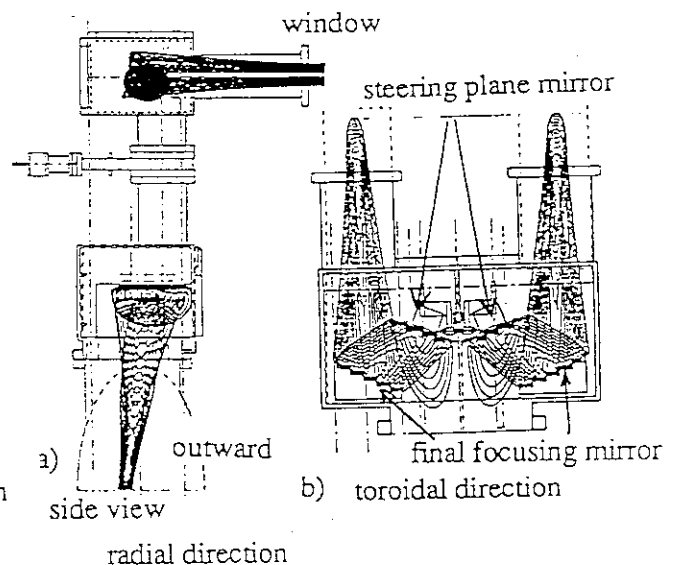

Fig.1   Waist size evloution along propagation

Fig.2 ECH launching system for CHS
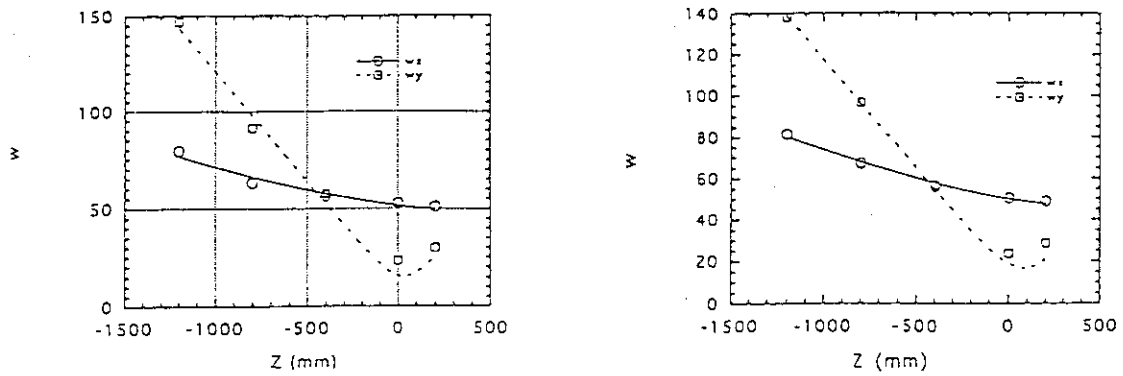
Fig.3 Measured beam waist size in for both launching system

a) #1 $w_{0,radial} = 15.4$ mm, $w_{0,toroidal} = 49.2$ mm

b) #2 $w_{0,radial} = 16.7$ mm, $w_{0,toroidal} = 46.3$ mm

These beams are at first converted by the elliptic beam generating mirror and shaped to the desired elliptic Gaussian beam by the final focusing mirror. These focused beam are directed to the desired direction in the poloidal plane by the steering plane mirrors. The result of the cold test for these two mirror sets are shown in Fig.3 a) and b). These figures show fairly in good agreement with the designed value. These cold tests demonstrated adequacy of the design concept. ECH experiment using these launching system is planned from December 1993.

PRELIMINARY DESIGN OF THE ANTENNA SYSTEM FOR LHD

LHD is the $m=2$ $l=10$ heliotron/torsatron type machine with the major and averaged minor radii, 3.9 and 0.6 meters, respectively. The main magnetic field is created by the super conducting helical coils surrounded by the bell jar, which makes the port access far from the plasma and special beam must be designed to get narrow power deposition profile. Total power of about 10 MW is required for the confinement experiment in the high electron temperature regime, where helical systems are expected to exhibit a specific feature theoretically. The present expectable power for unit ECH system is 1 MW. This means two or three launching systems should be installed on the limited port space on LHD. The similar physical requirements are posed also on LHD. The beam should be narrow as possible as one can in the radial direction.

The preliminary design of the injection antenna system is done using the similar technique. In Fig. 4 is shown the waist size evolution along propagating direction for several waist size on the mid-plane of the LHD with the focus mirror located 2.35 meters above mid-plane. The beam parameters for the LHD designed under the allowed port limitation at 84GHz are radially 15 mm and toroidaly 50 mm. Fig. 5 shows the preliminary design of the ECH launching system with focusing mirror, steerable plane mirror. Allowed beam size is limitted by the port space and long duct to the LHD vacuum vessel.

Spot size evolution

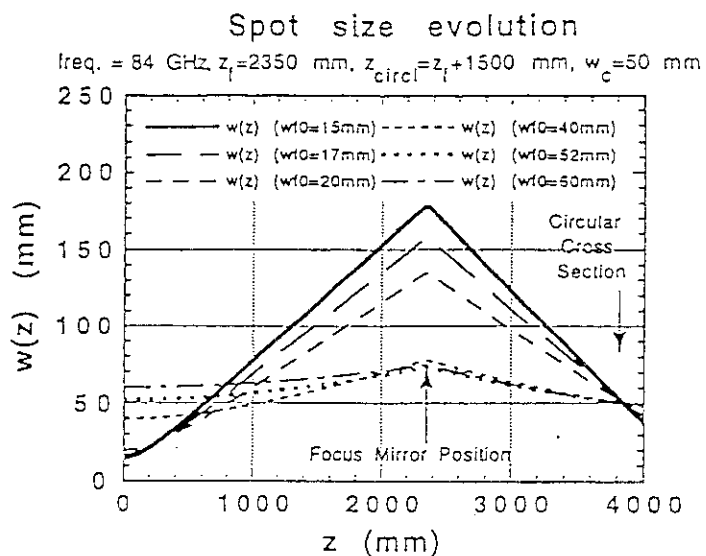freq. = 84 GHz z_f=2350 mm. z_{circl}=z_f+1500 mm, w_c=50 mm

Fig.4 Waist size evolution for various beam waists in case of focusing mirror set 2.35 meters above mid-plane.
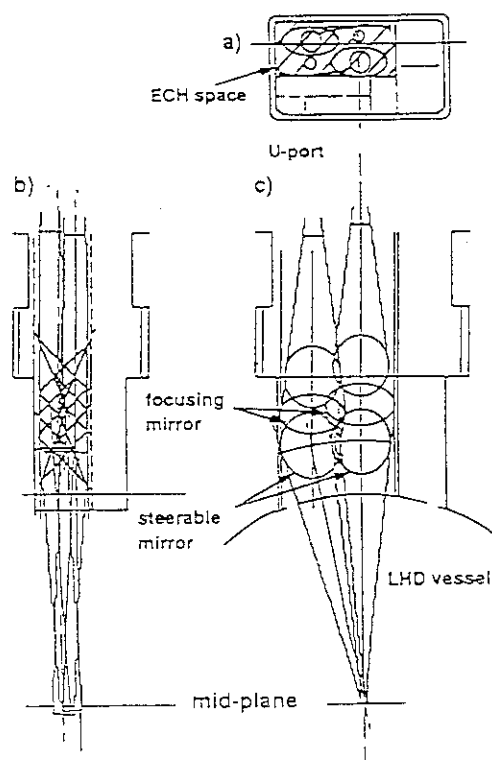

Fig.5 Design example of the ECH Launching system for LHD

SUMMARY

The effectiveness of the mirror surface definition for the focusing mirrors using constant phase concept is demonstrated and actually applied for the new antenna system for CHS.

Preliminary design of the ECH launcher for LHD is done based on the same idea. The minimum beam parameters are 15 mm in radial direction and 50 mm in toroidal direction under present allowed port space.

REFERENCES

[1]   S. Kubo et al.,Proc. Int. Workshop on 'Strong Microwaves in Plasmas', (1991) Vol.1, p.180.; S. Kubo et al Proc. 19th EPS (1992) Vol. 16c I-513.

[2]   H. Idei et al., Phys. Rev. Lett. 71(1993) 2220.

[3]   L. Gianonne et al.,Nucl. Fusion 32 (1992) 1985.

[4]   A.Yariv. Quantum Electronics (1967).

[5]   K. Ohkubo et al. Proc. 8th Joint workshop ECE and ECRH, Gut Ising Vol.II (1992), p.561.

Appendix List of Participants (including observeres)

EC	V.Bhatnagar	JET Joint Undertaking
	F.X.Soldner	JET Joint Undertaking
Germany	V.Erckmann	IPP Garching/ WVII-AS
France	G.Tonon	CEN Cadarache/ Tore Supra
	D.Moreau	CEN Cadarache/ Tore Supra
IAEA	V.Demchenko	Vienna, Austria
Italy	F. Santini	ENEA Frascati/ FTU
USA	R.Prater	GA/ DIII-D
	R.Callis	GA/ DIII-D
	C.Moeller	GA/DIII-D
	W. Baity	ORNL
	Y.Takase	MIT/ Alcator C-Mod
	R. Wilson	PPPL/ TFTR
	H.S. Staten	DOE
Japan	Y. Terumichi	Kyoto Univ.
	T.Watari	NIFS
	S.Kubo	NIFS
	S.Shiina	Nihon Univ.
	Y. Kiwamoto	Univ. of Tsukuba
	H. Arai	Yokohama National Univ.
	T.Shimada	Electrotechnical Lab.
	K.Miyamoto	Mitubishi Electric Co.
	N.Kobayashi	Toshiba Co.
	M.Ikeda	Sumitomo Heavy Industries Ltd.
	T. Sekiguchi	JAERI
	S.Tamura	JAERI
	Y.Tanaka	JAERI
	T.Yamamoto	JAERI
	H.Kimura	JAERI
	T.Imai	JAERI
	K.Hoshino	JAERI
	H.Kawashima	JAERI
	T.Ogawa	JAERI
	K.Ushigusa	JAERI
	O.Naito	JAERI
	T.Fujii	JAERI
	M. Saigusa	JAERI
	S. Moriyama	JAERI
	Y. Ikeda	JAERI
	S.Ide	JAERI
	M.Seki	JAERI